A NUMERICAL MODELING APPROACH FOR TRANSFORMATION-INDUCED FAILURES

BY

ABBA ABDULHAMID ABUBAKAR

A Thesis Presented to the
DEANSHIP OF GRADUATE STUDIES

KING FAHD UNIVERSITY OF PETROLEUM & MINERALS
DHAHRAN, SAUDI ARABIA

In Partial Fulfillment of the
Requirements for the Degree of

MASTER OF SCIENCE
In

MECHANICAL ENGINEERING

MAY, 2014

KING FAHD UNIVERSITY OF PETROLEUM & MINERALS

DHAHRAN- 31261, SAUDI ARABIA

DEANSHIP OF GRADUATE STUDIES

This thesis, written by ABBA ABDULHAMID ABUBAKAR under the direction of his thesis advisor and approved by his thesis committee, has been presented and accepted by the Dean of Graduate Studies, in partial fulfillment of the requirements for the degree of **MASTER OF SCIENCE IN MECHANICAL ENGINEERING.**

Dr. Sohail S. Akhtar
(Advisor)

Dr. Zuhair M. Gasem
Department Chairman

Dr. Abul Fazal M. Arif
(Member)

Dr. Salam A. Zummo
Dean of Graduate Studies

Dr. Khaled S. Al-Athel
(Member)

10/6/14
Date

Dedication

Dedicated to my Family

ACKNOWLEDGMENTS

Foremost, I would like to express my sincere gratitude to my advisor Dr. Syed Sohail Akhtar for the continuous support of my MSc study and research, for his patience, motivation, enthusiasm, and immense knowledge. His guidance helped me in all the time of research and writing of this thesis. I could not have imagined having a better advisor and mentor for my MSc study.

Besides my advisor, I would like to thank the rest of my thesis committee: Prof. Abul Fazal M. Arif, and Dr. Khalid Al-Athel, for their encouragement, insightful comments, and hard questions. I would also like to extend my sincere gratitude to my graduate coordinator, Dr. Esmail M. A. Mokheimer, and the mechanical engineering chairman, Dr. Zuhair M. Gasem, for giving me all the required support at KFUPM.

I thank my fellow labmates in Stress Analysis Lab.: Khalid Naseem, Osama Siddiqui, and Aliyu Arisekola, for the stimulating discussions, and for the sleepless nights we spent together. Also I thank all my friends in KFUPM.

My appreciation also goes to Dr. Abubakar B. Aliyu, Dr. Ibrahim I. Jidda, Dr. Ibrahim Abdullahi, Dr. Abdullahi A. Adamu and all other lecturers at the department of mechanical engineering, Bayero University Kano (B.U.K.). They spent a lot of effort in training me to become a good engineering student during my five years of Bachelor degree study. I also appreciate all supports given to me by B.U.K. during my graduate study at KFUPM.

Last but not the least; I would like to thank my parents, my entire family, and the Nigerian community at KFUPM for supporting me spiritually throughout my study.

TABLE OF CONTENTS

LIST OF TABLES

LIST OF FIGURES

LIST OF ABBREVIATIONS

PFM	:	Phase Field Method or Model
FEA	:	Finite Element Analysis
FEM	:	Finite Element Method
m-phase	:	Monoclinic phase
t-phase	:	Tetragonal phase
YSZ	:	Yttria Stabilized Zirconia
TBC	:	Thermal Barrier Coating
TGO	:	Thermally Grown Oxide
APS	:	Air Plasma Sprayed
EB-PVD	:	Electron-Beam Physical-Vapor Deposition
HTHC	:	High Temperature Hot Corrosion
LTHC	:	Low Temperature Hot Corrosion
PRZ	:	Planar Reaction Zone
MIRZ	:	Melt Infiltrated Reaction Zone
AISI	:	American Iron and Steel Institute
RVE	:	Representative Volume Elements

PDE	:	Partial Differential Equation
ODE	:	Ordinary Differential Equations
B.C.	:	Boundary Condition
FDA	:	Finite Difference Approximations
BDA	:	Backward Difference Approximations
WBM	:	Wheeler-Boettinger-McFadden
KKS	:	Kim-Kim-Suzuki
CALPHAD	:	Calculation of Phase Diagram
DICTRA	:	Diffusion-Controlled Transformations
SEM	:	Scanning Electron Microscopy
XRD	:	X-ray Diffraction
EDS	:	Energy Dispersive Spectrometry
BCC	:	Body Centered Cubic
HCP	:	Hexagonal Closed Packed

THESIS ABSTRACT (ENGLISH)

Full Name : ABBA ABDULHAMID ABUBAKAR

Thesis Title : A Numerical Modeling Approach For Transformation-Induced Failures

Major Field : Mechanical Engineering

Date : May, 2014

Phase transformations have a significant impact on the mechanical behavior of materials. Sometimes they are induced by diffusion of a chemical species from the external environment. Two cases of diffusion-induced phase transformations considered in the current work are the hot corrosion of Thermal Barrier Coatings (TBCs) and gas nitriding of steel.

As a result of diffusion of V_2O_5, transformation of zirconia from the monoclinic to tetragonal phase occurs during the hot corrosion of TBCs. Due to the 4-5% volumetric expansion that is associated with the transformation, high stresses are developed in the material which leads to the failure of the material.

Similarly, the evolution of the diffusion and compound layers during the two-stage controlled gas nitriding of AISI H 13 tool steel result in the development of residual stresses due to the volume misfit and difference in the mechanical properties of the coexisting phases. The high magnitudes of the residual stresses, especially at the sharp corners of Aluminum extrusion dies, results in severe brittleness and subsequent failure of the dies.

In the current work, the kinetics of microstructure evolution during the aforementioned phase transformations is estimated using a Phase Field Model (PFM) that is coupled with elasticity. The model is validated by comparison with experimental results. The failure stresses that develop during the transformations are accurately predicted. Commercial finite element package, COMSOL Multi-physics 4.3 is utilized for the numerical implementation. The results show that the model can be used in predicting transformation-induced failures.

THESIS ABSTRACT (ARABIC)

ملخص الرسالة

الاسم الكامل:أبا عبدالحميد أبوبكر

عنوان الرسالة:إستخدام طريقة النمذجة العددية لتوقع التغير فى الطور المسبب للإنهيار الميكانيكى

التخصص:الهندسة الميكانيكية

تاريخ الدرجة العلمية: مايو 2014

التحولات في الطور تأخذ تأثيرا مهما في السلوك الميكانيكي للمواد. وفي بعض الأحيان تعزز هذه التحولات بعمليات إنتشار الجزيئات الكميائية من البيئة المحيطة.فى هذه الرسالة تم التركيز على حالتين لتوقع التغير فى الطور عن طريق الإنتشار هما التآكل الساخن لطلاء الجدار الحرارى (TBCs) و إنتشار النيتروجين فى الحديد.

نتيجة لإنتشارأوكسيد الفناديوم (V_2O_5)، تحولت الزيركونيا من الطور الآحادى الى الطور الرباعى خلال التأكل الساخن لطلاء الجدار الحرارى. نتيجة للزيادة الحجمية بمقدار 4-5% المصاحبة للتحول تكونت إجهادات عالية فى مادة الزيركونيا (الطبقة الخارجية) هذه الإجهادات سببت الفشل الميكانيكى.

وبالمثل، فإن تشكيل طبقة الإنتشار والطبقة المركبة خلال مرحلتي إنتشار النيتروجين فى قالب الحديد(AISI H 13) نتج عنه تكوين و نمو الاجهادات المتبقية نتيجة عدم للزيادة الحجمية و الفرق في الخصائص الميكانيكية لأطوار الترافق.نتيجة للأجهادات العالية المتبقية وبالأخص فى اركان قوالب الألمونيوم المستخدمة فى البثق أدت الى هشاشة القالب. وفي النهاية إلى إنهيار القالب.

في هذه الدراسة الحالية، قدرت حركية التطور الجزئي التركيبى خلال التحولات المذكورة آنفاً باستخدام نموذج مجال الطور(PFM) المدمج مع المرونة والذي تم تقييمه بالمقارنة مع النتائج المعملية. ايضا تم توقع اجهادات الانهيار خلال تحولات الطور بدقة. وقد استخدمت في هذه الدراسة ايضا النسخة التجارية من برنامج العناصر المحددة (finite element package, COMSOL Multi-physics 4.3) لتنفيذ النموذج العددي. وقد أثبتت النتائج فعاليةالنموذج في تحليل إجهادات التحول المسببة للإنهيار.

CHAPTER 1

INTRODUCTION

Phase transformation in materials is among the broadest fundamental scientific fields. Its importance with regards to the design of advanced engineering alloys and new materials cannot be overestimated. Phase transformation in materials is sometimes a desirable process which results in the production of new precipitates that enhance the overall physical and mechanical properties of the material. However, in other cases it is disastrous, as it results in the formation of new phases that become a source of weakness or failure for such materials.

Thermal Barrier Coatings (TBCs) are highly advanced coating materials that are usually applied to turbine blades that operate at very high temperatures in order to increase their thermal and corrosion resistance. The use of TBCs in turbine blades results in tremendous improvement in the efficiency and performance of the thermal system. New phases evolve in the top coat of TBC due the use of low grade fuels in driving land-based turbine blades. This is caused by the reaction between the corrosive impurities in the fuel and the top coat material. Consequently, drastic changes in the mechanical, chemical and physical properties of the coating material lead to the subsequent failure of the system.

Nitriding is one of the most common surface-hardening processes for steel. It is mainly carried out in order to improve the fatigue strength, surface hardness, wear and corrosion resistance of such material. It is commonly used in transmission mechanical components such as gears, camshafts, valve parts, screws, forging dies, extrusion dies, e.t.c. Gas nitriding is the most common method of nitriding AISI H13 tool steel that is used for Aluminium extrusion dies. It involves diffusion of atomic nitrogen into the steel surface by holding it in a controlled environment of nitrogenous gas at a suitable temperature. Despite the fact that the gas nitriding of AISI H13 tool steel is performed using a computer-controlled system, an excess amount of nitrogen diffuses into the material during such process. The excess nitrogen atoms result in the formation of new phases and compositional strains in the microstructure of the material. Eventually, high brittleness and residual stresses causes decrease in the lifetime of extrusion dies.

The research to be carried out in the thesis is focused on the development of a model that can accurately predict the constitutive behavior of TBCs and AISI H13 tool steels during the phase transformations that occur in the materials. As mentioned previously, the new phases in the TBC material evolve due to the diffusion of V_2O_5 during the hot corrosion attack of land-based turbine blades. While the new phases in the AISI H13 tool steel evolve due to the diffusion of excess nitrogen during the two-stage controlled nitriding process.

1.1 Problem Definition

A lot of engineering materials fail due to their interaction with the external environment. In most cases, the prediction of the failure mechanism of such materials is nearly impossible using the common constitutive equations for such materials. In the literature, most of the developed models are limited to the cases where mechanical loads are the main cause of failures. However, certain scenarios involve the failure of solid materials due to their chemical interaction with the environment. Thus, there is need to develop a general numerical approach that can be used to model transformation-induced failures. In the current work, a model for transformation-induced failures in materials will be developed. The model will be tested on the failure of TBC due to V_2O_5 hot corrosion, and the failure of hot extrusion dies during the two-stage controlled nitriding process.

Previous experiments showed that, the hot corrosion reaction occurs in the top coat of TBC between a molten salt (V_2O_5) and Yttria-Stabilized Zirconia (YSZ) at high temperatures[**1**,**2**]. These reactions result in the formation new phases, YVO_4 and the monoclinic phase of zirconia. The overall effect of the evolution of these different phases is the volumetric expansion of the coating by 4-5%, the development of localized stresses in the coating, the formation of horizontal cracks and subsequent failure of the system[**3**,**4**].

Despite the use of computers in the control of gas nitriding process in AISI H13 tool steels, an excess amount of atomic nitrogen diffuses into the material. This causes the formation of a new phase that is normally called the compound layer. Eventually, residual stresses are developed due to the mismatch in the mechanical properties of the coexisting phases. Furthermore, the diffusion of the excess atomic nitrogen causes additional stresses due to the lattice expansion of the coexisting phases. The overall effect of the residual stresses is the decrease in the performance efficiency and lifetime of Aluminum hot extrusion dies.

In the current research, the Phase Field Method (PFM) will be used to develop a model for the phase transformations that occur during V_2O_5 hot corrosion of TBCs and gas nitriding of AISI H13 tool steels respectively. The phase transformation will be coupled with elasticity in order to predict the resulting stress field that leads to the failure of the systems. Consequently, more will be understood regarding the failure mechanism of the materials.

1.2 Methodology/Approach

Phase Field Method (PFM) has been selected as the main numerical approach for modeling of the phase transformations. It is an extremely versatile and powerful method of modeling solid-state phase transformations at mesoscale. The PFM will be coupled with elasticity in order to determine the mechanical behavior of the system during the phase transformations. Finite element technique will be utilized for the numerical implementation of the developed model.

The PFM is a general computational approach for solving interfacial problems. It was derived based on thermodynamic principles by Cahn and Hilliard [**5**] and Allen and Cahn [**6**]. PFM treats interfaces as surfaces of finite thickness using continuous field variables. Through minimization of the free energy functional of the thermodynamic system, sets of partial differential equations (PDEs) are developed using the Cahn and Hilliard [**5**] and Allen and Cahn [**6**] theorems. The numerical solution of the PDEs gives the evolution of the coexisting phases in terms of space and time. PFM is very useful in studying the phenomenon of phase transformations, because of the various advantages associated with the approach. It is less computationally intensive as compared to the sharp interface model, as there is no need to explicitly track the interface during the transformation. It is more powerful than other diffuse-interface methods, due to the fact that various energy contributions (chemical, elastic, electrostatic and magnetostatic) can be naturally integrated into the model.

However, virtually all of the previous phase field models for solid-state phase transformations were used in predicting phase evolution due to either martensitic transformation or the transformation is induced by diffusion within the microstructure. Recently, Wen et al. [**7**] proposed PFM for solid-state phase transformations that are induced by diffusion from external source. They demonstrated that, the model can be used to model oxidation, sulfidation or any corrosion process provided the various material (input) parameters are calibrated accurately.

For this reason, the present study mainly involves the application of the proposed model to a practical corrosion process, the V_2O_5 hot corrosion of TBC, in order to predict the microstructure evolution during the hot corrosion of the top coat. Additionally, the model will be used to predict the kinetics of the two-stage controlled nitriding process in Aluminum extrusion dies. Even though Wen et al. [**7**] did not couple the model with material constitutive equations, the PFM in the present study will be coupled with elasticity in order to predict the stress fields that are induced by the phase transformations. Commercial finite element packages, COMSOL Multiphysics 4.3 will be utilized for the analysis.

1.3 Motivation/Objectives

Frequent failure of turbine blades due to the hot corrosion attack has been one of the major sources of concern for Saudi Arabia energy companies. This is due to the cost and safety implications of gas turbines in the industries. In view of this, there has been active research on the development of a better surface coating technology for high temperature components such as turbine blades. Therefore, the current research work is not only important to the Saudi Arabia energy companies but also to aerospace industries. On the other hand, Aluminum extrusion dies are usually exposed to high pressure, temperature and frictional forces at the die-bearing surface during operation. The evolution of new phases during the gas nitriding of the die surfaces causes the development of residual stresses which reduce the performance of the die.

Having made a thorough literature search, it was found out that the modeling of TBCs failure due to V_2O_5 hot corrosion has not been carried out. Most of the experiments carried out were limited to the identification of the various phases that evolves during the process. In particular, the mechanical behavior of the materials during the hot corrosion process has not been fully understood. This is attributable to the localized nature of the degradation process and the high temperature that is involved. So, the PFM will be adopted in modeling the V_2O_5 hot corrosion of TBCs.

Similarly, the PFM has not been used to predict the residual stresses that are developed during the two-stage gas nitriding of AISI H13 tool steels. Similarly, most of the experiments performed previously were limited to the identification of the evolving phases. This is caused by the lack of proper instruments that can fully track the kinetics of the process. So, the PFM will be used to predict the kinetics of the nitriding process as well as the associated residual stresses.

The objective of the current work is to develop a numerical modeling approach for transformation-induced failures. The model will be applied to predict the failure stresses associated with the V_2O_5 hot corrosion of TBC and gas nitriding of AISI H13 tool steels. This will give more insight on the failure mechanism of the material systems.

1.4 Outline

Chapter 2 provides a detailed literature review on the fundamentals of the phase field theory and its applications to phase transformations in materials. Chapter 3 gives a brief review of the TBC system and its interaction with corrosive fuel impurities. Then, a brief theoretical background and review of the nitriding process in steel follows in Chapter 4.

Chapter 5 presents the proposed system model and research methodology in detail. Some details regarding the numerical implementation are dealt with in Chapter 6. Simulation results and discussions are provided in Chapters 7 and 8. The thesis ends with conclusions and recommendations in Chapter 9.

CHAPTER 2

FUNDAMENTALS OF THE PHASE FIELD METHOD

In this chapter, a general review of the primary computational technique that is used in the current work, the Phase Field Method (PFM), is made. After the method is fully introduced, a thorough review of the history and applications of the method is given. Then, the basic theory of the method follows, together with the associated numerical schemes. Finally, the challenges associated with the phase field method are discussed.

2.1 Introduction to Phase Field Model

In the literature, two different methods have been used to model phase transformations: **thermodynamic-based models** [**8**,**9**] which provides information more related to the thermodynamics of transformation and **crystallographic-based models** [**10**,**11**] which gives more information related to the crystallography of the transformation. However, none of the aforementioned methods can predict the complete thermodynamics and kinetics of phase transformations.

Another previous approach for modeling of phase transformations, **the sharp-interface model**, involves explicit tracking of the interface (of undefined thickness) between the growing and the parent phase by defining sets of interfacial boundary conditions. The method requires intensive computation due to the need for solving a set of differential equations for each interface. This makes the method to be strictly applicable to very simple multi-phase system. Computation of microstructure evolution using the sharp-interface method is mostly done using DICTRA [**12**,**13**].

A more recent approach, which defines the interface as a 2D object of finite thickness is called the **diffuse-interface model**[**14**]. It does not involve explicit tracking of the interface between the coexisting phases, and the numerical difficulty associated with the sharp-interface model is avoided. In this method, phase-field variables are used to represent the evolving microstructure in terms of space and time. The interfacial movement is implicitly given by the sets of PDEs for the evolution of the phase field variables, and constitutive equations or boundary conditions do not need to be defined at the interface. The most popular diffuse-interface models in the literature are: Cellular Automata[**15**], Level Set Method [**15**]and the Phase Field Method [**15**].

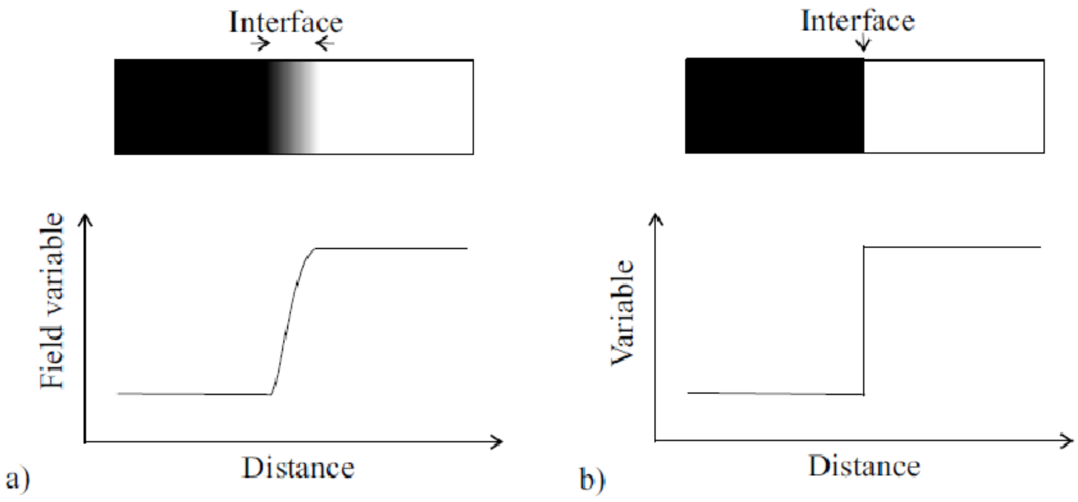

Figure 1: (a) Diffuse-Interface, and (b) Sharp-Interface models [14**]**

The phase field method is the most recent and fully-developed diffuse-interface method of simulating phase transformations. It uses a set of phase field variables (with smoothly varying interfacial properties) in tracking the evolution of the coexisting phases. The method can accurately predict the complete thermodynamics and kinetics of phase transformations in materials [**12**]. Phase Field Model has wide applications in:

microstructure evolution, solidification dynamics, viscous fingering and vesicle dynamics, fracture/crack dynamics, and dislocation dynamics.

2.1.1 Advantages of PFM

The following are some of the advantages of the PFM [**12**]:

- The interface equation becomes less complex as it is a simple reaction-diffusion equation
- The governing equations are far less than the number of particles in the system
- Result in models that are suitable for visualization of microstructure evolution
- Surface tension, which is naturally present at the interface, is automatically included
- Topological changes, such as pinching off or merging of interfaces, are easily treated

2.1.2 History of the Phase Field Method

The first use of a typical phase field model dates back to last few centuries when Van der Waals [**16**] modeled a two-phase system by means of a density function that varies smoothly across the interface. More than a century after, Ginzburg and Landau [**17**] used a complex-valued order parameter to develop a model for superconductivity; Cahn and Hillard [**5**] developed a thermodynamic relation describing multi-phase systems having diffuse interface. Hohenberg and Halperin [**18**] and Gunton et al. [**19**] later developed the stochastic theory describing the dynamics of phase transformations based on phase-field equations. However, microstructural modeling of diffuse-interface phase transformations was introduce only in the 1980s.

Chen [**20**]and Wang [**21**] developed the first type of phase field model that is developed from microscopic theory. In the model, phase field variables were related to local composition and long-range order parameters which can be used to distinguish the various phases. The model was successfully applied to solid-state phase transformations (e.g. precipitation [**22**], martensitic transformations [**23**], e.t.c.). Miyazaki [**24**] and Onuki and Nishimori [**25**] also applied the theory to simulate spinodal decomposition.

Langer [**26**] was the first to explore the second type of phase field model which is based on phenomenological phase-field theory. The model was used initially to model phase transformations during solidification phenomenon without the need for explicit tracking of the solid-liquid interface. Fruitful improvement in the phenomenological phase-field theory came later from the works of Caginalp and Fife [**27**], Kobayashi [**13**], Penrose and Fife [**28**], Wang et al. [**29**], Wheeler et al [**30**], Kim et al. [**31**], Karma [**32**], e.t.c.

Multiphase-field models were later developed by Steinbach et al. [**33**] and Wang et al.[**34**]. Vector-valued phase field model for the simulation of grain orientations in microstructure was also developed by Kobayashi et al. [**35**]. A common problem associated with phase field theory is that, the numerical convergence of the governing PDEs is difficult to be attained for atomic-length scale simulations. In view of this, the phase field crystal model, which allow the modeling of microstructure evolution at atomic scales and diffusive time scales was recently formulated [**36**,**37**,**38**].

Recently, better understanding of phase transformation is achieved through computations. Phase field method is the most recent and fully developed approach that is used to simulate microstructure evolution at mesoscale level. Unlike other models, PFM allows the thermodynamics and kinetics data associated with phase transformations to be fully incorporated. Since its full development, the phase field method has been widely used in the simulation microstructure evolution in materials. Reporting all the previous work as found in the literature is nearly impossible. However, Table A.1 in Appendix A summarizes the latest applications of Phase Field Model as found in the most recent papers in the open literature.

2.1.3 Phase Field Model of Diffusion-Induced Phase Transformations

Coupling of kinetic equations with diffusion equations in a multi-phase field model was previously achieved [**39**,**40**,**41**]. Similarly in another paper, kinetic cross-coupling between phase field and concentration field was used to develop a phase field model for isothermal transformations in binary alloys and step dynamics in molecular-beam-epitaxy [**42**]. The dynamics of first-order reaction solute precipitation and dissolution was also modeled using phase field approach by Xu et al. [**43**]. In contrast to temperature for solidification, solute concentration was used as the conserved variable which controls the process. Asymptotic analysis was carried, and validation of the model with 1-D solute dissolution/precipitation problem was accurately done [**43**].

A non-isothermal phase model for diffusion-induced hydride precipitation in Zirconium was also formulated by Ma et al.[**44**]. The concentration of the diffusing species, hydrogen, was represented by the concentration field, while the precipitated hydride was represented by the order parameter. The long-range (elastic) interaction term was incorporated in the free energy functional in order to predict the transformation-induced stress field, based on the Khachaturyan microelasticity theory [**45**].

A phase field formulation of diffusion-induced cracking during the stress corrosion of metals in aqueous environments was developed recently. Hydrogen concentration was represented by the concentration field, while the fractured region was represented by the phase field. The model was coupled with elasticity theory, and the results accurately predicted the failure of metals due to stress corrosion.[**46**].

A Galerkin finite element approximation for the solution of diffusion-controlled solid-state phase transformation in binary alloys was developed. Due to the fact that, the Cahn-Hillard diffusion equation is of 4th order and the thermo-elastic equations are of 2nd order, a mixed-order finite element discretization was used for the computation. The model qualitatively predicted the nucleation and growth of the intermediate phase in a thin-film diffusion couple with elasticity effects [**47**].

Tijjani et al. [**48**] was the first to develop a phase field model for microstructure evolution during nitriding process in low-carbon steel. The order parameter was coupled to the concentration field using a common free energy function, and sets of partial differential equations governing the phase transformations in the compound layer were formulated. The results show close qualitative and quantitative agreement with experiments. The short coming of their model is that they assumed a simple one-stage nitriding process which is no longer used in the industries. Furthermore, the elastic interaction due to the experimentally observed compositional straining of the nitride layers is not incorporated in the model.

Hierarchical coupling of finite element method and phase field model was done in order to analyze the deformation behavior of low carbon steel during austenite-to-ferrite phase transformation. As previously confirmed by Greenwood and Johnson, the transformation plasticity in the weaker phase was predicted using the thermo-elastic-plastic constitutive equations that were developed. Comparison of the simulation results with experimental observations lead to better understanding of the origin of transformation plasticity, quantitatively [**49**].

Recently, a phase field model was proposed for the modeling of corrosion kinetics under dual oxidants by Wen et al. [**7**]. Phase-dependent diffusivities and simple free energy models were used to demonstrate that the model can accurately predict the kinetics of corrosion processes with proper calibration of the simulation parameters. The essential difference between the proposed model (by Wen et al. [**7**]) and the previous diffusion-induced models is that, the phase transformation proceeds along the depth of the material. Furthermore, unlike the previous diffusion-induced transformations (where diffusion occurs within the microstructure), the phase transformations due to the corrosion process are induced by the diffusion of chemical species from external source.

In the current work, the phase field model proposed by Wen et al. [**7**] is applied to the high temperature V_2O_5 hot corrosion of TBCs and gas nitriding of AISI H13 tool steel. The concentration of the chemical species diffusing into the microstructure is coupled with the order parameter/phase field variable using the homogenous free energy function that was developed by Kim et al. [**31**].The model will be coupled with elasticity in order to predict the transformation-induced (failure) stresses. The effect of the processes on the mechanical behavior of the materials will be carefully studied. Finite element technique will be used for the numerical solution of the governing PDEs using the commercial finite element code, COMSOL Multiphysics 4.3.

2.1.4 Basics of the Phase Field Model

Phase Field Variables

As mentioned previously, the phase field method employs sets of field variables to represent the evolution of microstructure in a given material. These are variables that are used in tracking the various phases in a given microstructure in terms of space and time. Two class of phase field-variables are used in the literature, i.e. the conserved field-variable and the non-conserved field-variable [**12**].

Conserved field-variables are used in representing quantities (such as mass or molar fraction, concentration and temperature) that that obey the principle of mass conservation [**12**]. In other words, the volumetric integral of such variables at any given time in the domain is constant, as represented in Equation (2.1).

$$\int c_i \, dV = n_i \qquad (2.1)$$

Where,

$c_i = concentration\ of\ a\ given\ phase\ in\ the\ system$

$V = Total\ volume\ of\ the\ material$

$n_i = total\ number\ of\ moles\ of\ such\ phase\ in\ the\ system, a\ constant$

Conserved field-variables are normally used in diffusion-induced phase transformations such as transformations during spinodal decomposition [**50**], corrosion [**7**] , nitriding [**48**], binary phase transitions in alloys [**31**], e.t.c.

On the other hand, non-conserved phase-field variable does not obey conservation principles or laws and represents information regarding the type, structure and order of a given phase in the microstructure. Two types of non-conserved field-variables are used, the **order parameter** (η) and the **phase-field** (ϕ). For some systems, the order parameter is the same as the phase field. It is important to also note that, the more the number of phase-fields or order parameters, the more the complexity of the model [**12**].

The concept of order parameter originated from the Laudau theory [**51**] of phase transformations. It was used to identify a phase of given symmetry and order during a phase transformation that involves symmetry reduction. Order parameters are mostly used in describing martensitic or diffussionless phase transformations in materials. For example, in martensitic tetragonal-to-monoclinic phase transformation that was developed by Mamivand et al. [**52**], three order parameters were used to define the 3 variants of the monoclinic phase. Order parameters have values that range from -1 to 1. A point with order parameter of 1 signifies existing sublattice/phase, -1 signifies non-existing sublattice or phase, and 0 signifies unstable or disordered phase. Any value that falls between -1 to 0 and 0 to 1 signifies an interface. Order parameters are demonstrated in Fig. 2.

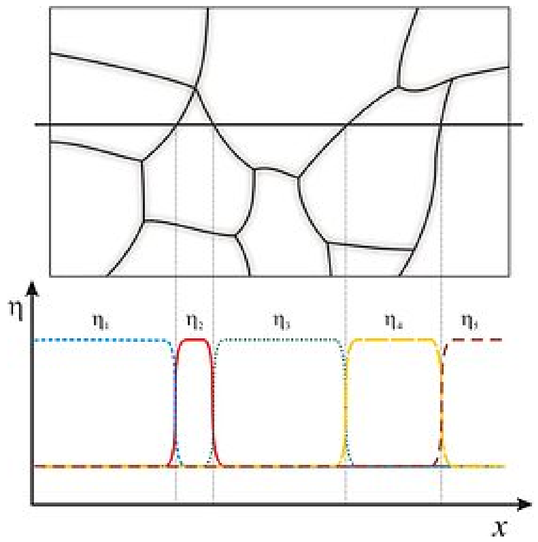

Figure 2: Multiple phase microstructure and order parameter profiles [**53**]

On the other hand, the concept of the phase-field originated by Langer [**26**]. It was used initially in identifying the phases that exists during solidification of materials. Later, Chen [**20**] and Wang [**29**] defined the order parameter in same way as the phase-field, with which the various phases coexisting within a microstructure can be identified. The phase-field has value that ranges from 0 to 1 (or -1 to 1); with 0 and 1 (or -1 and 1) denoting a given phase, and values falling between 0 and 1 (or -1 and 1) denoting an interface. An important property of the phase-field is that, the sum of all phase fields at a point is 1, the summation rule. The rule is mathematical represented as follows [**12**]. A diagrammatical description of the phase field is given in Fig.3.

$$\sum_{i=1}^{n} \phi_i = 1\,;\ \phi_i \geq 0\ or\ \phi_i \geq -1\,, \forall n \tag{2.2}$$

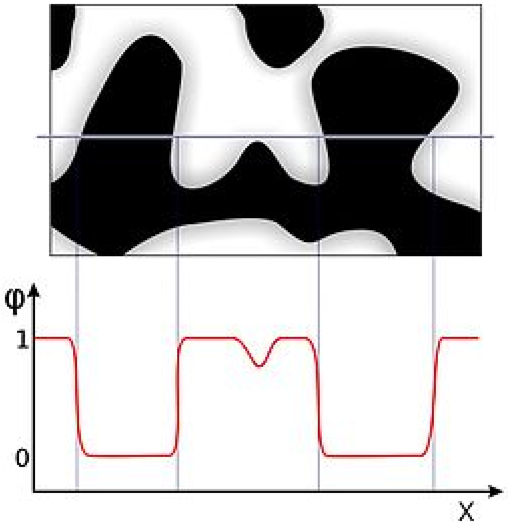

Figure 3: Two phase microstructure and the phase field profile [53]

Thermodynamic Energy Functional

Thermodynamically, microstructure evolution is only possible when the transformation occurs in such a way that total energy of the system reduces. Every phase of a given system has its own specific energy requirements for it to be stable. The thermodynamic energy functional is a summation of the functions of all the thermodynamic energy quantities associated with the phase transformation. Two of the thermodynamic quantities of interest with regards to microstructure evolution are: **Free Energy** and **Entropy**. For non-isothermal phase transformations, the entropy of the system is usually chosen as the thermodynamic driving force. However, free energy is mostly taken as the transformation driving force for isothermal solid-state phase transformations in the phase field literature.

Free Energy Functional

As said previously, the driving force for phase transformations comes from the total free energy of the thermodynamic system. Phase transformation is only possible if transition occurs in such a way that the total free energy of the system decreases. Thus, phase transition occurs when a system tries to attain equilibrium configuration by changing from state of high chemical potential (or higher free energy) to state of low chemical potential (or lower free energy).

The total free energy of the system may be represented as [**12**]:

$$F(\eta_i, c_i) = F_{bulk} + F_{int.} + F_{long} \qquad (2.3)$$

Where,

F_{bulk} is the bulk or local free energy of the system, F_{int} is the Interfacial energy *and* F_{long} long-range interaction energy, i.e. elastic strain energy, magnetic or electrostatic interaction energy. The free energy functional can be function of the phase field variables and their corresponding gradients, depending on the nature of the system.

The bulk (or chemical) free energy

The bulk free energy is a function of the chemical free energy of the system when it is at equilibrium. It determines the composition of the phases under equilibrium and it is defined by the volume integral of the free energy density as shown in equation (2.4).

$$F_{bulk} = \int f(\eta_i, c_i)\, dV \qquad (2.4)$$

Where, $f(\eta_i, c_i)$ is the free energy density in J/m^3. Different free energy densities have been used depending on the type of system and the nature of the problem. The most common free energy densities are discussed as follows (starting from the simplest ones).

Spinodal decomposition [**50**] is a mechanism whereby a mixture of liquids or solids rapidly unmixed to form two coexisting phases. The free energy density which was successfully used in the simulation of phase separation during spinodal decomposition is a simple double-well potential as shown in Equation (2.5). It is the simplest free energy density, as it is a function of only one phase field variable, the concentration field [**50**].

$$f(c) = \frac{1}{4}(1-c^2)^2 \qquad (2.5)$$

Where, c is the concentration field.

Furthermore, a free energy density with a double-well potential with minima at ϕ=-1 and ϕ=1 and a coupling term was successfully used to model solidification problems. In this case, the free energy density (originally derived by Caginalp [**54**]) is a function of both the temperature and the phase field, as shown in equation (2.6).

$$f(\phi, T) = \frac{1}{8a}(\phi^2-1)^2 - 2T\phi \qquad (2.6)$$

Where, ϕ is the phase field, T is the temperature, and a is a term that determines the height of the double-well potential.

A similar type of free energy density with small modification was used to model a dissolution/precipitation process. It has also a double-well potential, but with an odd function serving as the coupling term as shown in Equation (2.7) [**43**].

$$f(\phi, c) = \left(\frac{\phi^2}{2} + \frac{\phi^4}{4}\right)^2 + \lambda\left(\phi - \frac{\phi^3}{3}\right)c \qquad (2.7)$$

Where, λ is a dimensionless parameter which is used to control the strength of the coupling between the phase and concentration fields.

For diffusionless (martensitic) transformations, sixth-order Laudau polynomial is normally used as proposed by Wang and Khachaturyan [**55**]. In this case, the free energy density for the heterogeneous system is only a function of the order parameters as shown in equation (2.8).

$$f(\eta_1, \eta_2, \ldots\ldots, \eta_n) = \frac{1}{2}A\sum_{i=1}^{n}{\eta_i}^2 - \frac{1}{4}B\sum_{i=1}^{n}{\eta_i}^4 + \frac{1}{6}C\left(\sum_{i=1}^{n}\eta_i\right)^3 \tag{2.8}$$

Where, A, B, and C are phenomenological constants that can be obtained from thermodynamic database.

For the precipitation of ordered phases from disordered matrix, the concentration field is incorporated in the Laudau polynomial as shown in equation (2.9) [**56**].

$$\begin{aligned} f(c, \eta_1, \eta_2, \ldots\ldots, \eta_n) \\ &= \frac{1}{2}A(c - c_1)^2 + \frac{1}{2}B(c - c_2)\sum_{i=1}^{n}{\eta_i}^2 - \frac{1}{4}C\sum_{i=1}^{n}{\eta_i}^4 + \frac{1}{6}D\sum_{i=1}^{n}{\eta_i}^6 \\ &+ E\sum_{i \neq j}^{n}{\eta_i}^2{\eta_j}^2 + F\sum_{i \neq j \neq k}^{n}{\eta_i}^2({\eta_j}^2 + {\eta_k}^2) + G\prod_{i=1}^{n}({\eta_i}^2) \end{aligned} \tag{2.9}$$

Where, A, B, C,…,G are also phenomenological constants that can be obtained from thermodynamic database.

For phenomenological phase field models, such as solidification and transformation in binary alloys, a homogeneous free energy density is used. Initially, the WBM model [**30**] was the commonly used homogeneous free energy density which is defined by an interpolation function and an imposed double-well potential with height that linearly depends on the phase compositions, as shown in equation (2.10).

$$f(c,\phi,T) = \left(1 - h(\phi)\right) \cdot f^{\alpha}(c,T) + h(\phi) f^{\beta}(c,T) + \left((1-c)w_{\alpha} + c w_{\beta}\right) \cdot g(\phi) \quad (2.10)$$

Where,

$$h(\eta) = Interpolation\, function = \begin{cases} 3\phi^2 - 2\phi^3 & for\, TYPE\, II \\ \phi^3(6\phi^2 - 15\phi + 10) & for\, TYPE\, I \end{cases}$$

$g(\phi) = double - well\, potential = \phi^2(1-\phi)^2$

$f^{\alpha}(c,T)$ & $f^{\beta}(c,T) = chemical\, free\, energies\, of\, the\, \alpha\, and\, \beta\, phases$

w_{α} & $w_{\beta} = equilbrium\, mole\, or\, weight\, fractions\, of\, the\, \alpha\, and\, \beta\, phases$

The interpolation function is used to impose a smooth transition across the interface between the α and β phases. The double-well potential is used in defining the energy barrier between the coexisting phases, which have chemical free energy values that are obtained from the thermodynamic database. Gibb's free energy is often used for isothermal isobaric phase transformations, and Helmholtz free energy is used for isobaric isentropic phase transformations [**12**].

In the WBM model [**30**], the interface is defined in such a way that any point within the interface that is in equilibrium contains equal amount of the coexisting phases; this is not realistic. Moreover, another double-well potential appears beside the imposed one.

Consequently, the KKS model [**31**] (shown in equation (2.11)) was developed in order to address the issues by defining the interface to contain weighted-average mixture of the coexisting phases.

$$\mathrm{f}(c,\phi,T) = \left(1 - h(\phi)\right) \cdot f^{\alpha}(c,T) + h(\phi) \cdot f^{\beta}(c,T) + w \cdot g(\phi) \qquad (2.11)$$

Where,

$w = height\ of\ the\ imposed\ double - well\ potential$

The interfacial free energy

In reality, nucleation and the formation of an interface in a microstructure is only possible when some thermodynamic energy is gained by the material. Therefore, each interface needs certain threshold amount of energy before it forms. Due to the importance of interfacial properties to microstructure evolution, it is naturally incorporated into the physics of the phase field method. Grain boundary energy, surface energy, hetero-phase energy, and domain boundary energy are all sort of energies associated with an interface. The interfacial energy of the system is related to the gradient energy coefficients and the gradients of phase field variables as shown in equation (2.12) [**12**].

$$F_{int.} = \int \frac{1}{2} \sum_{i,j=1}^{n} \gamma_{ij}\, c_{,i} \cdot c_{,j} + \frac{1}{2} \sum_{k,l=1}^{n} \sum_{i,j=1}^{n} \alpha_{ijkl}\, \eta_{k,i} \cdot \eta_{l,j} \quad dV \qquad (2.12)$$

Where,

$\gamma_{ij} = gradient\ energy\ coefficients\ for\ the\ concentration\ fields$

$\alpha_{ijkl} = gradient\ energy\ coefficients\ for\ the\ phase\ field\ or\ order\ parameter$

Long-range interaction energy

For solid-state phase transformations, long-range interaction between the different phases of a material may have an effect on the microstructure evolution. This is due to the generation or absorption of energy as a result of such interactions. Thus, it is necessary to include the energy terms associated with long-range interaction in the phase field method. Elastic strain, magnetic and electrostatic interaction energies are the most common forms of long-range interaction energies. As elastic strain energy is more important to solid-state phase transformations, it is briefly explained as follows [**12**].

Elastic stresses that are formed during transformation may have an effect on the microstructure evolution. The size and the shape of the precipitates are greatly affected by magnitudes and types of the elastic stresses developed in the microstructure. Furthermore, lattice mismatch at the interface of the coexisting phases can be incorporated in the phase field theory by adding the terms for the elastic strain energy [**12**].

Khachaturyan [**45**] developed the micro-elasticity theory for multi-phase alloys. The theory is used to define the long-range interaction terms as a function of the phase field variables. The stress-free strain that is induced by the transformation is usually expressed as a linear or quadratic function of the phase field variables as shown in equation (2.13).

$$\varepsilon_{ij}{}^{0} = \varepsilon_{ij}{}^{c} \cdot \delta c + \sum_{k=1}^{n} \varepsilon_{ij}{}^{\eta_k} \, \eta_k{}^{2} \qquad (2.13)$$

Where,

${\varepsilon_{ij}}^0\ = stress - free\ strain$

${\varepsilon_{ij}}^c\ = compositional\ strain$

${\varepsilon_{ij}}^{\eta_k}\ = transformation\ or\ bain\ strain$

$\delta c\ = linear\ function\ of\ the\ concentration\ field$

The first term of equation (2.13), the compositional strain, is usually expressed as a linear function of the composition field according to Vegard's law [**12**,**47**]. The second term, the transformation-strain, is usually expressed as a quadratic function of the phase field or the order parameter [**47**].

Vegard's law states that a linear relation exists, at constant temperature, between the lattice parameter and the concentrations of the constituent elements of a given crystal [**57**]. Using the law, the compositional strain is expressed in equation (2.14).

$${\varepsilon_{ij}}^c\ = \frac{1}{a}\left(\frac{da}{dc}\right)\delta_{ij} \qquad (2.14)$$

And, the linear dependence of the lattice parameter with concentration is given by:

$$\delta c(\bar{r},t)\ = c(\bar{r},t) - c_0 \qquad (2.15)$$

Where,

$c_0\ = reference\ composition$

The transformation-strain is developed due to the lattice-mismatch between the coexisting phases. For small deformations, it is related to the lattice parameters of the coexisting phases by:

$$\varepsilon_{ij}{}^{\eta_k} = U_{ij}(\eta_k) - \delta_{ij} \qquad (2.16)$$

Where,

$U_{ij}(\eta_k) = right - stretch\, tensor\ of\ the\ induced\ deformation\ gradient$

The induced-stresses are related to the elastic strain by:

$$\sigma_{ij} = C_{ijkl} \colon \varepsilon_{kl}{}^{e} \qquad (2.17)$$

Where,

$C_{ijkl} = elastic\ stiffness\ matrix$

$\varepsilon_{kl}{}^{e} = elastic\ strain$

As the elastic stiffness matrix is different for each of the coexisting phase, it is usually expresses as a function of the phase field or the order parameter by:

$$C_{ijkl} = h(\eta) \cdot C_{ijkl}(\beta) + (1 - h(\eta))C_{ijkl}(\alpha) \qquad (2.18)$$

Where,

$h(\eta) = interpolation\ function$

$C_{ijkl}(\beta) = elastic\ stiffness\ matrix\ of\ the\ product\ phase$

$C_{ijkl}(\alpha) = elastic\ stiffness\ matrix\ of\ the\ parent\ phase$

The elastic strain is related to the stress-free strain by,

$$\varepsilon_{kl}{}^{e} = \varepsilon_{kl}{}^{total} - \varepsilon_{kl}{}^{0} \qquad (2.19)$$

Where,

$\varepsilon_{kl}{}^{total} = total\ strain$

The total strain is related to the displacement field by:

$$\varepsilon_{kl}{}^{total} = \frac{1}{2}\left(u_{k,l}(\bar{r}) + u_{l,k}(\bar{r})\right) \qquad (2.20)$$

Where,

$u_i(\bar{r}) = displacement\ field$

The total strain energy (F_{el}) of the system is usually expressed by:

$$F_{el} = \frac{1}{2}\int \sigma_{ij}\,\varepsilon_{ij}{}^{e} dV = \frac{1}{2}\int C_{ijkl}\,\varepsilon_{ij}{}^{e}\varepsilon_{kl}{}^{e} dV \qquad (2.21)$$

Thus, the variational derivative of the elastic energy functional becomes:

$$\frac{\delta F_{el}}{\delta \eta_k} = \frac{\partial f_{el}}{\partial \eta_k} = -\frac{1}{2} C_{ijkl}\varepsilon_{kl}{}^{\eta_k}\eta_k\left(u_{i,j}(\bar{r}) + u_{j,i}(\bar{r})\right) + C_{ijkl}\varepsilon_{kl}{}^{\eta_k}(k)\eta_k \sum_{y=1}^{n} \varepsilon_{ij}{}^{\eta_y}\,\eta_y{}^2$$
$$-\frac{1}{2} C_{ijkl}\varepsilon_{ij}{}^{\eta_k}\eta_k\left(u_{k,l}(\bar{r}) + u_{l,kj}(\bar{r})\right)$$
$$+\, C_{ijkl}\varepsilon_{ij}{}^{\eta_k}(k)\eta_k \sum_{y=1}^{n} \varepsilon_{kl}{}^{\eta_y}\,\eta_y{}^2 \quad (2.22)$$

$$\frac{\delta F_{el}}{\delta c} = \frac{\partial f_{el}}{\partial c} = -\frac{1}{2} C_{ijkl}\varepsilon_{ij}{}^{c}\left(u_{i,j}(\bar{r}) + u_{j,i}(\bar{r})\right) + C_{ijkl}\left(\varepsilon_{ij}{}^{c}\right)^2 \delta c(\bar{r}, t)$$
$$-\frac{1}{2} C_{ijkl}\varepsilon_{ij}{}^{c}\left(u_{k,l}(\bar{r}) + u_{l,kj}(\bar{r})\right) + C_{ijkl}\left(\varepsilon_{ij}{}^{c}\right)^2 \delta c(\bar{r}, t) \quad (2.23)$$

Phase Evolution Equations

The phase field equations are usually developed based on thermodynamic principles. The main partial differential equations describing the temporal and spatial evolution of the coexisting phases in the microstructure were developed by Cahn-Hillard [**5**] for the conserved phase field variable, Allen-Cahn/Ginzburg-Laudau [**6**] for the non-conserved phase field variable, and mechanical (stress) equilibrium equation for the displacement fields. It is important to note that the fundamental thermodynamics and kinetics information serves as the main input to phase field equations.

Cahn-Hillard Equation is derived from Fick's second law of diffusion based on principle of conservation of mass. It is a non-linear diffusion equation which is used to describe the evolution of conserved field variables (concentration, mass or composition or temperature). It has been successfully applied to phase separation problems, such as spinodal decomposition [**50**], corrosion kinetics [**7**], solid-state alloy transformations [**49**], etc. The Cahn-Hilliard equation is a 4th order PDE that relates the conserved field-variable (in this case concentration) to free energy functional as follows.

$$\frac{\partial c(\vec{r},t)}{\partial t} = \nabla \cdot M\,\nabla\left[\frac{\delta F(\eta_i, c)}{\delta c}\right] = \nabla \cdot M\,\nabla\left[\frac{\partial f(\eta_i, c)}{\partial c} - \nabla \cdot \gamma\,\nabla c(\vec{r},t) + \frac{\delta F_{el}}{\delta c}\right] \qquad (2.24)$$

Where, M is the kinetic mobility which may be a constant or function of the phase field variables [**7**]. Furthermore, the atomic mobility is mostly expressed as a function of the diffusivities by comparing equation (2.24) with Fick's second law of diffusion.

The Allen-Cahn Equation is the time-dependent form of the Ginzburg-Laudau Equation. It describes the linear dependence of the evolution rate of the non-conserved field variable (phase-field or order parameter) on the driving force. It has mainly been applied to the description of moving boundaries in multi-phase systems. The Allen-Cahn equation is a 2nd order PDE that relates the non-conserved field variable to the free energy functional as follows.

$$\frac{\partial \eta_i(\vec{r},t)}{\partial t} = -L_i \frac{\delta F(\eta_i, c)}{\delta \eta_i} = -L_i \left(\frac{\partial f}{\partial \eta_i} - \alpha_i \nabla^2 \eta_i + \frac{\delta F_{el}}{\delta \eta_i} \right) \qquad (2.25)$$

Where, the kinetic mobility (L_i) and the gradient energy coefficients (α_i) may be constants or functions of the phase field variables [**7**].

Sometimes, a Langevin noise term is added to right-hand side of the phase field equations in order to introduce noise that is associated with thermal fluctuations during microstructure evolution. A Gaussian noise field that satisfies fluctuation-dissipation theorem is commonly used. An alternative method to Langevin noise, is Explicit algorithm model, where a nuclei is introduced explicitly into the microstructure. In that case, the nucleation rate for the evolving phases is obtained by nucleation theory or calibration from experiments [**12**,**58**]

And, the equation for the mechanical equilibrium or local force balance of the system can be expressed by:

$$\frac{\partial \sigma_{ij}}{\partial r_j} = \frac{\partial \left[C_{ijkl} \colon \varepsilon_{kl}{}^{e} \right]}{\partial r_j}$$

$$= C_{ijkl} \left[\frac{1}{2} \left(u_{k,lj}(\bar{r}) + u_{l,kj}(\bar{r}) \right) \right] - \varepsilon_{ij}{}^{c} \frac{\partial(\delta c(\bar{r},t))}{\partial r_j} - \sum_{k=1}^{n} \varepsilon_{ij}{}^{\eta_k} \frac{\partial(\eta_k{}^2)}{\partial r_j}$$

$$= 0 \qquad (2.26)$$

Parameters Determination

A phase field model requires large number of parameters for the numerical implementation. The parameters are used to specify the various material properties of the various coexisting phases. For a typical phase field model, the required parameters are equilibrium compositions of coexisting phases, gradient energy coefficients, interface width, interfacial energy, height of double-well potential, diffusion coefficients, atomic (diffusion) mobility, kinetic mobility, free energies of coexisting phases, and off course temperature. Most of the parameters are temperature and pressure dependent, some are composition as well as phase dependent, and a few are anisotropic depending on the level of complexity of the model [**12**]. For a rigorous phase field model that is coupled with elasticity or plasticity, other parameters apart from the aforementioned ones are needed. This includes constants of elastic stiffness matrix, yield strength, stress-free strains, e.t.c [**12**].

Only few of the parameters are determined experimentally. Most of the parameters that are related to the thermodynamics of the system are obtained from thermodynamic databases (such as CALPHAD and DICTRA). Other parameters are obtained using atomistic calculations and yet few parameters are freely selected. Due to the difficulty associated with very sharp interfaces, the interface width is freely selected to a value that is suitable for numerical convergence [**12**].

Numerical Methods

Numerical realization of microstructure evolution based on the sharp-interface method is often difficult, due to the need for explicit tracking of the interface. This is not only impractical as well as numerically difficult, but also error prone. Recently, the phase field method is used to simulate microstructure evolution using a set of field variables and a diffused-interface, thus allowing a smooth transition of properties from one phase to another. It is not only more efficient, but also easier to implement [**43**]. Only analytical solution of the earliest phase field equations (for solidification phenomenon) exists. A number of numerical methods have been used to solve the equations which include: explicit & implicit finite difference schemes, finite element methods, finite volume methods and semi-implicit fourier spectral methods.

The explicit finite difference scheme is computationally expensive due to the small time step that is needed. Even though, the time step is larger using the implicit finite difference scheme, large number of equations at each time step makes the computation very intensive. Complex geometries and boundary conditions are often difficult to handle using all the finite difference schemes. Moreover, the high non-linearity associated with the phase field equations results in inconsistency and instability.

The finite element technique is the most suitable method for problems that are associated with complex geometries and boundary conditions. Non-linearity in the phase field equations are easier to handle with the finite element approximations. However, the required mesh density is very high for multiphase problems with irregular-shaped domains. This makes the computation to be very intensive and the numerical convergence of the equations difficult to attain.

The spectral method is the most suitable method for problems with periodic boundary conditions. It is the method having the least computational intensity and the best numerical stability and accuracy. Another associated advantage with the method is that, the gradient term of the Cahn-Hilliard equation can be treated implicitly without resulting into sets of coupled non-linear discrete equations. The only shortcoming of the method is that, it is not suitable for irregularly-shaped domains, and it is limited to problems that have periodic boundary conditions only. The following is a table that shows various numerical methods that are used in the most recent papers.

Table 1: Numerical Methods for solution of the phase field equations

Method	**Source**
Finite Difference Schemes	
Explicit in both space and time	[**59**,**60**,**61**]
Explicit in time, Crank-Nicolson scheme in space	[**60**,**62**,**63**]
Crank-Nicolson Adams-Bashforth scheme	[**64**]
Gilbert Strang splitting scheme	[**64**]
Alternating Direction Implicit Method	[**58**]
Finite Element Method	
Regular finite element method	[**65**]
Meshless method	[**66**]
Moving mesh method	[**67**]
Mixed-order finite element method	[**47**]
Fourier Spectral Method	

Pseudo-spectral method	[**68**,**47**]
Semi-Implicit Fourier-spectral method	[**58**,**69**]
Legrendre-and Chebyshev-spectral method	[**70**]

Associated Challenges

The following are some of the most recent challenges associated with the phase field method [**12**]:

- Nucleation is not adequately incorporated in the model. In most cases, nucleation is initiated using separate analytical models.
- Numerical stability of the phase field equations is difficult to obtain using the real interface widths due to the emergence of steep gradients.
- The method is restricted to the simulation of phase transformations at mesoscale.
- Experimental determination of the phase field parameters is very challenging. Therefore, the validity of the parameters which are obtained using the CALPHAD approach is yet to be confirmed.
- The quantitative experimental validation of phase field models is very difficult. Most of the models are validated qualitatively.
- The fundamental theory of the phase field method is still under development.

CHAPTER 3

HOT CORROSION IN TBC

In this chapter, the theoretical background of Thermal Barrier Coating (TBC) system is first presented. Then, previous experimental studies related to the hot corrosion of the top coat by V_2O_5 are highlighted. The review shows that the Phase Field Method (PFM) has not been used in capturing the phase transformation that occurs during the V_2O_5 hot corrosion of the top coat.

3.1 Thermal Barrier Coating (TBC)

Thermal Barrier Coatings (TBCs) are highly advanced coating materials that are usually applied to high temperature components for the sole purpose of improving their thermal and corrosion resistance. The use of TBC results in tremendous improvement in the efficiency and performance of the thermal system [**71**]. TBC consists of four layers: the single-crystal base metal for structural support, metallic bond coat for corrosion/oxidation resistance, thermally grown oxide for oxidation resistance, and ceramic topcoat for thermal insulation. The ceramic topcoat is composed of porous Yttria-Stabilized Zirconia (YSZ) which has a very low thermal conductivity and adequate stability at the operating temperatures typically seen in thermal systems. It enables the systems to withstand very hot gas, erosion, corrosion, and damage due to foreign objects [**72**,**71**]. Fig. 4 shows an SEM which describes the general layout of a typical TBC.

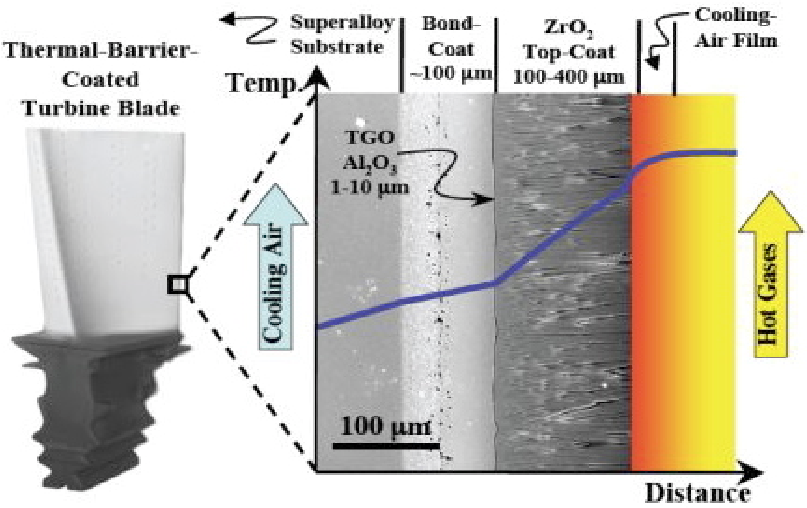

Figure 4: SEM through a cross-section of a typical TBC [73]

3.1.1 Ceramic Top Coat

Zirconia (ZrO_2) that is doped with 7 wt% Y_2O_3 is the most common ceramic material used for the top coat. This is due to its low thermal conductivity, high melting point, resistance to sintering, ease of deposition and long life [**74**]. Zirconia was named after Joseph Baddley in 1892, when he discovered the natural form of the material, baddelyite. Baddelyite contains about 96.5% to 98.5% of zirconia and approximately 2% HfO_2, hafnium oxide as impurity. It has a monoclinic crystalline structure, high strength, wear resistance, translucent appearance and fracture toughness at room temperature [**71**]. Its thermal conductivity is lower than any other engineering ceramic, which gives it the practical ability to reduce the temperature of the substrate material in TBC by several hundreds of degrees Celsius. Moreover, the linear thermal expansion coefficient and elastic modulus of zirconia enables it to survive coating failure during thermal cycling [**75**].

Unfortunately, pure ZrO_2 is polymorphic at ambient pressure. It exists in the monoclinic crystalline form from lower temperatures up to 1170°C. It then changes to the tetragonal form at 1170°C and remain in that state up to 2370°C. The cubic crystalline form results on reaching 2370°C and remains in that form so long as the temperatures is higher. These transformations are usually called the **destabilization transformations of zirconia** and causes severe contribution to the failure of the material [**76**]. The volumetric expansions as a result of the cubic-tetragonal or tetragonal-monoclinic transformation induce very large stresses that result in the cracking of the material upon cooling.

Therefore, in order to use zirconia components at higher temperatures, it is necessary to 'crystallograpically lock' the zirconia material from transformation. The addition of dopants at varying proportions stabilizes the cubic or tetragonal phase of zirconia partially or fully even at room temperature. This also results in the substantial improvement in the properties of the material, such as high flexural strength, high fracture toughness, good chemical resistance and low thermal conductivity [**77**,**78**].

Stabilization of zirconia is usually achieved by adding proper amount of larger cations that can expand the lattice or smaller cations that can create oxygen anion vacancies or a combination of the two. The creation of oxygen vacancies reduces the average co-ordination number and enhances relaxation of the oxygen sub-lattice towards cubic symmetry; this mechanism can be considered more effective than expanding the lattice [**77**]. Divalent alkaline earth metals (such as Mg^{2+} and Ca^{2+}), transition metals (such as Al^{3+} and Y^{4+}), tetravalent cations (such as Ce^{4+}) and rare earth trivalent cations [**76**] (such as as La^{3+}, Nd^{3+} , Sm^{3+} and Ga^{3+}) have all been successfully used as stabilizers for zirconia ceramics [**76**].

Yttria-Stabilized Zirconia (YSZ)

Despite the availability of various stabilizers for zirconia, yttrium oxide or yttria (Y_2O_3) has been the commonest stabilizer for the top coat material. Evidence has also shown that yttria-stabilized zirconia has the lowest-thermal-conductivity among the other TBC materials that have been discovered so far. Yttria-stabilized zirconia (YSZ) is a substitutional solid solution of yttrium in zirconia. The yttrium and zirconium ions are located in the cation lattice, while oxygen ions and vacancies are located in the simple cubic anion lattice. In the cubic fluorite structure (shown in Fig. 5), each cation is in the center of a cube of eight anions and each anion or vacancy is in the centre of a cation tetrahedron. Thus, the introduction of yttria creates charge compensating oxygen vacancies that become mobile at high temperatures; hence increases the conductivity of the material [**79**]. YSZ is an attractive material that is stable under both oxidizing and reducing conditions. It has good mechanical and optical properties at elevated temperatures. It also has a low absorption coefficient as well as high opacity in the visible and infrared spectrum.

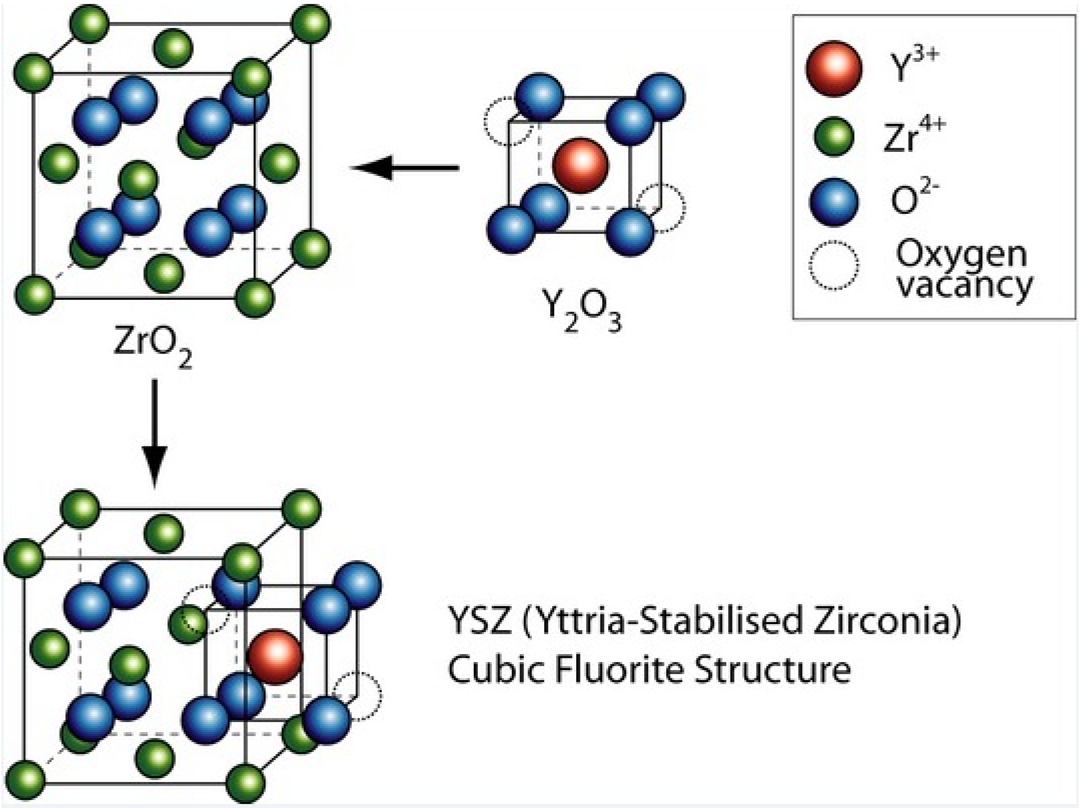

Figure 5:Yttria Stabilized Zirconia [75]

According to previous experimental studies, various phases can be generated from the solid solution depending on the composition of Y_2O_3-ZrO_2 system (as shown in Fig.6).

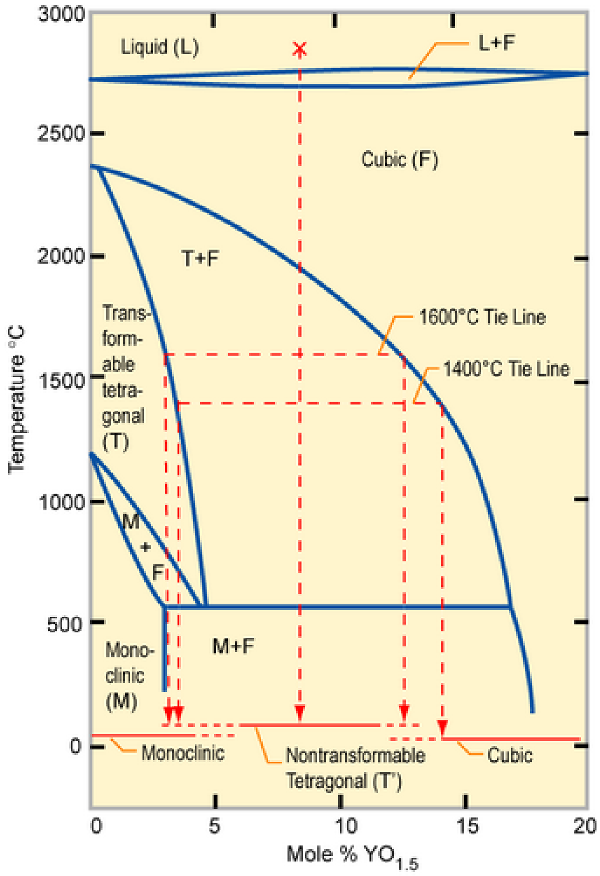

Figure 6: Yttria-Zirconia phase diagram [75]

3.1.2 Thermally Grown Oxide (TGO)

The TBC system is engineered in such a way that another layer (the TGO) emerge between the top coat and bond coat at higher temperatures. It forms due to the oxidation of the bond coat at temperatures above 700^0C. The growth of the TGO is enhanced by the presence of micropores in the top coat and the high affinity of oxygen by zirconia. The TGO layer has a very low oxygen ionic diffusivity, thus it provides excellent diffusion barrier to the bond coat oxidation [**71**].

Generally speaking, the TGO growth can be divided into two regimes [**71**]:

1. Fast initial growth of non-protective oxides before top coat deposition

2. Continuous protective scale growth after top coat deposition, largely controlled by diffusion

Usually, the resulting oxide is composed of alpha-alumina (Al_2O_3). However, a bond coat composed of NiCrAlY produces some spinels of $Ni(Cr,Al)_2O_4$, Y_2O_3, NiO, $AlYO_3$, and $Al_5Y_3O_{12}$ bands that are oriented perpendicular to the bond coat [33]. Also, a bond coat composed of FeCrAlY was found to produce $Fe_2Cr_2O_4$ and Cr_2O_3 after the oxidation [**71**]. Some elements that causes less adhesion at the TGO/Bond Coat interface, like Ti and Ta, are usually kept below certain level in the bond coat. Other elements that increase this adherence, like Si and Hf, are usually added in small quantities [**71**].

3.1.3 Bond Coat

Despite the favorable properties of the YSZ top coat, the difference in thermo-mechanical properties between the top coat and the metallic alloy is enough to require the introduction of an intermediate layer, the **bond coat**. The bond coat is an oxidation-resistant metallic layer (usually of 75-150 µm thickness) that is usually consisted of NiCrAlY or NiCoCrAlY alloy. It is important for adhesion and grading the thermal expansion mismatch between the top coat and substrate. It is also deposited using either the EB-PVD or APS method [**71**].

3.1.4 Substrate

The substrate material for turbine blades is usually formed either as a single crystal or polycrystalline material by investment casting. However, the single crystal form results in higher creep strength due to anisotropy. The most common substrate material for TBC is nickel or cobalt-based superalloy. Usually, alloying elements like Co, Cr, Mo, Al, Ta, Ti, C, Zr, B, etc are added in order to enhance the specific important properties such as high-temperature strength, ductility, oxidation resistance, hot corrosion resistance and castibilty [**71**]. Cool air is often passed through the internal hollow channels of the turbine blade in order to establish a temperature gradient in the system.

3.1.5 Spraying Methods

Although there are various methods for depositing the ceramic coatings on metal substrates, the two most important methods used for top-coat deposition are[**71**],[**73**]:

(i) air-plasma-spray (APS) deposition; and

(ii) electron-beam physical-vapor deposition (EB-PVD)

3.1.6 APS Deposition Methods

In this process, molten form YSZ (thermal plasma) is produced by passing the YSZ powder through an arc-plasma jet. With the gained thermal energy and momentum, the thermal plasma rapidly solidifies on any metallic surface it is projected or deposited unto. Usually, the process is carried out at ambient conditions, hence called Air or Atmospheric Plasma Spray (APS) deposition method. The thickness of the coating that can be obtained using the APS falls between 10-100 µm [**73**].

The independent solidifications of the molten particles result in the chaotic assemblage of the particles in the deposited microstructure, thereby resulting in splat-interfaces and porosity in the top coat [**73**]. Fig.7 shows a typical description of the APS spraying of TBC with an electron micrograph showing the morphology of the feedstock powder, a single splat and the aggregated coating material.

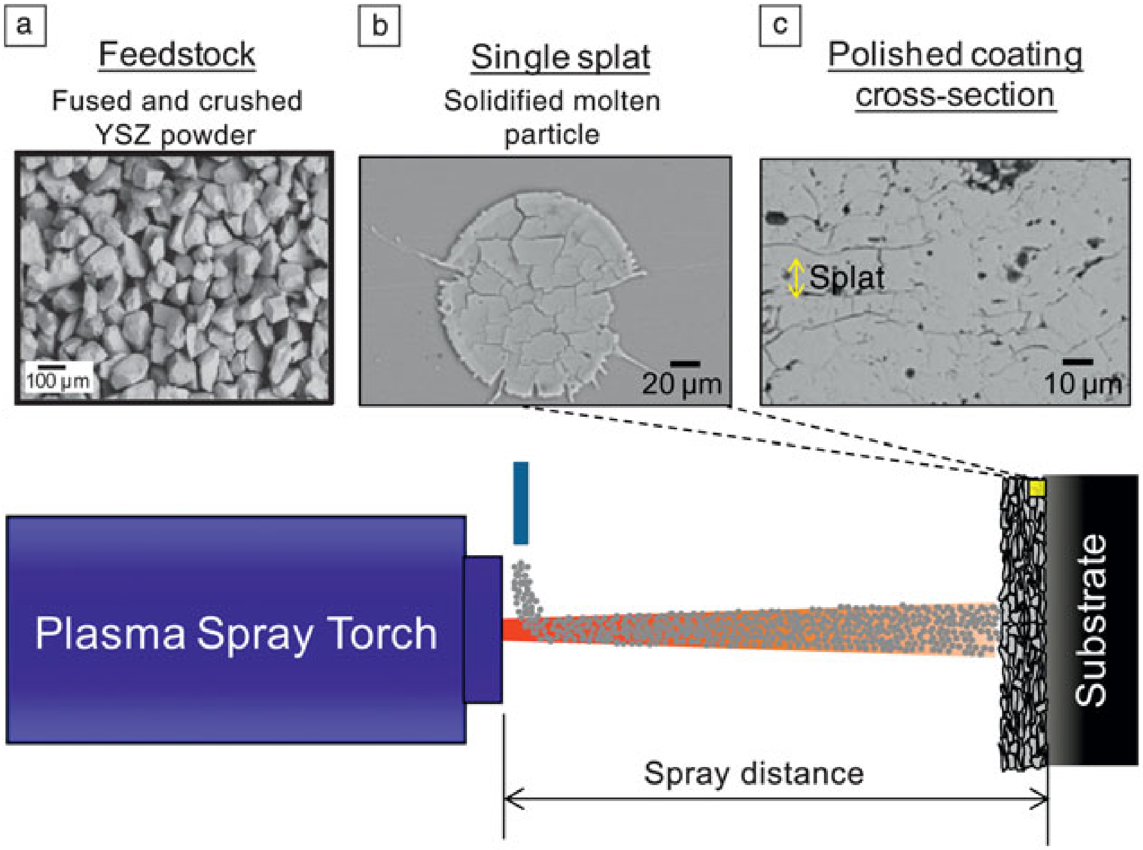

Figure 7: Air Plasma Spraying of TBC showing (a) feedstock powder (b) single splat (c) Assemblage of splats [73]

Factors of critical importance to the performance of APS TBC include particle trajectory, thermal and kinetic states, roughness of the bond coat/substrate material, temperature, geometry, relative movement, and speed of the torch [**80**]. The main advantages of APS over other deposition methods include: lower thermal conductivity and elastic modulus due to the formation of 15 to 25% porosity in the coating, formation of horizontal cracks, versatility and low production costs [**81**].

However, the undulating nature of the metal/ceramic interface produces out-of-plane stresses that are responsible for the shorter thermal-cycling lives of APS TBCs.

Therefore, this makes it suitable only for less exacting applications in aircraft engines [**71**].

3.1.7 EB-PVD Method

In this process, the molten YSZ is produced by scanning with a highly energetic electron beam. This forms a high pressure vapor on top of the molten pool within the vacuum chamber [**82**]. The placement of the high temperature substrate in the vacuum chamber causes the deposition of the vaporized ceramic material unto the substrate. In order to provide an uninterruptable deposition of the coating on the substrate, the crucibles are usually bottom-fed continuously with cylindrical ingots of the ceramic material. The usual depositing rate attained by EV-PVD method is 1 μ m/minute and the continuous rotation of the part is necessary for proper deposition of the melt [**73**].

As a result of the combined effect of surface diffusion, vapor deposition, and macroscopic shadowing, columnar microstructures and vertical cracks are produced which provide higher strain tolerance to the coating. Fig.8 shows the overall layout of a TBC Electron-Beam Physical Vapour Depositor with samples of various coating morphology that can be created with it [**73**].

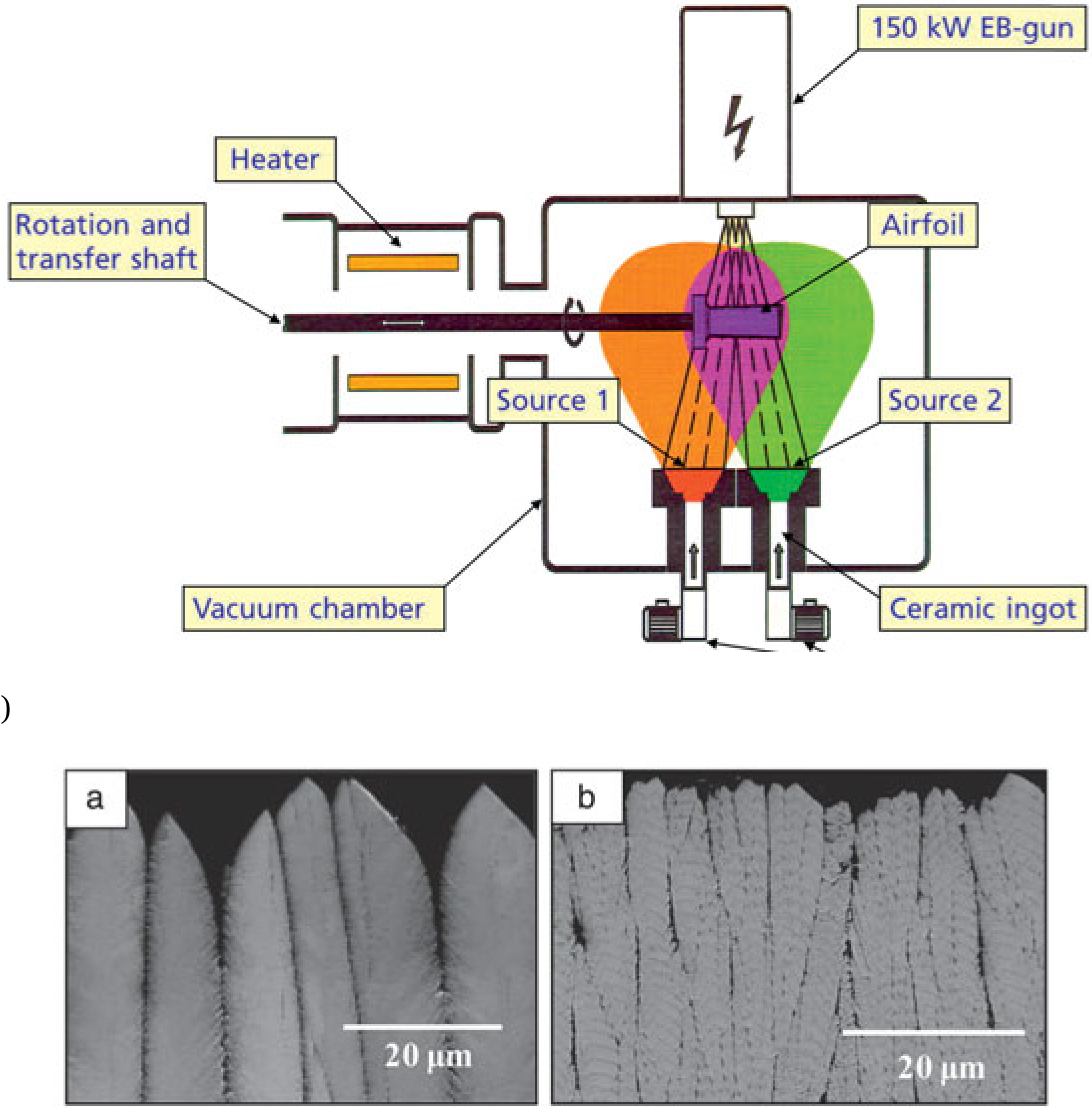

(a)

(b)

Figure 8: (a) General layout of a TBC EB-PVD, (b) Different morphologies of the columnar possible structures [73]

The main advantages of EB-PVD over other deposition methods includes: high strain tolerance, pseudo-plasticity, high erosion resistance, and smoother surface finish. However, the high cost associated with EB-PVD method, higher thermal conductivity of the resulting coating, waste due low utilization of the ceramic material and limitations associated with the vapour pressure are the main short-comings of EB-PVD [**73**].

3.2 Factors Mitigating the Performance of TBC

The main factors that were found to severely affect the performance of TBCs are bond oxidation and hot corrosion, as explained in the following sections.

3.2.1 Bond Coat Oxidation or TGO Growth

Due to the presence of porosities in the top coat, continuous transport of oxygen from the environment to the bond coat occurs. This is initially favorable, as it leads to the formation of an Al_2O_3 layer (i.e. the TGO) which covers the bond coat thereby making the coating system more oxidation resistant. However, continuous growth of the TGO results in the formation of large in-plane compressive stresses due to the thermal expansion mismatch between the TGO and the bond coat. This reduces the adhesion between the TBC and the substrate, thus resulting in the premature failure of the system [**83**].

3.2.2 Hot Corrosion

Hot corrosion is a type of high chemical reaction between a metal or metallic oxide and a molten salt in an oxidizing environment. Generally, two types of hot corrosion exist. In the first type, the type I or the high temperature hot corrosion (HTHC), the contaminant is in molten form and always results in uniform corrosion degradation of the substrate material. In the second, the type II or the low temperature hot corrosion (LTHC), the contaminant is in solid state and always results in the formation of pits in localized areas of the substrate material [**84**].Type-I Hot corrosion is one of the main causes of failure in thermal barrier coatings in Saudi Arabia. This is due to frequent use of low grade fuel in the kingdom, which contains a certain amount of impurities such as vanadium, sodium, phosphorous, sulfur, e.t.c.

Different types of hot corrosion mechanisms that occur in TBCs were reviewed by Jones [**85**,**86**]. Previous experiments showed that the hot corrosion of the top coat occurs as a result of the reaction between the vanadium impurities in fuel and ceramic top coat at high temperatures [**1**,**2**,**87**,**88**,**89**]. The reaction results in the leaching of a new phase, YVO_4 and the monoclinic-to-tetragonal transformation of zirconia. Overall effect of the evolution of the new phases is the volumetric expansion of the top coat by 4-5%, the development of localized stresses, propagation of horizontal cracks and subsequent failure of the TBC [**88**,**3**,**4**,**86**,**90**,**91**](shown in Fig.9). In fact, failure of the top coat due to hot corrosion can even precede failures due to sintering or development of a thermally grown oxide [**92**]. More explanation of the corrosion reaction can be found in Appendix B.

Usually, the operating temperature of land-based gas turbine blades in Saudi Arabia is 900^0C. Also the highest degradation of the coating for Type I hot corrosion was found to be 900^0C as shown in Fig.9 [**84**]. Therefore, in the present study the analysis is carried out at 900^0C. The reaction for the process is given as follows [**88**].

$$ZrO_2(Y_2O_3)(t-\text{phase}) + V_2O_5 \rightarrow ZrO_2(m-\text{phase}) + 2YVO_4$$

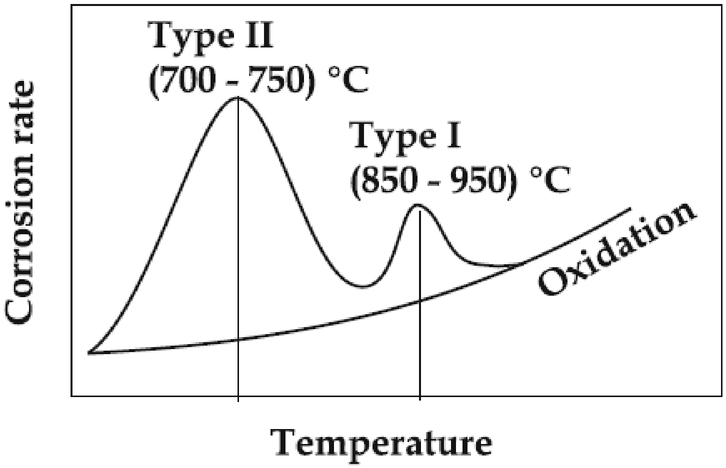

Figure 9: Corrosion rate as a function of temperature [**84**]

Previously [**89**,**93**,**88**,**94**], experimental investigation of the high temperature reaction between V_2O_5 and YSZ (carried out at temperatures ranging from 750^0-1200^0C) showed that the degradation process occurs in two zones. The first zone, the Planar Reaction Zone (PRZ), is a fine-grained section which grows continuously in a planar fashion near the surface of the coating. EDS showed that, the main reaction products are ZrV_2O_7, m-ZrO_2 and YVO_4, with ZrV_2O_7 disappearing completely above 750^0C. Results from SEM also showed that the YVO_4 crystals precipitate as rod-like structures (shown in Fig.12).

The second zone, the Melt Infiltrated Reaction Zone (MIRZ), forms due to the reaction between the V_2O_5 that infiltrates the body of the coating (through micropores and microcracks) and the coating material. Prior heat treatment was found to highly accelerate the degradation in the MIRZ due to the creation of larger pores. Conclusively, the evolving microstructure (shown in Fig.10) of hot corroded YSZ coating depend solely on the rate of the reaction between V_2O_5 and YSZ in the PRZ, the rate of infiltration of V_2O_5 into the MIRZ and reaction temperature [**89**]. Fig. 11 shows the kinetics of the hot corrosion process at 900^0C, and Fig. 13 also shows a sample of coating that failed due to hot corrosion [**94**].

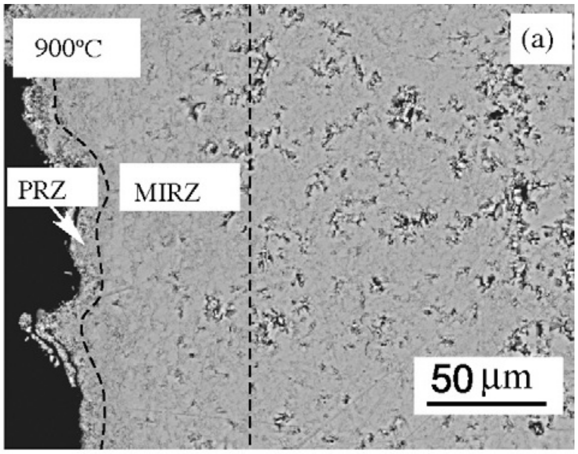

Figure 10: SEM of PRZ and MIRZ at 900^0C [89]

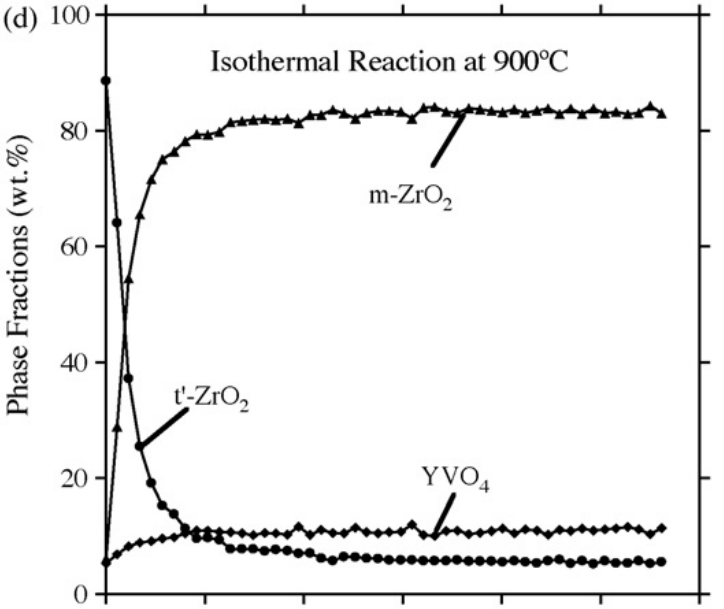

Figure 11: Corrosion kinetics and reaction products at 900^0C [93]

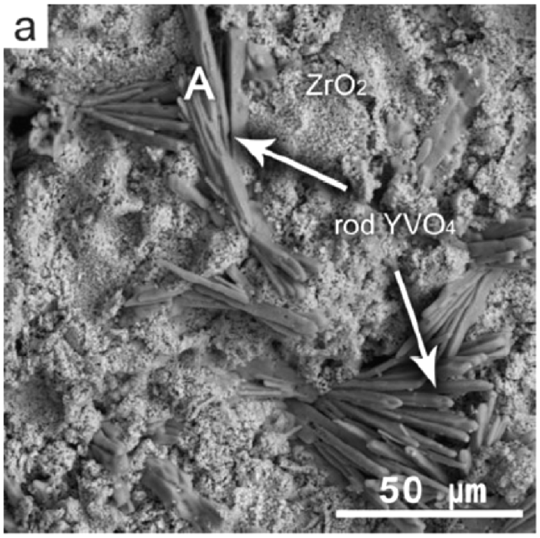

Figure 12: Morphology of corrosion products at 900^{0}C [88]

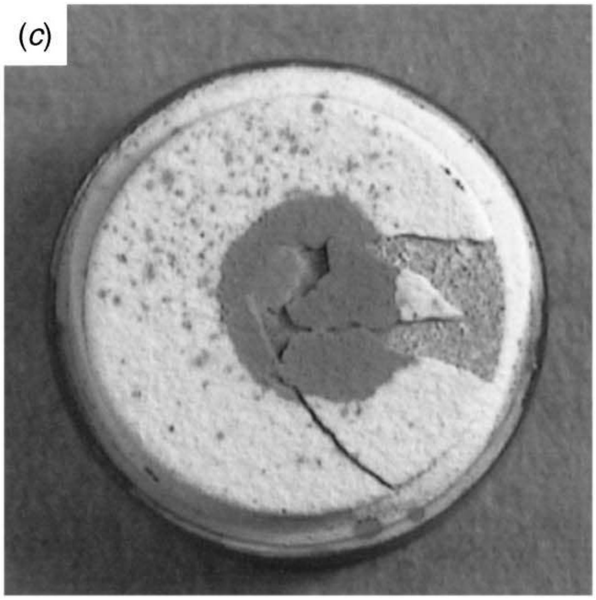

Figure 13: Failure of coating due to hot corrosion [95]

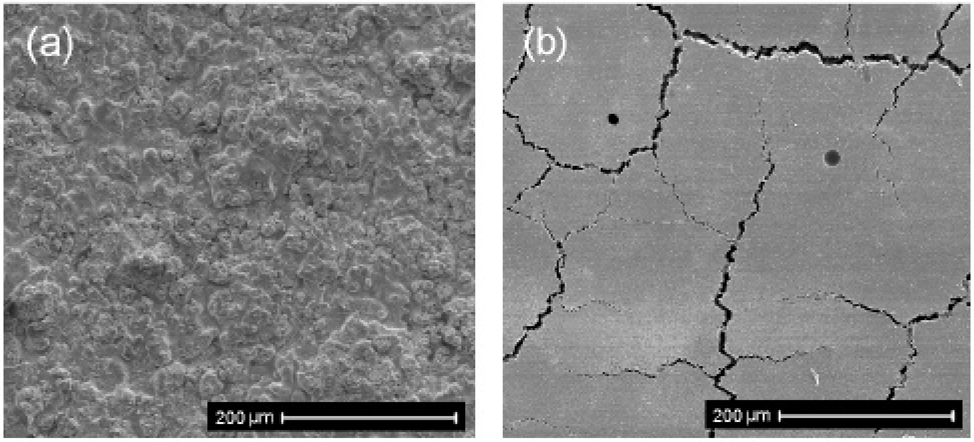

Figure 14: Failure of coating, (a) before corrosion test (b) after corrosion test [**96**]**.**

Active research is going on in developing a suitable corrosion inhibitor for improving the life time of TBCs[**97**]. Laser-glazing was also found to be among the surface sealing treatments that reduce the corrosion rate of TBCs [**96**]. Addition of 2-25 µm layer of Al_2O_3 to the surface of the coating was also found to reduce the corrosion and oxidation rates of TBCs [**98**]. Previous work also showed that, nanostructured coatings are more oxidation and corrosion resistant than as-sprayed TBCs due to the compactness and homogeneity of the microstructure [**99**]. Modeling of phase transformations during the hot corrosion of top coat has not been found in the open literature.

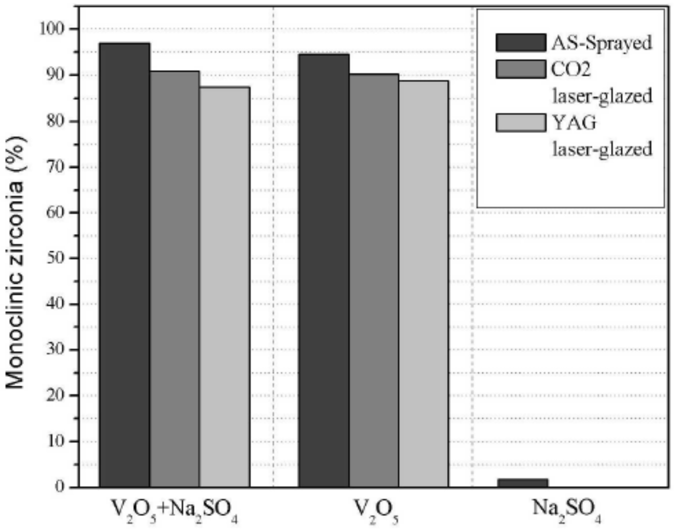

Fig. 5

Figure 15: Effect of laser glazing on coating performance [**96**]

3.3 Proposed Research

Even though Tijjani [**48**] developed a PFM for predicting the evolution of the compound layer during nitriding process, Wen et al. [**7**] was the first to propose a fully developed PFM for solid-state phase transformations that are induced by diffusion from external sources. They demonstrated that, the model can be used to predict the various phases that are formed during oxidation, sulfidation or any corrosion process provided the various material (input) parameters are calibrated accurately. For this reason, the current work mainly involves the application of the proposed model to a practical corrosion process, the V_2O_5 hot corrosion of TBC, in order to predict the microstructure evolution during the hot corrosion of the top coat. This will open a new and vital area of applications of the PFM, considering the importance of corrosion inhibition and protection in today's society. Additionally, in the present study the PFM is coupled with elasticity in order to predict the transformation-induced stresses. The induced stresses are important in assessing the failure of the material.

As mentioned previously, the ultimate goal of our research is to develop a numerical modeling approach for transformation-induced failures. The model will be applied to V_2O_5 hot corrosion of the top coat. The model will be used in determining the mechanical behavior of the material during its chemical interaction with the corrosive salt. This will help us in understanding more about the failure mechanism of hot-corroded TBCs. Once accomplished, the model is also expected to apply in general to any transformation-induced failure in material systems.

CHAPTER 4

NITRIDING OF EXTRUSION DIES

In this chapter, some theoretical background related to gas nitriding process in steel are first presented. Then, previous experimental and numerical works related to gas nitriding of steels are reviewed. It was found that, the phase field method has not been used in predicting the residual stresses that are induced during the two-stage controlled nitriding process that is used for Aluminum hot extrusion dies.

4.1 Gas Nitriding of Steel

4.1.1 Introduction

Recently, industrial production of steel has grown enormously due to its numerous applications. Desirable properties of steel such as high toughness, high strength, good machinability and low cost are main driving forces for such development [**48**]. Heat treatment has been the main process that is used to improve the physical, mechanical and chemical properties of steel. It mainly involves the heating and cooling of metals in order to alter their properties to the desired ones.

Surface-hardening has been among the thermo-chemical heat treatment processes that are used to improve the fatigue strength, surface hardness, wear and corrosion resistance of steel. It basically involves the diffusion of chemical species into a certain depth of the material at high temperatures. The most common surface hardening techniques include: nitriding, nitrocarborizing, carborizing, and carbonitriding. Among the surface hardening processes mentioned, nitriding is considered the most desirable due to less distortion, less deformations and better surface properties associated with it.

Nitriding is the most common surface-hardening process that is used for steel [**100**]. It basically involves the diffusion of atomic nitrogen from the surface of the steel to a certain depth at high temperatures. Quenching is not required, as the process does not involve heating of the steel to the austenite phase. This makes nitriding process better than other surface hardening processes [**101**]. Nitriding is commonly used in transmission mechanical components such as gears, camshafts, valve parts, screws, forging dies, extrusion dies, e.t.c.

Fig. 16 shows the various causes of distortion during heat treatment processes. Distortions produced during nitriding process are mainly due to phase changes/transformations as a result of the reaction between the nitrogen and the various constituents of steel [**48**].

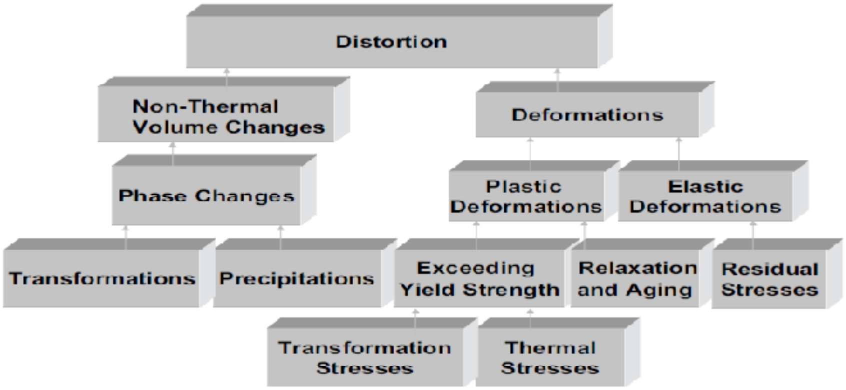

Figure 16: Causes of distortion during nitriding [**48**]

The diffusion of nitrogen into steel usually results in the formation of three layers, i.e. **compound, diffusion** and **matrix layer**. The compound or surface layer consists of new precipitates of iron nitrides. It forms near the surface of the steel as a result of the reaction between nitrogen and iron at high temperatures. The diffusion or nitriding layer forms below the compound layer and it consists of interstitial solid solution of nitrogen in ferrite lattice. It also contains the nitride precipitates of the alloying elements, such as aluminium, chromium, vanadium, tungsten, and molybdenum. The presence of the alloying element nitrides hardened the diffusion layer further by causing more strain on the ferrite lattice and thus strengthening dislocations. Unalloyed steels are usually not suitable for nitriding process because they result in a surface of high brittleness and low hardness. The third layer is the ferrite steel matrix (with some trace of alloying elements) which does not contain any amount of diffused nitrogen. Fig.17 gives a schematic of the various layers discussed [**102**].

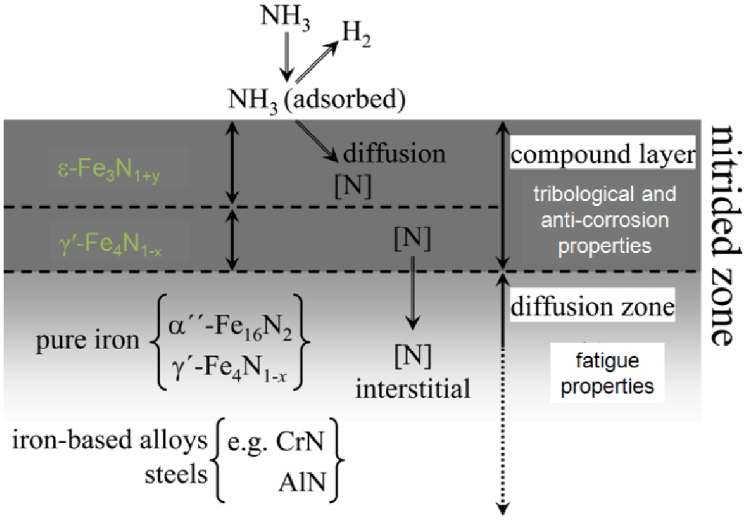

Figure 17: Various layers formed during nitriding [**48**]

4.1.2 Methods

The most common methods of nitriding steels are briefly discussed as follows [**48**].

Gas Nitriding: involves the diffusion of nitrogen into steel by exposing the metal surface to nitrogenous gas (such as ammonia) and holding it for some time at a suitable temperature. Gas nitriding is described in detail in the following sections.

Pack Nitriding: involves the diffusion of nitrogen into steel by packing it together with nitrogen-containing organic compound in a glass, ceramic or aluminium container and then heating it to very high temperature. This causes the emission of nitrogen from the organic compound, which then diffuses into the steel.

Plasma Nitriding: In plasma nitriding, plasma-discharge technology is used to deposit nitrogen ions (from the anode) onto the surface of steel (the cathode) at high voltage in vacuum. The interaction between the nitrogen ions and the cathode results in the formation of nascent nitrogen which diffuses into the steel. Due to the fast provision of nitrogen atoms and the inert nature of the process environment, excellent dimension control and desirable properties are obtained with plasma nitriding.

Salt Bath or Liquid Nitriding: involves the nitriding of steel by keeping it in contact with molten salt bath of cyanates or cyanides. Liquid nitrided steel usually has a long-term wear and corrosion resistance.

4.1.3 Gas Nitriding

Gas nitriding is a surface hardening process whereby nitrogen is diffused into steel surface by holding the steel in a controlled environment of nitrogenous gas at a suitable temperature (usually ranging between 495 to 565^{0}C). It is the most common method of nitriding steel, especially for complicated shapes of machine tools that require high surface hardness [**103**].

Ammonia is usually the nitrogenous gas, and it decomposes into nitrogen atoms and hydrogen gas on reaching the steel surface, as shown in equation below.

$$NH_3 \rightarrow [N] + \frac{3}{2}H_2$$

The atomic nitrogen then diffuses into the steel and occupies the interstitial sites in the ferrite lattice to form an interstitial solid solution. This is illustrated diagrammatically in Fig.17.

Continuous diffusion of nitrogen results in the formation of the compound layer on reaching the equilibrium concentration for the evolution of iron nitrides. Fig. 18 shows the various equilibrium concentrations for the precipitation of iron nitrides.

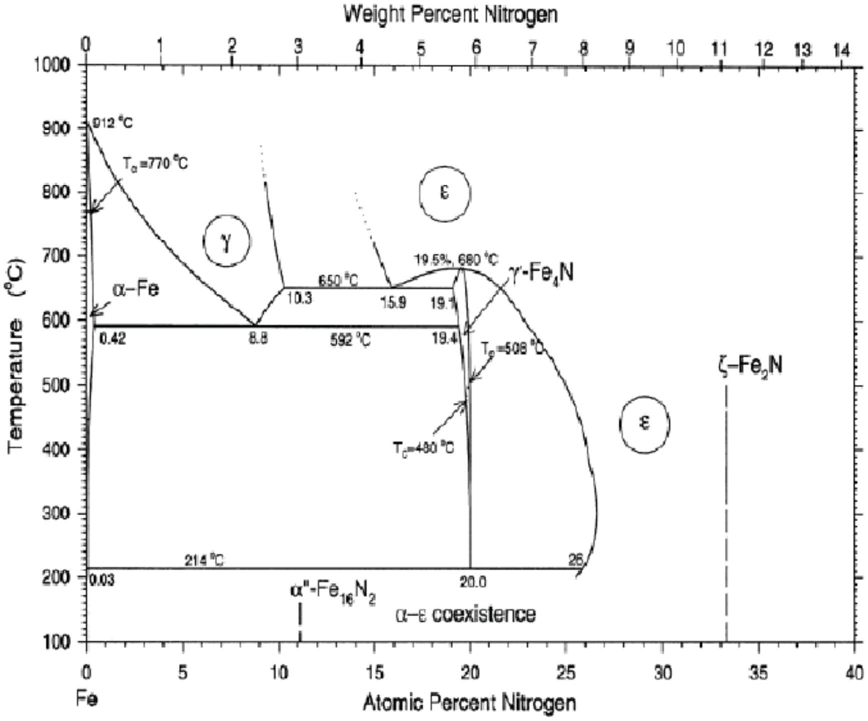

Figure 18: Fe-N Equilibrium diagram [48]

Depending on the concentration of the diffused nitrogen as well as the temperature of the process, two types of precipitates may be formed. The first is the γ1-phase which constitutes a precipitate of Fe_4N as demonstrated by the following equation.

$$4Fe + [N] \rightarrow Fe_4N$$

The second is ε-phase which consists of Fe_2N or Fe_3N precipitate depending on the concentration of nitrogen and the surface condition, as demonstrated by the following chemical equations.

$$Fe_4N + [N] \rightarrow 2Fe_2N$$

OR

$$3Fe_4N + [N] \rightarrow 4Fe_3N$$

Fig. 19 shows a microscopic observation of the nitrided region based on SEM technique. Surface kinetics immensely affects the nature and the type of the layers that forms during the nitriding process. Some factors that affect the process are: type of atmosphere, nitriding number, steel composition, alloying elements composition, process time, process temperature and pressure. The most significant factor is the nitriding number (or potential), which is defined as the ratio of partial pressures of ammonia to hydrogen in the nitriding atmosphere. It is given by the equation (4.1).

$$K_N = \frac{p_{NH_3}}{[p_{H_2}]^{3/2}} \qquad (4.1)$$

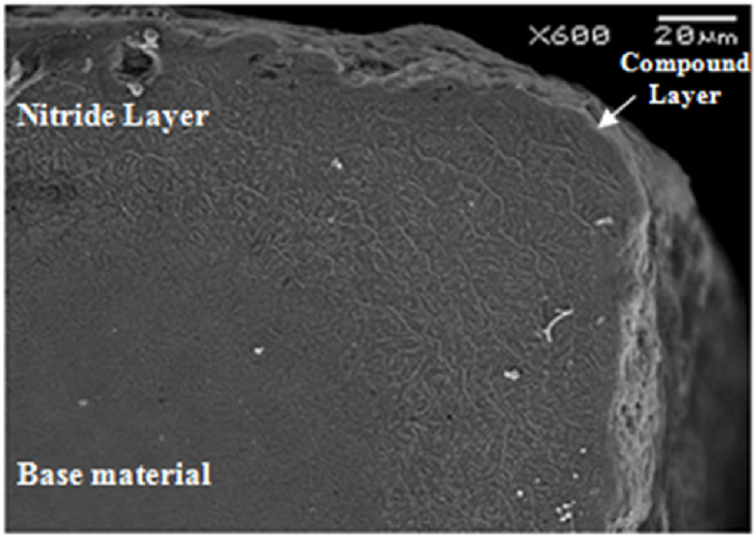

Figure 19: SEM of a nitrided corner for AISI H13 Steel [**104**]

The nitriding number is the controlling parameter for the process. And, it is related to the atmospheric nitrogen concentration by Henrys law as follows.

$$[a_N] = [\%N] = k \times K_N \qquad (4.2)$$

Where,

$a_N = nitrogen\ activity$

$k = Equilibrium\ constant\ at\ a\ particular\ temperature$

$K_N = nitriding\ number\ or\ potential$

The steel composition of the steel should also be a factor of interest. The composition of the compound layer has been found to be related to the amount of carbon in the steel. More ε-phase is formed with higher carbon concentration [**105**]. Some sparsely distributed alloy precipitates (further hardened the diffusion layer) are also formed due to the presence of alloying elements in the steel.

4.1.4 Gas nitriding of Aluminum hot extrusion dies

As mentioned previously, nitriding is commonly used for hardening the surface of transmission mechanical components and process equipments, among which is the hot extrusion dies [**104**]. Nitriding is essential for longevity of hot extrusion dies because of the high temperatures, large surface loads, and wear they are subjected to during operations [**104**]. Due to the complicated shapes of hot extrusion die cavities, gas nitriding is the most common method for nitriding the surface of the die cavities [**104**].

Despite the suitability of gas nitriding for the surface hardening of tool steels, it was shown that non-uniformity of nitrogen concentration profiles in complex and sharp features of hot extrusion dies cavities result in the development of residual stresses that cause the premature failure of the dies during operation [**104**,**106**]. The stresses were found to be more deteriorating in the compound layer due to the formation of new phases that have different physical and mechanical properties [**107**]. It was previously determined that, it is necessary to continuously reduce the nitriding potential during the process in order to control the thickness and constituents of the compound layer [**108**]. This is called the two-stage controlled gas nitriding process and details about it can be found in the next section. Even though the magnitude of the residual stresses is reduced with the controlled gas nitriding process, the failure of the extrusion dies still occurs at the sharp corners and uneven features of its geometry. Therefore, the study of the residual stresses that develop during gas nitriding cannot be neglected.

4.1.5 The two-stage controlled nitriding process

Traditional gas nitriding process was found to be inefficient in the gas nitriding of tool steels. High surface brittleness and thick compound layer develops due to the improper control of nitrogen diffusion during the traditional gas nitriding process. Furthermore, it is difficult to get repetitive results with traditional gas nitriding process due to lack of automatic monitoring and adjustment system. So, automated (or controlled) gas nitriding process is used nowadays for the gas nitriding of hot extrusion dies.

A popular automated (or controlled) gas nitriding set up is the two-stage controlled nitriding process. It involves the use of a software program in effectively carrying out all the stages that are required for nitriding of tool steels. The diffusion of atomic nitrogen from ammonia is controlled by a parameter called the nitriding potential (K_n). With the proper control of the nitriding potential, a compound layer of required thickness and phase composition results. A brief explanation of the steps that make up the two-stage controlled nitriding cycle is given as follows [**104**,**109**,**110**].

1. The furnace is first heated and equalized to the preset temperature of about 450^0C, which takes about 3 hours.
2. The atmospheric air is replaced with ammonia and nitrogen gas mixture in the retort. The filling is done automatically by the equipment and it takes about 2 hours.
3. The nitriding potential is set at 6.4 $(\text{atm})^{-1/2}$, while the furnace temperature is raised to about 490^0C. This is the first stage of the nitriding cycle, and the process takes about 2.5 hours depending on the type of sample and ammonia dissociation rate.
4. The nitriding potential is then reduced to 0.323 $(\text{atm})^{-1/2}$, while the furnace temperature is raised further to about 530^0C. This is the second stage of the nitriding cycle which takes about 3.8 hours.

5. Finally, a cooling fan is turned-on automatically and the temperature of the sample is lowered to about 110^{0}C. The cooling takes about 3 hours.

The actual nitriding process takes about 6.8 hours even though the total cycle time is about 15 hours. Fig.20 shows the variation of temperature during the cycle. While Fig. 21 shows the variation of the nitriding potential with time. The various stages that are involved in the process are highlighted in the figures.

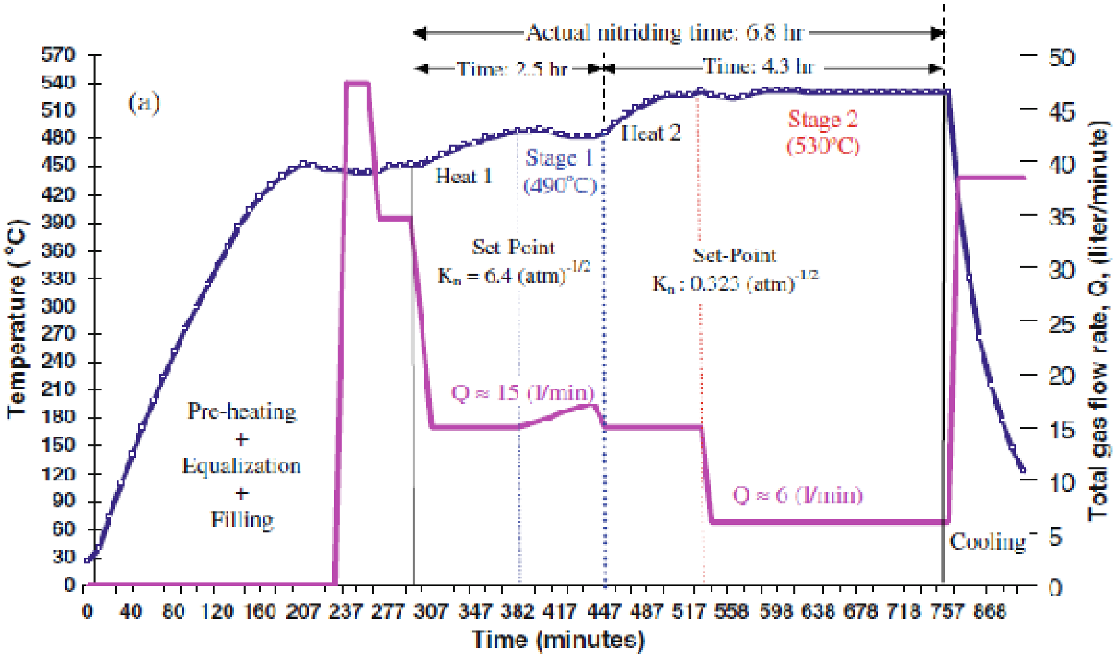

Figure 20: Variation of Temperature and Flow rate with process time [104]

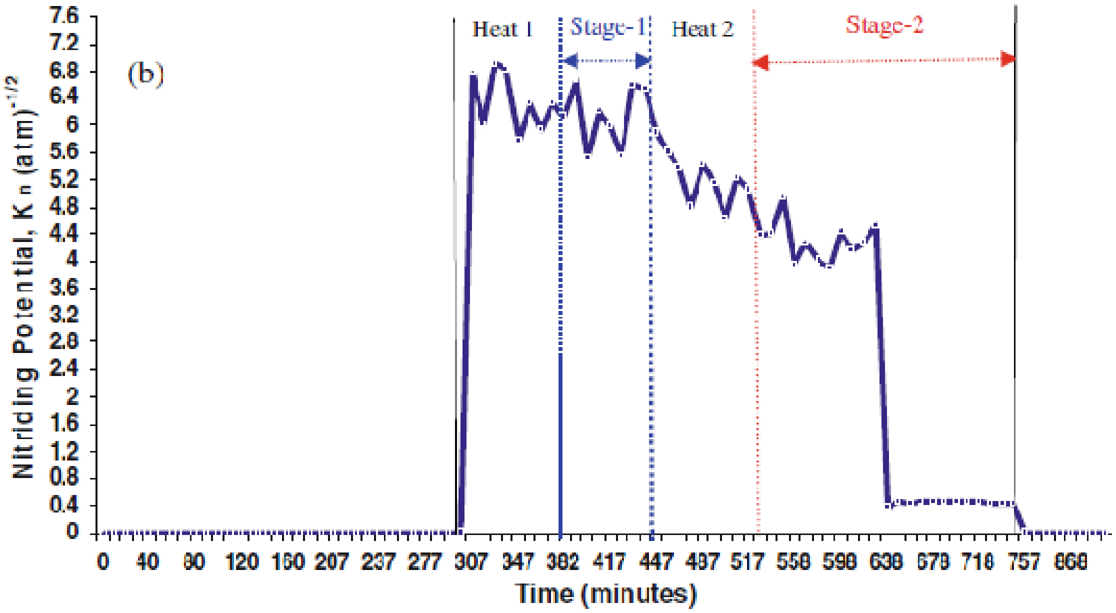

Figure 21: Variation of nitriding potential with process time [**104**]

4.1.6 Past Work

Research work pertaining to the effect of nitrogen on the surface properties of steel started independently in both Germany and America in 1920s. However, only the researchers from Germany were succeeded in developing the first nitrided steel at that time. The European researchers becomes the second to re-produced nitrided steels after the World War II. Much research has taken place in order to exploit the thermodynamics and kinetics of the reactions that are involved. The following paragraphs give a summary of the recent findings on the nitriding process.

Experimental investigation on the effect of process variables on the nitriding of steel was previously carried out [**111**]. The surface hardness was found to depend on both the nitriding potential and temperature, with the highest hardness on the surface. AISI H 13 tool steel was also gas nitrided using the two-stage controlled nitriding process and the nitride layer was characterized based on optical microscopy, SEM, XRD, EDS, and microhardness analysis techniques. It was found that in-process variation of the nitriding potential can be used to control the depths and surface properties of the nitrided regions, specifically the compound layer. It was further demonstrated that the process results in the life time improvement of extrusion dies [**104**].

The influence of surface roughness on the nitriding kinetics of AISI H13 tool steels was thoroughly investigated [**112**]. It was observed that increasing the surface roughness greatly enhance the diffusion of nitrogen into the material [**112**,**110**]. Three pre-treated samples under same experimental conditions were nitrided using the controlled nitriding process .It was found out that surface preparations (in form of grinding, polishing and lapping) prior to the process have a strong influence on the nitriding kinetics. The pre-treated samples were found to result in deeper case depth, better surface properties and longer die life [**110**]. Contrary to that, soft and shallow case depths were observed in samples that were not pre-treated. This leads to the suggestion that extrusion die surfaces should be properly polished before nitriding for improved surface properties [**113**].Other surface treatment methods for surface preparation of steels are surface ultrasonic peening [**114**], short peening [**115**], and cathode sputtering [**116**].

Previously, Grebman et al. [**117**] measured the residual stresses that are induced in the ε-phase of the compound layer. They found out that, the stresses are mainly due to the compositional strain (due to the variation of nitrogen concentration in the nitride layers) and thermal misfit between the ε-phase and other layers. They confirmed the previous investigation that, the stresses due the volume misfit between the compound layer and the α-Iron do not contribute to the residual stresses as they are fully accommodated plastically.

Mostly, modeling of nitriding process was carried out using simple models that were developed based on Fick’s law. Mathematical models that can accurately predict the nitrogen concentration profiles under various process conditions were developed by researchers [**118**,**119**,**120**,**103**]. From the numerical simulation of controlled gas nitriding, it was found that the nitriding potential has a great influence not only on the kinetics of the various layers developed, but also on the compositions of the material [**121**]. It was determined that, predictable phase compositions and thickness can be obtained by proper control of the nitriding potential [**121**]. Therefore, it was found out that it is necessary to continuously reduce the nitriding potential during the process in order to avoid the formation of the undesirable compound layer [**108**].

Physical and mathematical models for the numerical simulation of the uniaxial stress states that are developed during nitriding process were developed. Fick’s law was used to accurately predict the various layers in the nitrided region, and the diffusion result is sequentially-coupled with material constitutive equations. Prediction of the residual stresses was made and close agreement between experimental and numerical results was obtained. It was found out that the residual stresses that are developed in the compound layer have more negative effects on the performance of the nitrided steels than those developed in the diffusion layer [**107**,**122**,**123**,**124**,**125**].

A sequentially-coupled thermal-diffusion analysis of the two-stage controlled nitriding cycle was carried out and a close agreement was found between the simulation and experiments. It was found out that nitriding time, temperature and potential significantly affects the depth and hardness of the nitrided region [**126**]. The phase field method was used for predicting the evolution of the compound layer at 540^0C. The influence of the various material and process parameters on the nitriding kinetics was investigated. The model accurately predicts the experimentally measured thickness of the compound layer [**48**].

It can be seen that, the prediction of the developed residual stresses during the gas nitriding of tool steels was done based on simple models in the literature. Therefore, in the present study a more rigorous technique, the Phase Field Method, will be coupled with elasticity in order to predict the residual stresses that are developed during the nitriding of AISI H13 hot extrusion dies.

4.2 Proposed Research

The ultimate goal of the research is to numerically capture the phase transformation that occurs during the gas nitriding of steel, and to couple it with material constitutive models. This will enable the prediction of the developed residual stresses, and help in understanding the reason for the frequent failure of hot extrusion dies, especially at the sharp corners. The analysis will be carried out for both the compound and diffusion layer.

CHAPTER 5

METHODOLOGY

In this chapter, a brief description of the system model to be used in the current work is first presented. The proposed research as well as the research methodology then follows. Finally, a brief explanation for the numerical implementation of the governing equations is given.

5.1 System Model

For Hot Corrosion

As previously discussed, hot degradation process mainly occurs due to a reaction between the zirconia stabilizer (Y_2O_3) and the corrosive salt (V_2O_5). The reaction results in 4-5% volumetric expansion in the top coat due to the tetragonal-monoclinic phase transformation of zirconia as shown below.

$$\text{YSZ (tetragonal)} + V_2O_5\ (\textit{in melt}) \rightarrow 2YVO_4 + ZrO_2\ \text{(monoclinic)}$$

The Phase Field Method (PFM) will be used in modeling the tetragonal to the monoclinic phase transformation of zirconia in the top coat. The transformation is considered to occur due to the diffusion of the corrosive salt, V_2O_5, at 900^0C. The model will be coupled with elasticity in order to predict the transformation-induced stresses. Simulation experiments will be carried out at various level of melt composition. Analysis will also be carried out in both the PRZ and MIRZ of the top coat as shown in Fig.22.

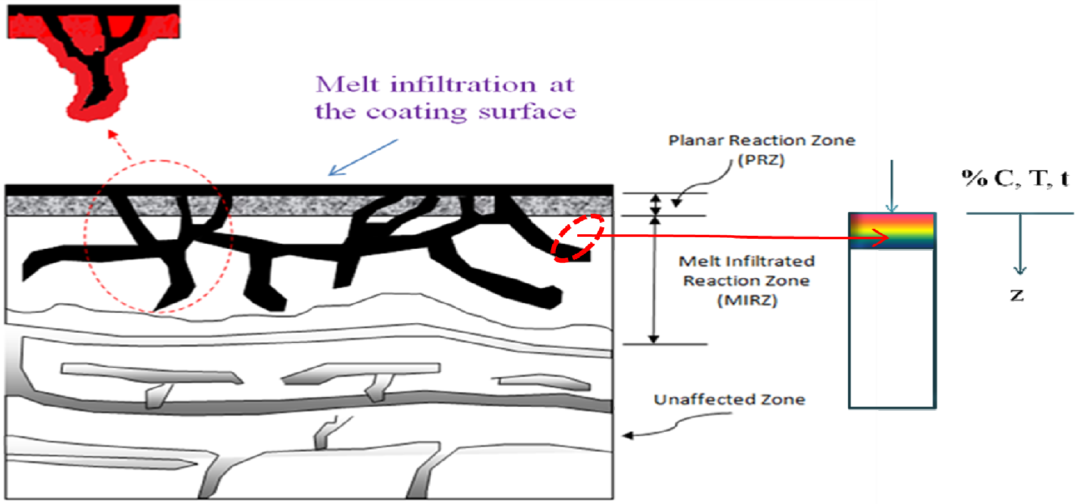

Figure 22: PRZ and MIRZ (Zoomed) in a typical YSZ Top Coat

For Gas Nitriding

The same model is expected to work well with gas nitriding of tool steels. In that case, new phases evolve as a result of the diffusion of atomic nitrogen into the material. The diffused nitrogen atoms react with material constituents of the steel to form various phases (in the diffusion and compound layers) which have a significant effect in the mechanical behavior of the system.

5.2 Phase Field Model

In the present study, an isothermal PFM is developed for diffusion-induced transformations. The order parameter (or phase field) coupling with the concentration field has enabled interfacial tracking of both the parent and growing phases.

5.2.1 Model assumptions

The following basic assumptions are made in developing the model:

- The transformation is unidirectional and proceeds in a direction that is normal to the surface.
- The system is considered to consist of only two phases.
- The materials of the coexisting phases are assumed to be Isotropic.
- Inhomogeneous elasticity is assumed with elastic constants that are defined by the TYPE II interpolation function.
- A plain strain assumption is adopted for the model.

5.2.2 Mathematical Formulations

Phase Field Variables

The **kinetic equations** that describe the evolution of the phase field variables are derived according to non-equilibrium (irreversible) thermodynamic principles. Considering a two-phase system, **two phase-field** variables are needed to represent the micro-structural distribution at a given time, t. They are, conserved variable which is used to describe the changes in the composition or concentration of the diffusion specie, and a non-conserved phase field variable which is used to track the evolution of the growing phase. The volume changes in the parent phase directly comes by the summation rule.

So, let

$\eta_1(r, t)$ = order parameter/field variable representing the evolution of the growing phase

X_S = concentration of the diffusion specie

5.2.3 Total Free Energy

The driving force behind microstructure evolution comes from the total free energy of the system. As mentioned previously, phase transformation is only possible if transition occurs in such a way that the total free energy of the system decreases.

The total free energy of the system may be represented as:

$$F(\eta_1, X_S) = F_{bulk} + F_{int.} + F_{el} \qquad (5.1)$$

Where,

F_{bulk} is the bulk or local free energy, F_{int} is the Interfacial energy and F_{el} is the elastic strain energy of the system.

The variational form of the free energy functional (F) can be represented by [**7**]:

$$F(\eta_1, C_S) = \int \left[f(\eta_1, X_S) + \frac{{\alpha_1}^2}{2} (\nabla\eta_1)^2 + f_{el}(u_i, \eta_1) \right] dV \qquad (5.2)$$

Where, α_1 is the gradient energy coefficient for Allen-Cahn equation [**6**], and u_i is the displacement field.

Based on the KKS model [**31**], a fictitious concentration is used to represent the interfacial (transitional) region as a mixture of the two phases with different compositions of equal chemical potential. The fictitious concentration and the chemical potentials are usually expressed as:

$$X_S = h(\eta_1) \cdot X_{Sg} + [1 - h(\eta_1)] \cdot X_{Sp} \qquad (5.3)$$

$$\frac{\partial f_g(X_{Sg}, T)}{\partial {X_g}^S} = \frac{\partial f_p(X_{Sp}, T)}{\partial {X_p}^S} \qquad (5.4)$$

X_{Sp} & X_{Sg} = $concentration\ fields\ for\ the\ melt\ in\ the\ two\ coexisting\ phases$

$T = temperature$

Using Kim-Kim Suzuki model [**31**], the local free energy function/density of the two phase zone can be expressed as:

$$f(\eta_1, X_S) = h(\eta_1) f_g(X_{Sg}, T) + [1 - h(\eta_1)] f_p(X_{Sp}, T) + w_1 g(\eta_1) \qquad (5.5)$$

Where,

$w_1 = determining\ the\ height\ of\ the\ imposed\ free\ energy\ barrier.$

$f_g(X_{Sg}, T) = chemical\ free\ energy\ of\ growing\ phase$

$f_p(X_{Sp}, T) = chemical\ free\ energy\ of\ parent\ phase$

$h(\eta_1) = TYPE\ II\ interpolation\ function = -2{\eta_1}^3 + 3{\eta_1}^2$

$g(\eta_1) = Double - well\ potential = {\eta_1}^2 (1 - \eta_1)^2$

The interfacial energy (σ) and thickness (l) are usually expressed as:

$$\sigma = \frac{1}{3\sqrt{2}} \sqrt{\alpha_1 \cdot w_1} = \frac{4}{3\sqrt{2}} \sqrt{\alpha_1 \Delta f_{max}} \approx \sqrt{\alpha_1 \Delta f_{max}} \qquad (5.6)$$

$$l = \alpha^* \sqrt{2} \sqrt{\frac{\alpha_1}{w_1}} = \frac{2.94}{2\sqrt{2}} \sqrt{\frac{\alpha_1}{\Delta f_{max}}} \approx \sqrt{\frac{\alpha_1}{\Delta f_{max}}} \qquad (5.7)$$

Where,

$\Delta f_{max} = height\ of\ the\ energy\ barrier\ with\ minima\ at\ 0\ and\ 1$

$\alpha^* = 2.94, for\ \ interface\ width\ as\ the\ distance\ between\ \eta_1 = 0.05\ and\ \eta_1 = 0.95$

It was previously demonstrated by Hu et al.[**127**] that, the growth kinetics is not sensitive to the type of approximation that is used for the chemical free energy. The chemical free energies of the growing ($f_g(X_{Sg}, T)$) and parent phase ($f_p(X_{Sp}, T)$) can be expressed using simple parabolic approximations as shown in equation (5.8) & (5.9).

$$f_p(X_{Sp}, T) = A(T)(X_S - {X_p}^S)^2 \qquad (5.8)$$

$$f_g\left(X_{Sg},T\right) = B(T)\left(X_S - {X_g}^S\right)^2 \qquad (5.9)$$

Where,

$A(T)$ & $B(T) = Constants\ for\ fitting\ the\ chemical\ free\ energy\ to\ a\ parabola$

Analytical solution for the KKS free energy density exists as:

$$f(\eta_1, X_S) = \frac{A(T)\cdot B(T)\left[X_S - {X_p}^S - \left({X_g}^S - {X_p}^S\right)\cdot h(\eta_1)\right]^2 + w_1 g(\eta_1)}{B(T) + [A(T) - B(T)]h(\eta_1)} \qquad (5.10)$$

For parabolic chemical free energy approximations with similar curvatures, the free energy density reduces to:

$$f(\eta_1, X_S) = A(T)\left[X_S - {X_p}^S - \left({X_g}^S - {X_p}^S\right)\cdot h(\eta_1)\right]^2 + w_1 g(\eta_1) \qquad (5.11)$$

Where,

$$A(T) = \frac{\Delta G(X_0, T)}{\left({X_g}^S - {X_p}^S\right)^2} \qquad (5.12)$$

Where,

$\Delta G(X_S, T) = transformation\ driving\ force = f_p(X_S, T) - f_g(X_S, T)$

The atomic or diffusion mobility is related to the diffusivity of the chemical specie by:

$$M_S = \frac{D(T)}{2A(T)} \qquad (5.13)$$

Where,

$D(T) = diffusion\ coefficient\ of\ the\ chemical\ specie\ into\ the\ material$

5.2.4 Governing Equations

The main equations governing the temporal and spatial evolution of the microstructure evolution in solid-state phase transformations were developed by Cahn-Hillard [**5**] for the concentration, Allen-Cahn/ Ginzburg-Laudau [**6**] for the order parameter, and mechanical (stress) equilibrium equations for displacement fields. The Cahn-Hilliard equation governs the rate of diffusion of the chemical specie into the microstructure of the material. The Allen-Cahn equation governs the transformation rate according to the chemical reaction. The mechanical (stress) equilibrium equations governs the elastic interaction of the coexisting phases during the phase transformation. Since the elastic relaxation occurs faster than that of the diffusion and kinetic equations, the displacement fields are considered to reach equilibrium abruptly during the simulation.

The constitutive model is developed, based on a micromechanics approach to take care of the deformations that is associated with the phase transformations. A direct-coupled approach, where the computed results of the phase transformation are affected by the elastic deformation of the material and vice versa, is adopted.

Applying the Allen-Cahn, Cahn-Hillard and stress equilibrium equations to the diffusion-induced transformation, both in variational as well as partial differential forms, gives [**7**]:

$$\frac{\partial X_S(\vec{r},t)}{\partial t} = \nabla\cdot\left[M_S\nabla\left(\frac{\delta F(\eta_1,X_S)}{\delta X_S}+\frac{\delta F_{el}(u_i,\eta_1,X_S)}{\delta X_S}\right)\right] \qquad (5.14)$$

$$\therefore \qquad \frac{\partial X_S(\vec{r},t)}{\partial t} = \nabla\cdot\left[M_S\nabla\left(\frac{\partial f(\eta_1,X_S)}{\partial X_S}+\frac{\partial F_{el}(u_i,\eta_1,X_S)}{\partial X_S}\right)\right] \qquad in \quad \Omega$$

$$\frac{\partial \eta_1(\vec{r},t)}{\partial t} = -L_1\left(\frac{\delta F(\eta_1,X_S)}{\delta \eta_1}+\frac{\delta F_{el}(u_i,\eta_1,X_S)}{\delta \eta_1}\right) \qquad (5.15)$$

$$\therefore \qquad \frac{\partial \eta_1(\vec{r},t)}{\partial t} = -L_1\left(\frac{\partial f(\eta_1,X_S)}{\partial \eta_1}-\alpha_1\nabla^2\eta_1+\frac{\partial f_{el}(u_i,\eta_1,X_S)}{\partial \eta_1}\right) \qquad in \quad \Omega$$

$$\frac{\partial \sigma_{ij}}{\partial r_j} = \frac{\partial\left[C_{ijkl}\colon \varepsilon_{kl}{}^{e}\right]}{\partial r_j} = C_{ijkl}\left[\frac{1}{2}\left(\frac{\partial^2 u_k}{\partial r_l \partial r_j} + \frac{\partial^2 u_l}{\partial r_k \partial r_j}\right)\right] - \varepsilon_{ij}{}^{c}\frac{\partial\left(\delta c(\bar{r},t)\right)}{\partial r_j} - \varepsilon_{ij}{}^{\eta_1}\frac{\partial(\eta_1{}^2)}{\partial r_j}$$

$$= 0 \qquad (5.16)$$

Where,

$i, j, k, l = 1{,}2 \quad ; \quad r_1 = x \;\;\&\;\; r_2 = y$

$$C_{ijkl} = C_{mn} = \begin{cases} C_m\,, & m = n = 1{,}2{,}3 \\ C_{1+m+n,} & m \neq n, and\; m = 1{,}2 \end{cases}$$

$\vec{r}$ represents spatial coordinates, x and y.

t represents time

L_1 represents kinetic mobility that describes the transformation rate; and

M_S represents diffusion/atomic mobility of the chemical specie in the solid material.

$u_i = displacement\ field$

$\varepsilon_{ij}{}^{\eta_1} = transformation\ or\ bain\ strain$

$\varepsilon_{ij}{}^{c} = compositional\ strain$

$\delta c(\bar{r}, t) = linear\ function\ of\ composition\ according\ to\ vegard's\ law$

$C_{ijkl} = Elastic\ stiffness\ tensor$

$\sigma_{ij} = Stress\ tensor$

The kinetic mobility, a proportionality constant for the rate of transformation, is usually taken as constant. The diffusion/atomic mobility is either taken as a constant or a phase-dependent function. It should be noted that, the elastic strain energy is usually taken as a function of only the order parameter or the concentration field or both.

The partial derivatives of the free energy density with respect to the phase field variables are expressed as:

$$\frac{\partial f(\eta_1, X_S)}{\partial C_S} = 2A(T)\left[X_S - X_p{}^S - \left(X_g{}^S - X_p{}^S\right) \cdot h(\eta_1)\right] \qquad (5.17)$$

$$\frac{\partial f(\eta_1, X_S)}{\partial \eta_1} = -2A(T)\left[X_S - X_p{}^S - \left(X_g{}^S - X_p{}^S\right) \cdot h(\eta_1)\right] \times \frac{\partial h(\eta_1)}{\partial \eta_1} \times -\left(X_g{}^S - X_p{}^S\right)$$
$$+ w_1 \frac{\partial g(\eta_1)}{\partial \eta_1} \qquad (5.18)$$

$$\frac{\partial f_{el}(u_i, \eta_1, X_S)}{\partial \eta_1}$$
$$= -\left[2(C_{11}\, \varepsilon_{11}{}^{\eta_1}\, \eta_1 + C_{12}\;\, \varepsilon_{12}{}^{\eta_1}\, \eta_1)u_{1,1} + 4C_{66}\, \varepsilon_{21}{}^{\eta_1}\left(u_{1,2} + u_{2,1}\right)\right.$$
$$\left. + 2(C_{12}\, \varepsilon_{11}{}^{\eta_1}\, \eta_1 + C_{22}\, \varepsilon_{22}{}^{\eta_1}\, \eta_1)u_{2,2}\right]$$
$$+ 2(C_{11}(\, \varepsilon_{11}{}^{\eta_1})^2\, \eta_1{}^2 + 2C_{12}\, \varepsilon_{11}{}^{\eta_1}\, \varepsilon_{22}{}^{\eta_1}\, \eta_1{}^2 + 4C_{66}(\, \varepsilon_{12}{}^{\eta_1})^2\, \eta_1{}^2$$
$$+ C_{22}(\, \varepsilon_{22}{}^{\eta_1})^2\, \eta_1{}^2) \qquad (5.19)$$

$$\frac{\partial f_{el}(u_i, \eta_1, X_S)}{\partial X_S}$$
$$= -\frac{1}{2}(C_{11} + C_{21})\, \varepsilon_{11}{}^c\left[u_{1,1} - \, \varepsilon_{11}{}^c\left(X_S - \bar{X}_{avg}\right)\right]$$
$$- (C_{12} + C_{22})\, \varepsilon_{22}{}^c\left[u_{2,2} - \, \varepsilon_{22}{}^c\left(X_S - \bar{X}_{avg}\right)\right] \qquad (5.20)$$

Thus, the governing PDEs become:

$$\begin{aligned}\frac{\partial X_S}{\partial t} = \nabla \cdot M_S \Big(& 2A(T)\big[\nabla X_S - \big(X_g{}^S - X_p{}^S\big) \cdot \nabla h(\eta_1)\big] \\ & + \nabla \Big\{ -\frac{1}{2}(C_{11} + C_{21})\, \varepsilon_{11}{}^c \big[u_{1,1} - \varepsilon_{11}{}^c\big(C_S - \bar{C}_{avg}\big)\big] - (C_{12} \\ & + C_{22})\, \varepsilon_{22}{}^c \big[u_{2,2} - \varepsilon_{22}{}^c (X_S - \bar{X}_{avg})\big]\Big\}\Big) \qquad (5.21)\end{aligned}$$

$$\begin{aligned}\frac{\partial \eta_1}{\partial t} = -L_1 \Big[\Big[\Big\{ & 2A(T)\big[X_S - X_p{}^S - \big(X_g{}^S - X_p{}^S\big) \cdot h(\eta_1)\big] \times \frac{\partial h(\eta_1)}{\partial \eta_1} \times -\big(X_g{}^S - X_p{}^S\big) \\ & + w_1 \frac{\partial g(\eta_1)}{\partial \eta_1} - \alpha_1 \nabla^2 \eta_1 \Big\} \\ & - \big[2(C_{11}\, \varepsilon_{11}{}^{\eta_1}\, \eta_1 + C_{12}\, \varepsilon_{12}{}^{\eta_1}\, \eta_1) u_{1,1} + 4C_{66}\, \varepsilon_{21}{}^{\eta_1}\big(u_{1,2} + u_{2,1}\big) \\ & + 2(C_{12}\, \varepsilon_{11}{}^{\eta_1}\, \eta_1 + C_{22}\, \varepsilon_{22}{}^{\eta_1}\, \eta_1) u_{2,2}\big] + 2(C_{11}(\varepsilon_{11}{}^{\eta_1})^2\, \eta_1{}^2 \\ & + 2C_{12}\, \varepsilon_{11}{}^{\eta_1}\, \varepsilon_{22}{}^{\eta_1}\, \eta_1{}^2 + 4C_{66}(\varepsilon_{12}{}^{\eta_1})^2\, \eta_1{}^2 \\ & + C_{22}(\varepsilon_{22}{}^{\eta_1})^2\, \eta_1{}^2)\Big] \qquad (5.22)\end{aligned}$$

$$\begin{aligned} & C_{11} u_{1,11} + C_{12} u_{2,21} + C_{44}\big(u_{2,12} + u_{1,22}\big) - (C_{11}\, \varepsilon_{11}{}^{\eta_1} + C_{12}\, \varepsilon_{22}{}^{\eta_1}) \frac{\partial(\eta_1{}^2)}{\partial x} \\ & \qquad - 2C_{44}\, \varepsilon_{12}{}^{\eta_1} \frac{\partial(\eta_1{}^2)}{\partial y} - (C_{11}\, \varepsilon_{11}{}^c + C_{12})\, \varepsilon_{22}{}^c \frac{\partial X_S}{\partial x} = 0 \qquad (5.23)\end{aligned}$$

$$\begin{aligned} & C_{22} u_{2,22} + C_{12} u_{1,12} + C_{44}\big(u_{1,21} + u_{2,11}\big) - (C_{12}\, \varepsilon_{11}{}^{\eta_1} + C_{22}\, \varepsilon_{22}{}^{\eta_1}) \frac{\partial(\eta_1{}^2)}{\partial y} \\ & \qquad - 2C_{44}\, \varepsilon_{21}{}^{\eta_1} \frac{\partial(\eta_1{}^2)}{\partial y} - (C_{21}\, \varepsilon_{11}{}^c + C_{22}\, \varepsilon_{22}{}^c) \frac{\partial X_S}{\partial y} = 0 \qquad (5.24)\end{aligned}$$

The simplification of the set of PDEs for one phase system reduces to Fick's second law of diffusion. This confirms the fact that, the Cahn-Hilliard equation is non-linear diffusion equation for multi-phase systems as shown in equation (5.14); while the Allen-Cahn equation is a kinetic or transformation equation as shown in equation (5.15). The simplification is done as follows.

$$\frac{\partial X_S}{\partial t} = 2M_S A(T)\left[\nabla^2 X_S - \cancel{\left(X_g{}^S - X_p{}^S\right) \cdot \nabla^2 h(\eta_1)}\right] = \cancel{2} \times \frac{D(T)}{\cancel{2A(T)}} \times \cancel{A(T)} \times \nabla^2 X_S$$

$$\therefore \ \frac{\partial X_S}{\partial t} = D(T) \cdot \nabla^2 X_S \quad Fick' second\ law\ of\ diffusion \qquad (5.25)$$

$$\cancel{\frac{\partial \eta_1}{\partial t} = -L_1 \left\{ 2A(T)\left[X_S - X_p{}^S - \left(X_g{}^S - X_p{}^S\right) \cdot h(\eta_1)\right] \times \frac{\partial h(\eta_1)}{\partial \eta_1} \times -\left(X_g{}^S - X_p{}^S\right)\right.}$$

$$\cancel{\left. + w_1 \frac{\partial g(\eta_1)}{\partial \eta_1} - \alpha_1 \nabla^2 \eta_1 \right\} \quad + \quad 0} \ = \ 0$$

Thus, the Cahn-Hilliard equation simplifies to Fick's second law and the Allen-Cahn equation vanishes for one phase.

5.2.5 Normalization

For ease of computation at mesoscale, the phase field and mechanical equilibrium equations are usually normalized. All length scales are normalized by a characteristic length (l_0) and all energy terms are normalized by the height of the energy barrier between the stables phases. The characteristic length is selected in such a way that the interface has about 4-6 grid points in order to make the computation smooth

The normalization detail is given in Appendix D, and the normalized variables are presented as follows.

$$\bar{x} = \frac{x}{l_0}\,, \quad \bar{f} = \frac{f}{\Delta f_{max}}\,, \quad \bar{t} = \frac{M_S \cdot \Delta f_{max} \cdot t}{(l_0)^2}\,, \tag{5.26}$$

$$\bar{M}_S = 1\,, \quad \bar{\mathrm{L}}_1 = \frac{\mathrm{L}_1 (l_0)^2}{M_S}\,, \; \bar{\alpha}_1 = \frac{\alpha_1}{(l_0)^2 \cdot \Delta f_{max}} \tag{5.27}$$

$$\bar{C}_{ijkl} = \frac{C_{ijkl}}{\Delta f_{max}} \tag{5.28}$$

Therefore, the normalized PDEs become:

$$\frac{\partial X_S(\vec{\bar{r}}, t)}{\partial \bar{\mathrm{t}}} = \bar{\nabla}^2 \left(\frac{\partial \bar{f}(\eta_1, X_S)}{\partial X_S} + \frac{\partial f_{el}(u_i, \eta_1, X_S)}{\partial X_S} \right) \tag{5.29}$$

$$\frac{\partial \eta_1(\vec{\bar{r}}, t)}{\partial \bar{\mathrm{t}}} = -\bar{\mathrm{L}}_1 \left(\frac{\partial \bar{f}(\eta_1, X_S)}{\partial \eta_1} - \bar{\alpha}_1 \nabla^2 \eta_1 + \frac{\partial \overline{f_{el}}(\bar{u}_1, \bar{u}_2, \eta_1)}{\partial \eta_1} \right) \tag{5.30}$$

$$\bar{C}_{ijkl} \left[\frac{1}{2} \left(\frac{\partial^2 \bar{u}_k}{\partial \bar{r}_l \partial \bar{r}_j} + \frac{\partial^2 \bar{u}_l}{\partial \bar{r}_k \partial \overline{r_j}} \right) \right] - \varepsilon_{ij}{}^{c} \frac{\partial\big(\delta c(\bar{r}, t)\big)}{\partial r_j} - \varepsilon_{ij}{}^{\eta_1} \frac{\partial ({\eta_1}^2)}{\partial \overline{r_j}} = 0 \tag{5.31}$$

In complete form, the PDEs can be expressed as:

$$\begin{aligned} \frac{\partial X_S}{\partial \bar{t}} = \nabla \cdot \Bigg[\frac{2A(T)}{\Delta f_{max}} \Big[\bar{\nabla} X_S - \big({X_g}^S - {X_p}^S \big) \cdot \bar{\nabla} h(\eta_1) \Big] \\ + \nabla \Big\{ -\frac{1}{2} (\bar{C}_{11} + \bar{C}_{21})\, \varepsilon_{11}{}^{c} \big[\bar{u}_{1,1} - \varepsilon_{11}{}^{c} \big(X_S - \bar{X}_{avg} \big) \big] - (\bar{C}_{12} \\ + \bar{C}_{22})\, \varepsilon_{22}{}^{c} \big[\bar{u}_{2,2} - \varepsilon_{22}{}^{c} (X_S - \bar{X}_{avg}) \big] \Big\} \Bigg] \end{aligned} \tag{5.32}$$

$$\frac{\partial \eta_1}{\partial \bar{t}} = -\bar{L}_1 \Bigg[\Bigg\{\Bigg(\frac{2A(T)}{\Delta f_{max}}\big[X_S - {X_p}^S - \big({X_g}^S - {X_p}^S\big)\cdot h(\eta_1)\big] \times \frac{\partial h(\eta_1)}{\partial \eta_1} \times -\big({X_g}^S - {X_p}^S\big)\Bigg)$$

$$+ \frac{w_1}{\Delta f_{max}}\frac{\partial g(\eta_1)}{\partial \eta_1} - \bar{\alpha}_1 \nabla^2 \eta_1\Bigg\}$$

$$- \big[2(\bar{C}_{11}\, {\varepsilon_{11}}^{\eta_1}\, \eta_1 + \bar{C}_{12}\, {\varepsilon_{12}}^{\eta_1}\, \eta_1)u_{1,1} + 4\bar{C}_{66}\, {\varepsilon_{21}}^{\eta_1}\big(u_{1,2} + u_{2,1}\big)$$

$$+ 2(\bar{C}_{12}\, {\varepsilon_{11}}^{\eta_1}\, \eta_1 + \bar{C}_{22}\, {\varepsilon_{22}}^{\eta_1}\, \eta_1)u_{2,2}\big] + 2(\bar{C}_{11}(\,{\varepsilon_{11}}^{\eta_1})^2\, {\eta_1}^2$$

$$+ 2\bar{C}_{12}\, {\varepsilon_{11}}^{\eta_1}\, {\varepsilon_{22}}^{\eta_1}\, {\eta_1}^2 + 4\bar{C}_{66}(\,{\varepsilon_{12}}^{\eta_1})^2\, {\eta_1}^2$$

$$+ \bar{C}_{22}(\,{\varepsilon_{22}}^{\eta_1})^2\, {\eta_1}^2)\Bigg] \qquad (5.33)$$

$$\bar{C}_{11}\bar{u}_{1,11} + \bar{C}_{12}\bar{u}_{2,21} + \bar{C}_{44}\big(\bar{u}_{2,12} + \bar{u}_{1,22}\big) - (\bar{C}_{11}\, {\varepsilon_{11}}^{\eta_1} + \bar{C}_{12}\, {\varepsilon_{22}}^{\eta_1})\frac{\partial({\eta_1}^2)}{\partial x}$$

$$- 2\bar{C}_{44}\, {\varepsilon_{12}}^{\eta_1}\frac{\partial({\eta_1}^2)}{\partial y} - (\bar{C}_{11}\, {\varepsilon_{11}}^{c} + \bar{C}_{12}\, {\varepsilon_{22}}^{c})\frac{\partial X_S}{\partial x} = 0 \qquad (5.34)$$

$$\bar{C}_{22}\bar{u}_{2,22} + \bar{C}_{12}\bar{u}_{1,12} + \bar{C}_{44}\big(\bar{u}_{1,21} + \bar{u}_{2,11}\big) - (\bar{C}_{12}\, {\varepsilon_{11}}^{\eta_1} + \bar{C}_{22}\, {\varepsilon_{22}}^{\eta_1})\frac{\partial({\eta_1}^2)}{\partial y}$$

$$- 2\bar{C}_{44}\, {\varepsilon_{21}}^{\eta_1}\frac{\partial({\eta_1}^2)}{\partial y} - (\bar{C}_{21}\, {\varepsilon_{11}}^{c} + \bar{C}_{22}\, {\varepsilon_{22}}^{c})\frac{\partial X_S}{\partial y} = 0 \qquad (5.35)$$

It can be seen that the PDEs expressed in equations (5.32)-(5.35) are highly non-linear, stiff and strongly coupled.

5.2.6 Initial & Boundary Conditions

Initial conditions (at t=0) for the phase field and local force balance equations are:

$$X_S(\vec{r}, 0) = 0 \text{ , chemical specie has zero concentration in } \Omega \qquad (5.36)$$

$$\eta_1(\vec{r}, 0) = 0, \text{only the parent phase exist in } \Omega \qquad (5.37)$$

$$u_i(\vec{r}, 0) = 0, \qquad \text{in } \Omega \qquad (5.38)$$

The PDEs are usually solved with different types of boundary conditions. Dirichlet Boundary conditions that are commonly applied to the model are:

$$\eta_1(\overline{r_1}, t) = 1, \; X_S(\overline{r_1}, t) = C_1 \qquad on \;\; \partial\Omega \quad \overline{r_1} = (x_1, y_1, z_1) \qquad (5.39)$$

$$\eta_1(\overline{r_2}, t) = 0, \; X_S(\overline{r_2}, t) = C_2 \qquad on \;\; \partial\Omega \quad \overline{r_2} = (x_1, y_1, z_1) \qquad (5.40)$$

$$u_i(\overline{r_i}, t) = 0 \; or \; any \; value \; z, \qquad on \;\; any \; given \; \partial\Omega \quad \bar{r}_i = (x_i, y_i, z_i) \qquad (5.41)$$

The most general Neumann (flux) boundary condition that are usually applied to the model are:

$$\left.\frac{\partial X_S}{\partial n}\right|_{n=a} = \phi(\bar{r}, t, \eta_1, X_S) \qquad on \; any \; \partial\Omega \; having \; defined \; flux \qquad (5.42)$$

$$\left.\frac{\partial \eta_1}{\partial n}\right|_{n=a} = \lambda(\bar{r}, t, \eta_1, X_S) \qquad at \; any \; \partial\Omega \; having \; defined \; flux \qquad (5.43)$$

$$\left.\frac{\partial u_i}{\partial n}\right|_{n=a} = \omega(\bar{r}, t, \eta_1, X_S) \qquad at \; any \; \partial\Omega \; having \; defined \; flux \qquad (5.44)$$

Where,

$\{\phi(\bar{r}, t, \eta_1, X_S), \lambda(\bar{r}, t, \eta_1, X_S), \omega(\bar{r}, t, \eta_1, X_S) \quad are \; constants \; or \; functions \;\; of \;\; equation \; variables$

$n = unit \; vector \; that \; is \; normal \; to \; the \; boundary, a$

Robin boundary condition is commonly used for problems in which the maximum surface concentration of the chemical specie in the microstructure is not attained abruptly. This is more realistic as it incorporates the effect of mass convection during the diffusion of the chemical specie into the material. This means that, it takes some time for the chemical specie to completely diffuse into the microstructure. The Robin boundary condition commonly applied to the model is:

$$-D\left.\frac{\partial X_S}{\partial n}\right|_{n=a} = g - \beta \cdot X_S \qquad at\ any\ \partial\Omega\ having\ mass\ convection \qquad (5.45)$$

Where,

$\beta = mass\ transfer\ coefficient\ at\ the\ surface (m/s)$

$g = \beta \cdot X_g$

$X_g = gas\ or\ liquid\ concentration\ of\ the\ diffusion\ specie\ outside\ the\ material$

5.3 Implementation Method

Due to its numerous advantages, the finite element method is used to solve the systems of coupled PDEs that govern the microstructure evolution. As in conventional finite element schemes, the PDEs are first expressed in the variational form after which an approximation for the solution is obtained using a space of continuous piecewise interpolation functions. This results in a system of non-linear algebraic equations which can be easily solved using common numerical schemes for the solution of large system of equations. For the purpose of demonstration, only 1D weak formulation for the diffusion (Cahn-Hilliard) and kinetic (Allen-Cahn) equations is described. However, the approach equally applies to the elastic interaction coupling terms as well as the stress equilibrium equations. The author neglects the elastic coupling terms in order to avoid expressing cumbersome equations and make the weak formulation easier to understand.

5.3.1 Weak Formulation

Due to the high non-linearity associated with the PDEs, phase field equations are first converted to the weak form before the solution. In the weak form, a PDE is not required to hold absolutely in the computational domain. Instead, the PDE only has solution with respect to certain test functions that are equivalent to the Global Basis Function. This is equivalent to formulating the problem to require a solution in the sense of a distribution. The weak form is derived by multiplying both sides of the PDE by the test functions, and then carrying out integration of the terms by part (based on Green's theorem).

The weak formulation for the PDEs is as follows:

$$\int \frac{\partial X_S}{\partial t} \vartheta_1 dxdy - \int M_S \nabla \vartheta_1 \cdot \nabla \frac{\partial f}{\partial X_S} dxdy = 0 \qquad (5.46)$$

$$\int \frac{\partial \eta_1}{\partial t} \vartheta_2 dxdy + \int L_1 \vartheta_2 \frac{\partial f}{\partial \eta_1} dxdy - \int L_1 \alpha_1 \nabla \vartheta_2 \cdot \nabla \eta_1 dxdy = 0 \qquad (5.47)$$

Where, ϑ1 avd ϑ2 are the test or global basis functions that are used for the finite element discretization.

Moreover, the time discretization is done using Backward Difference Approximation (BDA) of 1st-5th order. It should be noted that, the boundary terms have vanished during the integration due to the use of Dirichlet boundary conditions at the boundaries.

5.3.2 Finite Element Discretization

Space Discretization

Let the domain ($0 < x < l$) be discretized such that the subspace of piecewise function ($V_{h,0}$) vanishes at $x = 0\ and\ x = l$. And, let the finite element approximation for the solution be a part of the subspace (i.e.$X_{Sh}, \eta_{1h} \in V_{h,0}$). Then, the weak formulation for the approximate solution becomes:

$$\begin{cases} \int_0^l \frac{\partial X_{Sh}}{\partial t} \vartheta_1 dx - \int_0^l M_S \nabla \vartheta_1 \cdot \nabla \frac{\partial f}{\partial X_{Sh}} dx = 0 \\ \int_0^l \frac{\partial \eta_{1h}}{\partial t} \vartheta_2 dxdy + \int_0^l L_1\, \vartheta_2 \frac{\partial f}{\partial \eta_{1h}} dxdy - \int_0^l L_1\, \alpha_1 \nabla \vartheta_2 \cdot \nabla \eta_{1h} dxdy = 0 \end{cases} \tag{5.48}$$

and $\vartheta_1, \vartheta_2 \in V_{h,0}$; $0 < t < T$

Employing the usual hat basis functions for the space, we have:

$$\int_0^l \frac{\partial X_{Sh}}{\partial t} \varphi_{1i} dx - \int_0^l M_S \nabla \varphi_{1i} \cdot \nabla \frac{\partial f}{\partial X_{Sh}} dx = 0 \tag{5.49}$$

$$\int_0^l \frac{\partial \eta_{1h}}{\partial t} \varphi_{2i} dx + \int_0^l L_1\, \varphi_{2i} \frac{\partial f}{\partial \eta_{1h}} dx - \int_0^l L_1\, \alpha_1 \nabla \varphi_{2i} \cdot \nabla \eta_{1h} dx = 0 \tag{5.50}$$

Where,

$$\varphi_{1i}, \varphi_{2i} = usual\ hat\ basis\ functions\ for\ V_{h,0}$$

$$i = 1,2, \dots \dots, n-1$$

The finite element solution for the dependent variables is expressed as a linear combination of the hat functions at each time step. Therefore, the finite element solution of the dependent variables is:

$$X_{Sh} = \sum_{j=1}^{n-1} \mu_{1j}(t)\, \varphi_{1i} \qquad (5.51)$$

$$\eta_{1h} = \sum_{j=1}^{n-1} \mu_{2j}(t)\, \varphi_{2i} \qquad (5.52)$$

Where,

$\mu_{2j,}\, \mu_{2j}$ $= time - dependent\ coefficient\ vectors\ for\ the\ solution$

Thus, the discretized equations become:

$$\sum_{j=1}^{n-1} \dot{\mu}_{1j}(t) \int_0^l \varphi_{1j}\, \varphi_{1i} dx - \ M_S \sum_{j=1}^{n-1} \mu_{1j}(t) \int_0^l \nabla\varphi_{1i} \cdot \nabla f(\varphi_{1j,} \varphi_{2j}) dx = 0 \quad (5.53)$$

$$\sum_{j=1}^{n-1} \dot{\mu}_{2j}(t) \int\limits_0^l \varphi_{2j}\, \varphi_{2i} dx + L_1 \sum_{j=1}^{n-1} \mu_{2j}(t) \int\limits_0^l \varphi_{2i}\, f\big(\varphi_{1j,} \varphi_{2j}\big) dx$$

$$- L_1 \alpha_1 \sum_{j=1}^{n-1} \mu_{2j}(t) \int\limits_0^l \nabla\varphi_{2i} \cdot \nabla\varphi_{2j} dx = 0 \qquad (5.54)$$

By assigning the corresponding matrices notations, we have:

$$\gamma_j(t) = \sum_{j=1}^{n-1} \mu_{1j}(t) \qquad \& \qquad \dot{\gamma}_j(t) = \sum_{j=1}^{n-1} \dot{\mu}_{1j}(t) \qquad (5.55)$$

$$\xi_j(t) = \sum_{j=1}^{n-1} \mu_{2j}(t) \qquad \& \qquad \dot{\xi}_j(t) = \sum_{j=1}^{n-1} \dot{\mu}_{2j}(t) \qquad (5.56)$$

$$A_{ij} = \int_0^l \varphi_{1j}\, \varphi_{1i} dx \qquad \& \qquad B_{ij} = \int_0^l \nabla\varphi_{1i} \cdot \nabla f(\varphi_{1j,} \varphi_{2j}) dx \qquad (5.57)$$

$$C_{ij} = \int_0^l \varphi_{2j}\,\varphi_{2i} dx\ ,\ D_{ij} = \int_0^l \varphi_{2i}\, f\left(\varphi_{1j,}\varphi_{2j}\right) dx\ \&\ E_{ij} = \int_0^l \nabla\varphi_{2i} \cdot \nabla\varphi_{2j} dx \quad (5.58)$$

Therefore, the discretized equations become:

$$A_{ij} \cdot \dot{\gamma}_j(t) - M_S \cdot \gamma_j(t) \cdot B_{ij} = 0 \qquad (5.59)$$

$$C_{ij} \cdot \dot{\xi}_j(t) + L_1\xi_j(t)D_{ij} - L_1\alpha_1\xi_j(t)\, E_{ij} = 0 \qquad (5.60)$$

$$0 < t < T$$

Where,

$A_{ij}, C_{ij} = Mass\ Matrices$

$B_{ij}, D_{ij}, E_{ij} = Stiffness\ matrices$

Equation (5.59) and (5.60), gives the space semi-discretization for the PDEs, which represents $n-1$ set of non-linear Ordinary Differential Equations (ODEs) for $n-1$ time steps. It is called semi-discretized form of the PDE due to the fact that, it is only discretized in space. Because of the non-linearity associated with the PDEs, the load vector has vanished.

Time Discretization

For stable solution, COMSOL solvers discretized the time derivatives by the use finite difference approximations (based on the Backward Euler Method of 1th – 5th accuracy) for non-linear PDEs. Depending on the time step, the solver tries to find a compromise between accuracy and the time of computation. For the purpose of demonstration, the finite difference approximations of only 1st and 3rd order will be shown.

The FDA based on backward difference approximation of 1st order accuracy is:

$$\gamma_j(t) = \gamma_t \qquad \& \qquad \xi_j(t) = \xi_t \qquad (5.61)$$

$$\dot{\gamma}_j(t) = \frac{\gamma_t - \gamma_{t-1}}{\Delta t} \qquad \& \qquad \dot{\xi}_j(t) = \frac{\xi_t - \xi_{t-1}}{\Delta t} \qquad (5.62)$$

While, the FDA based on backward difference approximation of 3rd order accuracy is:

$$\dot{\gamma}_j(t) = \frac{\gamma_t - 3\gamma_{t-1} + 3\gamma_{t-2} - \gamma_{t-3}}{\Delta t^3} \ \& \ \dot{\xi}_j(t) = \frac{\xi_t - 3\xi_{t-1} + 3\xi_{t-2} - \xi_{t-3}}{\Delta t^3} \quad (5.63)$$

CHAPTER 6

NUMERICAL IMPLEMENTATION

The numerical implementation of the model, as applied to the V_2O_5 hot corrosion of thermal barrier coatings and gas nitriding of Aluminum extrusion dies will be discussed. The Representative Volume Elements (RVEs) are selected based on the microscopic observation of the phase transformations. Then, the governing equations, initial and boundary conditions and required simulation parameters are briefly discussed. Finally details of the implementation method, discretization and validation of the results are given.

6.1 Hot Corrosion of TBC

6.1.1 Planar Reaction Zone (PRZ)

The phase field model (PFM), already developed in Chapter 5, is applied to the V_2O_5 hot corrosion of the top coat. Although, PFM was used in predicting the diffusionless tetragonal-to-monoclinic phase transformation of zirconia [**52**], it has not been applied to the hot corrosion of the top coat (to the best of our knowledge). Previous experimental work [**89**] showed that, the rate of monoclinic-to-tetragonal transformation of zirconia during the hot corrosion of the top coat is not diffusionless but depends on the extent of the coating exposure to the corrosive salt.

In the following section, a PFM for tetragonal-to-monoclinic phase transformation of zirconia in the top coat is formulated. The model is applied to the Type-I hot corrosion process, where the solid-state phase transformation is induced by the diffusion of chemical specie (V_2O_5) into the top coat. The phase transformation is coupled with the microelasticity theorem in order to predict the transformation-induced stresses. Commercial finite element packages, COMSOL Multiphysics 4.3 is used for the analysis.

Geometric Model

Based on the microscopic observation of the PRZ [**89**], the phase transformation is considered to be unidirectional, and proceeds from the coating surface to a certain depth. The experiment revealed that, the depth of transformation in the PRZ does not exceed 50 µm. Therefore, a RVE of 50µm x 10µm is selected for the analysis in the PRZ as shown in Fig. 23.

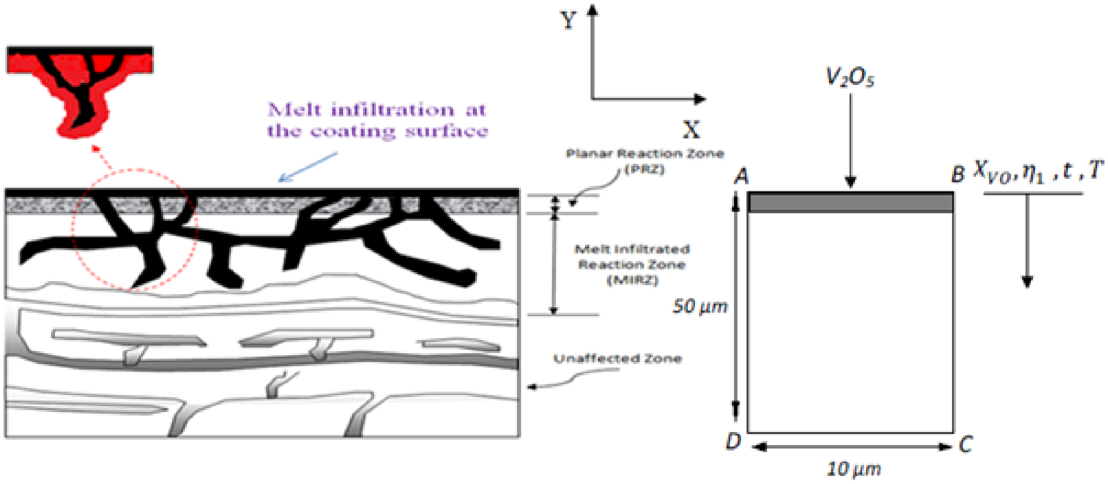

Figure 23: RVE for transformation in the PRZ

Governing Equations

As in chapter 5, the main equations governing the temporal and spatial evolution of the microstructure evolution during the solid-state phase transformation are the Cahn-Hillard

[**5**] equation for the diffusion of V_2O_5, Allen-Cahn/ Ginzburg-Laudau [**6**] for the transformation of zirconia and stress equilibrium equations for displacement fields. However, the governing partial differential equations have to be normalized first before implementation as explained in chapter 5.

The Cahn-Hilliard, Allen-Cahn and mechanical equilibrium equations are given by equations (5.14), (5.15) and (5.16) (in chapter 5). There is sufficient experimental evidence [**89**] that, the diffusion of V_2O_5 does not cause any lattice expansion of both the tetragonal/monoclinic phases of zirconia. Therefore, the stress-free strain contains only the contribution by the transformation or bain strain; and the compositional strain is zero. This implies that, the stresses are induced due to the transformation-mismatch between the monoclinic and tetragonal phases of zirconia in the top coat. Thus, the components of compositional strain in equations (5.32)-(5.35) are set as zero.

$$\therefore \; {\varepsilon_{11}}^{c} = {\varepsilon_{22}}^{c} = 0 \qquad (6.1)$$

The governing equations for the analysis in the PRZ can be found in Appendix E.

Initial & Boundary Conditions

Initially, the concentration of V_2O_5 in the top coat is considered to be zero. This implies that, the other dependent variables are also initially zero. Thus, the initial conditions are given by equations (5.36)-(5.38) (in chapter 5).

For the concentration, a Dirichlet boundary condition is applied at the top (exterior) boundary, because previous experimental results [**97**,**89**] showed that the hot corrosion process starts with the immediate exposure of the material to V_2O_5. Thus, the diffusion of

V_2O_5 into the surface of the material can be considered to occur very rapidly and Dirichlet boundary condition is a good approximation for such type of problem. As in conventional diffusion problems, a zero flux (Neumann) boundary condition is applied at the bottom (interior) boundary. This means that the transformation depth does not affect the final results. Therefore, the applied concentration boundary conditions are:

$$X_S(\overline{r_1}, t) = C_1 \qquad on\ \partial\Omega\ \ AB \qquad (6.2)$$

$$-D\frac{\partial X_S}{\partial n}\bigg|_{n=a} = 0 \qquad on\ \partial\Omega\ \ CD \qquad (6.3)$$

For the order parameter, Dirichlet boundary conditions are applied at both the top (exterior) and bottom (interior) boundaries in order to nucleate the m-phase. As used by Wen et al.[7], the boundary conditions ensure that the phase transformation proceeds along a direction that is normal to the transformation depth (unidirectional transformation). The applied boundary conditions for the order parameter are:

$$\eta_1(\overline{r_1}, t) = 1, \quad on\ \partial\Omega\ \ AB \qquad (6.4)$$

$$\eta_1(\overline{r_2}, t) = 0, \quad on\ \partial\Omega\ \ CD \qquad (6.5)$$

For the displacement field, the top boundary was set free while the bottom boundary was constrained to move in the vertical direction. That is,

$$u_2 = 0\,, \qquad on\ \ given\ \partial\Omega\ CD \qquad (6.6)$$

Periodic boundary conditions for all the dependent variables are applied at the left and right boundaries. The left boundary is taken as the source boundary, while the right boundary is taken as the destination boundary. The interaction between the source and the destination boundary is prescribed in such a way that the periodicity or continuity of the RVE is achieved. That is,

$$-n_{src}\cdot\left[-D\frac{\partial\rho}{\partial n}-\alpha\cdot\rho+\gamma\right]_{src}=-n_{dst}\cdot\left[-D\frac{\partial\rho}{\partial n}-\alpha\cdot\rho+\gamma\right]_{dst}\quad on\ \partial\Omega\ BC\&DA \tag{6.7}$$

Where the dependent variable, $\rho = X_S, \eta_1, u_i$

Simulation Parameters

Simulation parameters that were used for the simulation are given in Table 2. A constant temperature of 900^0C was used for the analysis. Appendix B also gives more details about the equilibrium mole concentrations.

Table 2: Input parameters for the simulation in the PRZ

Parameters	**Value**	**Source**
Time of Diffusion (t)	90 mins	
Temperature (T)	900^0C	
Equil. Conc. of V_2O_5 in YSZ($X_{t-z}{}^{eq}$)	1.6 mol%	[**128**,**75**]
Equil. Conc. of V_2O_5 in m-ZrO_2($X_{m-z}{}^{eq}$)	8 mol%	[**128**,**75**]
Diffusion Coefficient($D(T)$) of V_2O_5 in YSZ matrix	$5.0\times10^{-12}m^2/s$	[**129**,**130**]
Chemical Driving Force	5.162×10^{10} J/m^3	[**131**,**52**]
Kinetic Coefficient(L_1)	2 m^3/ J s	[**52**]
Thickness of Interface(l)	$1\ \mu m$	
Gradient Energy Coefficient(α_1)	$1\times10^{-8}J/m$	[**52**]
Characteristic Length (l_o)	$1\mu m$	

Transformation or Bain Strains	$\varepsilon_{11}{}^{\eta_1} = 0.0049$	[**132**]
	$\varepsilon_{12}{}^{\eta_1} = \varepsilon_{12}{}^{\eta_1} = 0$	
	$\varepsilon_{22}{}^{\eta_1} = 0.013$	
Effective Young's modulus		
m-phase	243.58 GPa	[**133**,**52**]
t-phase	40GPa	[**134**]
Effective poisson ratio		
m-phase	0.284	[**133**,**52**]
t-phase	0.22	[**134**]

A plain strain model assumption was adopted, because the thickness of the cross section is far greater than planar dimensions of the RVE. The materials of the coexisting phases were assumed to be Isotropic, and Inhomogeneous elasticity with phase-dependent elastic constants was used. Therefore, a smooth variation of the elastic constants at the interface was defined using the Type-II interpolation function (defined in Equation (5.5)). The change in the lattice structure is according to the ABC correspondence. The transformation strains are computed from the lattice parameters. It is important to note that for the 2D-axis selected (i.e. the $a-b$ plane), only dilational parts of the transformation strains exist; the shear components of the transformation strain vanish. Details for selected simulation parameters are given in Appendix C.

Implementation Details

The coupled sets of PDEs were solved numerically using the commercial finite element package, COMSOL Multiphysics 4.3. The domain was discretized by 8,000 Lagrange quadratic elements of aspect ratio of 1. Mapped mesh with four-noded quadilateral elements were used; resulting in a total of 129,924 degree of freedoms for numerical calculation. An implicit time stepping scheme was used based on a backward difference approximation (BDA) of 1^{st}-5^{th} order of approximation. Therefore, time step as small as 1 x 10^{-7}s was used in order to ensure the convergence and stability of the solution. High relative tolerance of 1 x 10^{-10} was used in order to ensure that accuracy of the integration at each time step. Convergence test has indicated that, the finite element solution has converged. More details concerning the implementation can be obtained in Appendix F.

Validation of Results

Previous microscopic observation [**89**,**93**] shows that, the thickness of the PRZ (at 900^0C) is about 10 μm after 90 minutes of transformation. While in the present study, PRZ thickness of about 12 μm was obtained for the same duration of time. Therefore, qualitatively the current model has predicted the experimentally observed thickness of the PRZ (shown in Fig.24). Quantitative comparison of the phase evolution of the m-phase is not possible due to the lack of proper experimental results for such comparison. Virtually, all previous experimental observations were based on microscopic observations [**89**]. However, the transformation-induced stresses are in good agreement with a previous work [**52**], where modeling of the diffusionless tetragonal-to-monoclinic transformation was carried out.

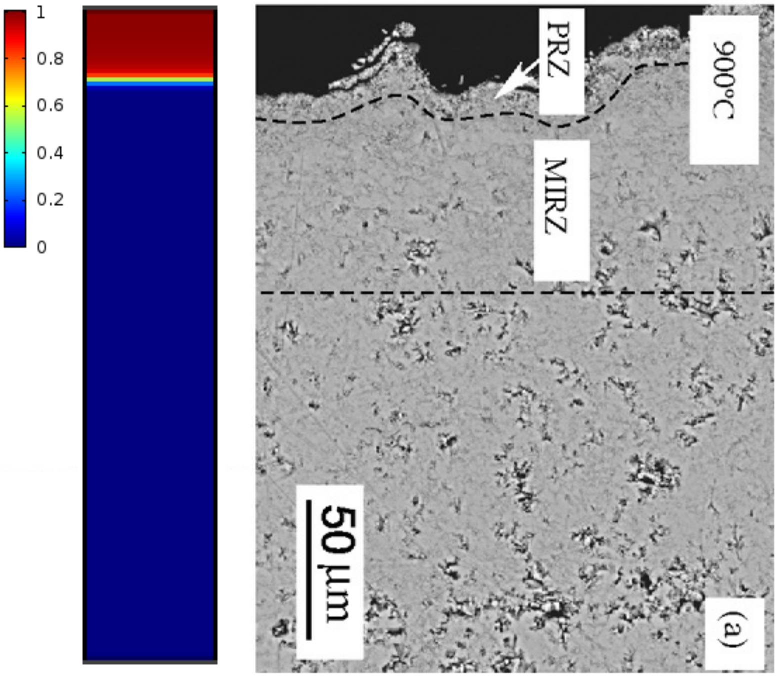

Figure 24: Comparison of the transformation in the PRZ with experiments [89]

6.1.2 Melt-Infiltrated Reaction Zone (MIRZ)

As mentioned previously, the MIRZ forms as a result of the V_2O_5 infiltration through the microcracks and micropores in the air-plasma-sprayed TBC. It was reported that, the infiltration starts immediately as the melt is in contact with the surface of the coating [**89**]. The time required for the melt to infiltrate through 300 µm depth of the coating (at 750^{0}C) was found to be 30 minutes from experiments [**89**], and 3 seconds from Washburn Infiltration Model [**135**]. The discrepancy between experiments and the model is due to the various simplifying assumptions used by Washburn et al. [**135**].

However, estimation of the infiltration time at 900^{0}C was not found in the open literature, and the Washburn model proves to be unreliable in predicting the infiltration time. For this reason, the infiltration time effect is neglected in the current work. And, the micropores/microcracks are assumed to be already filled with V_2O_5 when the transformation starts. The assumption is valid for the temperature and the typical crack section considered in the current work (shown in Fig.25 & 26).

Geometric Model

A typical crack-section of dimension 0.32 x 0.18 μm is taken for the analysis. The average pore diameter is taken as 0.02 μm as determined experimentally [**89**]. As in the PRZ, the melt is assumed to diffuse in a direction that is normal to the reaction surface. Similarly, plane strain assumption is adopted for the analysis in the MIRZ.

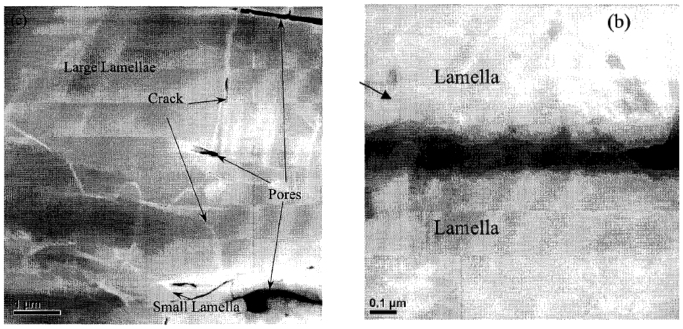

Figure 25: SEM of MIRZ section showing cracks and pores in TBC [173]

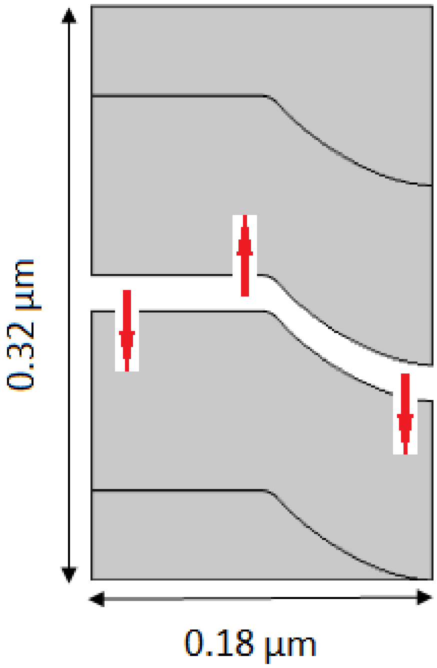

Figure 26: Geometrical Model

Analysis in the MIRZ

The analysis in the MIRZ was carried out using the same sets of equations, initial and boundary conditions, implementation method and simulation parameters that were used for the PRZ. The only exception is that, the domain size, time scale and interface thickness for the simulation in the MIRZ are much smaller, as shown in Chapter 7. Note that the interface thickness, which is usually freely selected in the phase field literature (as in Ref. [**58**]), is reduced to 0.01 µm in order to obtain the desired results. The domain was discretized by 9,000 Lagrange-quadratic elements of average aspect ratio of 0.5301. Triangular elements with three nodes were used, resulting in a total of 145,324 degree of freedoms for numerical calculation. An implicit time stepping scheme was used based on a backward difference approximation (BDF) of 1st-5th order of approximation. Therefore, time step as small as 1 x 10^{-7}s was used in order to ensure the convergence and stability of the solution. High relative tolerance of 1 x 10^{-10} was used in order to ensure that accuracy of the integration at each time step. A test for convergence of the finite element analysis was also carried out. Appendix F gives more details about the implementation of the analysis in the MIRZ

6.2 Gas Nitriding of Extrusion Dies

Although, PFM was developed for the evolution of compound layer during conventional nitriding of steels [**48**], it has never been used to predict the associated residual stresses during the process. Therefore, the phase field model (developed in chapter 5) is used to predict the nitriding kinetics and the developed residual stresses during the two-stage controlled nitriding process. In the following section, a PFM formulation for evolution of the diffusion and compound layer in H13 tool steels is discussed briefly. The solid-state phase transformation is induced by the diffusion of nitrogen gas into the microstructure of the material.

Geometric Model

For the purpose of comparison of numerical result with previous experiments[**104**,**136**,**136**], the actual sample geometry that was used in the experiments is selected for the analysis. The geometry (shown in Fig. 27) has a rough size of 5 x 15 mm dimensions, and only results at some selected regions are presented in the present study. It can be seen that the sample contains all possible sharp and corner features that are obtainable in Aluminum hot extrusion dies as demonstrated in Table 3.

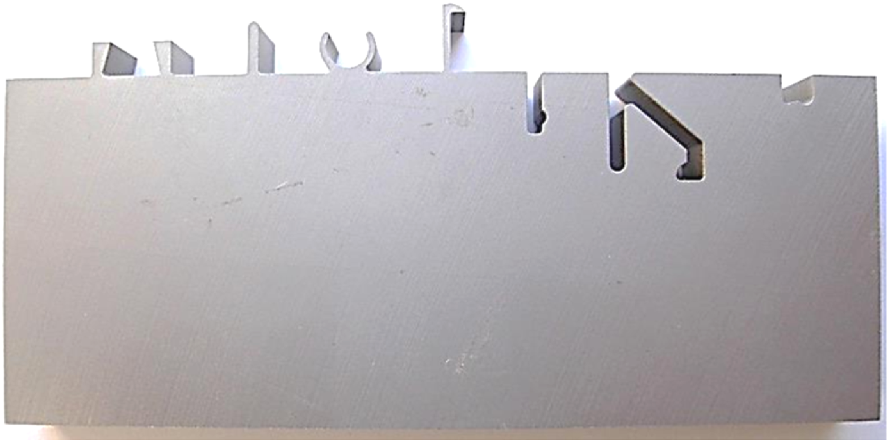

Figure 27: Sample after EDM wire cutting (Dimensions are in mm)

Table 3: Selected profile and corner features [136]

	Feature Sketch	Feature description
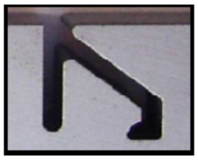	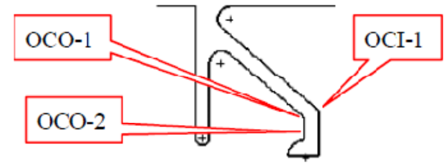	OCO-1: ObtuseCorner Outer-1 OCI-1: Obtuse-Corner Inner-1 OCO-2: Obtuse-Corner Outer-2
		ACO-1: Acute-Corner Outer-1 RCO-1: Right-Corner Outer-1
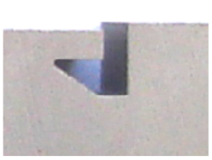	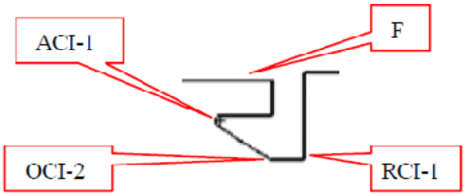	ACI-1: Acute-Corner Inner-1 RCI-1: Right-Corner Inner-1 OCI- 2: Obtuse-Corner Inner-2 F: Flat Surface
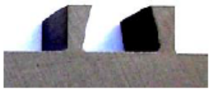	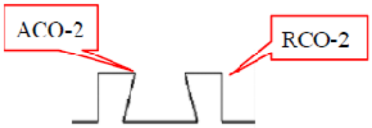	RCO-2: Right-Corner Outer-2 ACO-2: Acute-Corner Inner-2
	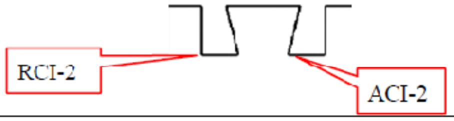	RCI-2: Right-Corner Inner-2 ACI-2: Acute-Corner Inner-2

Governing Equations

The domain is considered to consist of only two phases, the ε-phase and α-iron. Based on our experimental work [**110**], it was observed that the two-stage controlled-nitriding process produces very negligible amount of the $\gamma^{'}$-phase, and the nitride layers were observed to grow in a direction that is normal to the steel surface. So, the evolution of the $\gamma^{'}$-phase is neglected in the current analysis.

Therefore, the main equations governing the temporal and spatial evolution of the diffusion layer and ε-phase phase are Cahn-Hilliard [**5**] for concentration of atomic nitrogen, Allen-Cahn/ Ginzburg-Laudau [**6**] for the evolution of the compound layer, and mechanical (stress) equilibrium equations for the displacement fields. The Cahn-Hilliard equation governs the rate of diffusion of atomic nitrogen into the microstructure of the material. The Allen-Cahn equation governs the transformation rate of the α-iron to the ε-phase according to the chemical reaction. The mechanical (stress) equilibrium equations governs the displacements of the coexisting phases during the phase transformation.

The α-iron to ε-phase transformation is one of the diffusional phase transformations that occur during the gas nitriding of tool steels. It was determined experimentally [**117**] that, the transformation strain due to the volume misfit between the α-iron (BCC crystals) and ε-phase (HCP crystals) is fully relaxed by transformation plasticity.

Thus, the governing equations for the nitriding process are given by equations (5.14)-(5.16) (in chapter 5). The stress-free strain is considered to contain only the contribution by the compositional strain; and the transformation or bain strain is zero. This implies that, the stresses are developed mainly due to the expansion of the α-iron and ε-phase unit cells through the formation of interstitial solid solution with atomic nitrogen.

Depth and residual stresses in the diffusion layer

Due to the fact that the thickness of the compound layer is negligible, the total depth of nitrogen concentration is tracked by considering the domain to contain only the α-iron phase. This reduces the Cahn-Hilliard equation to the linear diffusion equation that is based on Fick's second law as explained in chapter 5. Even though the kinetic equation for the formation of the ε-phase is vanished, the mechanical equilibrium equation still holds. Therefore, the governing equations are obtained by setting some selected parameters (in equation (5.32)-(5.35)) as follows.

$$\varepsilon_{11}{}^{\eta_1} = \varepsilon_{12}{}^{\eta_1} = \varepsilon_{21}{}^{\eta_1} = \varepsilon_{22}{}^{\eta_1} = 0 \qquad (6.8)$$

$$\eta_1 = 0 \qquad (6.9)$$

$$M_S = D_\alpha(T) \qquad (6.10)$$

$$\delta c(x, y, t) = X_S - X_{avg} \qquad (6.11)$$

The governing equations can be found in Appendix E.

Depth and residual stresses in the compound layer

For the evolution of the compound layer, the complete evolution equations are needed. The following parameters (in equations (5.32)-(5.35)) are set as follows.

$$\varepsilon_{11}{}^{\eta_1} = \varepsilon_{12}{}^{\eta_1} = \varepsilon_{21}{}^{\eta_1} = \varepsilon_{22}{}^{\eta_1} = 0 \qquad (6.12)$$

$$M_S = \frac{\eta_1 D_\alpha(T) + [1 - \eta_1] D_\varepsilon(T)}{2 \cdot A(T)} \qquad (6.13)$$

$$\delta c(r, y) = X_S - X_{avg} \qquad (6.14)$$

Thus, the evolution equations are the Cahn-Hilliard equation, Allen-Cahn equation, and mechanical equilibrium equations. Note that, a linear interpolation is used for the variation of the diffusion mobility during the process. The governing equations can be found in Appendix E.

Initial and Boundary Conditions

Even though the actual sample geometry was used for the simulation, the following simple geometry will be used for the description of the boundary conditions.

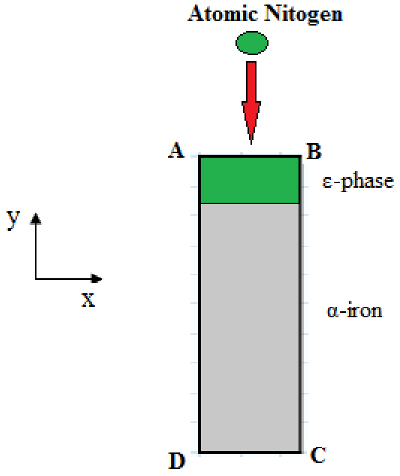

Figure 28: Description of boundary conditions

As in the hot corrosion problem, natural initial condition is adopted. The initial conditions are represented in equations (5.36)-(5.38).

Boundary, AB, is the surface of the tool steel that is exposed to the nitrogenous gas atmosphere. Therefore, a Robin boundary condition is needed for the concentration field due to the mass convection of atomic nitrogen into steel. For the order parameter, a

Dirichlet boundary condition is required at the steel surface as explained previously. The boundary conditions are expressed as follows.

$$-D\left.\frac{\partial X_S}{\partial y}\right|_{n=j} = \beta \cdot \left(X_g - X_{sf}\right) ; Robin\ B.C. \qquad (6.15)$$

$$\eta_1 = 1 \qquad ; Dirichlet\ B.C. \qquad (6.16)$$

Where,

β = $mass\ transfer\ coefficient\ of\ atomic\ nitrogen$

X_g = $controlled\ Nitrogen\ conc.\ (shown\ in\ Fig.\ 3)$

X_{sf} = $concentration\ of\ atomic\ nitrogen\ on\ steel\ surface$

While, boundary DC is subjected to the Neuman (Zero flux) boundary conditions for the concentration and phase field variables. Moreover, the displacement of the boundary in the vertical direction is constrained. The boundary conditions are applied as follows.

$$-D\left.\frac{\partial X_S}{\partial y}\right|_{n=j} = 0 ; Neumann\ B.C. \qquad (6.17)$$

$$-L_1\left.\frac{\partial \eta_1}{\partial y}\right|_{n=j} = 0 ; Neumann\ B.C. \qquad (6.18)$$

$$u_2 = 0 \qquad ; Dirichlet\ B.C. \qquad (6.19)$$

As in the hot corrosion problem, boundaries BC and AD are subjected to periodic boundary conditions with respect to all the dependent variables. The equations for such boundary conditions are expressed in equation (6.7).

Simulation Parameters

For simplicity, the materials of coexisting phases are assumed to be isotropic. However, anisotropic Vegard's constant was used for the lattice expansion of the ε-phase. Inhomogenous elasticity was also used, where the elastic stiffness matrix and the Vegard's constant were smoothly varied from the α-iron to the ε-phase using the Type II interpolation function. Table 4 summarizes the input parameters that were used for the analysis.

Table 4: Input parameters for the nitriding model

Parameter	**Value**	**Source**
Temperature(T)	Varied according to cycle	[**104**]
Diffusion coefficient of nitrogen $D_{\varepsilon\text{-phase}}$ $D_{\alpha\text{-iron}}$	$4.43 \times 10^{-3} \exp(-113180/T)$ cm^2/s $2.027 \times 10^{-6} \exp(-5451/T)$ cm^2/s	[**48**] [**118**]
Mass transfer coefficient of nitrogen in steel(β)	$6.21 \times 10^{-3} \exp(-6267/T)$ cm^2/s	[**118**]
Gas constant (R)	8.314 J/mol K	
Chemical free energies $f(X_e,T)$ $f(X_a,T)$	-3.56 J/mol -2.9 J/mol Evaluated at cycle average temperature, 755.7 K	[**48**]
Gradient energy coefficient	2.5×10^{-9} J/m	
Interfacial energy	0.5×10^{-2} J/m^2	[**48**]
Vegard's constant for ε-phase β_a for ε-phase	9.13×10^{-4} /wt%	[**117**]

β_c for ε-phase	2.24×10^{-3} /wt%	
β_a for α-iron	7.54×10^{-5} /wt%	
Interface thickness	0.5 μm	
Kinetic mobility	6.966×10^{-3} $m^3/J\ s$	Diffusion controlled
Young's modulus		
E_e	243 GPa	[**117**]
E_a	168.4 GPa	
Poisson ratio		
ν_e	0.29	[**117**]
ν_a	0.29	
Equilibrium conc.		
X_e^{eq}	7.5 wt%	[**48**]
X_a^{eq}	5.9 wt%	
Characteristic length	1 μm	

The controlled nitrogen concentration (X_g) in the nitrogenous atmosphere was varied based on the variation of the nitriding potential during the cycle (shown in Fig.29). Similarly, variation of temperature with time during the simulation is given in Fig.30. The average concentration of nitrogen at each time step, which is the reference concentration for the computation of the compositional strain is also given in Fig.31.

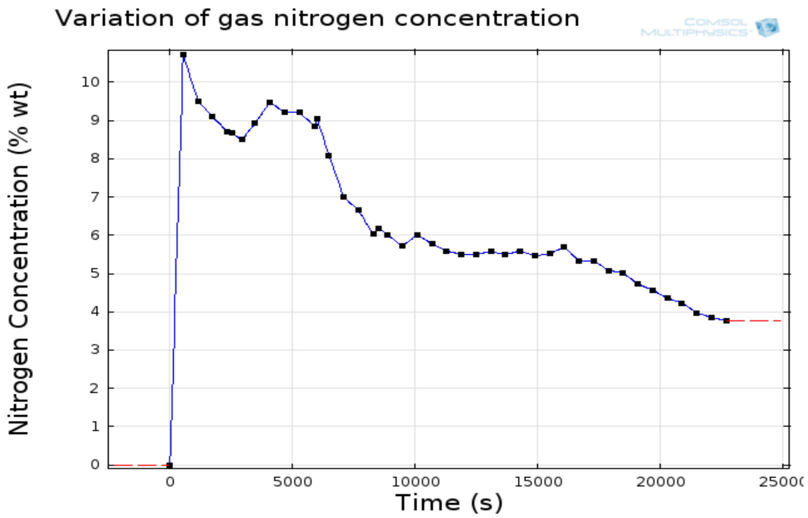

Figure 29: Variation of nitrogen gas concentration with process time

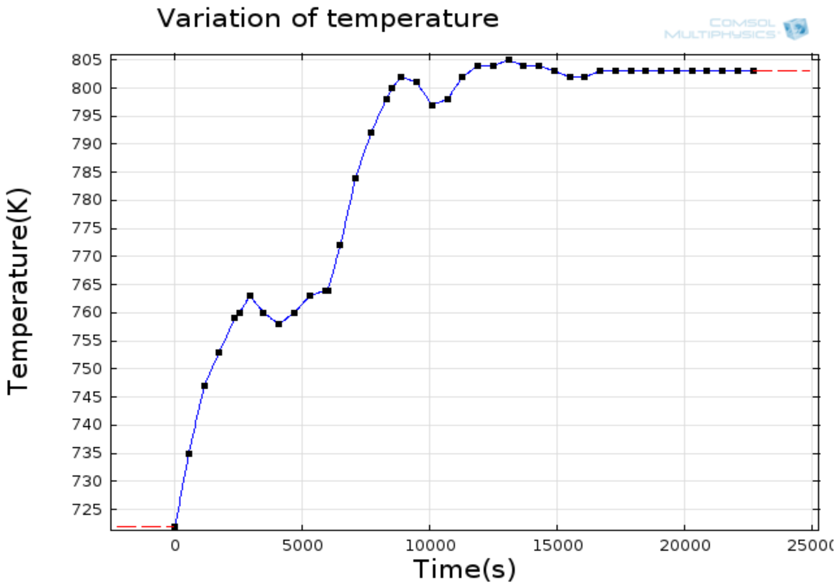

Figure 30: Variation of temperature with process time

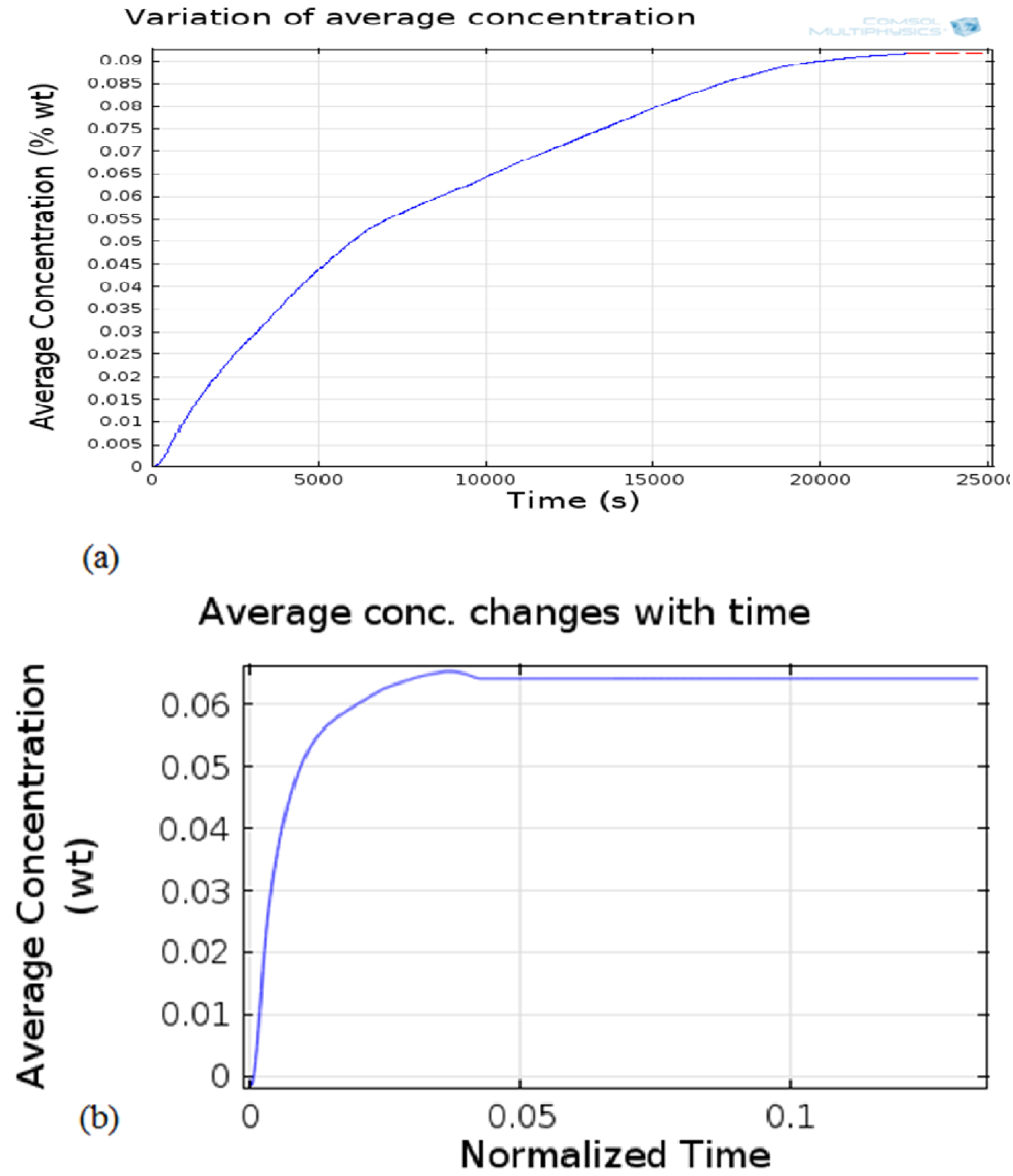

Figure 31: Average nitrogen concentration in (a) diffusion layer, (b) compound layer

Implementation Details

Commercial finite element package, COMSOL Multiphysics 4.3, was used for the analysis. Proper mesh with Lagrange-quadratic elements and implicit time stepping scheme were used for the analysis. Convergence results showed that all the finite element calculations converged. Details regarding the convergence test, relative error, etc are given in Appendix F.

Validation of Results

Analysis in the diffusion layer

For the purpose of validation, the results at some selected corners are compared with previous experimental results [**136**]. Four corners (i.e. C-1, C-2, C-3 and F) are selected as shown in Fig. 32.

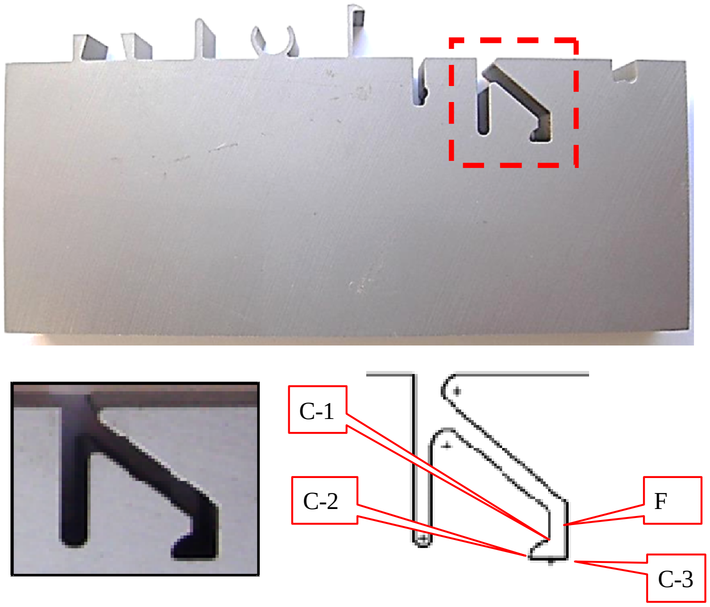

Figure 32: Selected regions for comparison with experiment

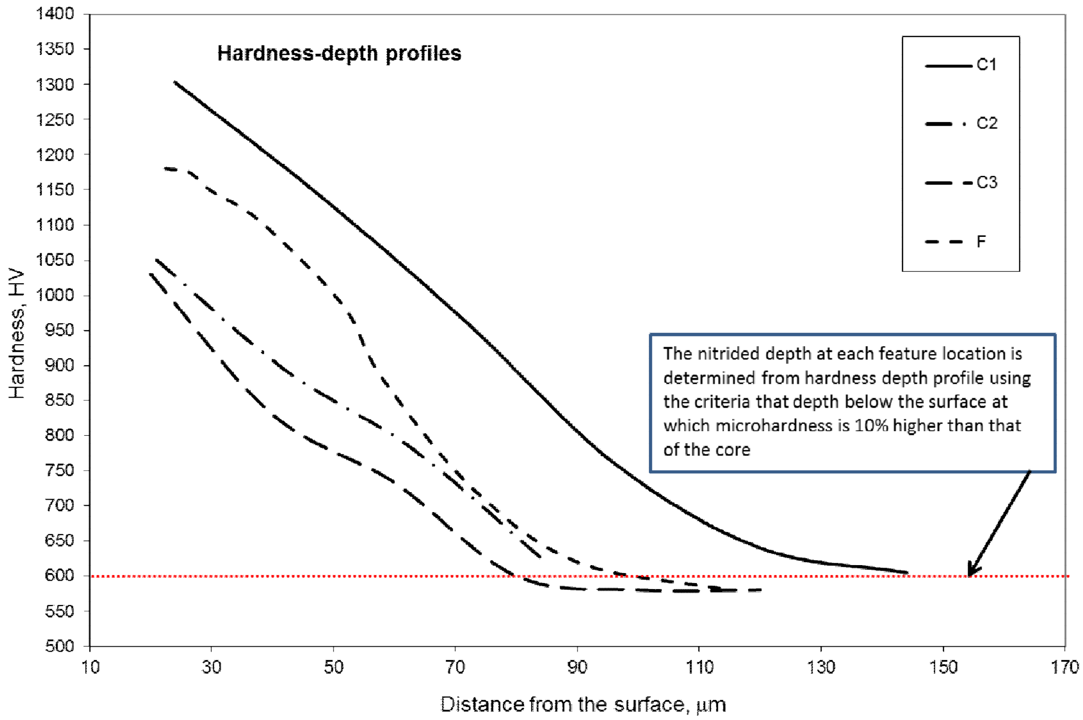

The nitrided depth at each feature location is determined from hardness depth profile using the criteria that depth below the surface at which microhardness is 10% higher than that of the core

Figure 33: Hardness depth profile obtained from an experiment

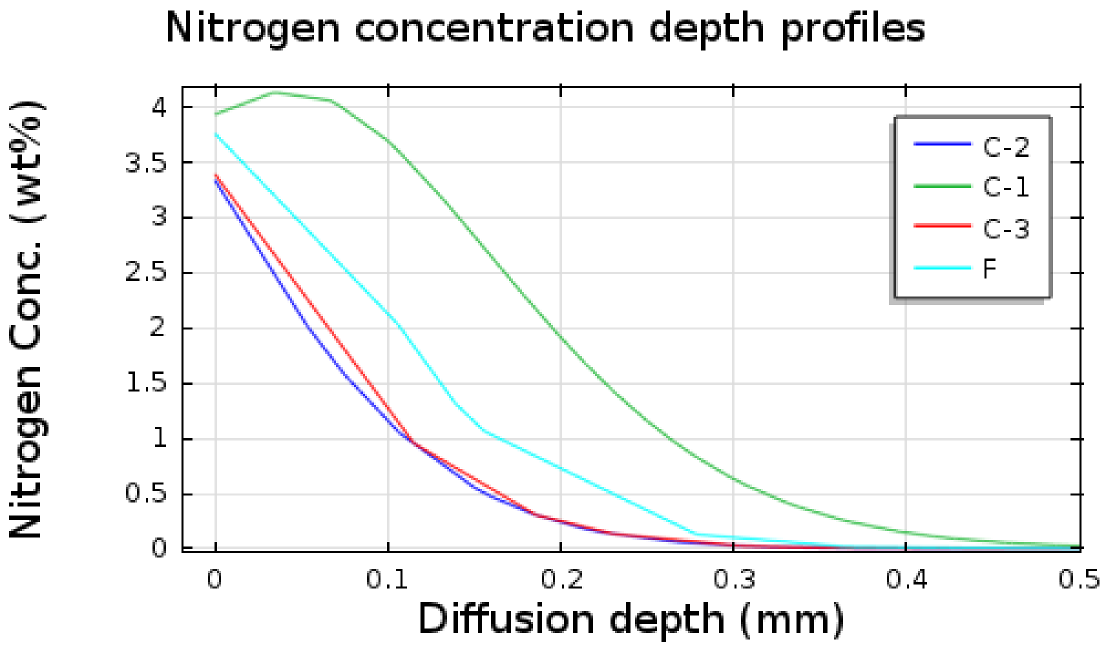

Figure 34: Nitrogen concentration profile at selected points

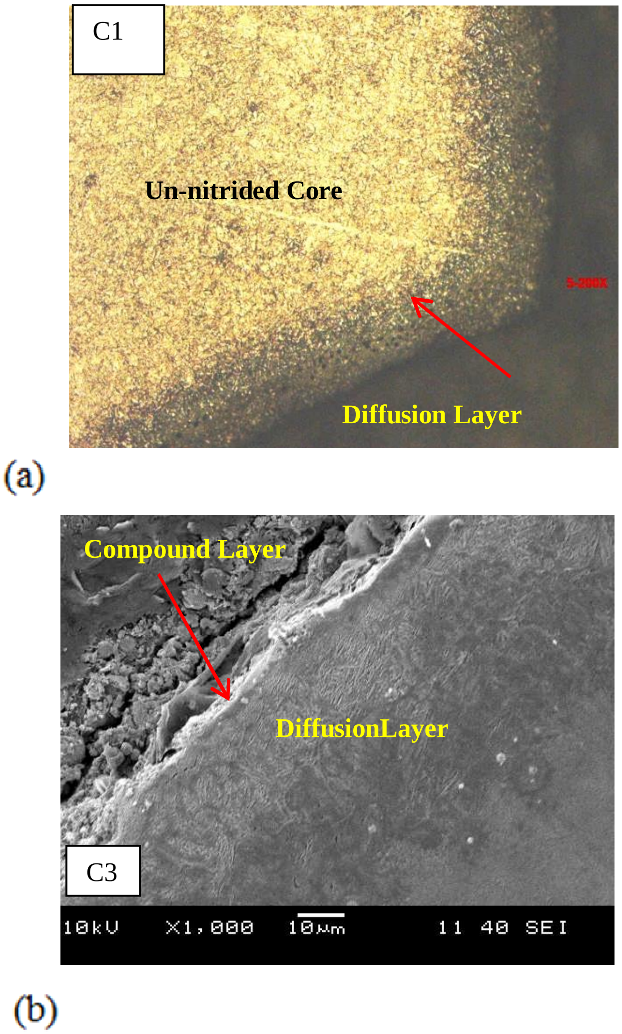

Figure 35: (a) Optical Micrograph at C1, (b) SEM at C3

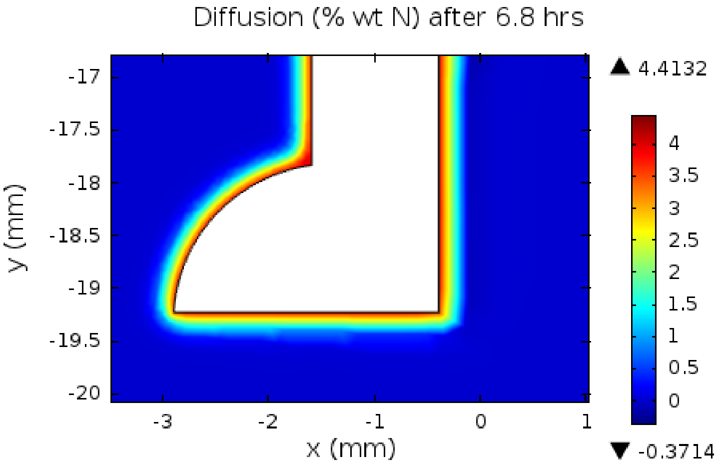

Figure 36: Nitrogen concentration at selected regions

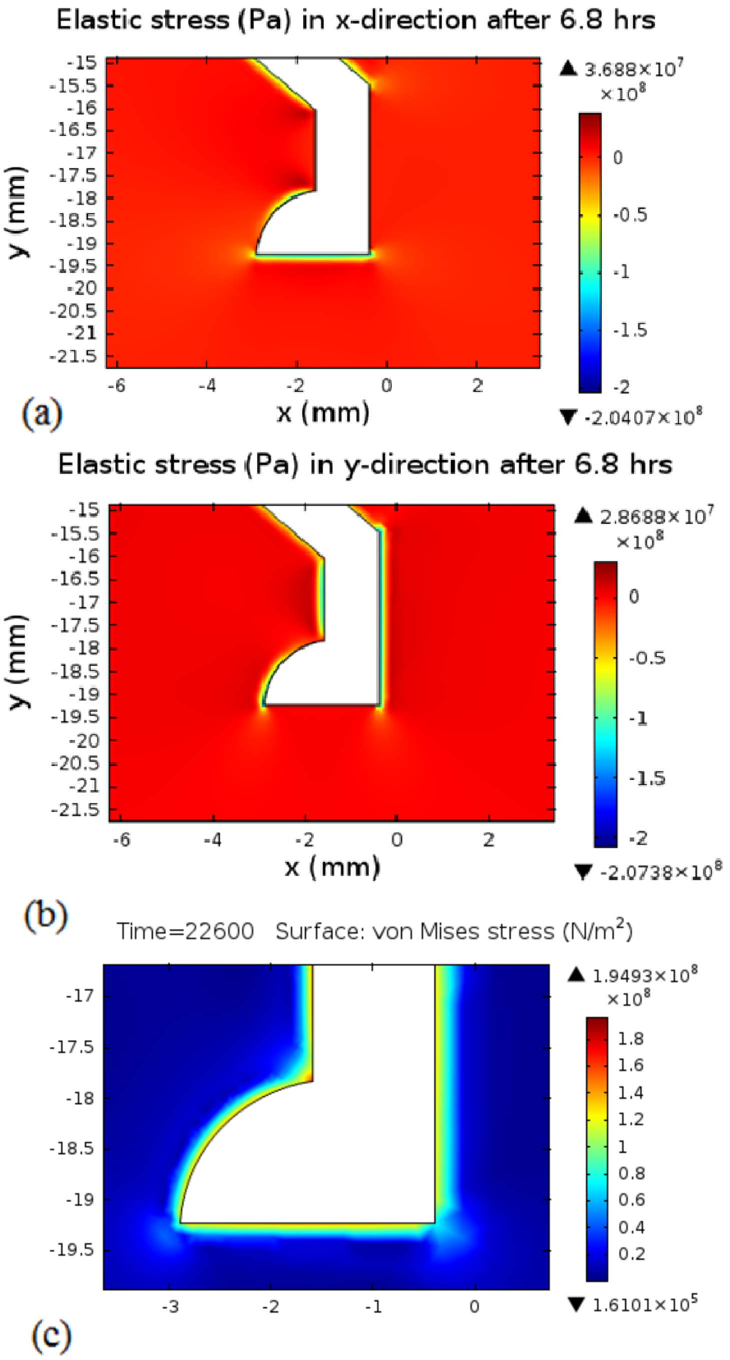

Figure 37: (a) Stress in X-direction, (b) Stress in Y-direction,

(c) Von-Mises Stress at seleced regions

From Fig. 34, it can be seen that the nitrogen concentration at the corner points varies considerably. Point C2 and Point C1 have the smallest and largest case depth respectiely. It can also be observed that the simulation predicts case depth of about 150 μm, which compares well with previous experimental results [**104**]. Moreover, the nitrogen concentration profiles also conform to the measured hardness depth profiles (shown in Fig.33). It is important to observe that, the simulation has predicted the increased nitrogen concentration at the outer corners, as observed experimentally (shown in Fig. 35 and 36). The induced residual stresses at the flat regions of the sample geometry indicate that a compressive stress of about -50 MPa is developed in both X and Y-directions (as shown in Fig. 37 (a) & (b)). This compares well to a previous numerical as well as experimental investigation which mentions that the induced compressive stress at the surface is about -40 MPa [**125**]. Moreover, it is observed that the induced compressive stresses at the steel surface are balanced by a tensile stress of 29-39 MPa from the interior regions. This was also predicted in the previous investigation[**125**]. Due to the fact that the surface stresses at the outer corner points are not balanced, the sum of induced residual stresses at the outer corners is very high, as shown by the von Mises stress plot that is Fig. 37(c).

Therefore, it can be said that the current model has, with some level of accuracy, predicted the nitriding kinetics in the diffusion layer during the two-stage controlled nitriding process. The small discrepancy between the numerical and experimental results is due to the various modeling assumptions used in the present analysis.

Analysis in the compound layer

For the purpose of validation, SEM image of the compound layer at the flat regions and Right-Outer-Corner (RCO) points are presented in Fig. 38 and 40. By comparing the numerically predicted compound layers (shown in Fig.39 and 41) with the experimental results, it can be seen that the model qualitatively predicts the experimental observations. In previous experiments [**104**], it was shown compound layer thickness of about 6-8 μm is developed during the two-stage controlled nitriding process. In the simulation, a compound layer thickness of about 6.5 μm is predicted (shown in Fig. 39). Therefore, it is interesting to see that present results has conforms to the experimental results quantitatively. Furthermore, the thickness of the numerically predicted compound layer at the ROC point is higher than that at the flat sections (as shown in Fig. 41), as in the experimental observations (shown in Fig. 40). This is due to the simultaneous diffusion of nitrogen from the two edges of the corner.

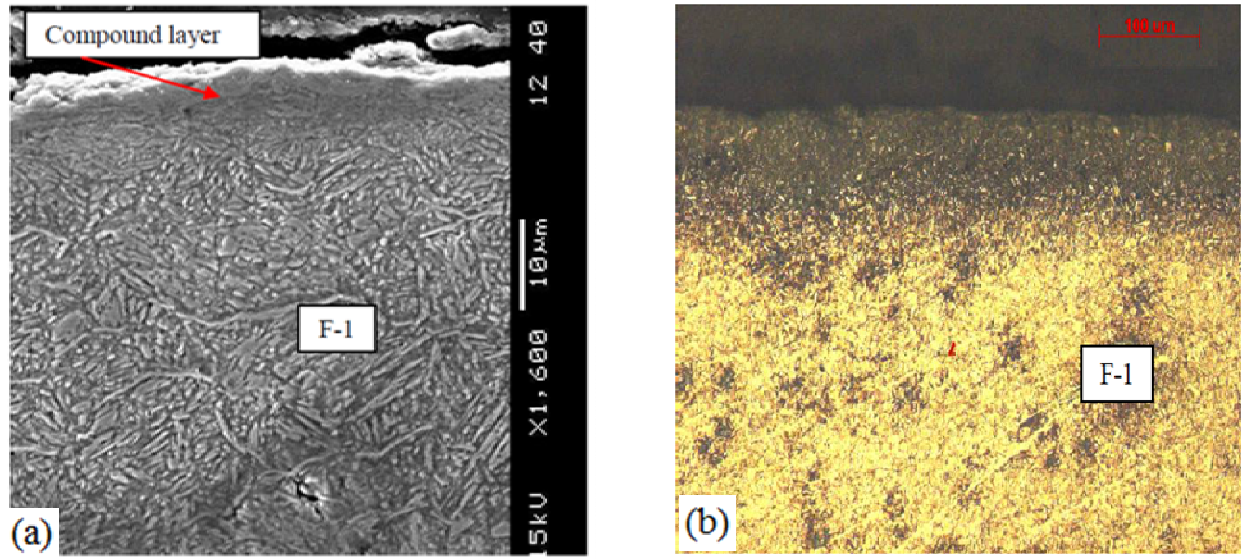

Figure 38: (a) SEM and Optical Micrograph (b) of the compound layer [**136**]

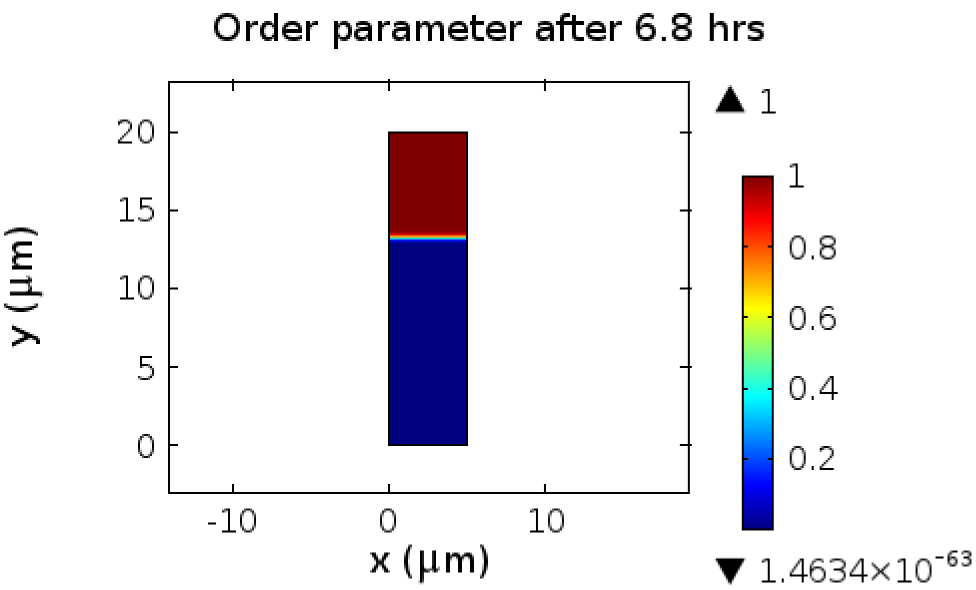

Figure 39: The thickness of compound layer after process

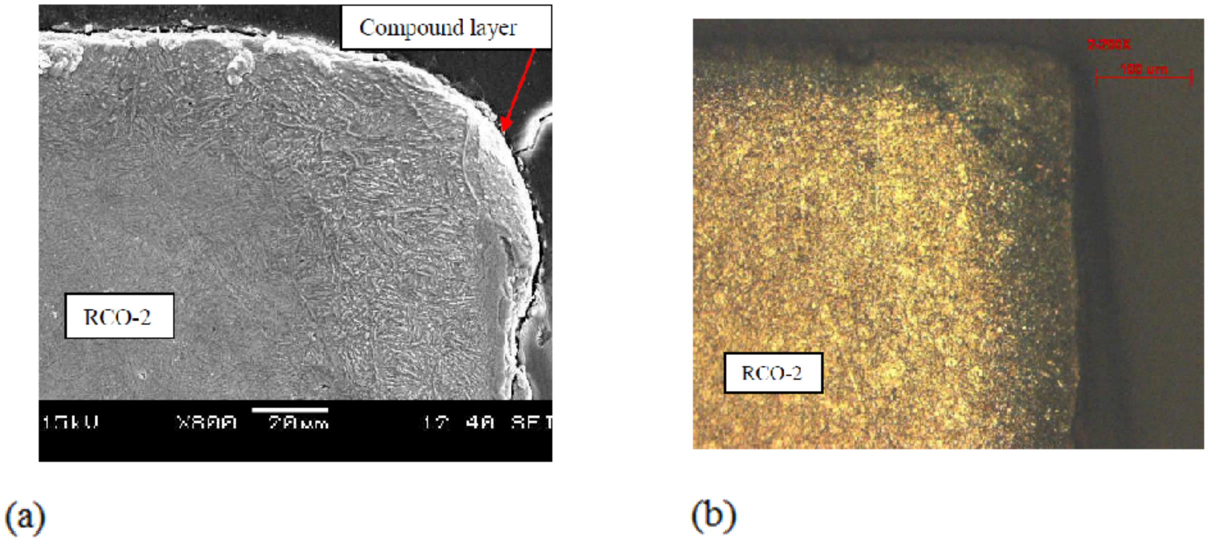

Figure 40: (a) SEM and Micrograph (b) of compound layer at RCO point [136]

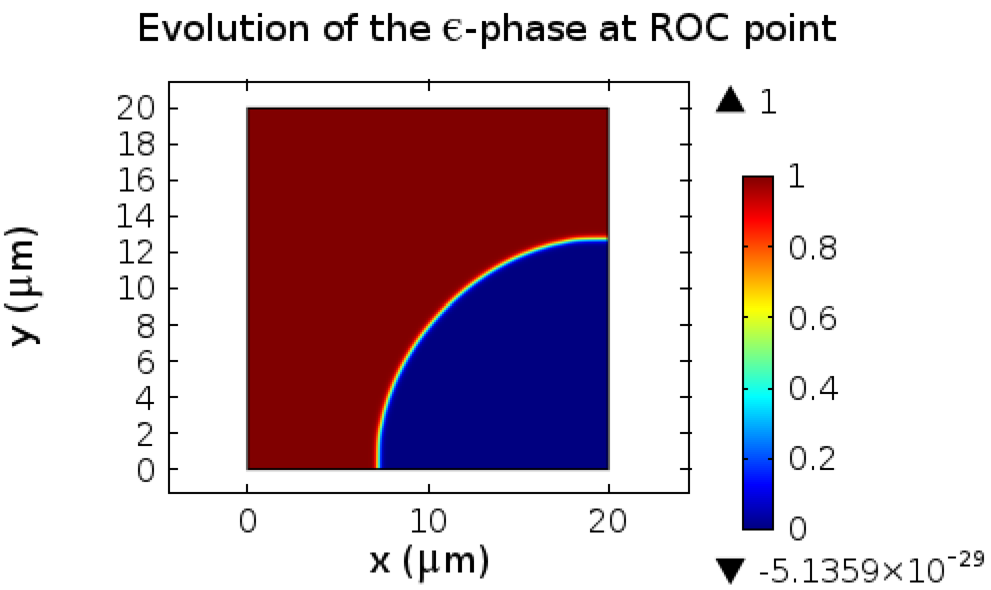

Figure 41: Numerically predicted compound layer at the sharp corners

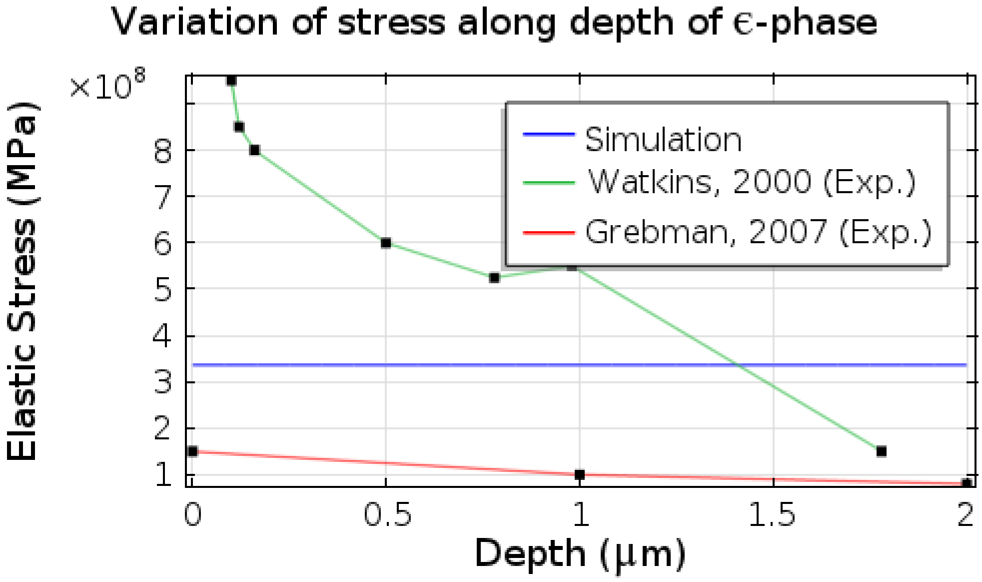

Figure 42: Validation for stress results

Quantitative validation of the developed residual stresses is not possible due to the lack of data from relevant experiments. However, the stress magnitudes are found to be within acceptable ranges of previous experiments by Watkins et al. [**137**] and Grebman et al. [**117**]. The deviation of the current result (shown in Fig.42) from the experiments is due to the neglection of thermal stresses. Only the residual stresses due to the compositionally-induced strains are considered in the current work. However, it is expected that the numerical result will be closer to Grebman et al. [**117**] experiments when the thermal (compressive) stresses are incorporated.

CHAPTER 7

HOT CORROSION: RESULTS AND DISCUSSIONS

The microstructure evolution during the hot corrosion of the top coat was predicted using a Phase Field Model (PFM) that is coupled with elasticity. The transformation occurs due to the diffusion of a molten salt V_2O_5 at 900^0C into the Planar Reaction Zone (PRZ) and Melt Infiltrated Reaction Zone (MIRZ) of the coating. The transformation was prescribed to proceed in a direction that is normal to the surface. Elastic stresses that are induced during the process were also predicted.

7.1 Planar Reaction Zone

7.1.1 Corrosion Kinetics

Fig. 43(a) shows the evolution of the V_2O_5 composition field in the top coat during the hot corrosion process. It can be seen that, the m-phase evolves in any region that contains 8 mol% composition or more of V_2O_5 along the depth of the coating. This is due to the leaching out of the zirconia dopant (Y_2O_3) at 8 mol% V_2O_5 composition according to the V_2O_5-Y_2O_3 phase diagram. On the other hand, the top coat remains unaffected at regions containing diffused V_2O_5 of 1.6 mol% composition or less. The interfacial region (with composition between 1.6 mol% and 8 mol%) contains the weighted-average mixture of the coexisting phases depending on the interfacial location. All interfacial points which are closer to a stable phase contain more amounts of that phase, and vice versa.

From Fig. 43(b), it can be seen that the order parameter (phase indicator with values, 1 in the m-phase and 0 in the t-phase) describes the evolution of the m-phase during the corrosion process. The L-shaped curve, the interface, with order parameter values between 0.05 and 0.95 moves during the transformation. The PDE's were solved for a total duration of 90 minutes (0.005356093 normalized time) and a PRZ thickness of about 12 μm was obtained. This conforms to a previous experimental observation [**89**,**93**] where a PRZ thickness of about 10 μm was observed for the same duration of time. So, qualitatively the current model has predicted the thickness of the PRZ that was obtained from the previous experiment. Quantitative comparison of the phase evolution of the m-phase is not possible due to the lack of proper experimental results for such comparison. Virtually, all previous experimental observations were based on microscopic observations [**89**].

Fig. 44 shows the variation of the transformation depth with time. As expected, the conventional parabolic growth of the diffusing species is obtained due to the use of the Cahn-Hillard diffusion equation. Thus as in conventional diffusion processes, the rate of diffusion of the chemical species (V_2O_5) into the material reduces with time. Similarly, it can be seen that a PRZ thickness of about 12 μm is obtained after 90 minutes of transformation (0.005356093 normalized time).

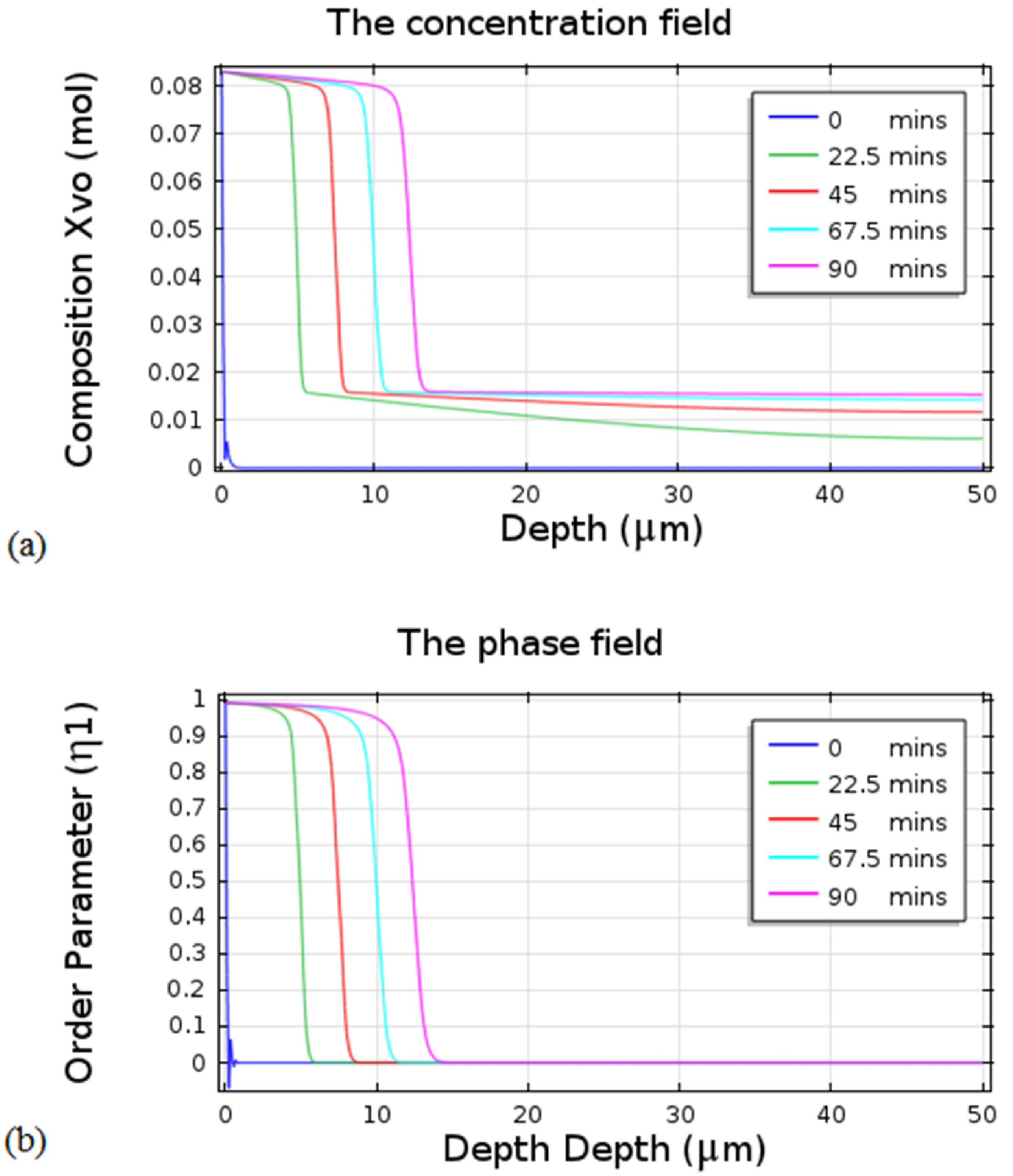

Figure 43: (a) V_2O_5 composition field (b) phase field during corrosion process

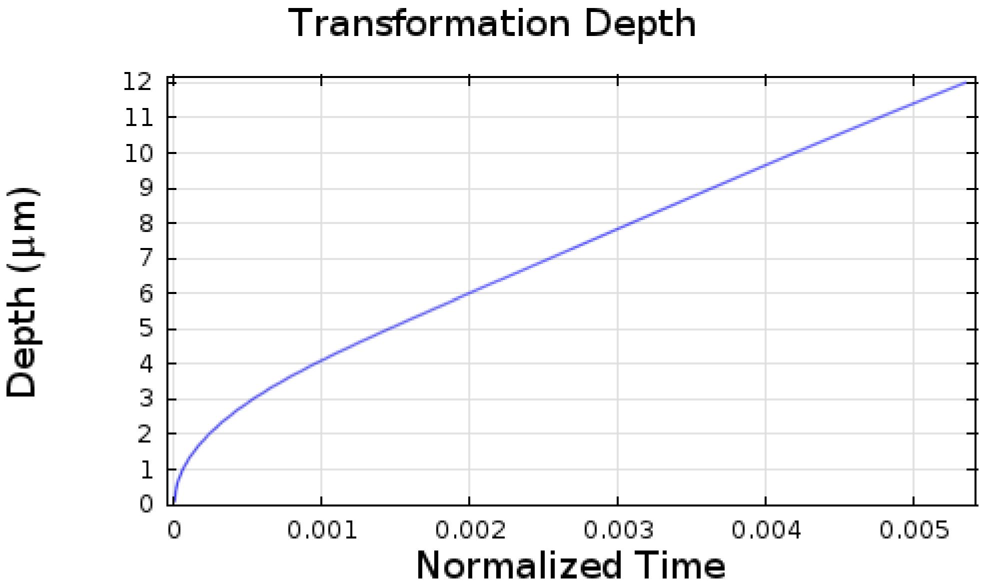

Figure 44: Corrosion kinetics

Fig.45 shows the plots of the composition field in the RVE during the transformation. It can be seen that, the diffusion of V_2O_5 proceeds in a direction that is normal to the surface of the top coat. Fig. 46 similarly shows that, the temporal and spatial evolution of m-phase is due to the continuous diffusion of V_2O_5 into the top coat. The mixed nature of the phases across the interface can clearly be seen. The results obtained for the order parameter and composition field are in conformity with conventional phase field model results.

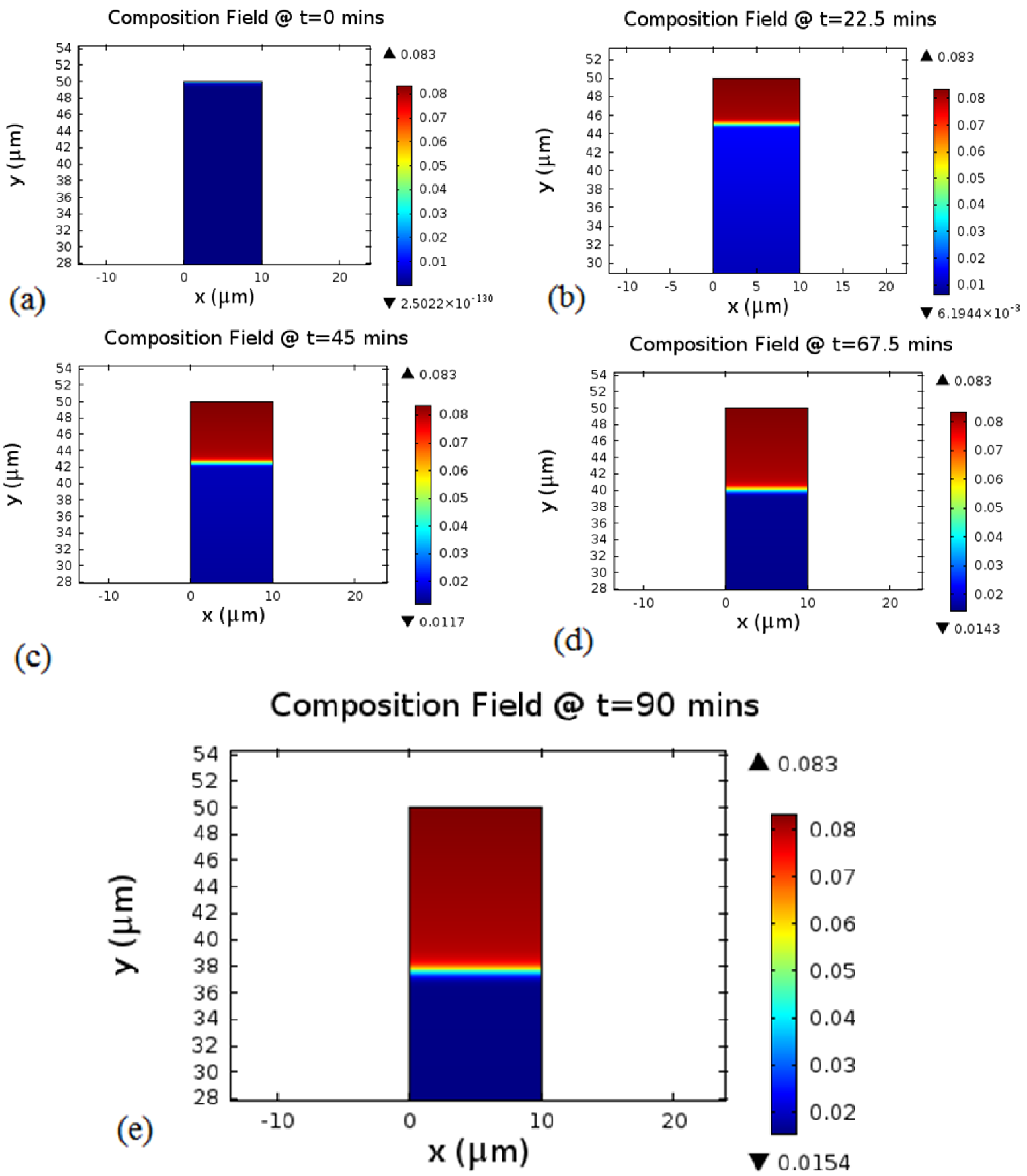

Figure 45: Evolution of the composition field

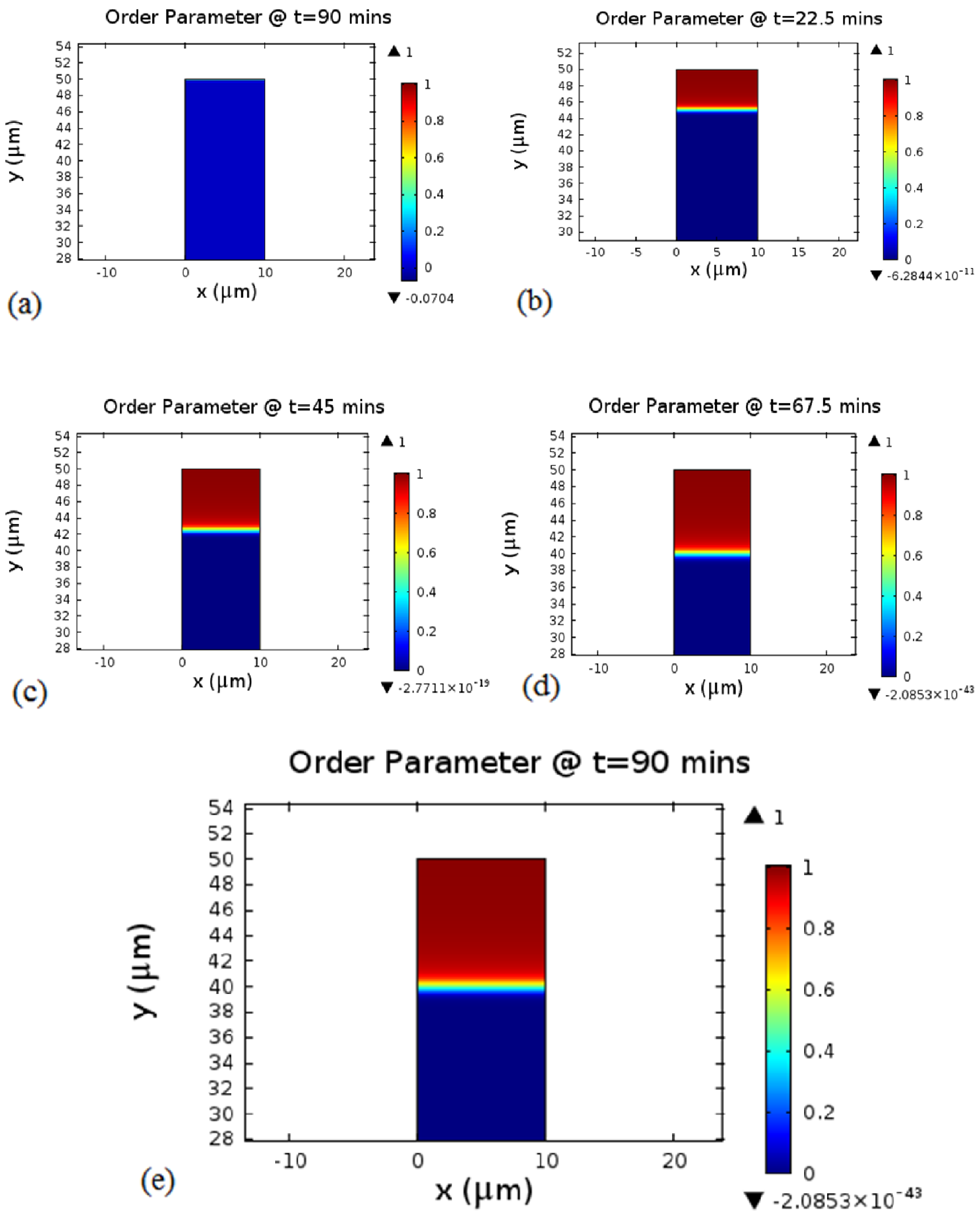

Figure 46: Evolution of the phase field

Therefore, the PFM has successfully predicted the V_2O_5 hot corrosion kinetics of TBC at 900^0C. The model shows that, continuous diffusion of V_2O_5 results in the precipitation of a new phase (the m-phase) due to the destabilization transformation of zirconia. The coupling of Cahn-Hillard and Allen-Cahn equations by the use of a free energy density function (developed by Kim et. al. [**31**]) has enabled the complete description of the corrosion process using chemical free energies that are available in thermodynamic databases.

7.1.2 Stress Analysis

Due to the fact that the surface of the coating is assumed to be load-free, the displacement of the top coat material due to the transformation is mainly in the Y-direction. Fig. 47 shows the displacement (in the Y-direction) of the coating surface during the transformation. The surface of the coating has a final displacement of about 0.1697 μm in the Y-direction due to the volumetric expansion during the transformation. The displacement of the top coat in the X-direction is very negligible as compared to that in the Y-direction. This is due to the constraint imposed by the periodic boundary condition applied at the boundaries, BC and DA.

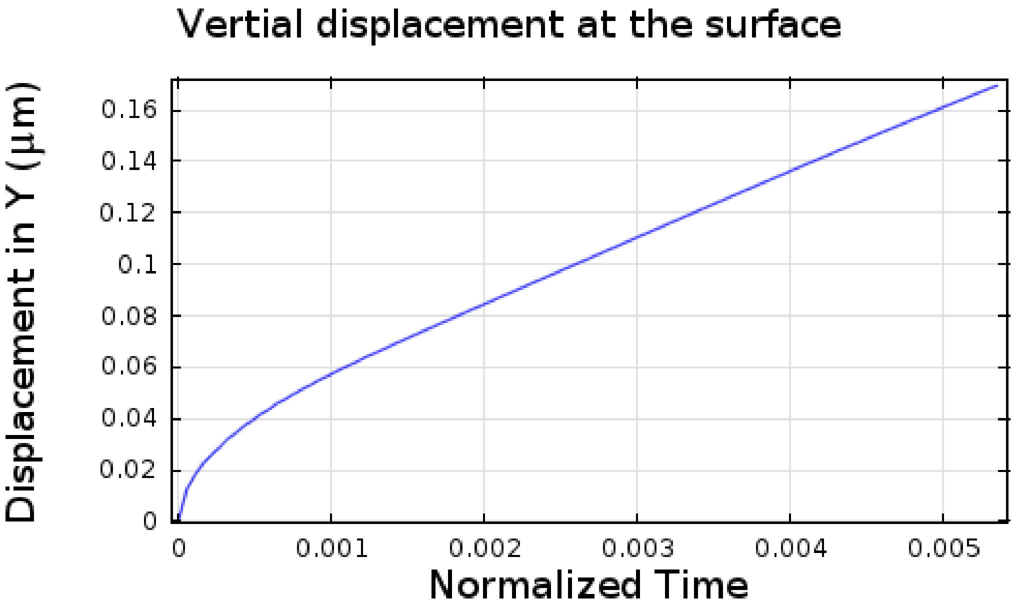

Figure 47: Vertical surface displacement during the process

Fig. 48 shows the plots of the displacements fields in the X and Y-directions after the transformation. From Fig. 48(a), it is observed that the displacement of the top coat in the X-direction is very small due to the periodicity of the RVE in that direction. It is equally important to observe that the boundaries, BC and DA, have interacting displacement fields due to the periodic boundary conditions applied. Similarly, Fig.48 (b) shows that the displacement of the top coat is mainly in the Y-direction. Because the surface of the top coat is free of external loads, the highest value of the vertical displacement is found at the surface. It can also be observed that, the t-phase is subjected to a slight compression due to the volumetric expansion of the m-phase.

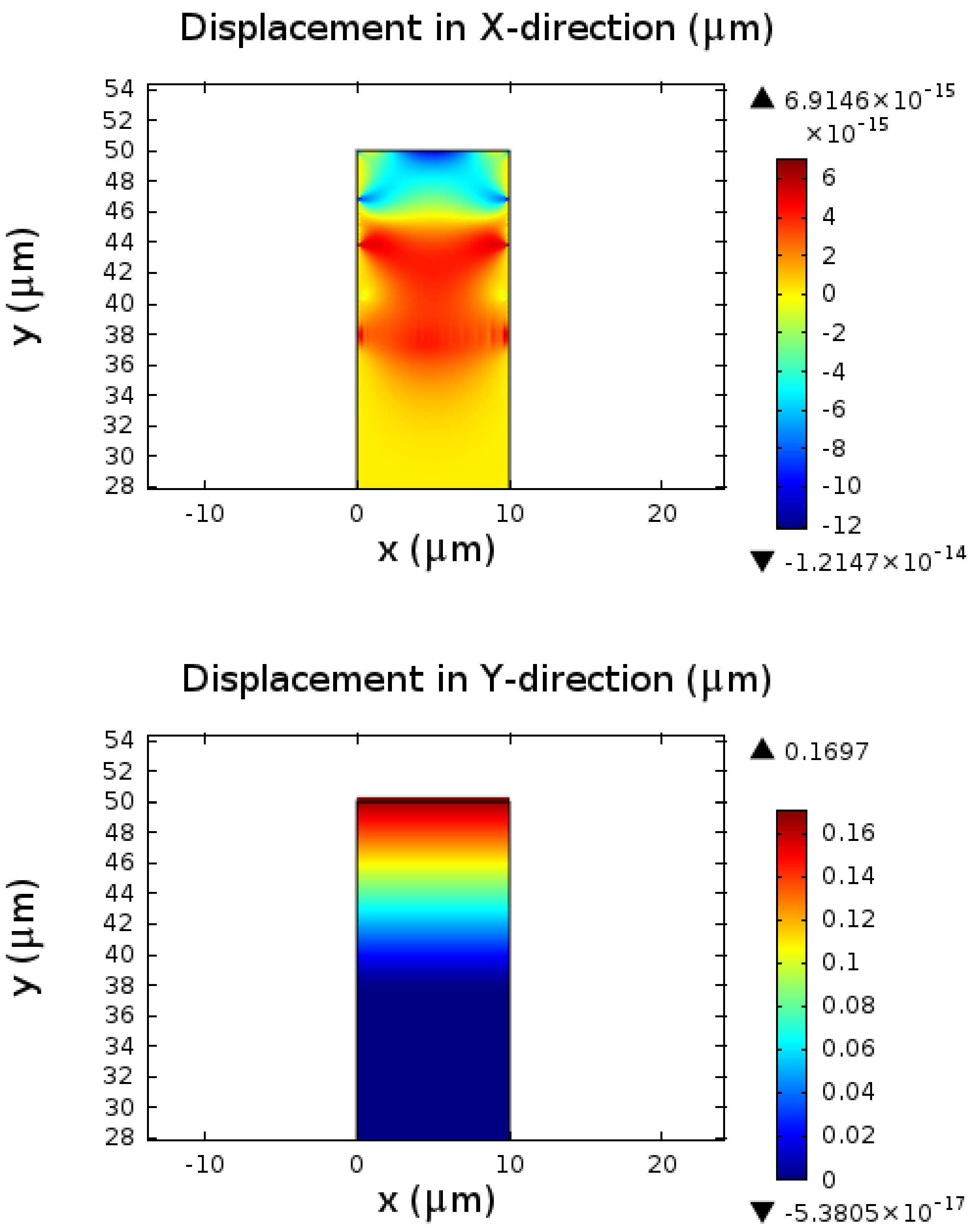

Figure 48: Displacement fields in (a) X-direction (b) Y-direction in the top coat

Fig. 49(a) shows the induced elastic strains in the X-direction after the transformation. It is observed from the result that, elastic (compressive) strain of about -4.9 x 10^{-3} and elastic (tensile) strain of about 2.1612 x 10^{-16} are induced in the m-phase and t-phase respectively. As explained previously, the elastic strain in the X-direction is compressive due to the periodic constraint that is imposed in the X-direction. On the other hand, Fig. 49(b) shows the induced elastic strains in the Y-direction. Contrary to the elastic strain in the X-direction, elastic (tensile) strain of about 1.96 x 10^{-3} and elastic (compressive) strain of about -4.9802 x 10^{-5} are induced in the m-phase and t-phase respectively. The elastic strain signs are reversed (when compared with elastic strains in the X-direction) due to the fact that the surface of the top coat is load-free. It is important to also observe that the induced elastic strain in the m-phase is lower in Y-direction even though the displacement field in the Y-direction has higher magnitudes. This can be explained by the fact that, such higher displacement is mainly due to the transformation strain which is stress-free.

Due to the plane strain model assumption that was adopted, no strain is induced in the Z-direction. This is because the displacement in that direction is negligible as compared to the thickness of the coating. Similarly, the shear strains along the coating thickness are approximately zero. It is important to also observe that, there is no shear strain in the XY-plane because the shear components of the transformation strain are considered to be zero (as shown in Fig.50). Fig. 51 shows the plots of the induced principal strains after the transformation. It can be seen that, the first and second principal strains in the m-phase are 1.96 x 10^{-3} and -4.9 x 10^{-3} respectively. The principal strain values are very close to the strains in the X and Y-directions, and this implies that the principal strains lie in the XY-plane.

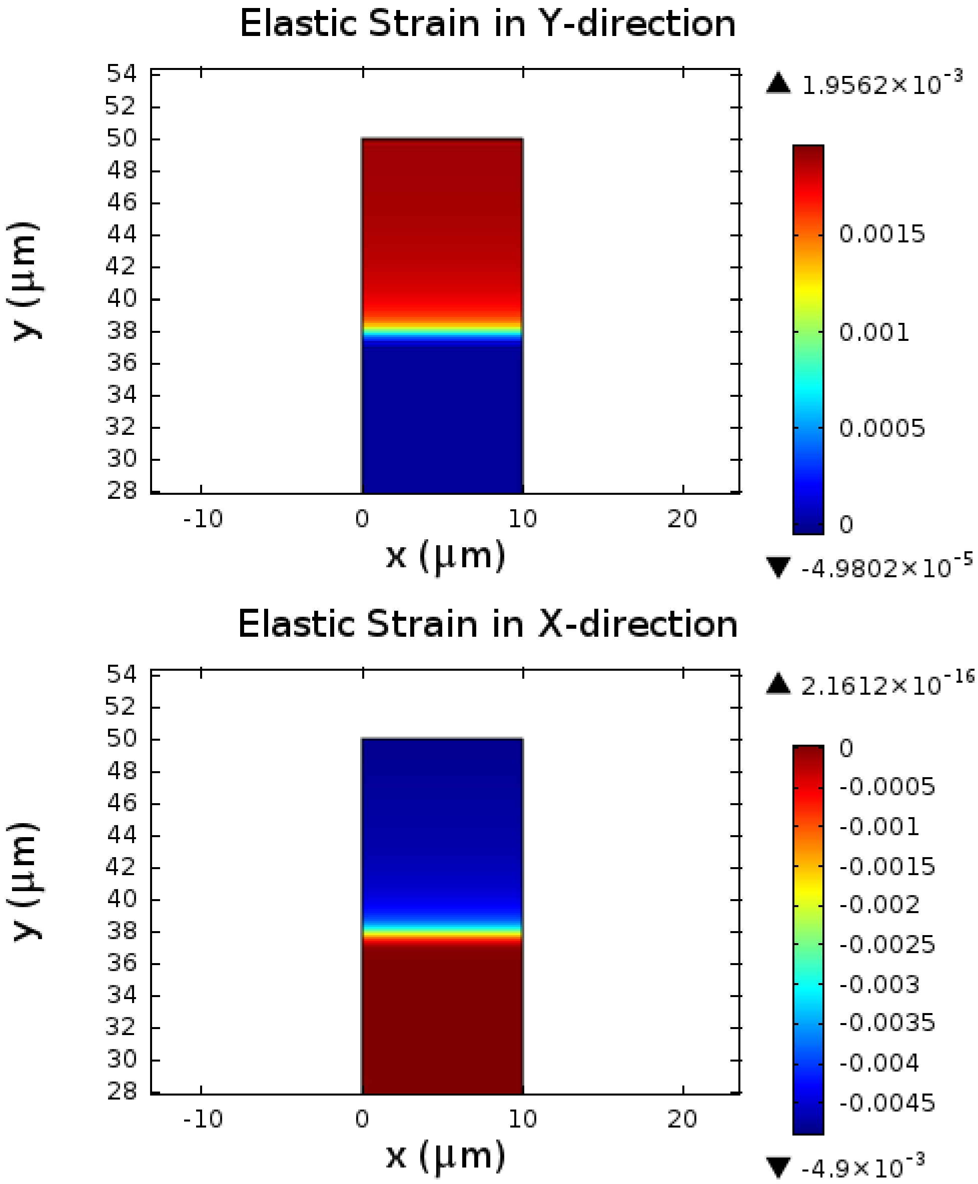

Figure 49: Induced elastic strains in (a) X-direction (b) Y-direction in top coat

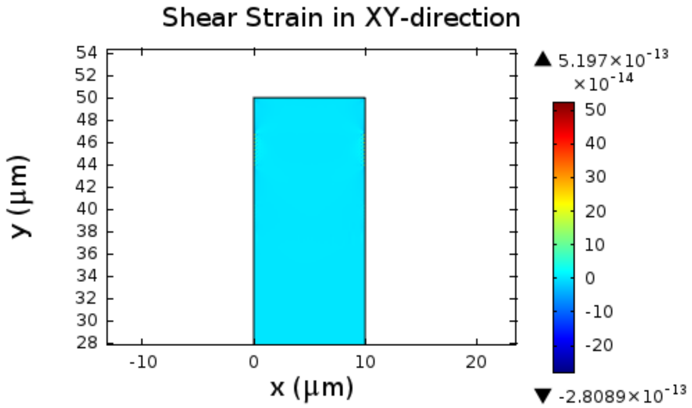

Figure 50: Induced shear strain in the top coat

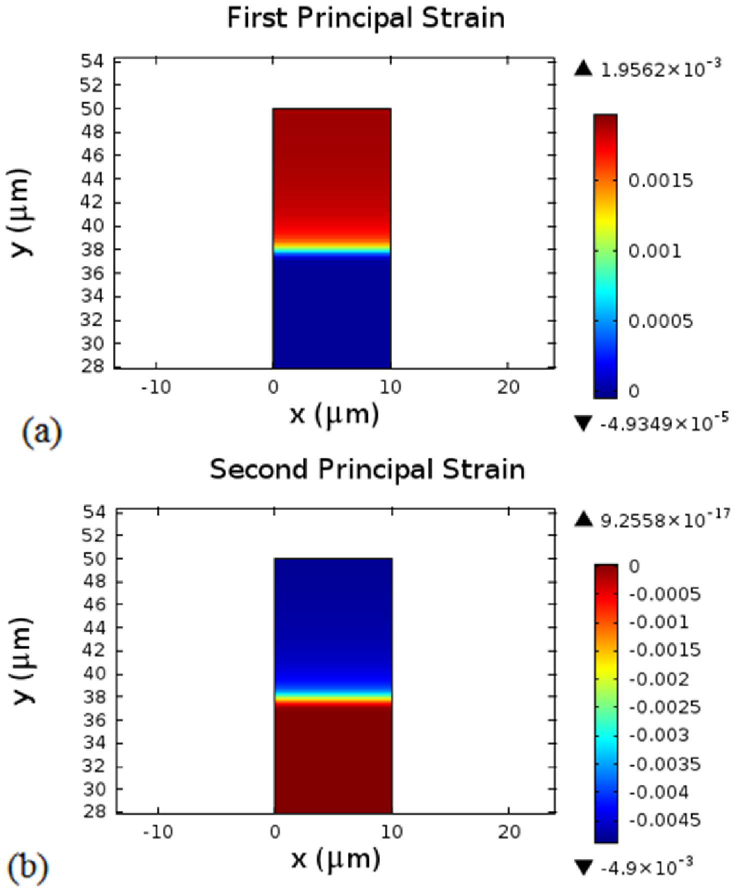

Figure 51: (a) First, and (b) Second principal strains

Fig.52 shows that the total strains induced in the top coat. It is important to remember that, the total strain is the summation of the elastic and transformation strains. It can be seen that, the total strain in the Y-direction is higher (in the m-phase) even though the smallest stress is in that direction. This is because a larger percentage of such strain is stress-free. On the other hand, the total strain in the X-direction is very small due to the annihilation of the transformation (tensile) strain by elastic (compressive) strain.

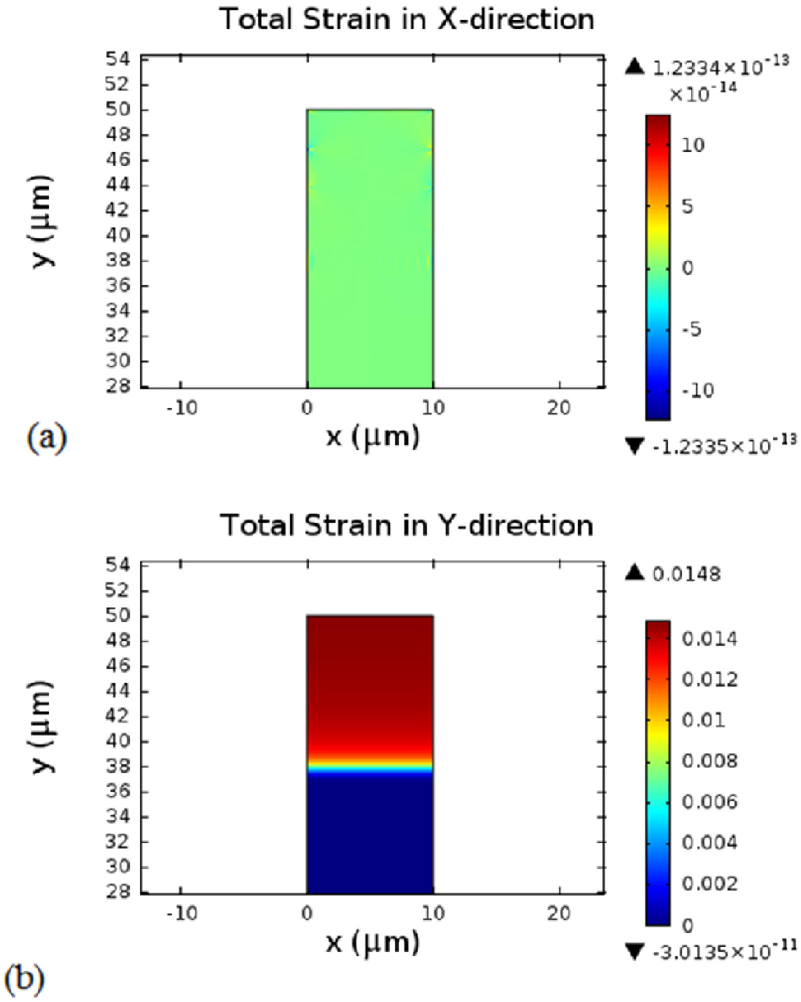

Figure 52: Total strains in (a) X-direction (b) Y-direction in the top coat

Fig. 53 shows the stress fields that are developed in the top coat after the transformation. From the elastic stress field in the X-direction (shown in Fig.53 (a)), it can be observed that a compressive stress of about 1.31 GPa and a tensile stress of about 101MPa are induced in the m-phase and t-phase respectively. As explained previously, the high compressive stress in the X-direction is due to the applied periodic constraint in that direction. Coincidentally, it was reported [**138**] that the fracture of ceramic materials proceeds along grain boundaries where the material is very weak (shown in Fig.56). Thus, the cracks in the top coat are initiated through the sliding of the grain boundaries when the material is compressed. Therefore, the large compressive stress in the X-direction explains the emergence of the experimentally-observed horizontal cracks that lead to the spallation or delamination of the coating. In fact, the hot corrosion process affects the as-sprayed coating more due to the existence of splat grains as shown in Fig.55.

The elastic stress field in the Y-direction (shown in Fig.53 (b)) is very small, because the surface of the coating is considered to be load-free. This is a valid assumption considering the fact that the operating pressure of land-based gas turbines is very small (not more than 50 MPa [**139**]). Therefore, the compression due to the gas pressure is very small as compared to the volumetric expansion that is associated with the transformation. Even if the pressure is very high, it will accelerate the failure of the top coat by inducing additional compressive stresses. From Fig.53(c), the elastic stress field in the Z-direction shows that compressive stress of about 384 MPa and tensile stress of about 0.013 MPa are induced in the m-phase and t-phase respectively. This will also assist in the failure of the coating by grain boundary sliding as mentioned previously.

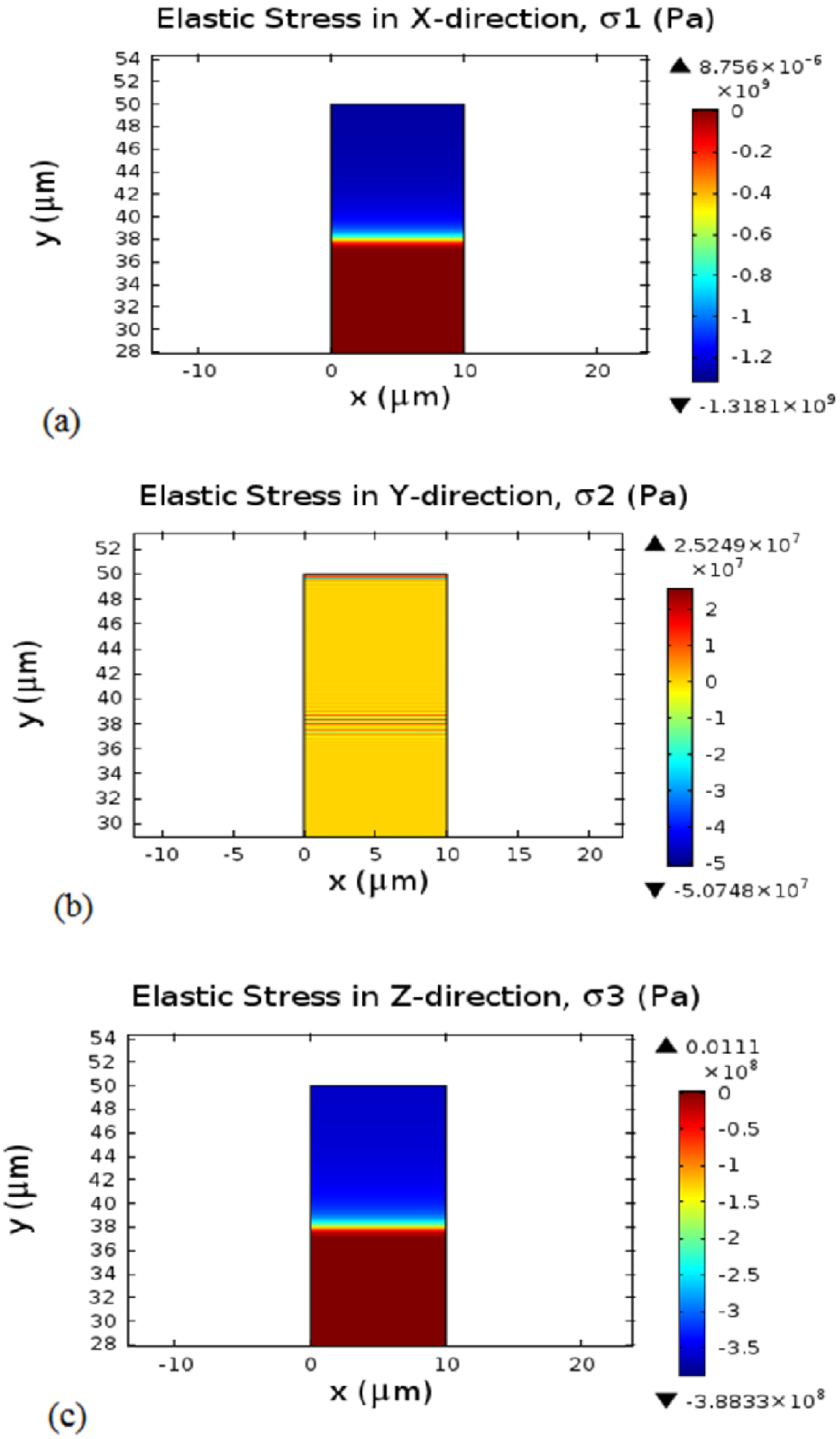

Figure 53: Induced elastic stress in (a)X-direction (b)Y-direction (c)Z-direction

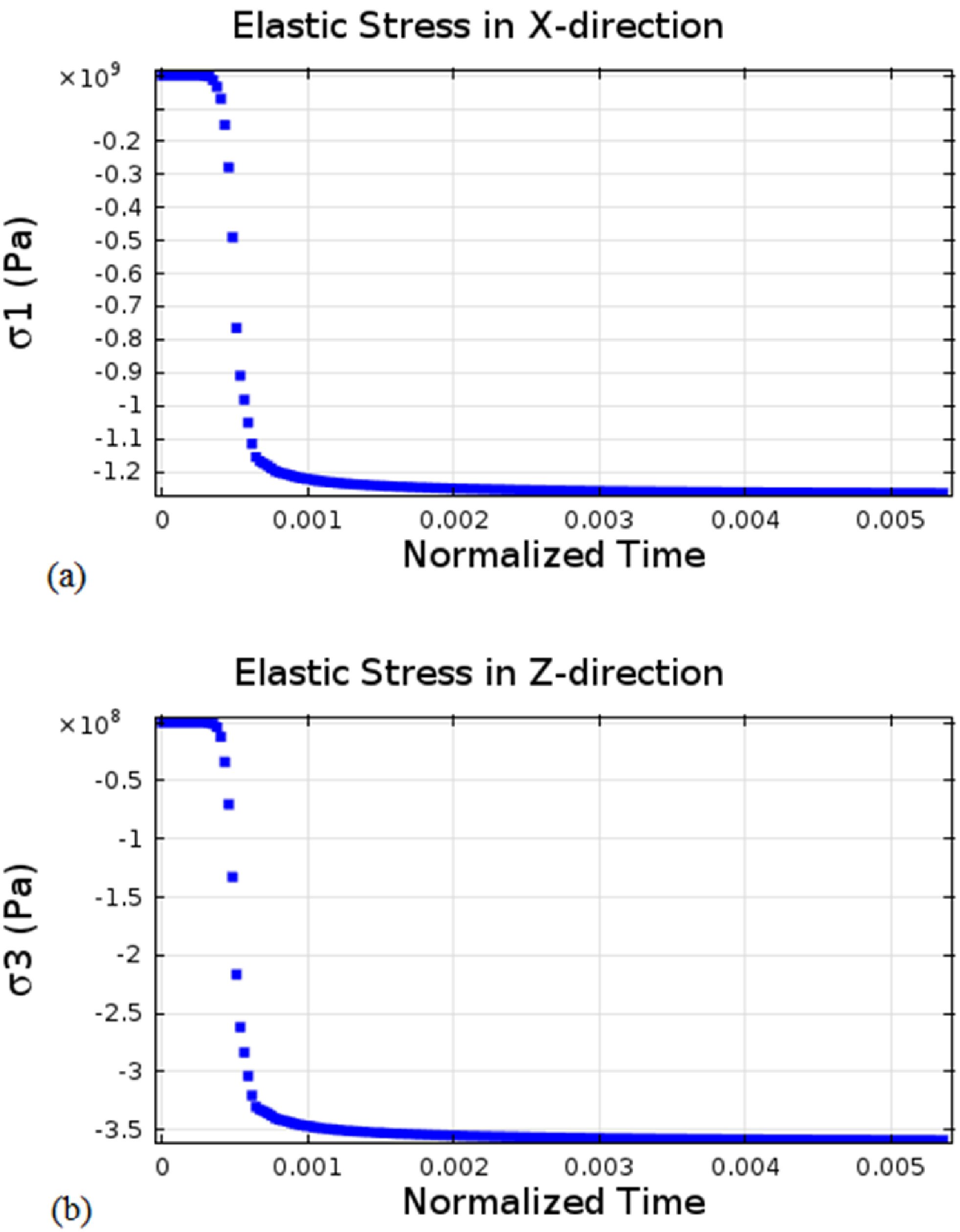

Figure 54: Variation of elastic stresses with time (a) in X-direction, (b) in Y-direction

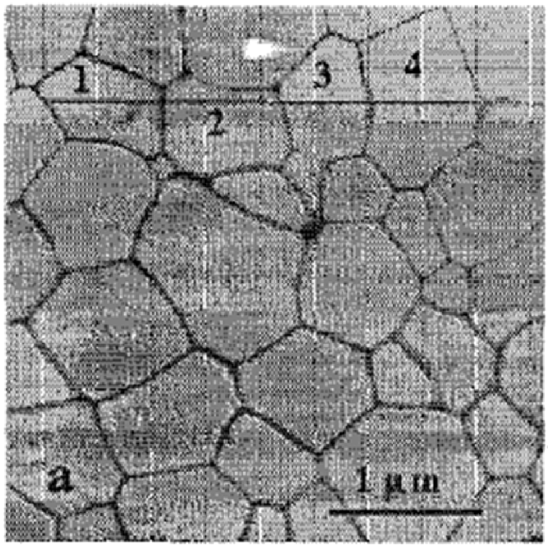

Figure 55: Splat structures in APS TBC

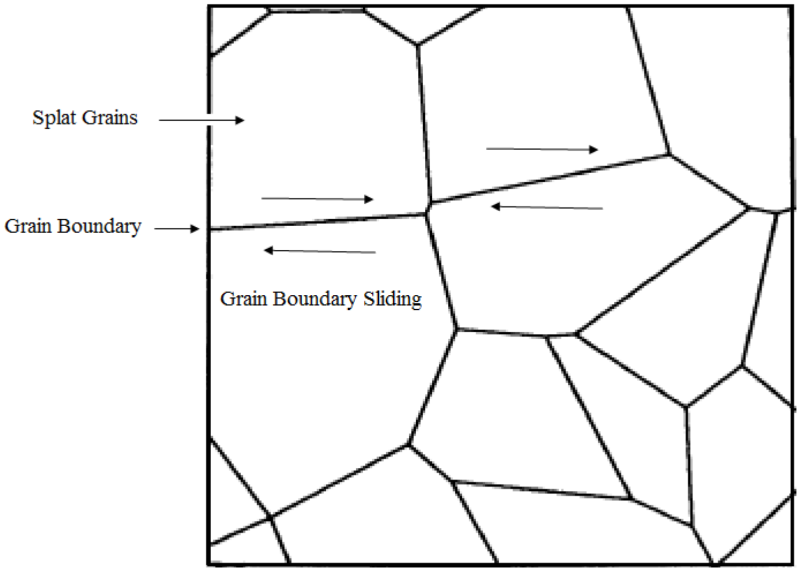

Figure 56: Demonstrating cracking of the top coat by grain boundary sliding

Fig.54 shows the variation of the stress field in X and Z-directions at the point (5μm, 45μm) during the transformation. It can be seen that, stresses start to develop after the transformation has reached the point. Thus, the coupling of the phase transformation with the elastic interaction is successfully achieved. The induced stresses in the YSZ layer (or untransformed region) are much smaller as compared to the stresses in the transformed region as shown previously. This can be explained by the fact that, the volumetric expansion of the top coat does not impose much stress in the untransformed region due to the load-free nature of the top coat surface.

As mentioned previously, the shear transformation strains are considered to be zero. Therefore, there is no induced shear stress in the top coat after the transformation (as shown in Fig. 57). The plots of the principal stresses are shown in Fig.58. The first principal stress is about -541 MPa and 0.2 MPa in the m-phase and t-phase respectively. The second principal stress is about -878.58 MPa and 0.03 MPa in the m-phase and t-phase respectively. While the third principal stress is about 1.51 GPa and 0 GPa in the m-phase and t-phase respectively. Using the numerical value of the principal stresses, the von Mises stress is computed at each point and time step during the transformation. Fig.59 shows a plot of von Mises stress after the transformation, where stress of about 1GPa is developed in the transformed region (the m-phase).

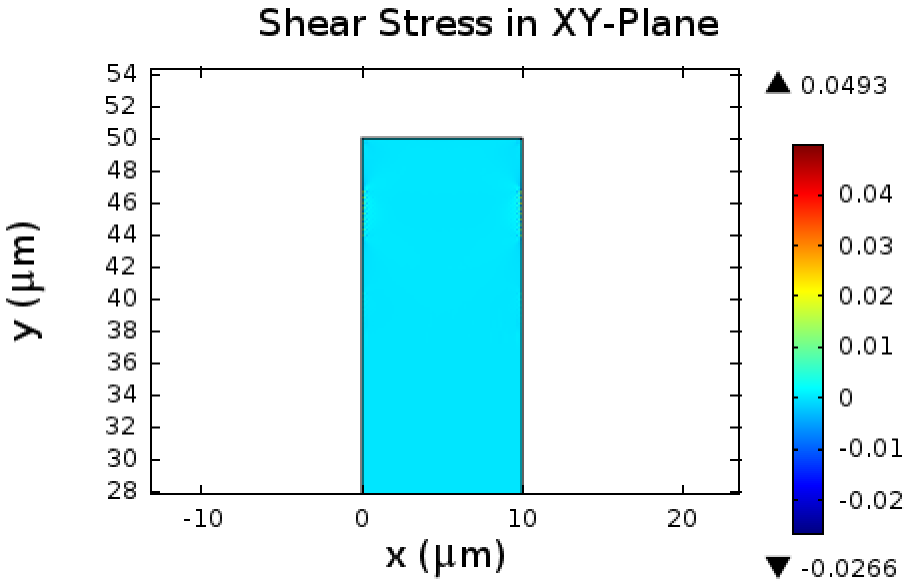

Figure 57: Induced shear stress

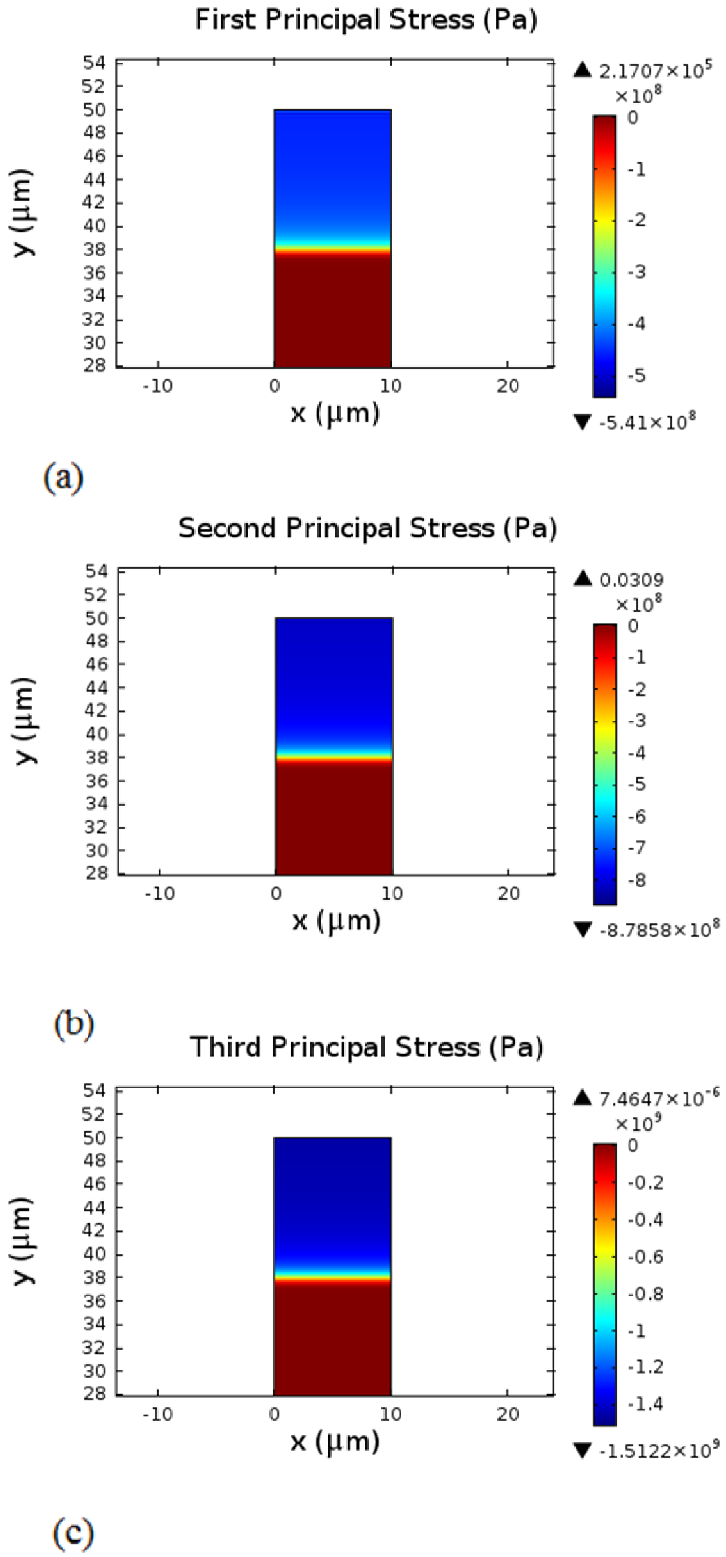

Figure 58: Principal stresses

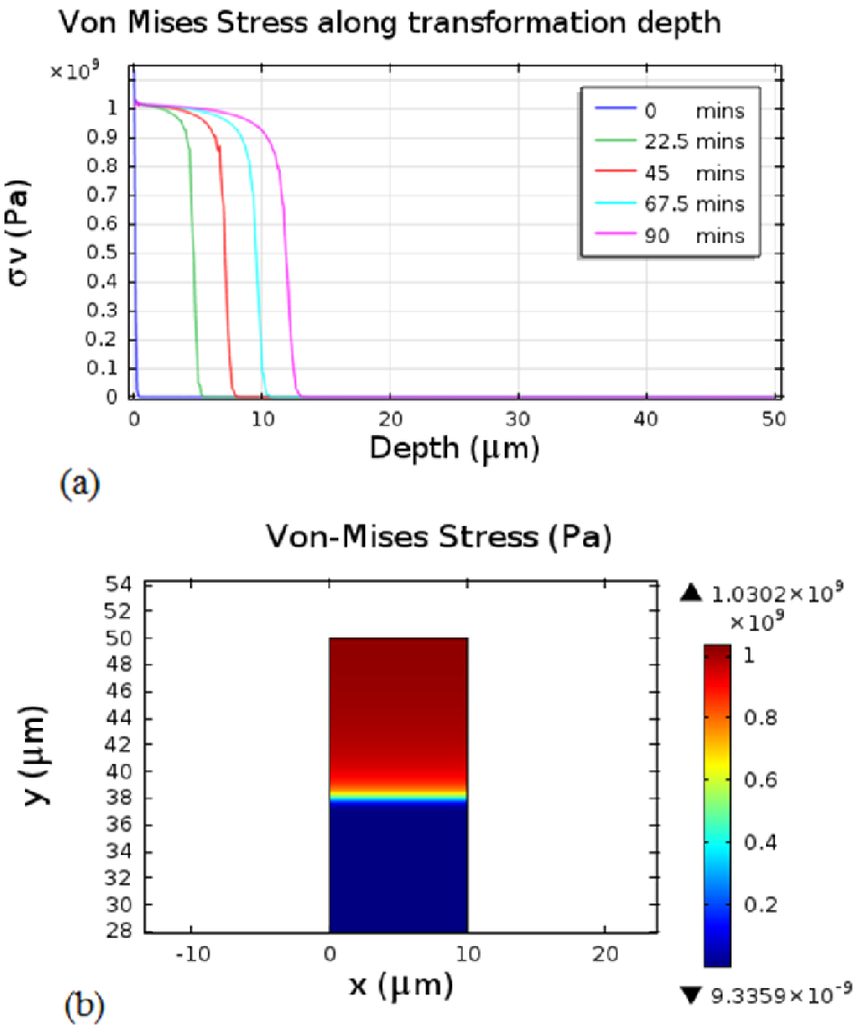

Figure 59: von Mises stress

Thus, the phase field method has been successfully used in determining the effect of Type I hot corrosion on the mechanical behavior of the top coat. Based on the results presented, the degradation process results in severe transformation-mismatch stresses that lead to the propagation of horizontal cracks in the top coat. Consequently, total spallation or delamination failure of the coating occurs. To the best of our knowledge, there is no experiment that can confirm the stress field results in the current work. However, the results are in close agreement with that of a previous study [**52**] on the stresses that are developed during the diffusionless tetragonal-to-monoclinic transformation of zirconia.

7.2 Melt Infiltrated Reaction Zone (MIRZ)

7.2.1 Corrosion Kinetics

Fig. 60(a) shows the evolution of the V_2O_5 composition field in the MIRZ of the top coat during the hot corrosion process at the line x=0.01μm. As in the PRZ, it can be seen that the m-phase evolves in any region that contains 8 mol% composition or more of V_2O_5. While, the t-phase remains unaffected at regions containing diffused V_2O_5 of 1.6 mol% composition or less due to the inability of the V_2O_5 to leach out the zirconia dopant. Similarly, Fig. 60(b) shows the evolution of the order parameter (phase indicator with values, 1 in the m-phase and 0 in the t-phase) along the line x=0.01 μm during the transformation in the MIRZ. It is equally important to observe that, the thickness of interface in the MIRZ (about 0.01 μm) is smaller than the one in the PRZ (about 1 μm). This is valid as the interface thickness is freely selected in the phase field literature depending on the length scale of the simulation. The PDE's were solved for a total duration of 30 milliseconds (2.975607×10^{-4} normalized time) and a maximum MIRZ thickness of about 0.03 μm was obtained. The short time for the completion of transformation in the MIRZ conforms to previous experimental findings [7], where it was found out that the reaction kinetics in the MIRZ stops in less than 30 minutes. However, the reaction kinetics in the PRZ was shown to continue up to 120 minutes [**93**].

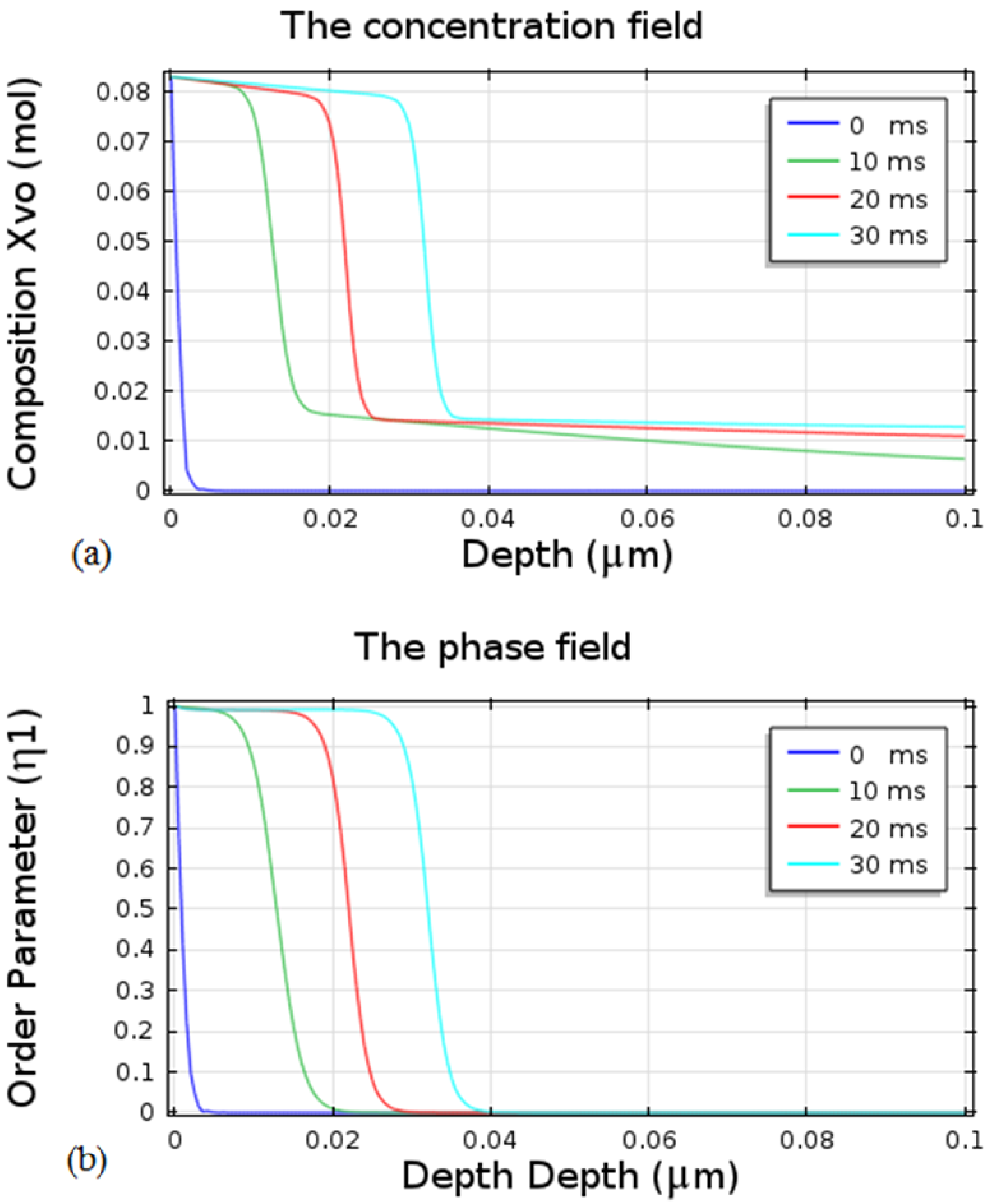

Figure 60: Transformation in the MIRZ, (a) Composition field, (b) Phase field

Similarly, Fig. 61 and 62 show the evolution of the composition and phase field in 2D respectively. An important observation is that, the evolution of both the concentration and phase field is no longer uniform (or unidirectional) even thought the transformation is prescribed to be unidirectional. This can be explained by the fact that, the curved nature of the selected RVE has caused the deformation of the transformed region to vary considerably at various points. Thus, the elastic strain energy which offers resistance to the transformation driving force varies with location. For this reason, the region that experience the largest deformation (i.e. or highest elastic strain energy) has the smallest transformation thickness. This is why the fillet-corner between the curved and the flat sections of the RVE have the smallest transformation depth.

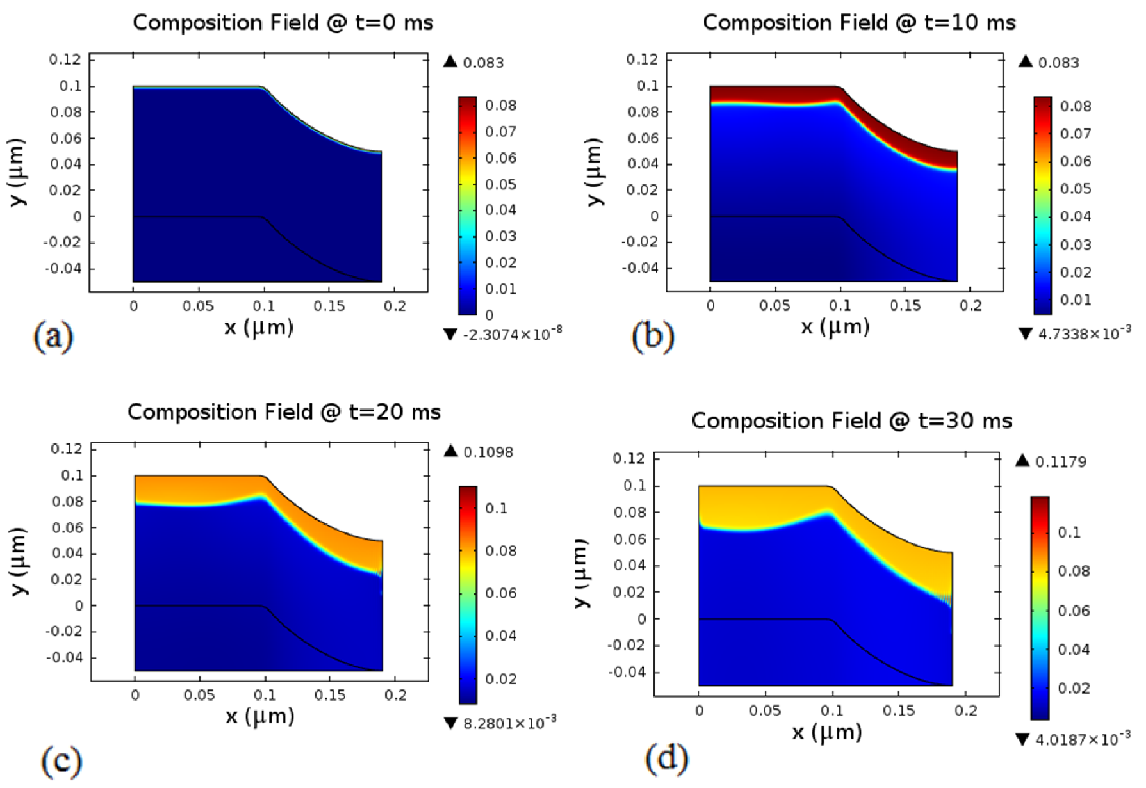

Figure 61: Evolution of composition field

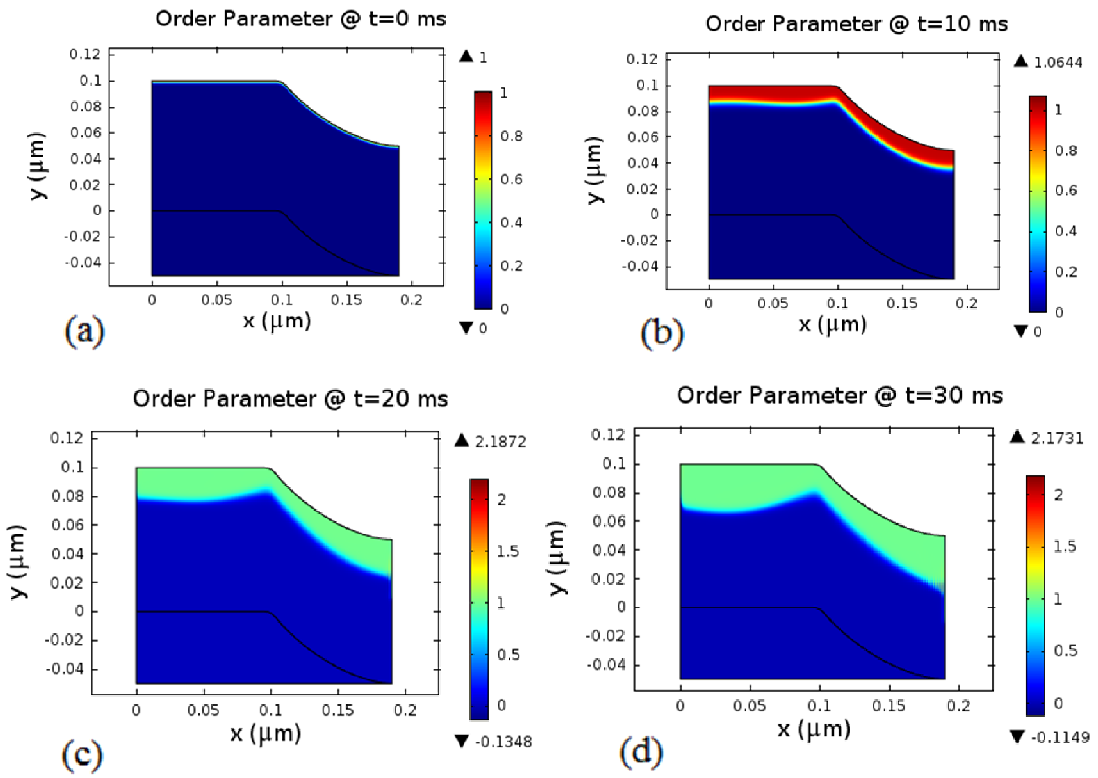
Order Parameter @ t=0 ms

Order Parameter @ t=10 ms

Order Parameter @ t=20 ms

Order Parameter @ t=30 ms

Figure 62: Evolution of the phase field

Hence, PFM is successfully used to predict the V_2O_5 hot corrosion kinetics of TBC in the MIRZ at 900^0C. The model shows that, continuous diffusion of the melt results in the precipitation of a new phase (the m-phase) in the micropores/microcracks of TBC due to the destabilization transformation of zirconia.

7.2.2 Stress Analysis

Fig 63 shows the displacement fields in the X and Y-directions after the transformation stops. It can be seen that, the flat section of the micropore has a contraction in both the X and Y-directions. The curved section of the micropore has expansions in both the X and Y-directions. It is observed that, the fillet-corner has the largest volumetric expansion because the micropore is considered to be load-free (as shown in Fig. 63). Therefore, the transformation at the fillet region is having the smallest transformation depth due to the high elastic strain energy at such region. As in the PRZ, the largest displacement (0.03 μm) is found in the Y-direction and at the fillet corner. It is equally important to observe that the periodicity of the RVE is reflected in the result for displacement in X-direction.

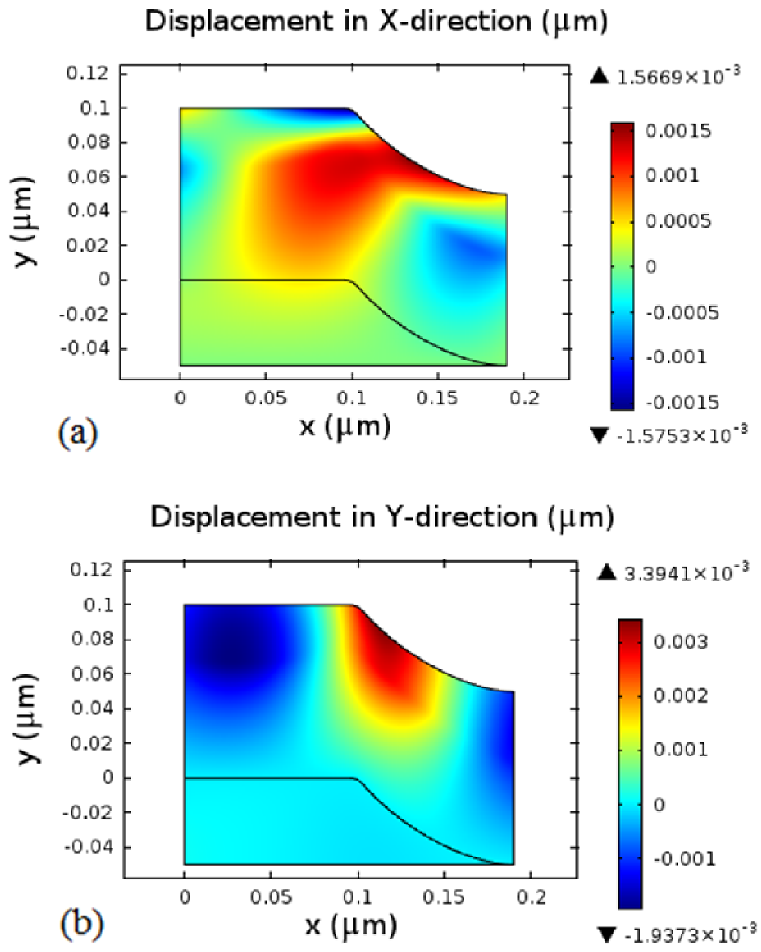

Figure 63: Displacement fields in (a) X-direction, (b) Y-direction

Fig.64 shows the developed elastic and shear strains after the transformation. From Fig.64 (a), it can be seen that a tensile elastic strain of about 0.0612 and compressive elastic strain -0.0344 develop at the flat section and the curved sections of the micropore respectively. Also, a contraction occurs in the X-direction at some regions below the curved section of the micropore due to the periodicity of the RVE in the X-direction.

Similarly, Fig.64 (b) shows that a maximum tensile elastic strain of about 0.06 occurs at some regions and the average tensile elastic strain at the interior surface of the micropore is about 0.02. As in the PRZ, the elastic strain in the Y-direction is almost purely tensile due to the load-free nature of the micropore.

However, due to the curved nature of the RVE a shear strain is developed in the XY-plane. A maximum shear strain of about 0.04 is developed after the transformation (as shown in Fig. 64(c)). Fig.65 shows the plots of the first and second principal strains, where a complex principal strain field is observed. Similarly, Fig. 66 shows the total strain that is developed in the Y-direction is higher than that in the Y-direction due to periodicity of the RVE in the X-direction.

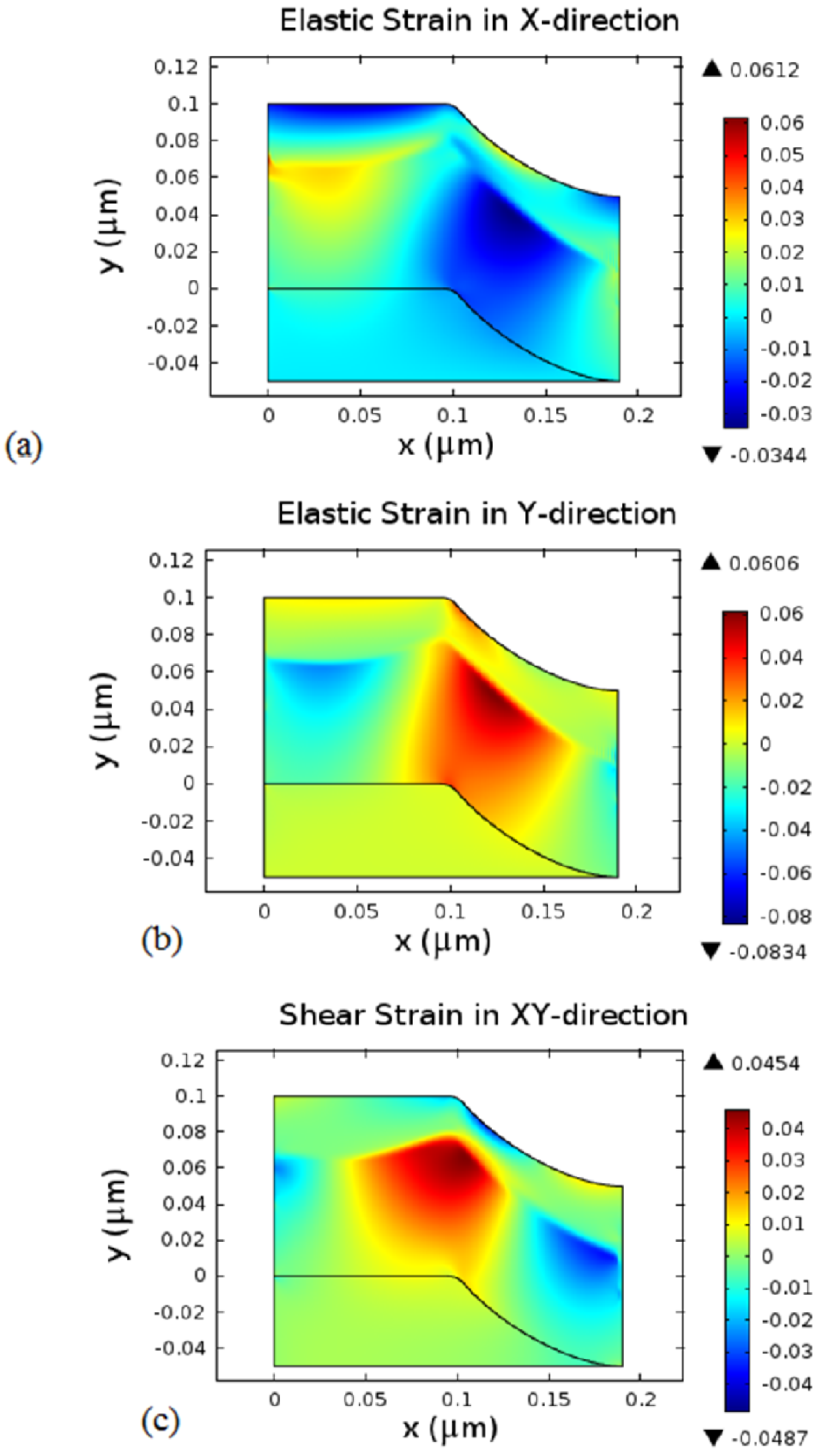

Figure 64: Induced elastic and shear strains

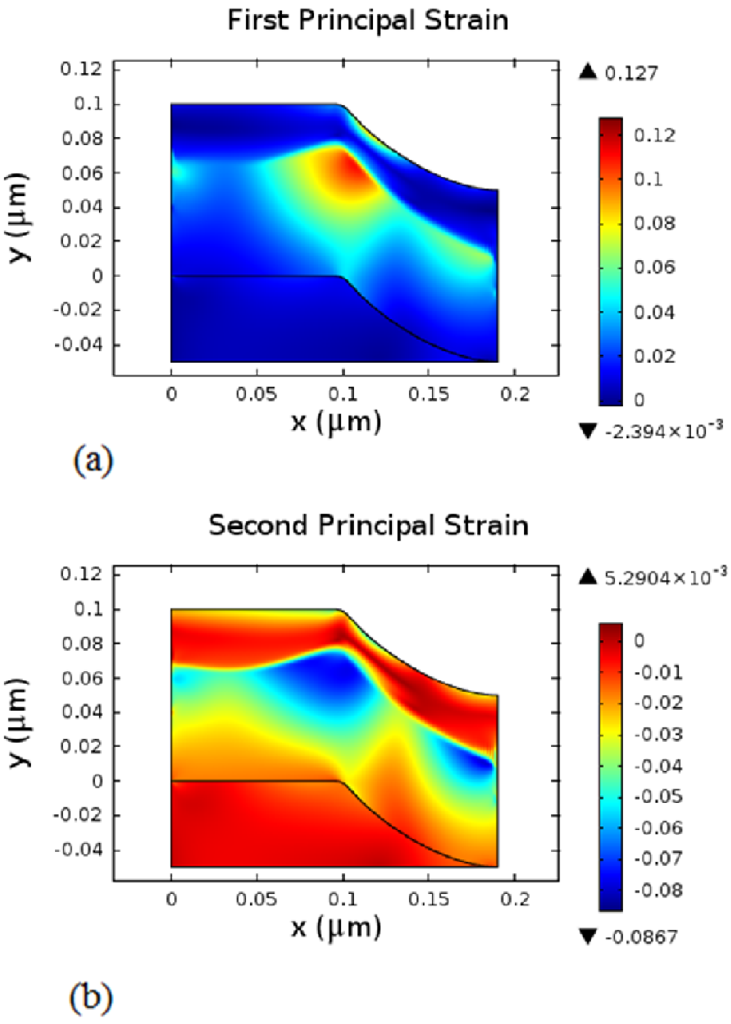

Figure 65: Principal strains

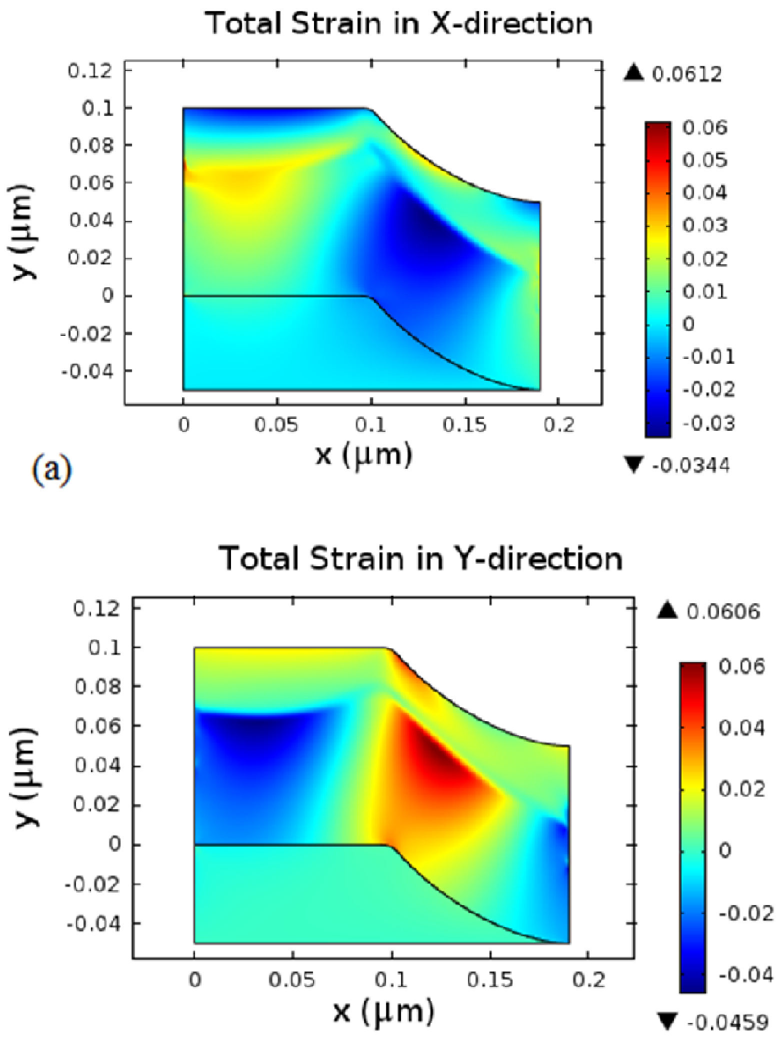

Figure 66: Total strains

Fig. 67 shows the induced elastic stresses after the transformation in the MIRZ. Similar to the elastic strain field, the elastic stress field is very complex due to the curved nature of the RVE. Fig. 67(a) shows that a tensile elastic stress of about 5 GPa is developed at the curved section of the micropore in the X-direction. However, a compressive stress of about -5 GPa is developed at the flat section. Similarly, elastic stresses of 8 GPa (tensile) and 0 GPa (compressive) develop at the flat and curved sections of the micropore in the Y-direction respectively (shown in Fig. 67(b)). The flat section has almost a zero stress in the Y-direction because the micropore is free of external loads .Similarly, the elastic stress in the Z-direction (shown in Fig. 67(c)) is observed to be similar to the one in the X-direction. However, the stress magnitudes in the Z-direction are smaller (i.e. 4 GPa at curved section and -2 GPa at the flat sections). Unlike the PRZ, shear stress is developed in the MIRZ in the XY-pane. It can be seen that maximum and minimum shear stresses of -2 GPa and -1GPa are developed in the XY-plane respectively (shown in Fig.68). The contour plots of the principal stresses and the von Mises stress are also given in Fig. 69 and 70 respectively.

Therefore, the phase field method is found to be effective in predicting the effect of the hot corrosion process on the mechanical behavior of the top coat in the MIRZ. Additionally, the results show that the top coat geometry has effect on the corrosion kinetics as well as the transformation-induced stresses. Based on the results presented, the the hot corrosion process is found to result in complex stress field that may lead to the weakening of coating in the MIRZ. Being nearer to the TGO/bond coat, the stresses in the MIRZ can be considered to be a contributing factor to the rumpling of the top coat. Furthermore, the stresses are expected to be higher at the micropores surface due to cracks closure during the transformation. Infact, it was reported [**89**] that the corrosion process in the MIRZ stops within a short period of time due to closure of the cracks. It is important to mention that, micropore or microcrack of concave curvature was found to result in higher stresses, and that is why it is selected for the analysis. To the best of our knowledge, there is no available experimental result that can confirm the results in the MIRZ. However, it is interesting to find out that the model can be used in predicting corrosion kinetics and the transformation-induced stresses at very small mesoscale, such as the one in MIRZ. Therefore, the phase field method is a very powerful tool that can be used even in the design of new materials.

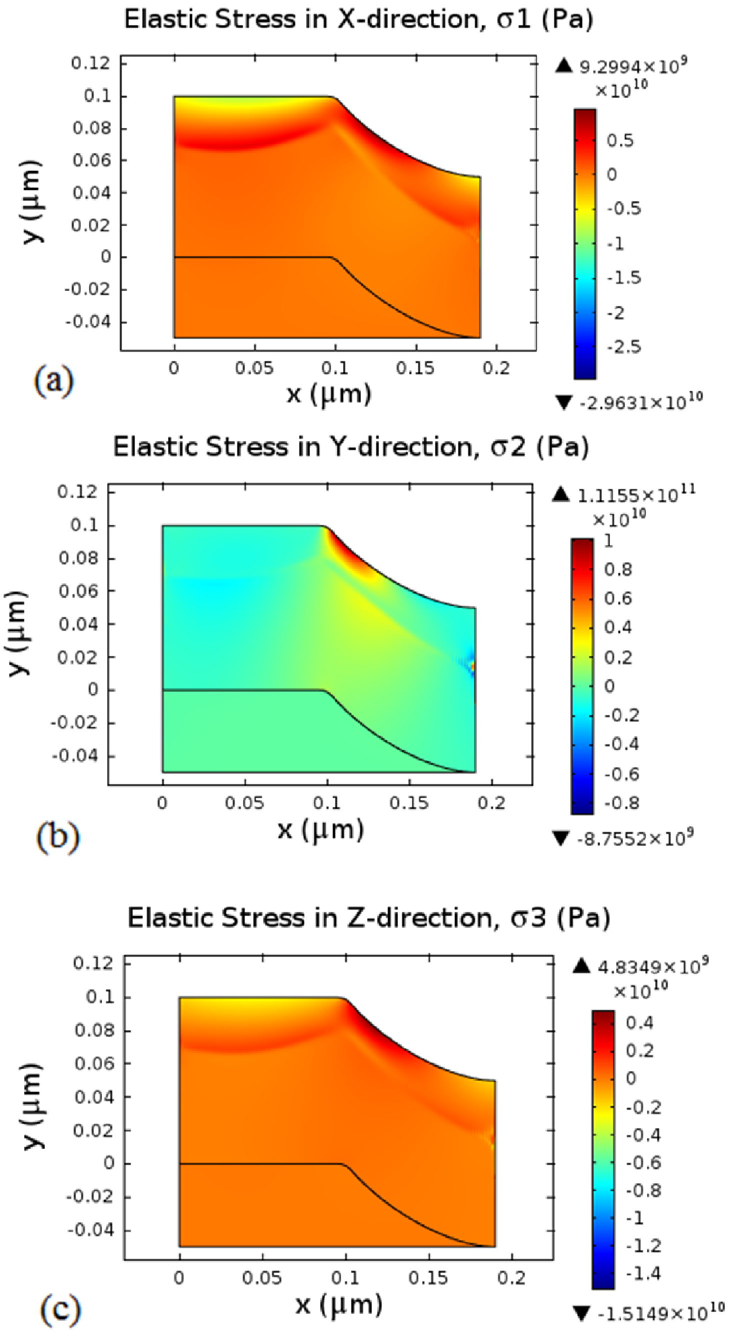

Figure 67: Elastic stresses in (a) X-direction, (b) Y-direction, (c) Z-direction

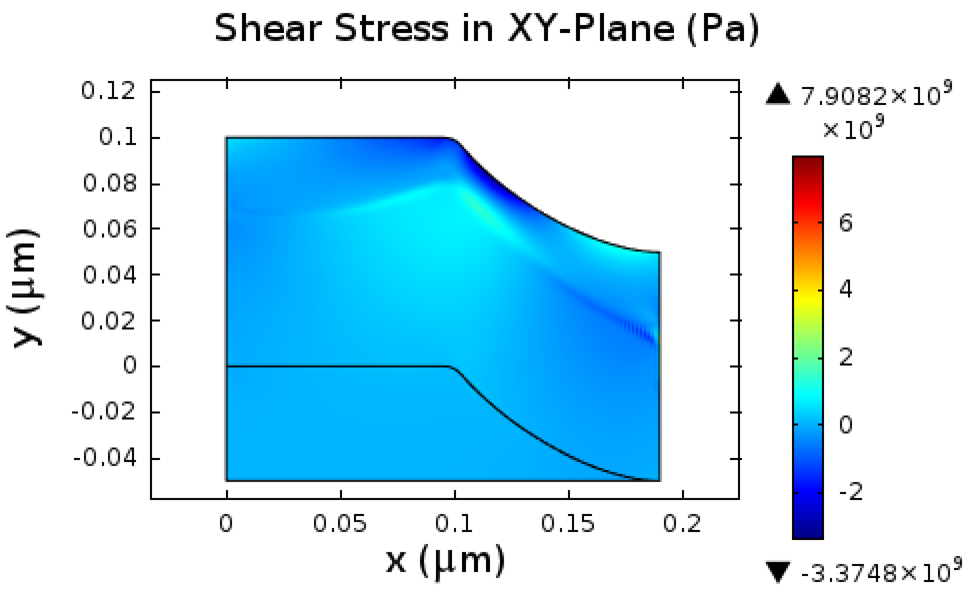

Figure 68: Induced shear strain

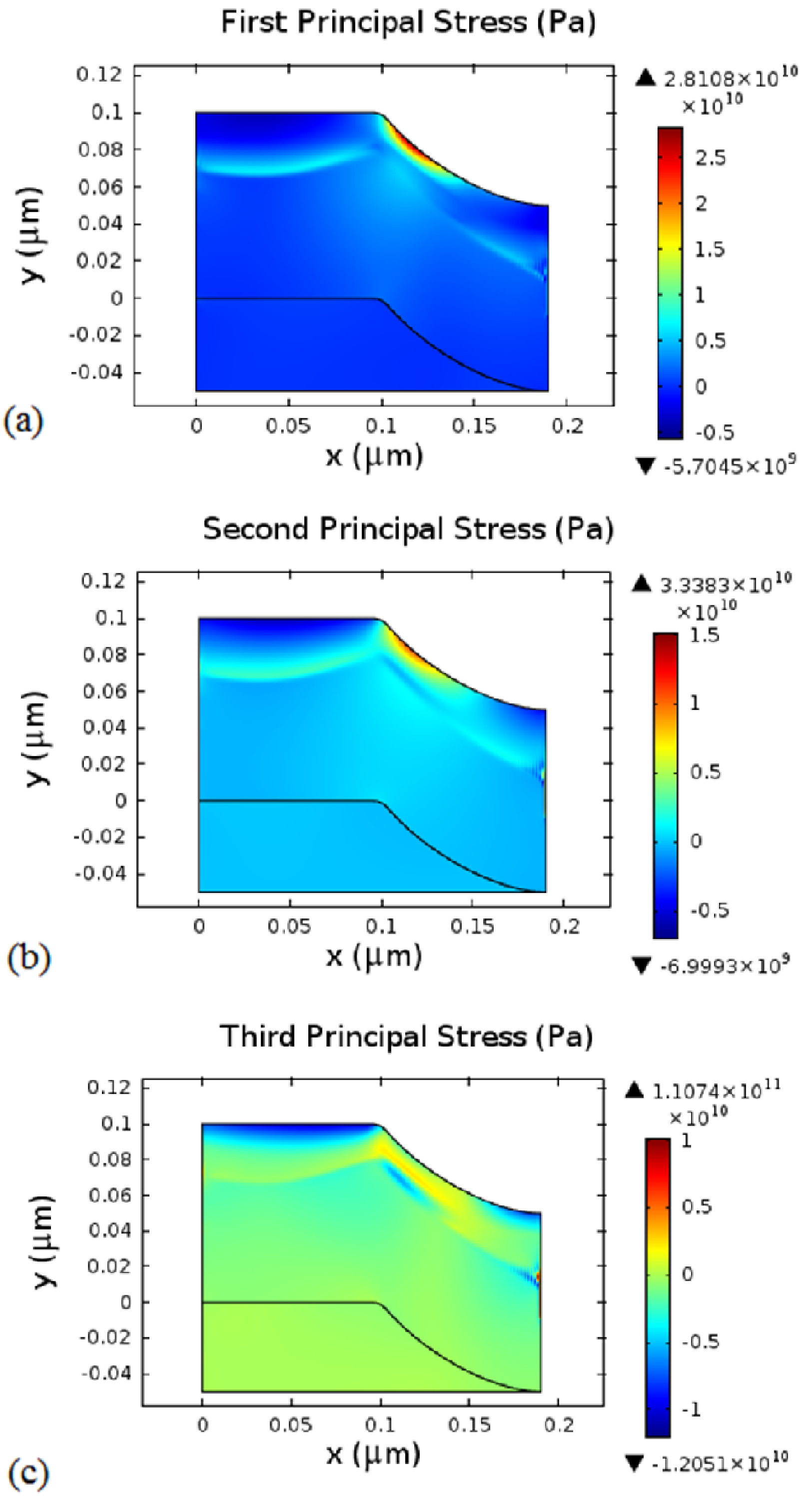

Figure 69: Principal stresses

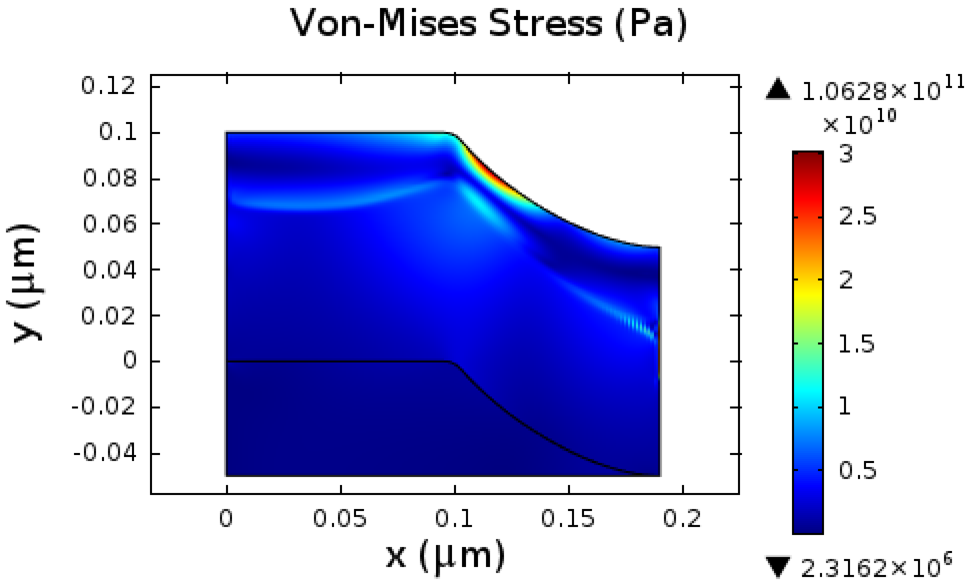

Figure 70: Von Mises stresses

7.3 Influence of some input parameters on the corrosion kinetics

In order to check the response of the model, a parametric study was carried out by varying the some sensitive (input) parameters. A brief discussion of the simulation experiment is done as follows.

7.3.1 Effect of surface melt composition on the corrosion kinetics

Surface reaction kinetics is very important for corrosion modeling. The kinetics of the process depends on the extent of exposure of the coating to the corrosive salt. In previous experiments, it was found out that, deeper degradation (or transformation) depth was observed under higher surface composition of the V_2O_5. Therefore, the surface melt composition is increased in order to check that the behavior of the model.

The surface melt composition was varied from 0.083 to 0.095 moles as shown in Fig. 71. As in the experiments, the depth of transformation is found to increase with increase in the surface melt composition. This is due to the increased rate of transformation at higher concentration driving force. Since the transformation is diffusion-controlled, it can be seen that the transformation growth follows the conventional parabolic growth. Thus, the sensitivity of the model to the surface reaction kinetics conforms with the experimental results.

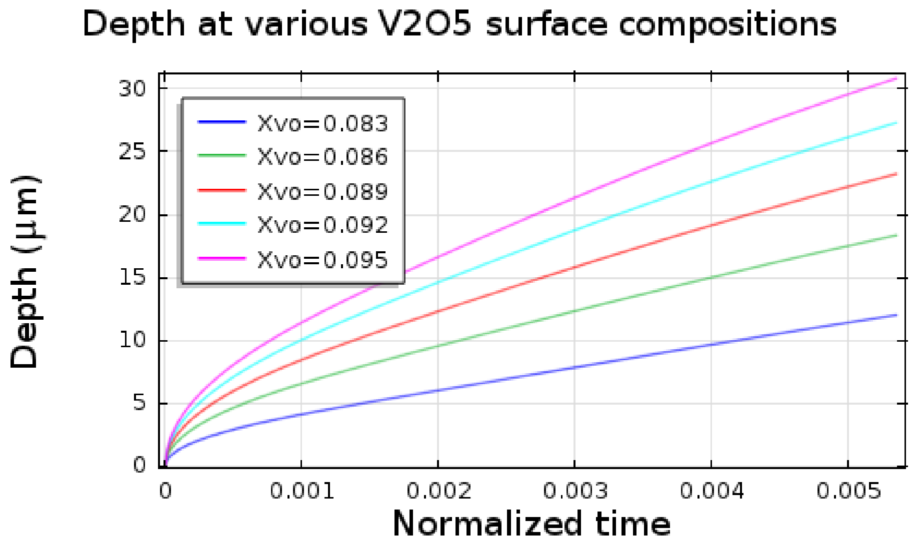

Figure 71: Sensitivity of the model to V_2O_5 surface concentration

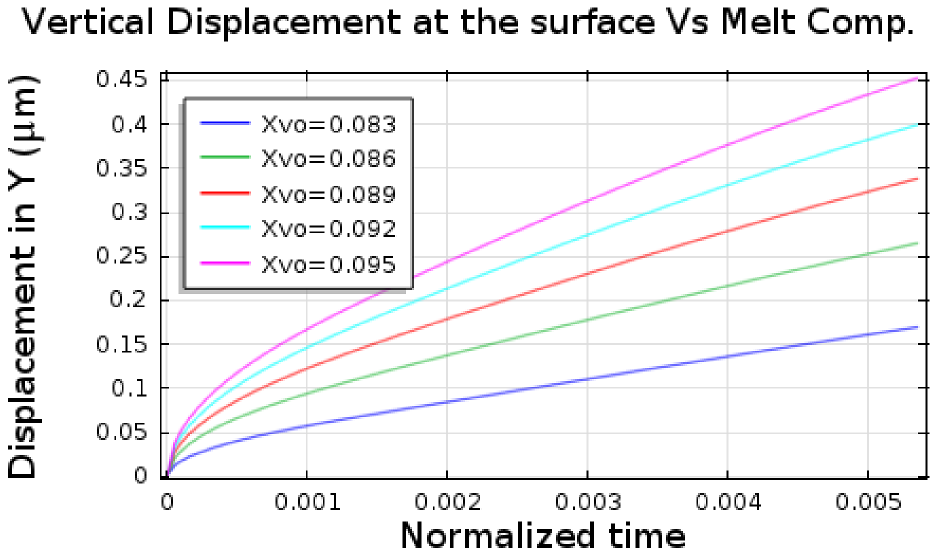

Figure 72: Variation of surface vertical displacement with V_2O_5 concentration

Fig.72 shows the variation of the surface displacement of the top coat (in the Y-direction) with surface melt composition. It can be seen that, the variation of the surface displacement with melt composition is similar to that of the corrosion kinetics. This is due to the strong coupling between the phase field equations and elasticity. Thus, higher surface melt compositions result in deeper transformation depth and volumetric expansion.

Fig. 73 & 74 shows the variation of the elastic stresses (in X and Z-direction) with surface melt composition at the point (5 μm, 45 μm) during the transformation. It can be observed that the induced stresses develop quickly for higher surface melt compositions Thus, a coating that is exposed to high composition of V_2O_5 fails quickly than those exposed to low compositions as observed experimentally[**89**].

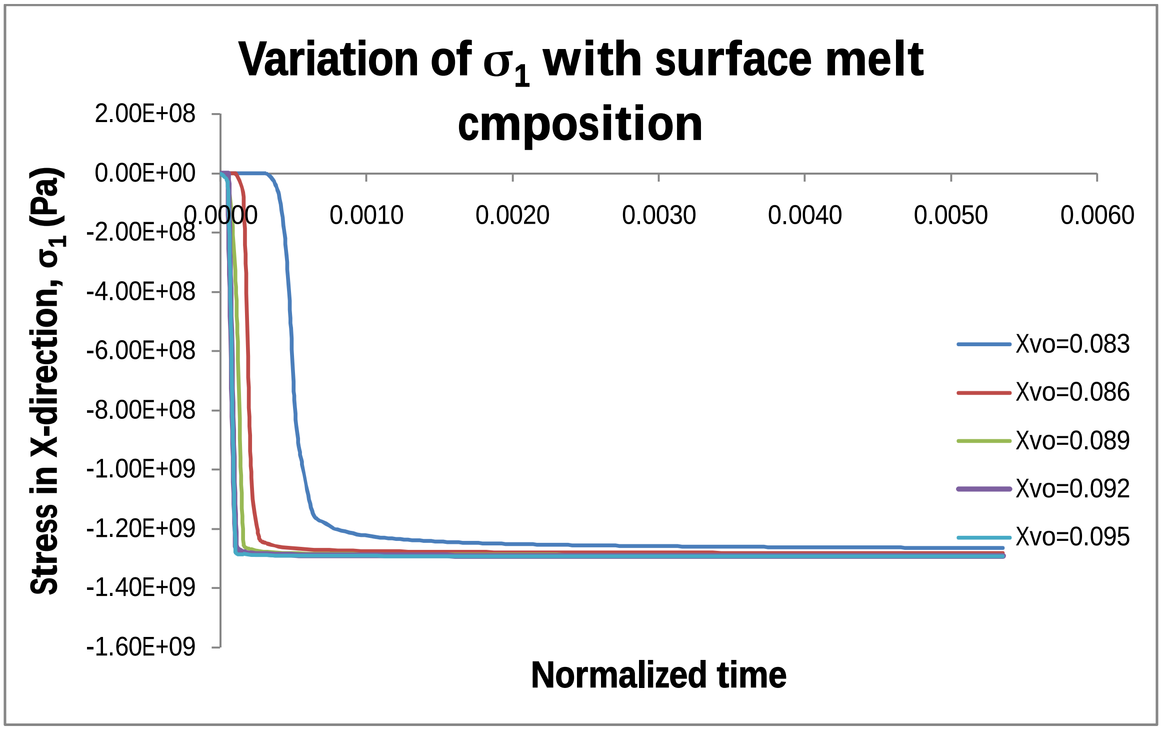

Figure 73: Variation of elastic stress in X-direction with corrosion kinetics

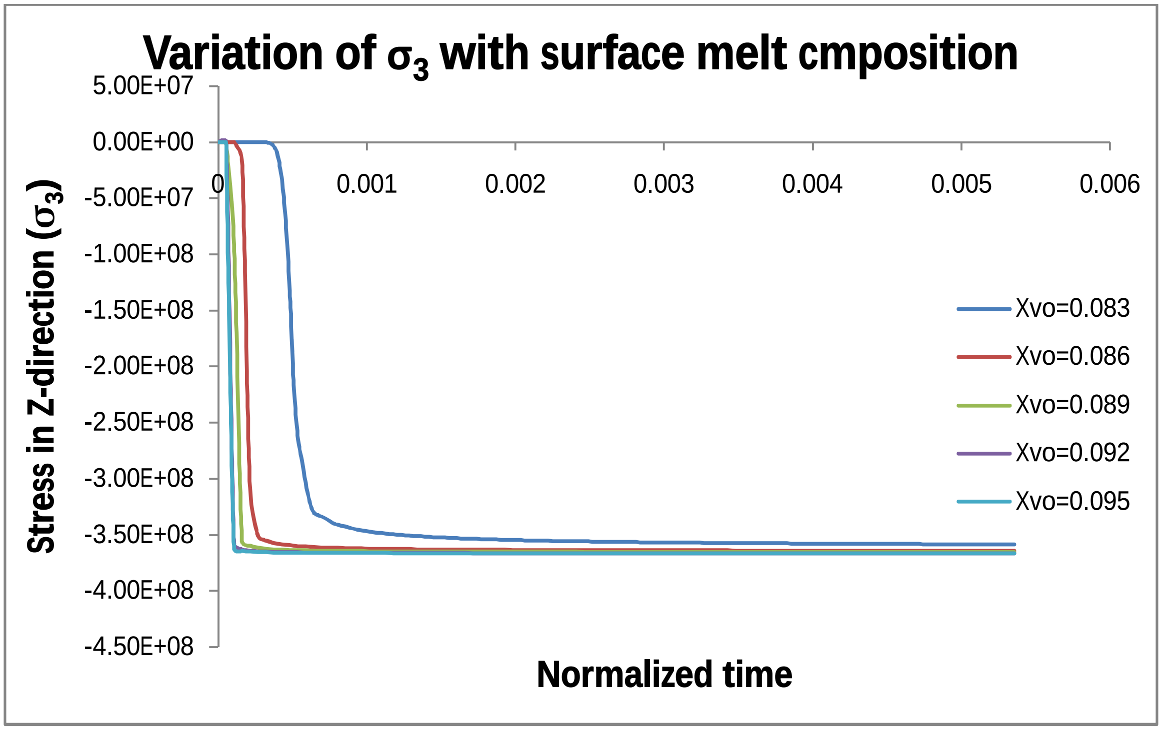

Figure 74: Variation of elastic stress in Z-direction with corrosion kinetics

7.3.2 Effect of elastic interaction on the corrosion kinetics

In order to investigate the effect of the elastic interaction (between the m-phase and t-phase) on the corrosion kinetics, the transformation strains are switched-off and the simulation is run. It can be seen that, the attained transformation depth when the elastic interaction is switched off is always higher (shown in Fig.75 (b)). Thus as expected, the elastic interaction offers some resistance to the transformation driving force. It is equally important to observe that the elastic interaction does not have a significant effect on the transformation (shown in Fig.75 (a)). This is due to the fact that, the resistance that is offered by the elastic interaction between the coexisting phases is very small when compared to the thermodynamic driving force for the transformation.

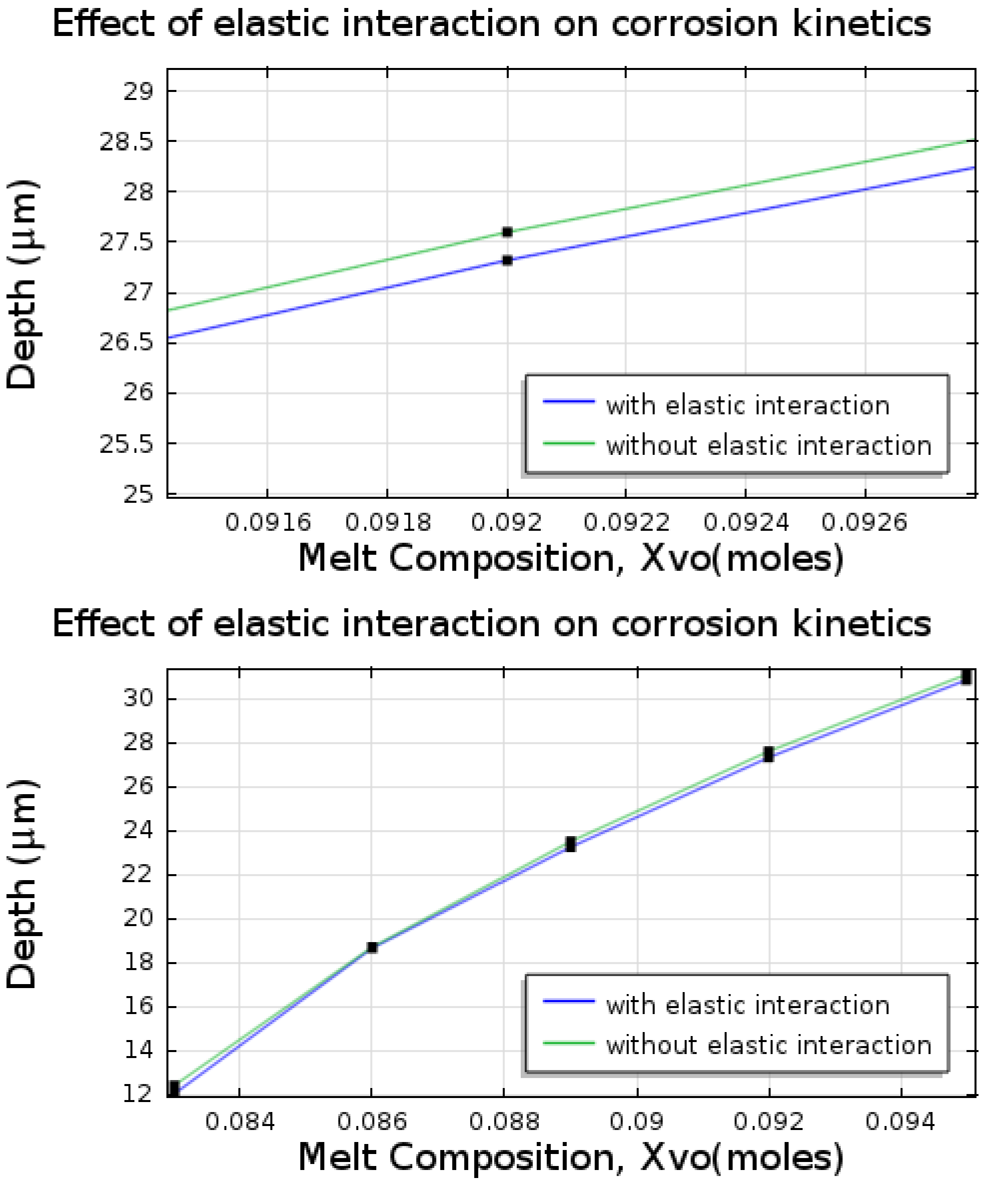

Figure 75: Sensitivity of the model to elastic interaction (a) Zoomed, (b) Actual

7.3.3 Effect of V_2O_5 diffusion coefficient on the corrosion kinetics

Similarly, the simulation is run at various values of V_2O_5 diffusion coefficient as shown in Fig. 76. The diffusion coefficient which is proportional to the atomic (or diffusion) mobility is increased from 1 x 10^{-15} m^2/s to 1 x 10^{-10} m^2/s. The results show that the depth of transformation increases with diffusivity. This can be explained by the fact that, increased V_2O_5 diffusion coefficient results in higher rate of diffusion and deeper transformation depth. Therefore, the response of the model to the diffusivity of the melt conforms to conventional diffusion-induced transformations.

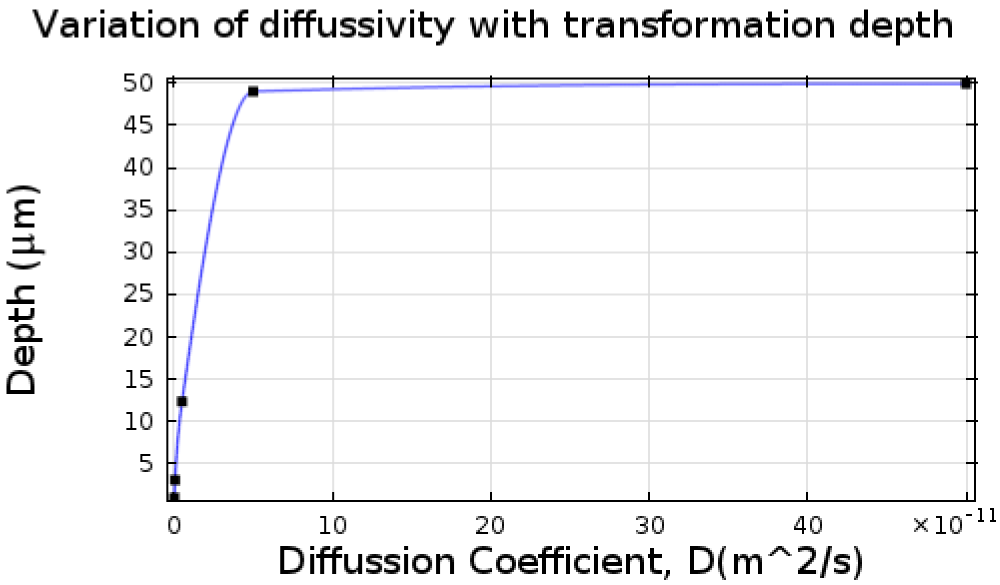

Figure 76: Sensitivity of the model to diffusivity of melt

7.3.4 Effect of kinetic mobility on the corrosion kinetics

In the literature [**58**], the kinetics of phase transformations is usually controlled through the ratio of atomic (or diffusion) mobility to kinetic mobility. When the ratio is very small, the kinetics is diffusion-controlled; when the ratio is high the kinetics is interface-controlled. Thus, it can be observed (from Fig. 77) that the current model behavoir conforms to the convention. When the kinetic mobility is set as 2 m^3/Js, the corrosion process becomes diffusion-controlled. This implies that the phase transformation becomes more sensitive to the concentration driving force; and a very large percentage of the driving force is dissipated in long-range diffusion. On the other hand, setting the kinetic mobility as 2.1 x 10^{-11} results in interface-controlled phase transformation. This implies that a large percentage of the driving force is dissipated in local rearrangement of atoms.

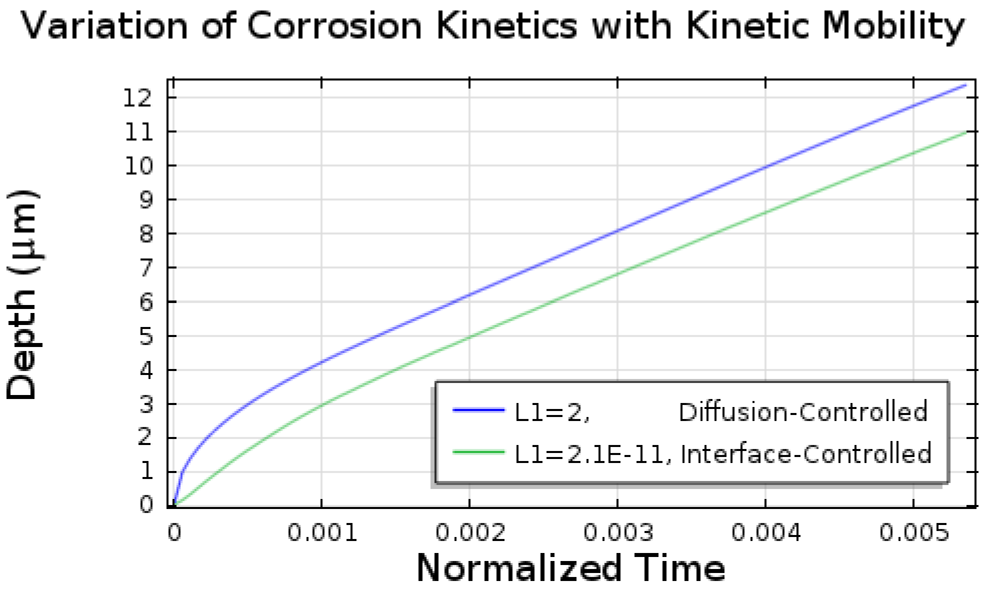

Figure 77: Sensitivity of the model to the kinetics of the transformation

7.4 Conclusion

Previous experimental observations show that Vanadium impurities present in low grade fuels react with the zirconia stabilizer, Y_2O_3, in the top coat to cause tetragonal-to-monoclinic phase transformation of zirconia which is usually accompanied by volumetric expansion. Consequently, severe internal stresses that cause the failure of the coating are developed in the TBC system.

A numerical modeling approach is developed that predicts the V_2O_5 hot corrosion kinetics in both the PRZ and MIRZ of the top coat. The model was directly coupled with elasticity in order to predict the effect of the transformation on mechanical behavior of the system. It was found out that, severe compressive stresses that lead to the formation of horizontal cracks were developed in the PRZ of the coating. The stresses were found to be higher in the MIRZ which is nearer to the TGO and bond coat. Eventually, total delamination or rumpling of the top coat occurs after the hot corrosion attack.

The following conclusions can be made from the results obtained:

1. The present study shows that the phase field method can be used to predict the kinetics of microstructure evolution during the hot corrosion of TBC. To the best of our knowledge, this is the first application of the method to a practical corrosion process. The results are found to be in good agreement with previous experimental observations[**89**]. Moreover, with correct input parameters the model can adequately be used in the study of any phase transformation that is induced by the diffusion of external chemical species.
2. The present study has also demonstrated that the phase field method can be used to study the effect of corrosion kinetics on the mechanical behavior of materials. The microelasticity theory[**45**] was found to be helpful in predicting the transformation-induced stresses. An extensive study of the induced stresses also shows that the failure of the top coat is due to the grain boundary sliding. The high compressive stresses that are developed in the X and Z-directions justify the reason for the emergence of the experimentally-observed horizontal cracks in hot corroded TBCs.

CHAPTER 8

GAS NITRIDING: RESULTS AND DISCUSSIONS

The evolution of the diffusion and compound layers during the two-stage controlled gas nitriding of AISI H13 tool steels was modeled using a Phase Field Model (PFM) that is coupled with elasticity. The various nitride layers form due to the diffusion of atomic nitrogen into the tool steel. Based on microscopic observations, the transformation was prescribed to proceed in a direction that is normal to the surface. The residual stresses that are developed in the nitrided region during the heat treatment process were also predicted.

8.1 Diffusion Layer

8.1.1 Process kinetics

Fig. 78 shows the results of the final nitrogen concentration profile on the actual sample geometry. It can be seen that, the depth of diffusion layer cannot be seen because the actual sample (of about 5 mm depth) is used for the analysis. However, the figure shows that a maximum final nitrogen concentration of about 4 wt% is attained at the surface of the material. For the purpose of demonstration, the variation of the nitrogen concentration profile during the process at the flat section of the sample is shown in Fig. 79. It can be seen that the nitrogen concentration is initially very high, but reduces continuously due to the decrease in the controlled nitrogen gas concentration (or nitriding potential) during the process. As mentioned previously, the continuous reduction of the nitrogen concentration is done in order to ensure the formation of very thin compound layer. Fig. 79 also shows that even though the surface nitrogen concentration reduces during the process, the case depth of the diffusion layer is not affected. It can also be observed that the simulation predicts case depth of about 150 μm, which compares well with previous experimental measurements [**110**] and previous numerical prediction [**104**].

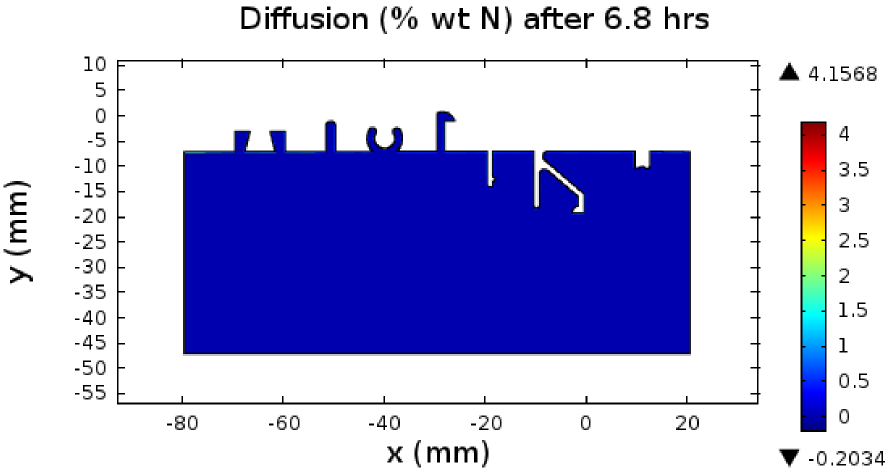

Figure 78: Nitrogen concentration profile in actual sample geometry

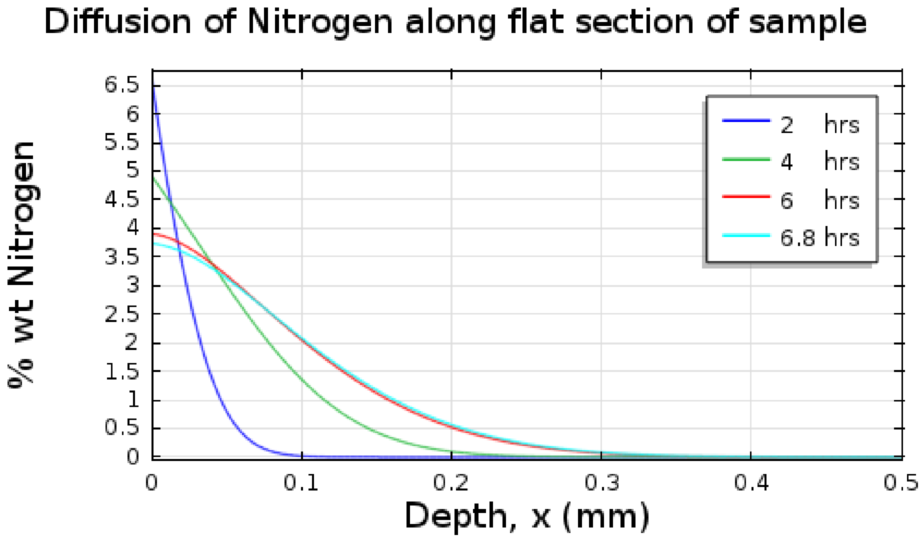

Figure 79: Nitrogen concentration profiles along a flat region of the sample

An important observation in the current numerical study is that, the nitrided depth at some corners is more than that at the flat sections of the sample as shown in Fig. 80 and 81. This was also observed both experimentally and numerically by Aktar et al. [**104**]. This is due to the simultaneous diffusion of nitrogen along converging directions from the two edges of the corner. The implication of the high nitrogen concentration at the corner points is that, the thickness of the compound layer as well as the magnitudes of the residual stresses will be high. This may affect the performance of gas nitrided extrusion dies.

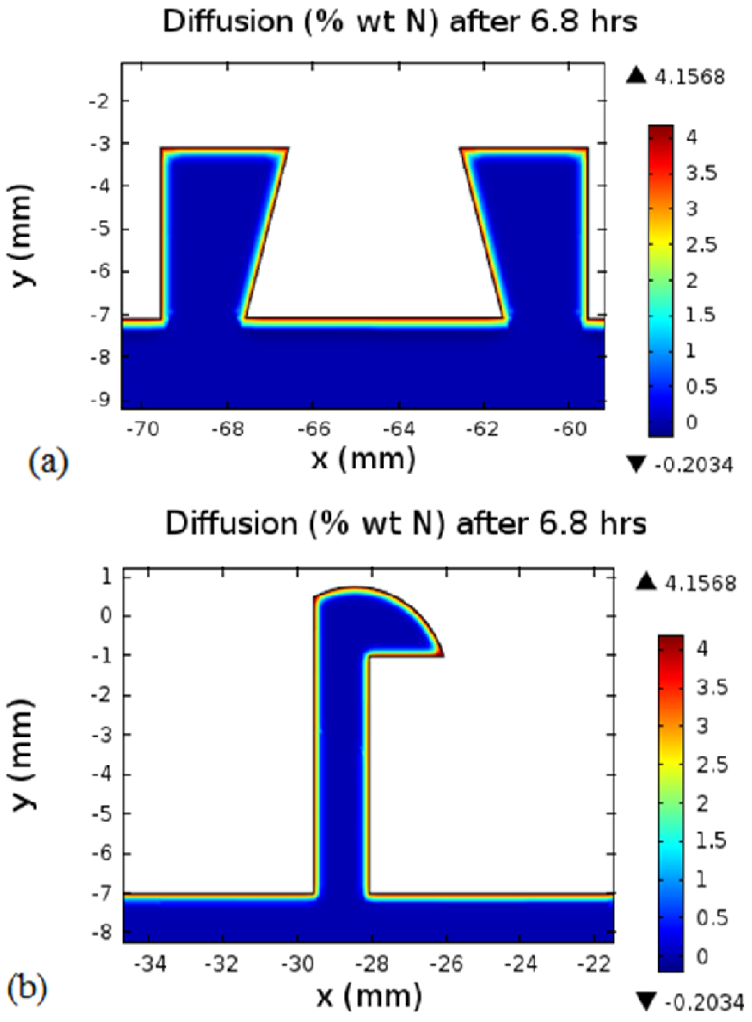

Figure 80: Nitrogen concentration profiles at some selected regions of sample-I

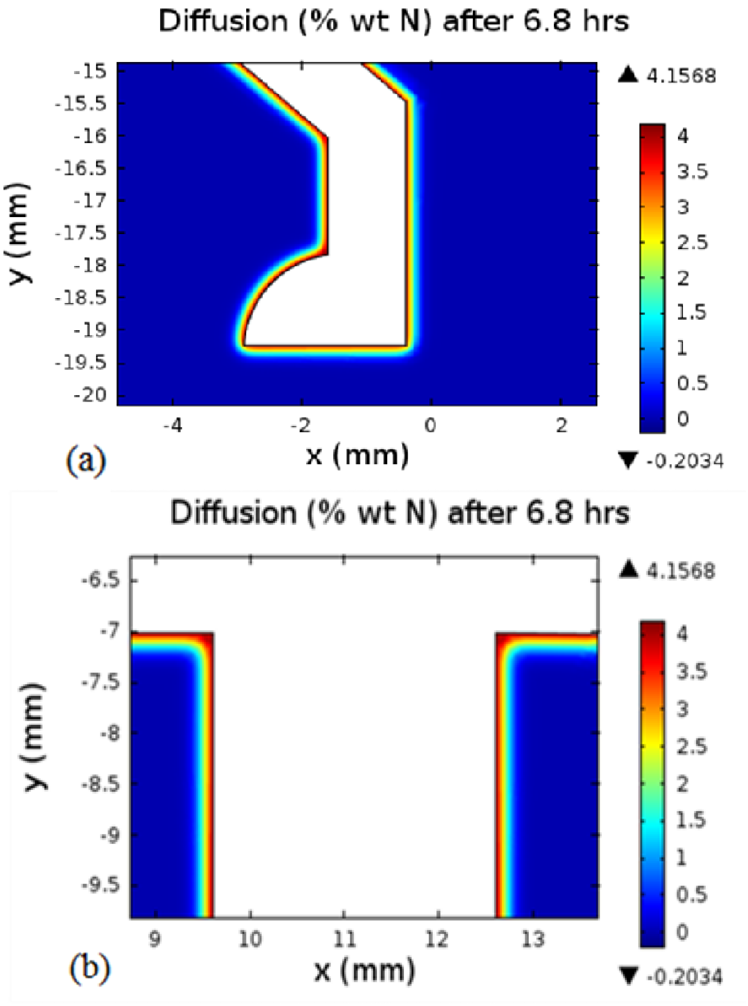

Figure 81: Nitrogen concentration profiles at some selected regions of sample-II

In the current work, special types of corner points are selected for the analysis. Fig. 82(a) shows the variation of final nitrogen concentration with depth at flat sections and Right-Outer Corner (ROC) regions. It can be seen that, the variation of nitrogen concentration along the depth of flat sections is uniform; and the temporal variation of the nitrogen concentration profile is previously shown in Fig. 79. However, the more thickness of the diffusion layer at the ROC points is found as shown in Fig. 82(b). This is due to the simultaneous diffusion of atomic nitrogen from two converging directions. Thus, the surface hardness of the material is more at such corner point. On the other hand, Fig.83

shows that the thickness of the diffusion layer at Right-Inner-Corner (RIC) point is less than that at the flat sections. This is due to the diffusion of nitrogen along diverging directions. Thus, the surface hardness of the material at RIC is less than that of a flat section.

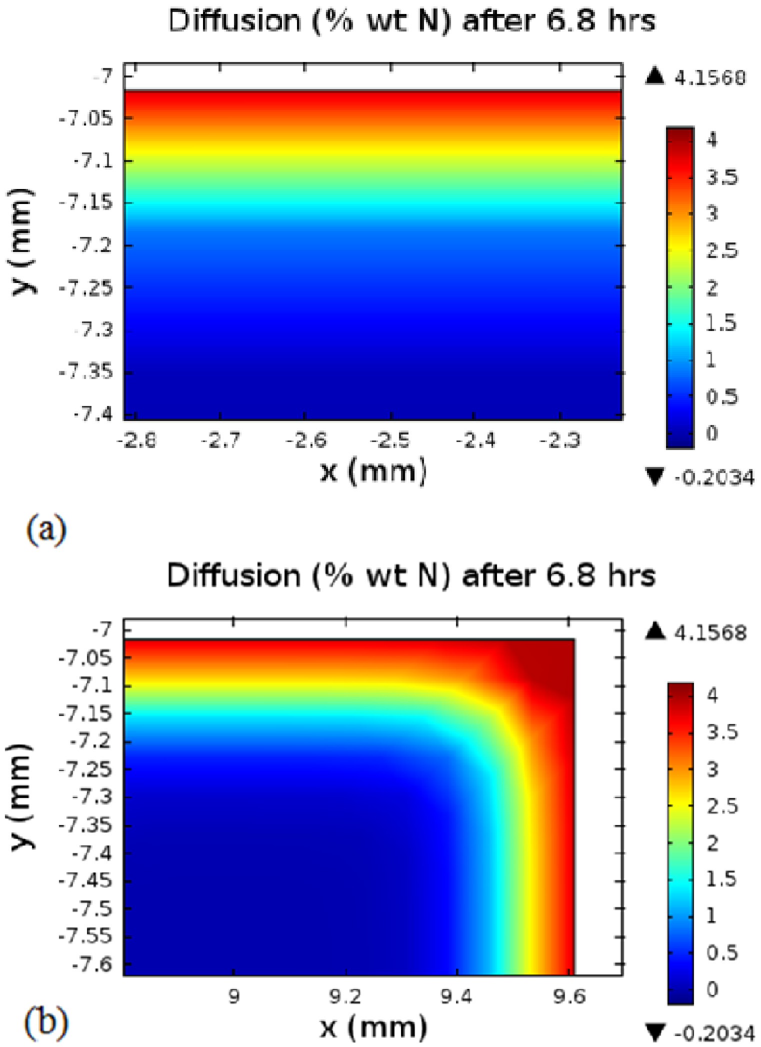

Figure 82: Nitrogen concentration at (a) Flat section, (b) ROC point

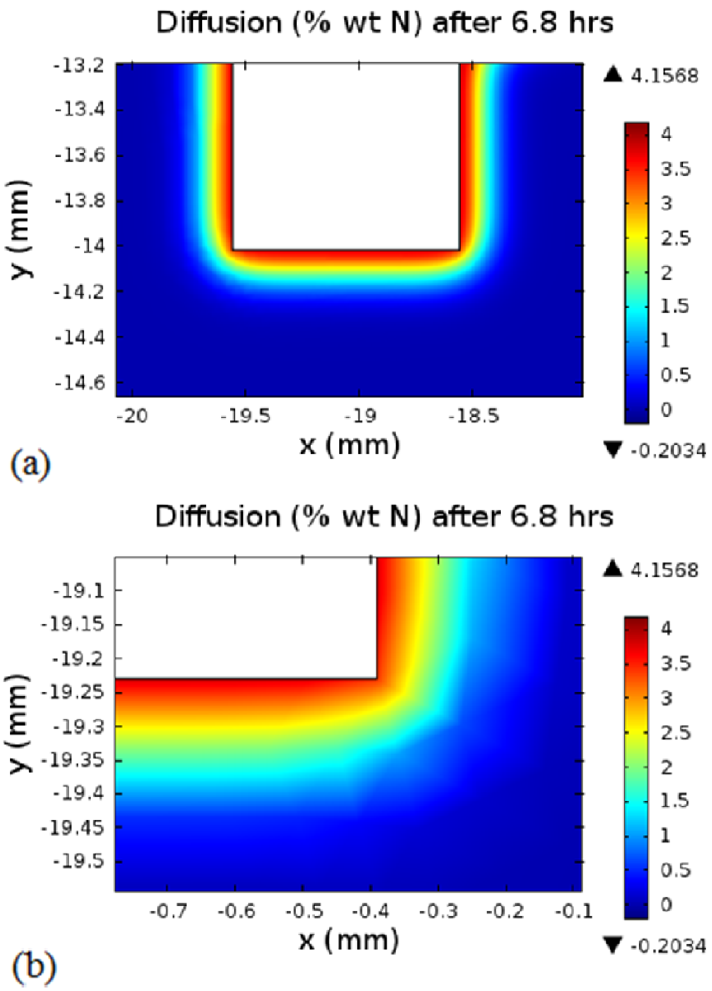

Figure 83: Nitrogen concentration at (a) RIC point, (b) RIC point (Zoomed)

Similarly, Fig. 84 shows the depth of the diffusion layer at other type of corners. Fig. 84 also shows that Acute-Outer-Corner (AOC) points result in more case depth than Obtuse-Outer-Corner (OOC) points. The large case depth associated with the AOC can be vividly seen in Fig. 85. Fig. 84 shows that Acute-Inner-Corner points result in a very thin case depth due to the divergence of the diffusing nitrogen at such points. The same observation is made at the Obtuse-Inner-Corner (OIC) points as shown in Fig. 86. However, the case depth at OIC is slightly greater than that at AIC.

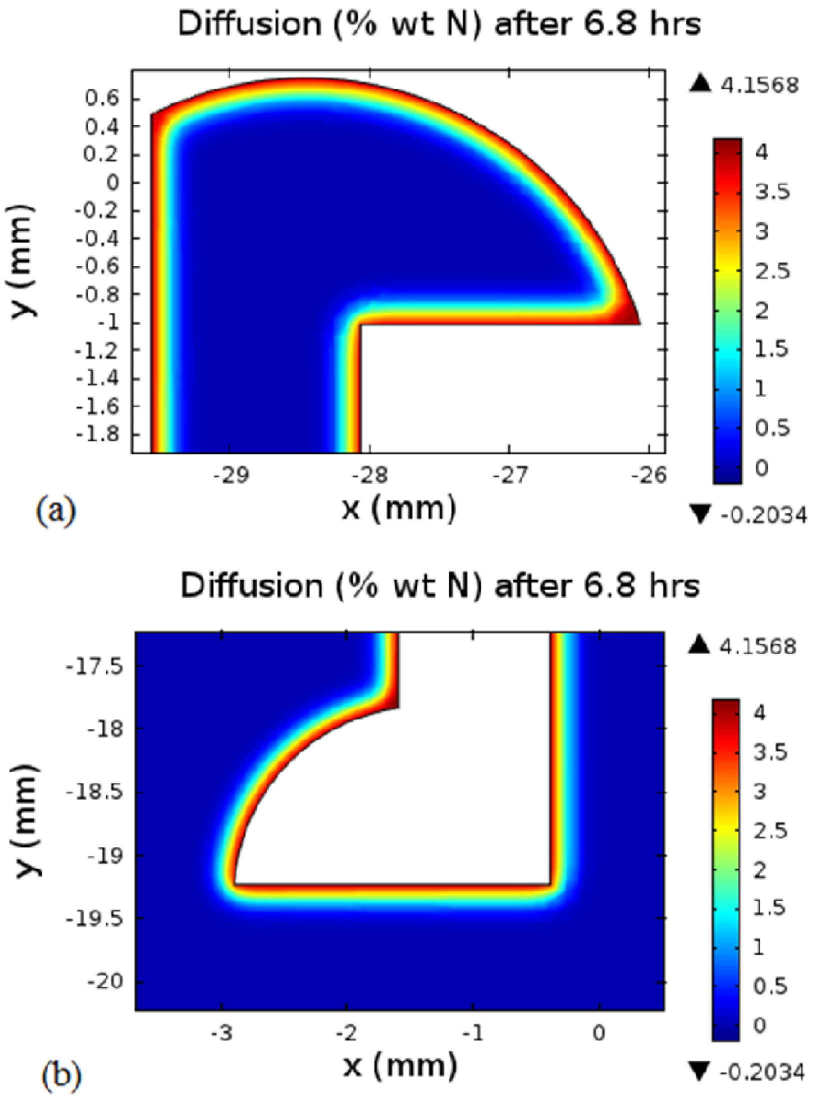

Figure 84: Nitrogen concentration at some corner points (compared)

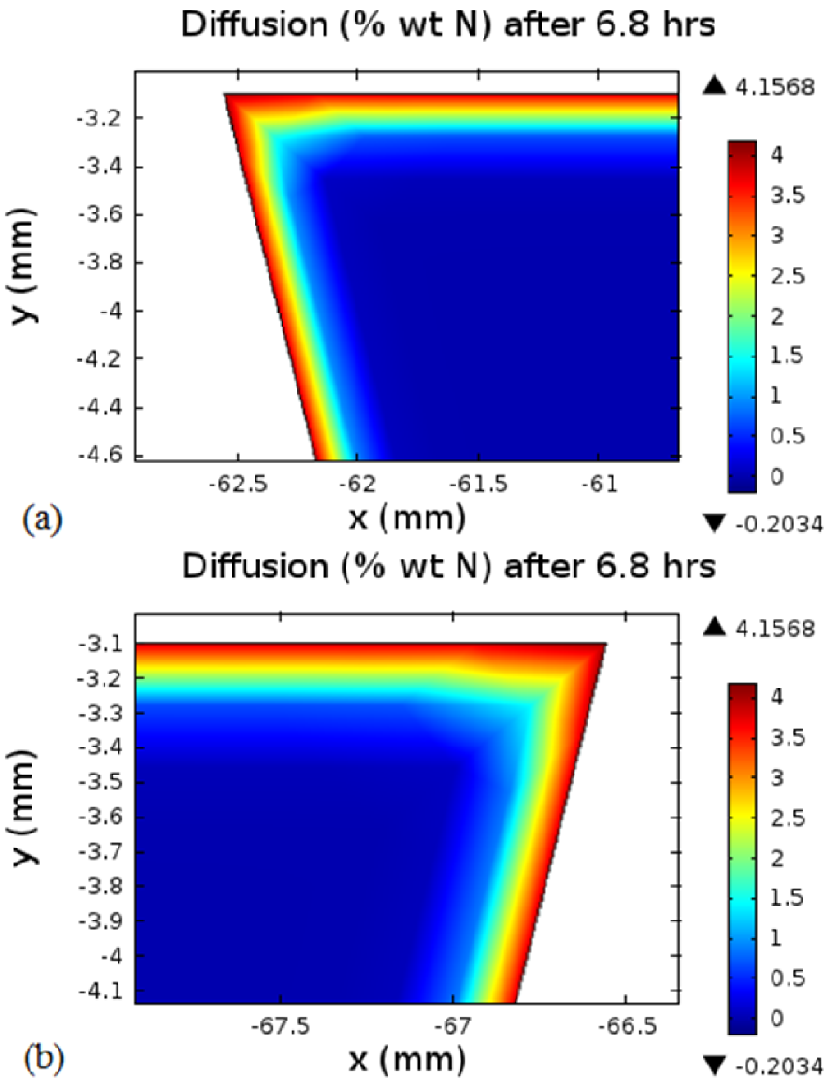

Figure 85: Nitrogen concentration at AOC points

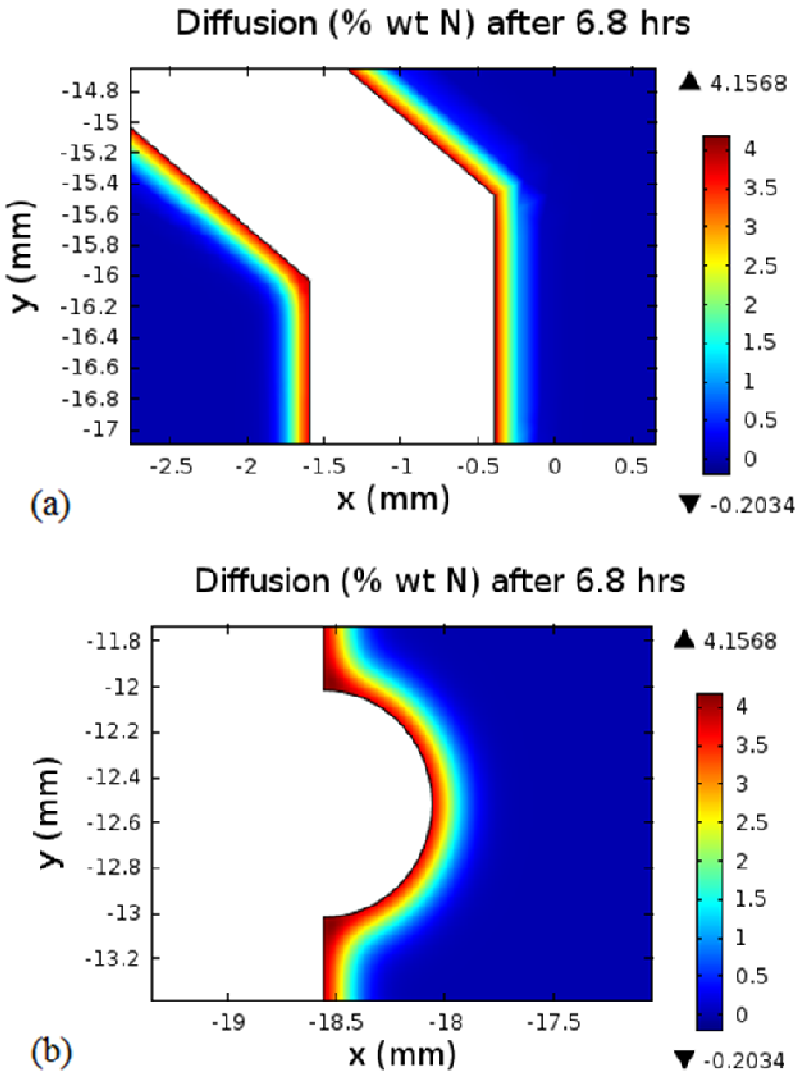

Figure 86: Nitrogen concentration at (a) OOC and OIC points, (b) OOC points

Contrary to the variation of nitrogen concentration at sharp corner points, it is found that fillet corners result in uniform nitrogen concentration profile regardless of the complexity of the die cavity. Fig. 87 and 88 show that both inner and outer fillets at die sharp corners result in a uniform depth and hardness of the nitride layer. Fig. 90 compares the variation of nitrogen concentration profiles for some selected regions of the sample geometry. It can be seen that, outer corner points have higher case depth than inner corners or flat sections. The current analysis also shows that AOC points have the highest nitrogen penetration depth depending on the orientation of the corner point. It is also found that, the very small outer corner angles result in very large depth of nitrogen diffusion.

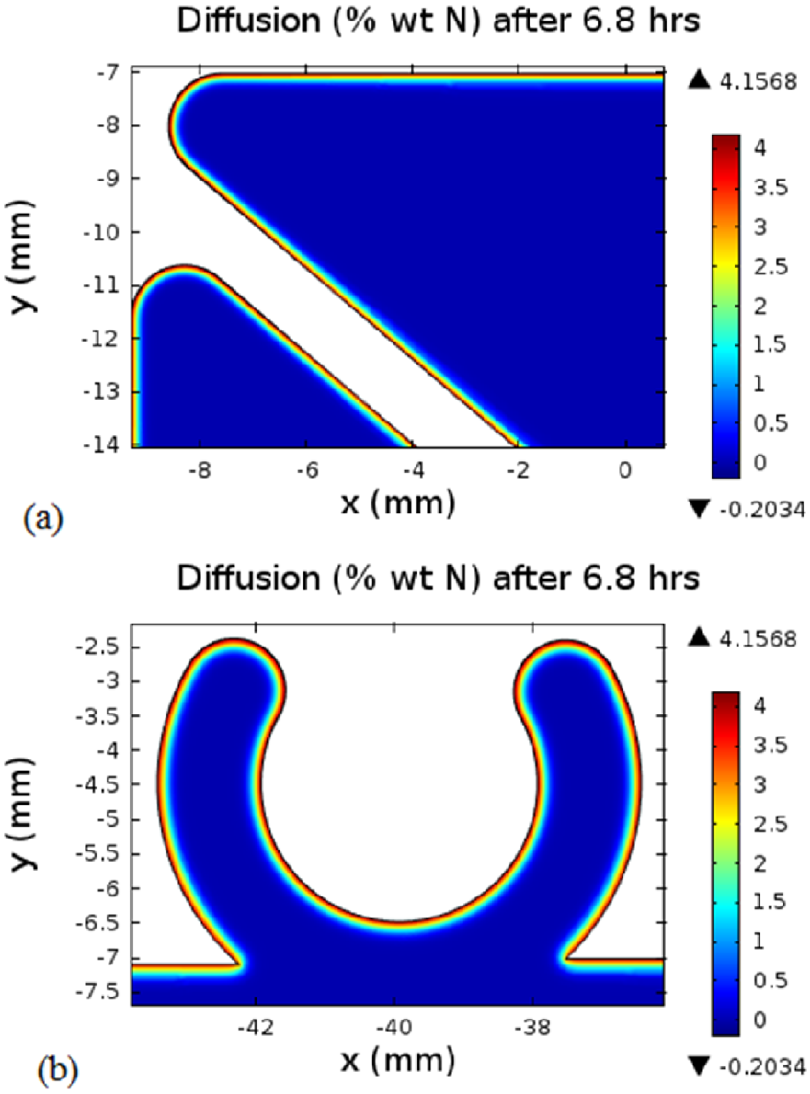

Figure 87: Nitrogen concentration at fillet regions-I

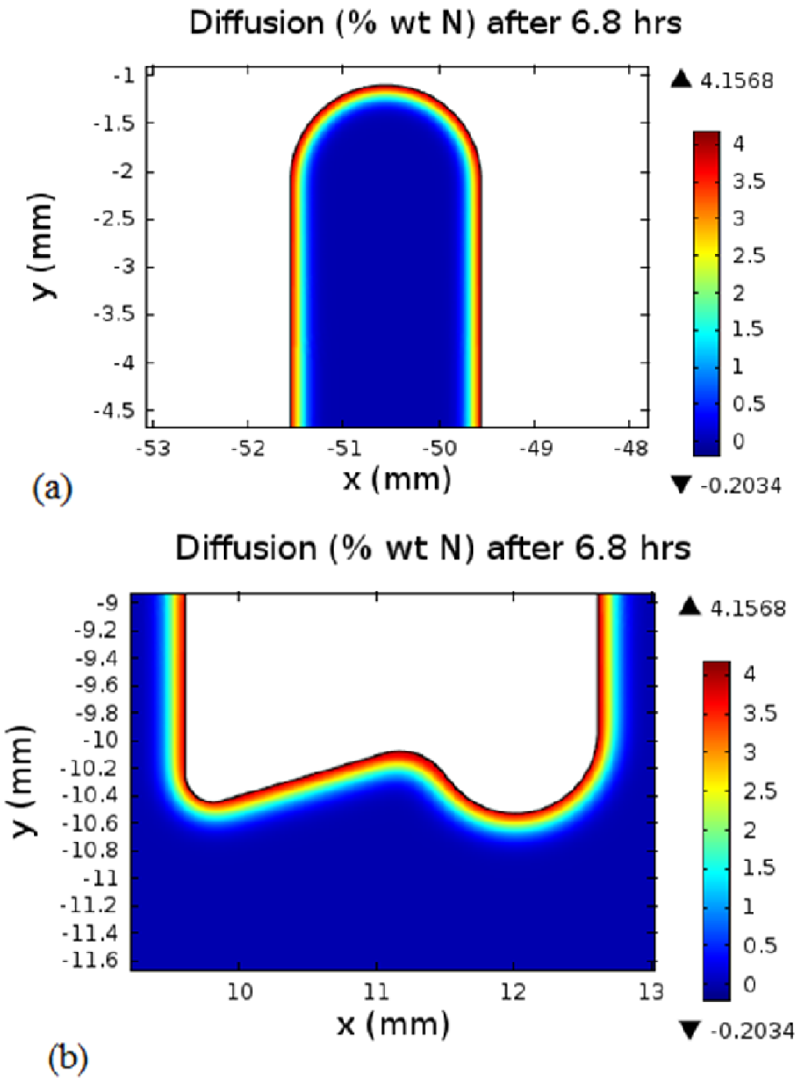

Figure 88: Nitrogen concentration at fillet regions-II

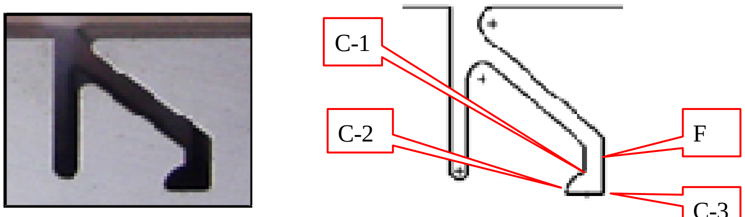

Figure 89: Selected regions for comparison of concentration profiles

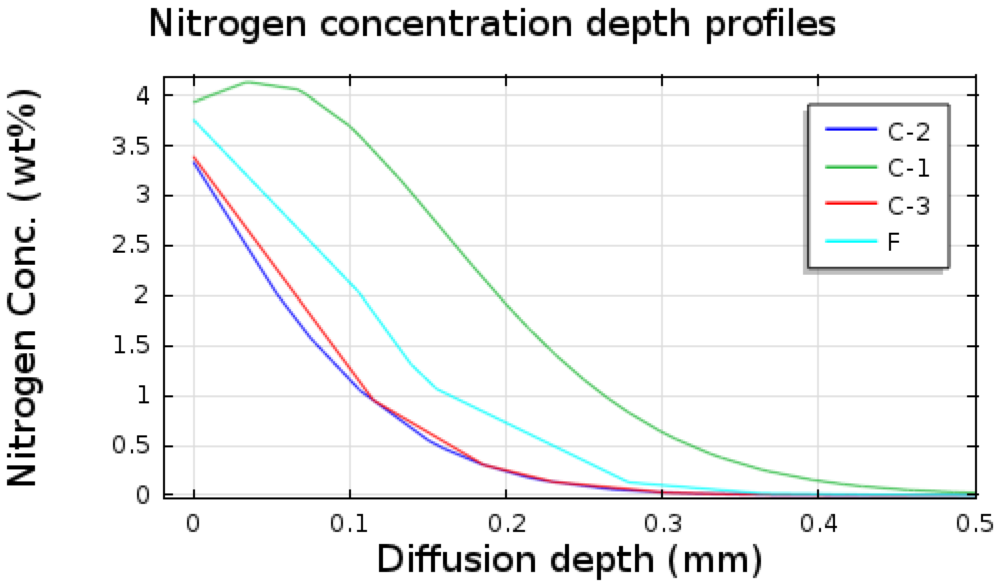

Figure 90: Concentration profiles at selected corner points

Thus, the coupling of the phase field model with elasticity has enabled precise prediction of the case depth that result from the various complex features of hot extrusion dies. The result shows that, outer corners result in very high nitrogen concentration due to simultaneous diffusion of nitrogen along converging directions. The current result conforms to a previous experimental result [**109**], both quantitatively and qualitatively.

8.1.2 Residual stresses

The main objective of the current work is to numerically predict the residual stresses that are developed due to the expansion of the material lattice parameters by the diffusion of nitrogen. It was determined that, the lattice parameters of the BCC α-iron expand when it forms interstitial solid solution with nitrogen atoms in the diffusion layer. The lattice expansion was experimentally observed to follow the Vegard's law which states that the lattice expansion is linearly related to the amount of dissolving nitrogen atoms in the solution.

Fig. 91 shows the variation of the displacement fields in the X and Y-direction after the nitriding process. Maximum and minimum displacements of 0.59 µm and -0.93 µm are found in the X-direction respectively. On the other hand, the maximum and minimum displacements in the Y-direction are 0.89 µm and -0.49 µm repectively. The displacement fields are shown at some selected parts of the sample geometry as shown in Fig. 92 and 93. It can be seen that, the maximum displacements are found at the outer sharp corners of the die cavity due to the increased atomic nitrogen concentration at such points. Thus, the diffusive residual stresses that are induced during the process are expected to be higher at such points. Furthermore, it was observed in the industries that the cracking of extrusion dies is always initiated at such corners.

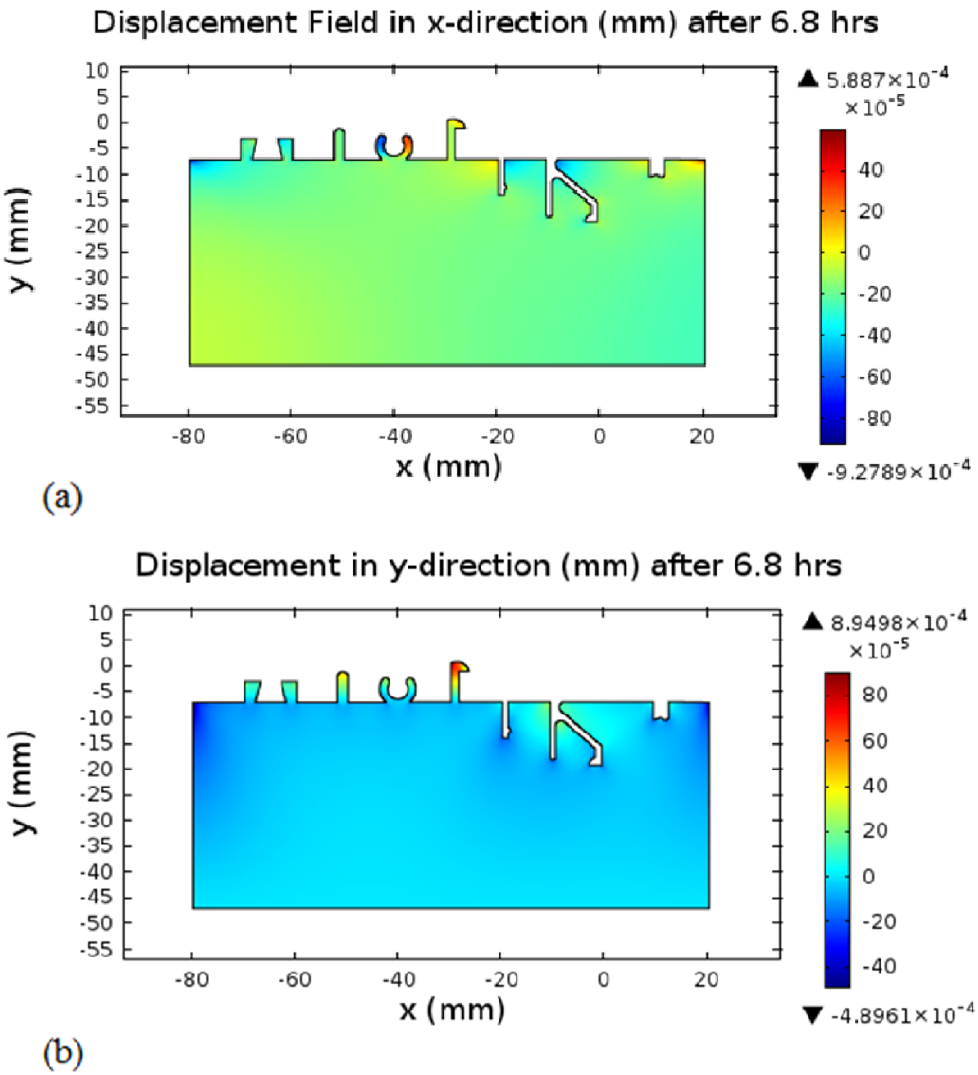

Figure 91: Displacement fields in (a) X-direction, (b) Y-direction

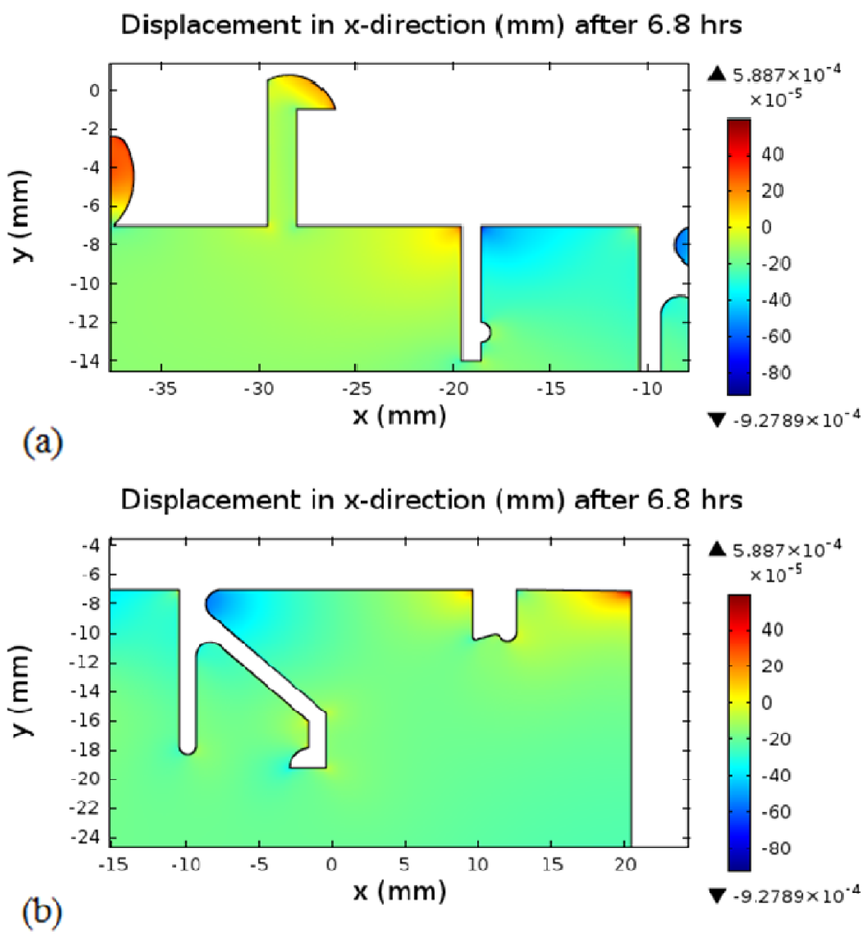

Figure 92: Displacement field in X-direction at some selected regions

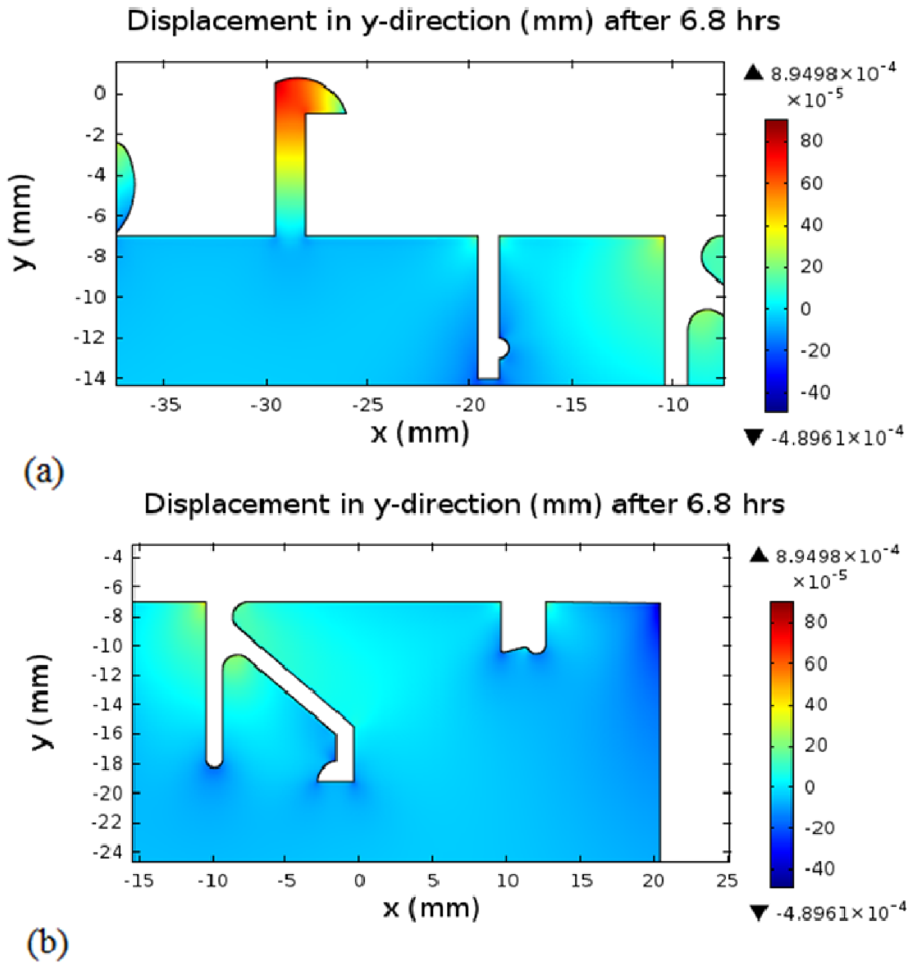

Figure 93: Displacement field in Y-direction at some selected regions

Fig. 94 and 95 shows the induced elastic strains in the X and Y-directions respectively. It can also be observed that, the magnitudes of the induced strains at the outer corner points are higher than those at the inner corner points or the flat sections of the sample geometry. It is also noticed that, the induced elastic strains at the fillet sections are found to be more or less equal to those at the flat sections. Fig. 96 shows the induced shear strain in the XY-plane at some regions of the sample geometry, where it can be observed that the complex die features result in the development of higher shear strains at some regions. However, the numerical value of the shear strain is not large enough to cause serious distortion of the geometry.

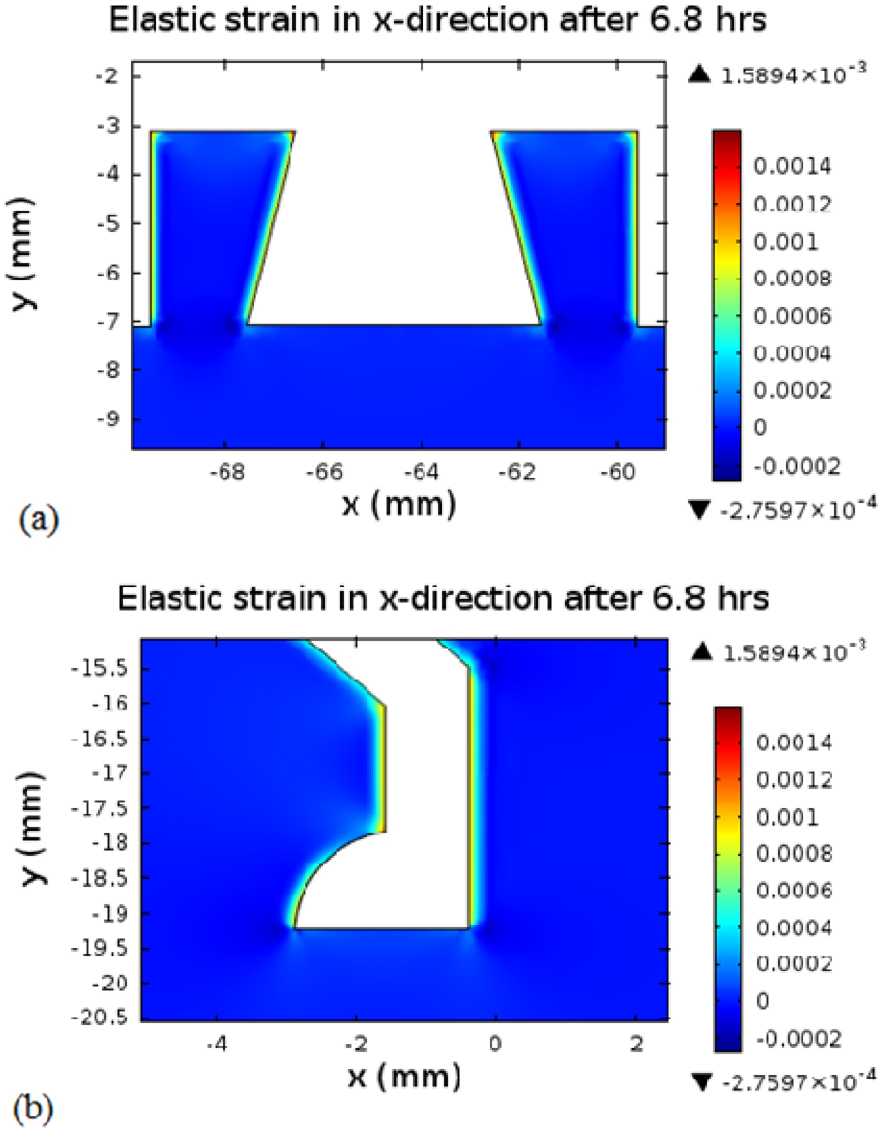

Figure 94: Elastic strain in X-direction at some selected regions

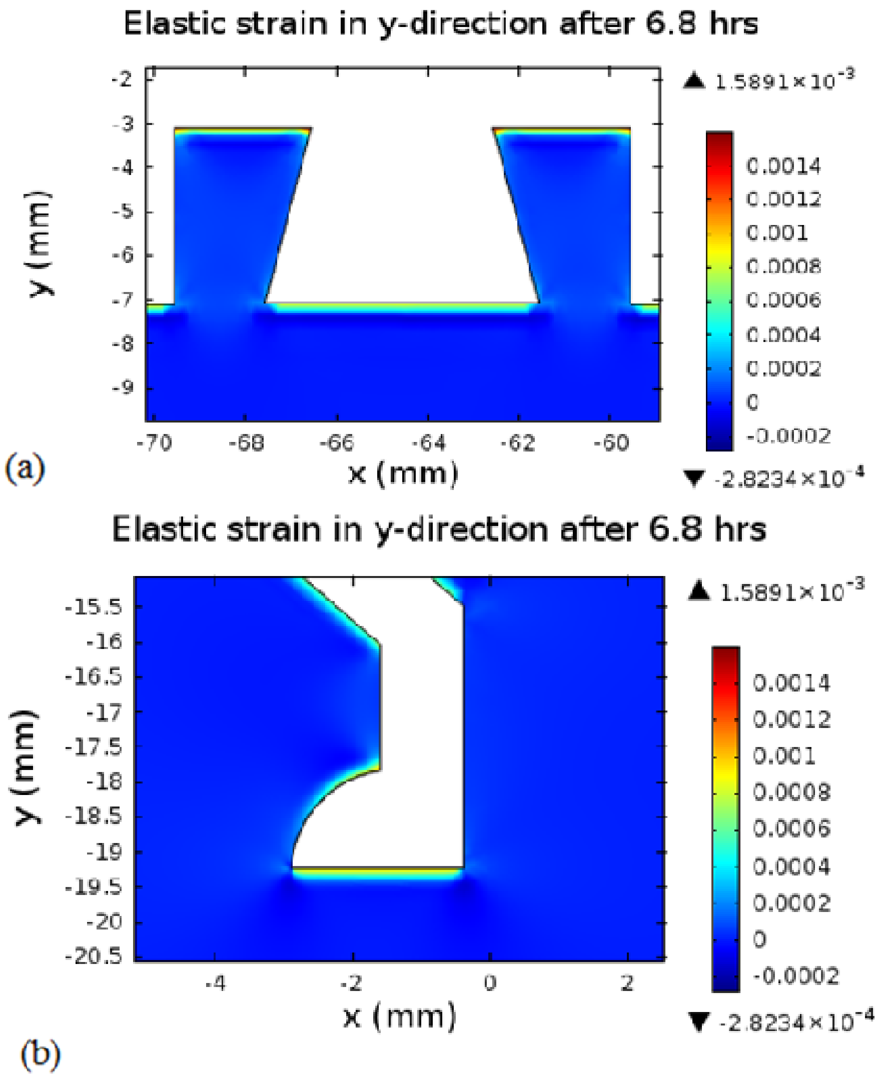

Figure 95: Elastic strain in Y-direction at some selected regions

For the stress field, Fig. 97 and 98 shows the induced stress field in the X-direction. It can be seen that, a compressive (elastic) stress of about -50 MPa is induced at the surface of the flat or fillet sections of the geometry. As in previous numerical work[**125**], it is observed that the surface compressive stress is balanced by a tensile (elastic) stress of about of 37 MPa from the interior regions of the geometry. This results in an overall stress magnitude of about -13MPa at the flat regions of the geometry. As reported in a previous work, this justifies that the residual stresses on the flat sections of the geometry will not have any effect on the performance of hot extrusion dies. Similar observation is made from the induced stress field in the Y-direction (shown in Fig.99 and 100), where a surface compressive stress of about -50 MPa is balanced by a tensile stress of about 27 MPa from interior regions of the geometry.

However, the outer corner points are observed to have tensile stresses of about 37 MPa and 27 MPa in the X and Y-direction respectively. Unlike the flat sections, it is observed that the surface tensile stresses are not balanced by any stress from the interior at the outer corner points. Thus, the sum of the residual stresses at the outer corners is expected to be very high. For the induced shear stresses, it can be seen from Fig. 101 & 102 that the sharp corners induce a maximum shear stress of about 95 MPa or 83 MPa depending the location of the corner. Still outer corners are observed to develop more shear stress than the other sections.

Furthermore, the balancing of the compressive stresses at flat regions is clearer from the plots of the principal stresses (shown in Fig. 103 and 104). The principal stresses indicate that the induced stresses are mainly compressive in nature, especially at the surface. Fig. 104(b) shows the von Mises stress field where it can be seen that the absolute magnitude of the induced von Mises stress at the outer corner points is the highest (about 160 MPa). As mentioned previously, this is due to the fact that the induced stresses at the outer corner points are not balanced by any tensile stress from the interior. On the other hand, the magnitude of the induced von Mises stress at the flat or fillet regions is about 80 MPa. Inner corner points have the least magnitude of stresses based on our observations.

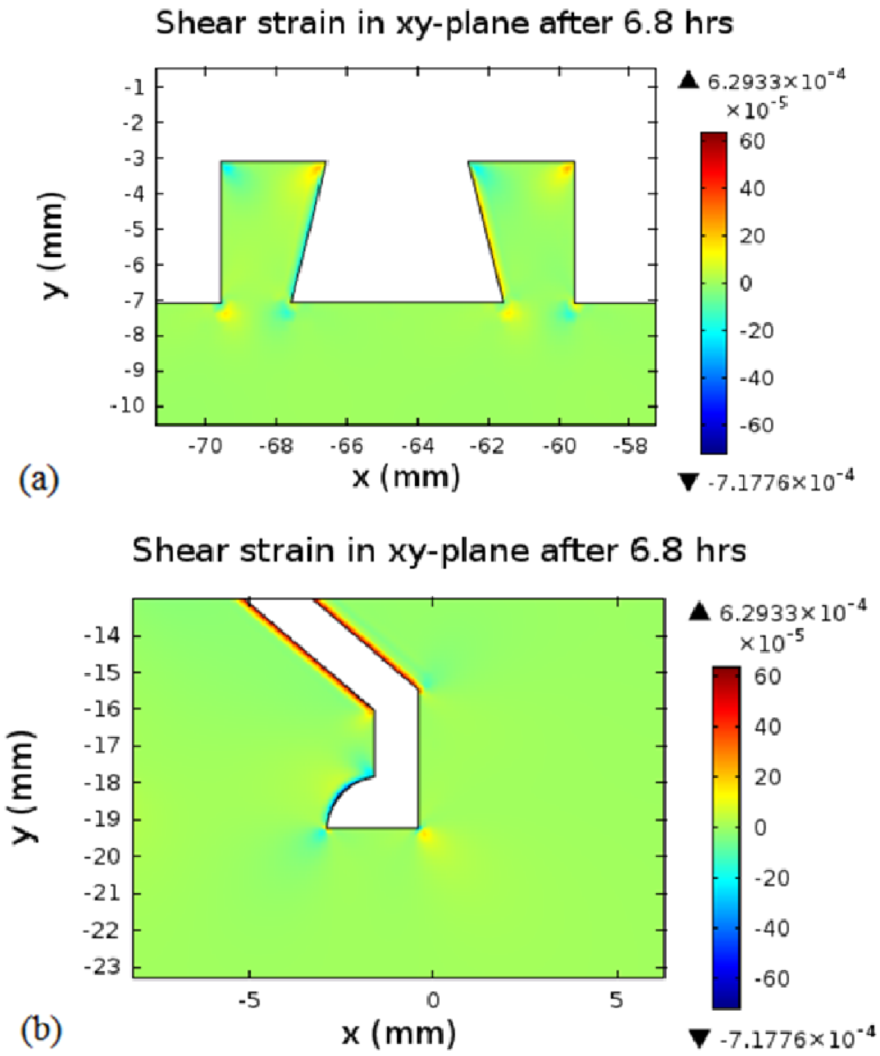

Figure 96: shear strain in XY-plane at some selected regions

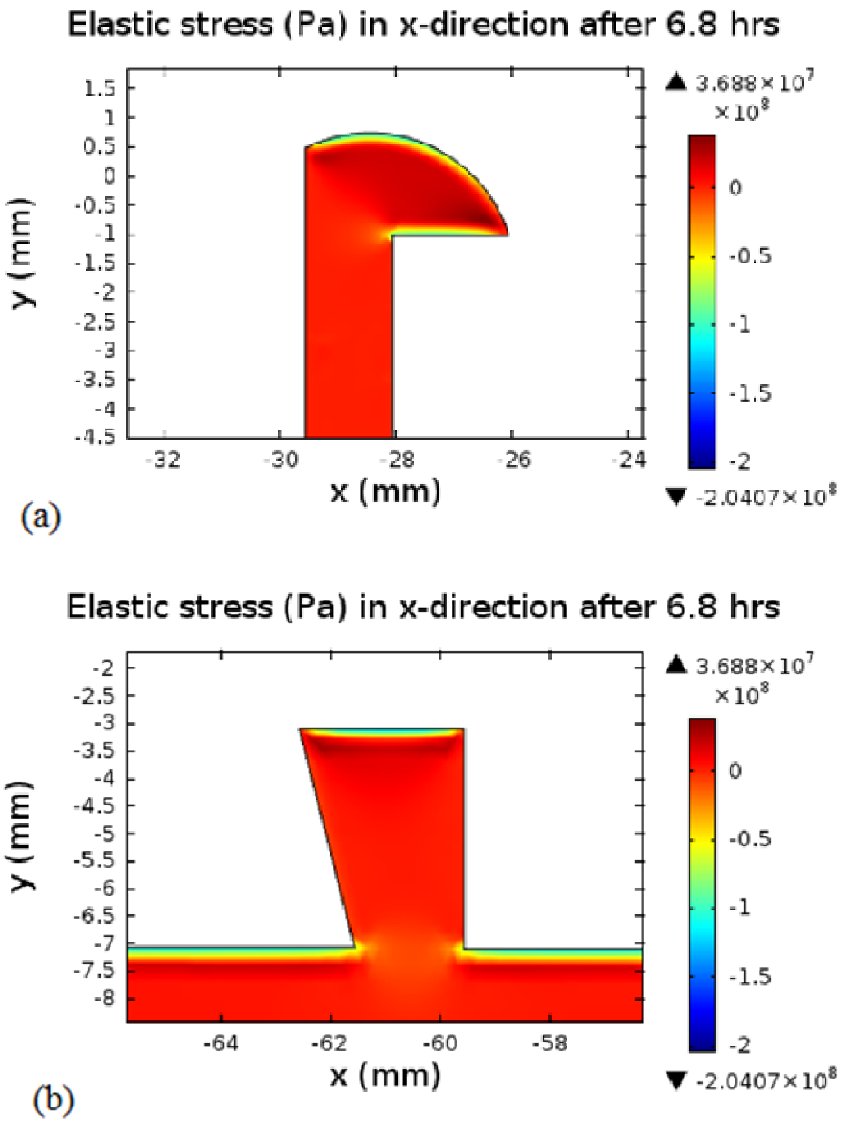

Elastic stress (Pa) in x-direction after 6.8 hrs

Elastic stress (Pa) in x-direction after 6.8 hrs

Figure 97: Elastic stress in X-direction at some selected regions-I

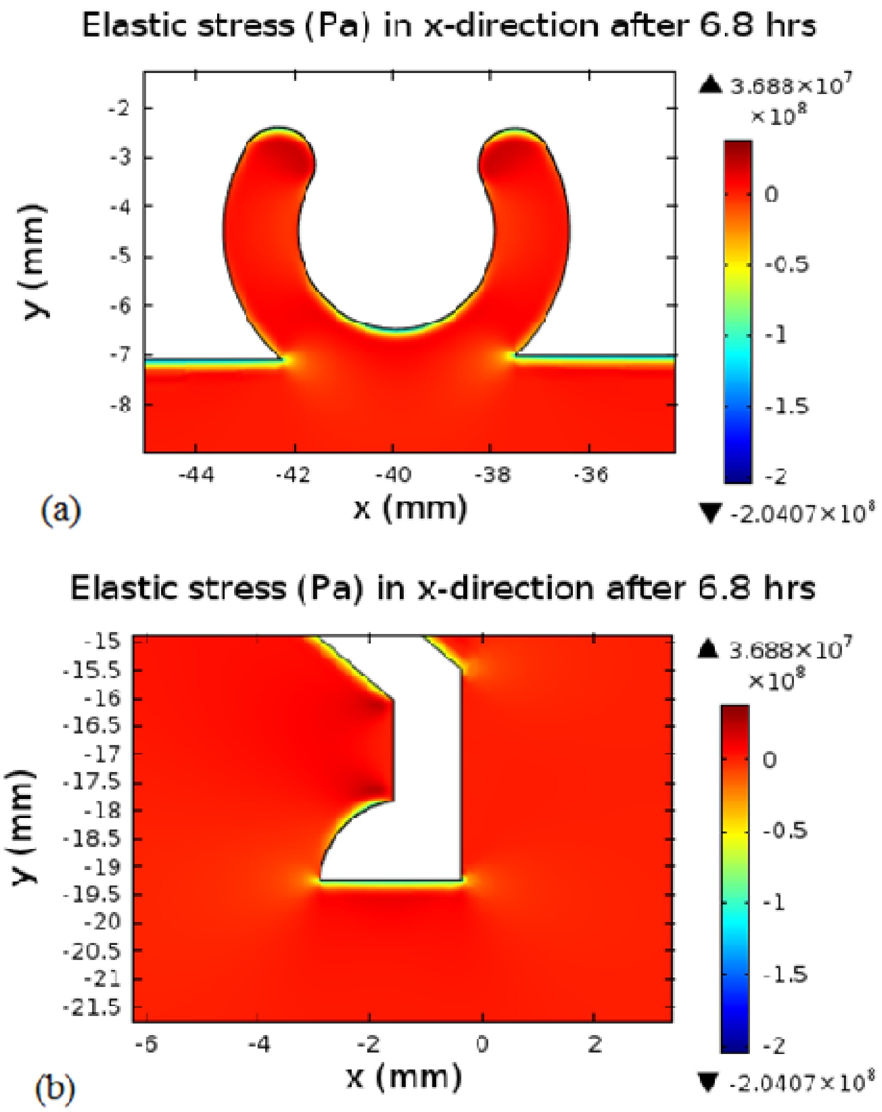
Elastic stress (Pa) in x-direction after 6.8 hrs

Elastic stress (Pa) in x-direction after 6.8 hrs

Figure 98: Elastic stress in X-direction at some selected regions-II

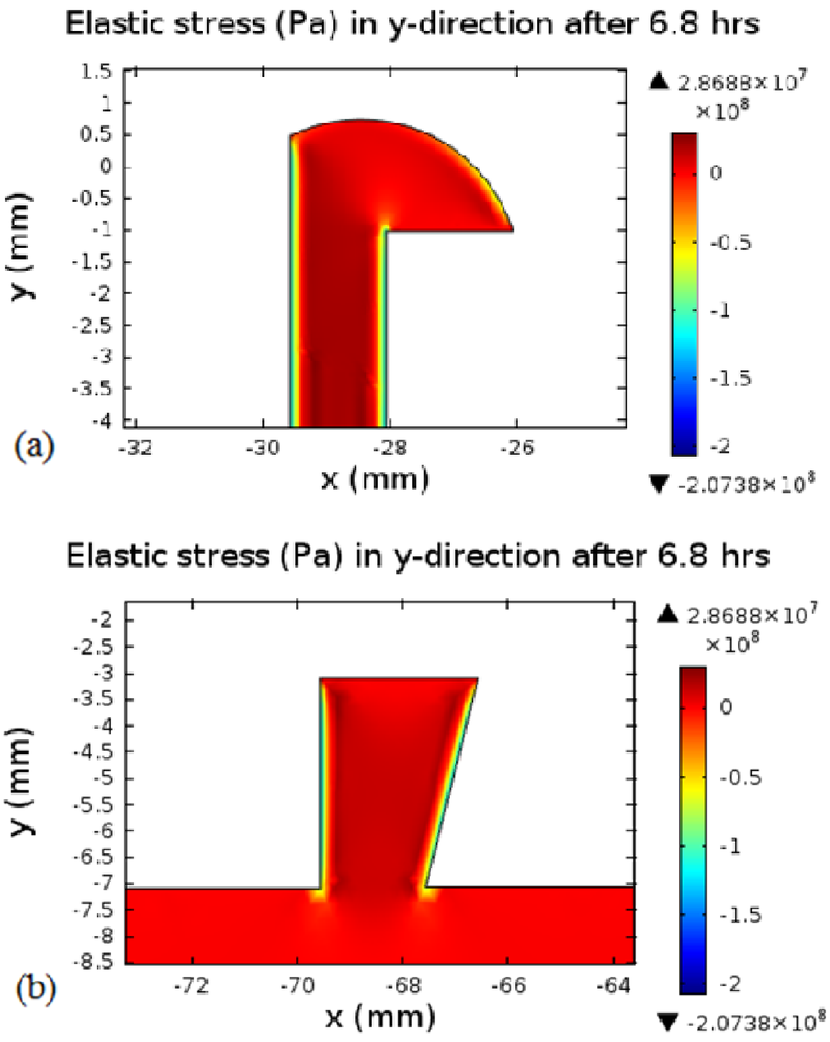

Figure 99: Elastic stress in Y-direction at some selected regions-I

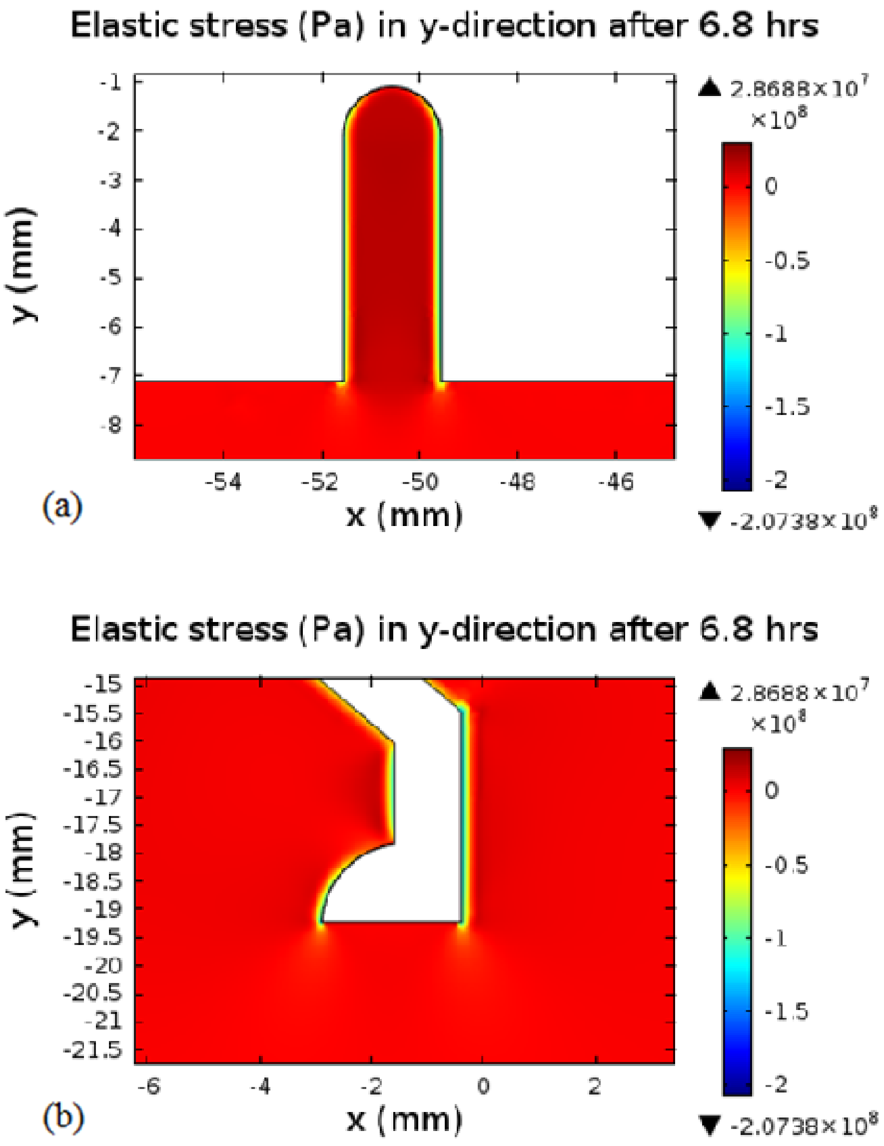

Figure 100: Elastic stress in Y-direction at some selected regions

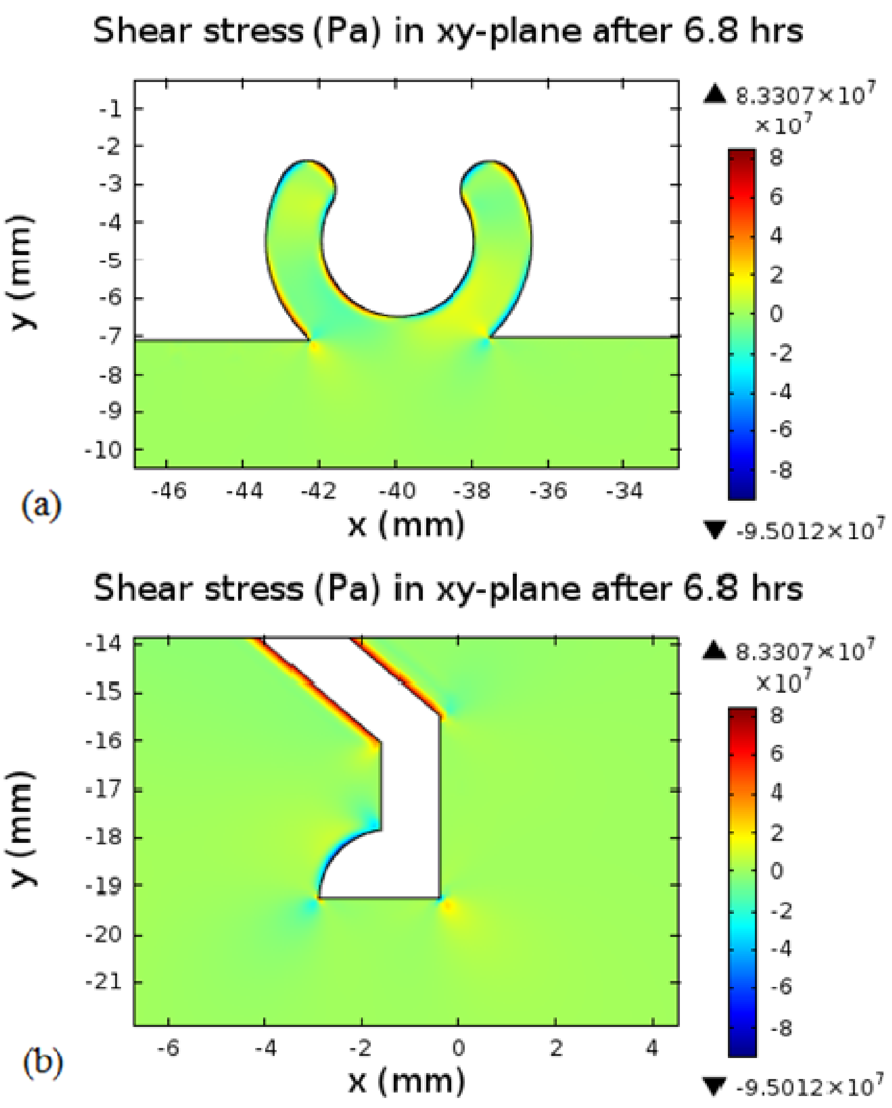

Figure 101: Shear stress in XY-plane at some selected regions-I

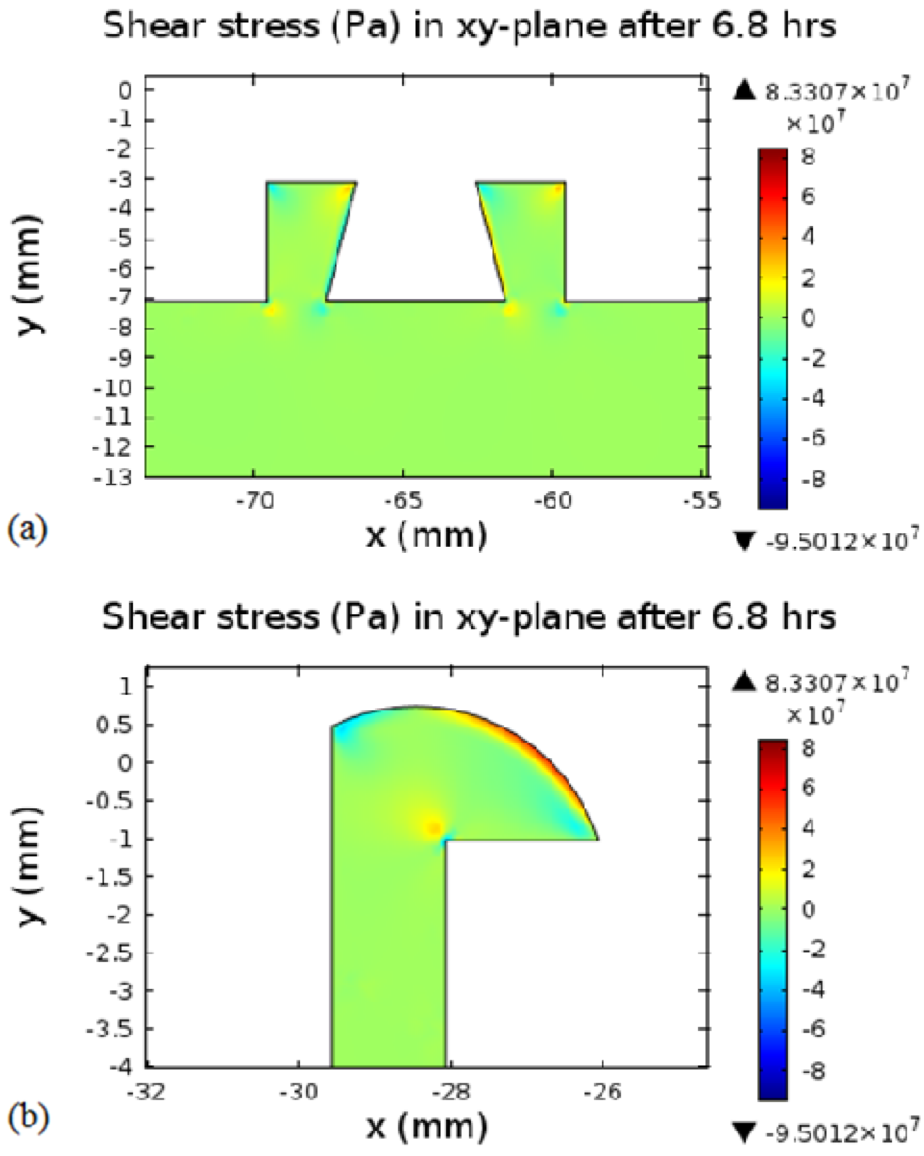

Figure 102: Shear stress in XY-plane at some selected regions-II

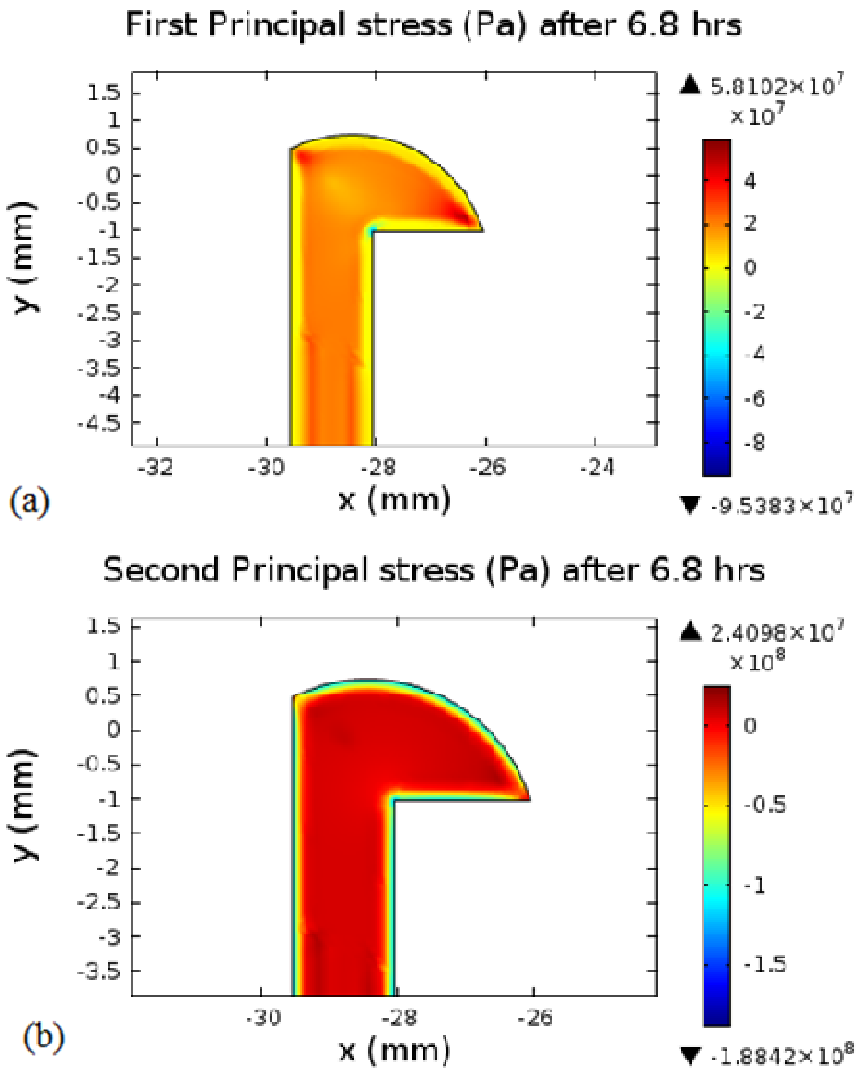

Figure 103: (a) first principal stress, and (d) second principal stress

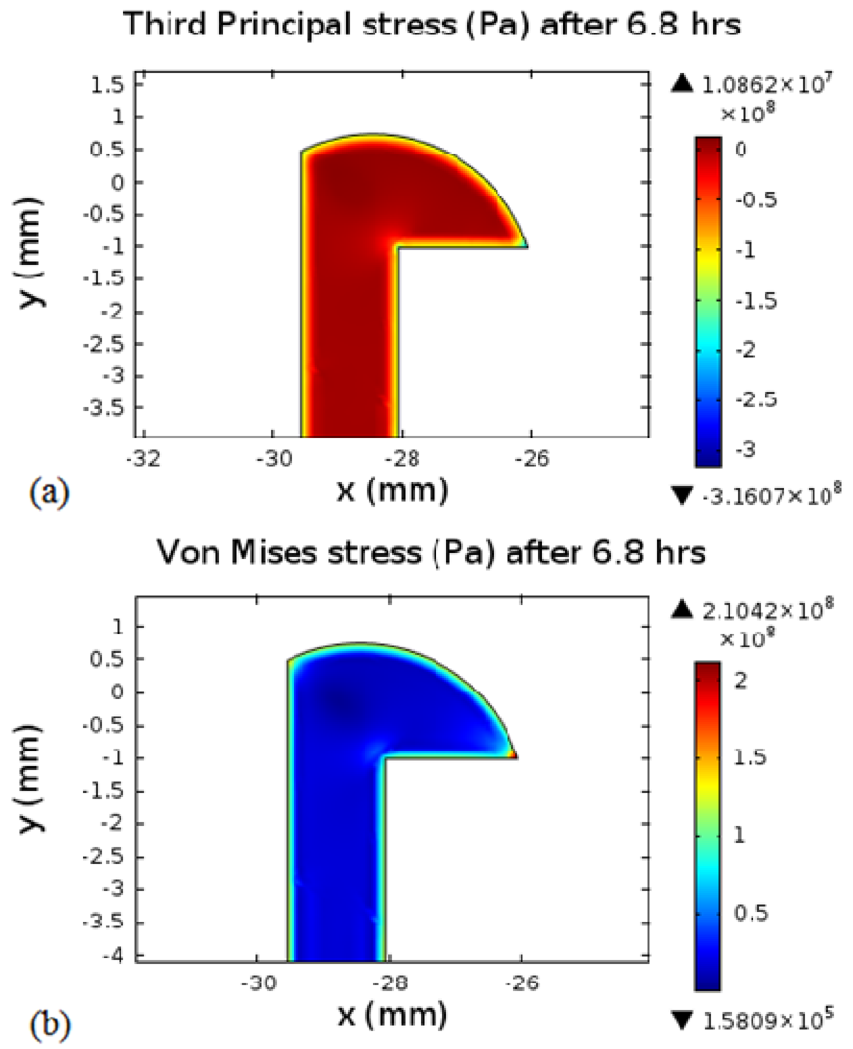

Figure 104: (a) third principal stress, and (d) von Mises stress

The coupling of the phase field method with elasticity has enabled the prediction of the residual stresses that are induced in the diffusion layer during the two-stage nitriding process in hot extrusion dies. The results indicates that, the stresses that are induced at flat or fillet regions of the sample geometry are smaller in magnitudes when compared to the stresses that are induced at the outer corner points. This is due to the balancing of the compressive surface stresses with tensile stresses from the interior at the flat regions. However, the induced stresses are not balanced at the outer corner points. This explains the reason for the frequent failure of extrusion dies at such corner points in the industry. It can also be seen that, the sharp corners and their orientations have significant effect on the case depth, surface hardness and performance of Aluminium extrusion dies. Therefore, it is suggested that sharp corner features (especially the outer corners) should be avoided if possible or be modified by incorporating a fillet of appropriate radius.

8.2 Compound layer

8.2.1 Process Kinetics

Due to the complexity associated with the convergence of the phase field equations on the actual sample geometry, only a thin slice of the sample (of dimension 20µm x 5µm) was selected for the analysis. Fig. 106 (a) shows the evolution of the phase field or order parameter with time. It can be seen that, the continuous diffusion of nitrogen atoms results in the evolution of the ε-phase. Phase field value of 1 denotes the ε-phase and 0 denotes the α-iron phase. Even though the actual nitriding cycle time (6.8 hours or 0.134838 normalized time) was used for the simulation, the transformation stops after 145 minutes or 0.05065 normalized time. This is due to the fact that the nitrogen concentration decreases to a point where the atmospheric nitrogen concentration is so low that the continuous formation of stable ε-phase is not possible. Similarly, Fig. 106 (b) shows that the concentration field follows the same trend. The jump in the concentration field for some time steps is due to the rapid increase in the atmospheric nitrogen concentration, as shown in Fig.3. However after reaching a time of low nitrogen gas concentration, the excess nitrogen concentration diffuses more into the case depth and thus moves the phase transformation forward.

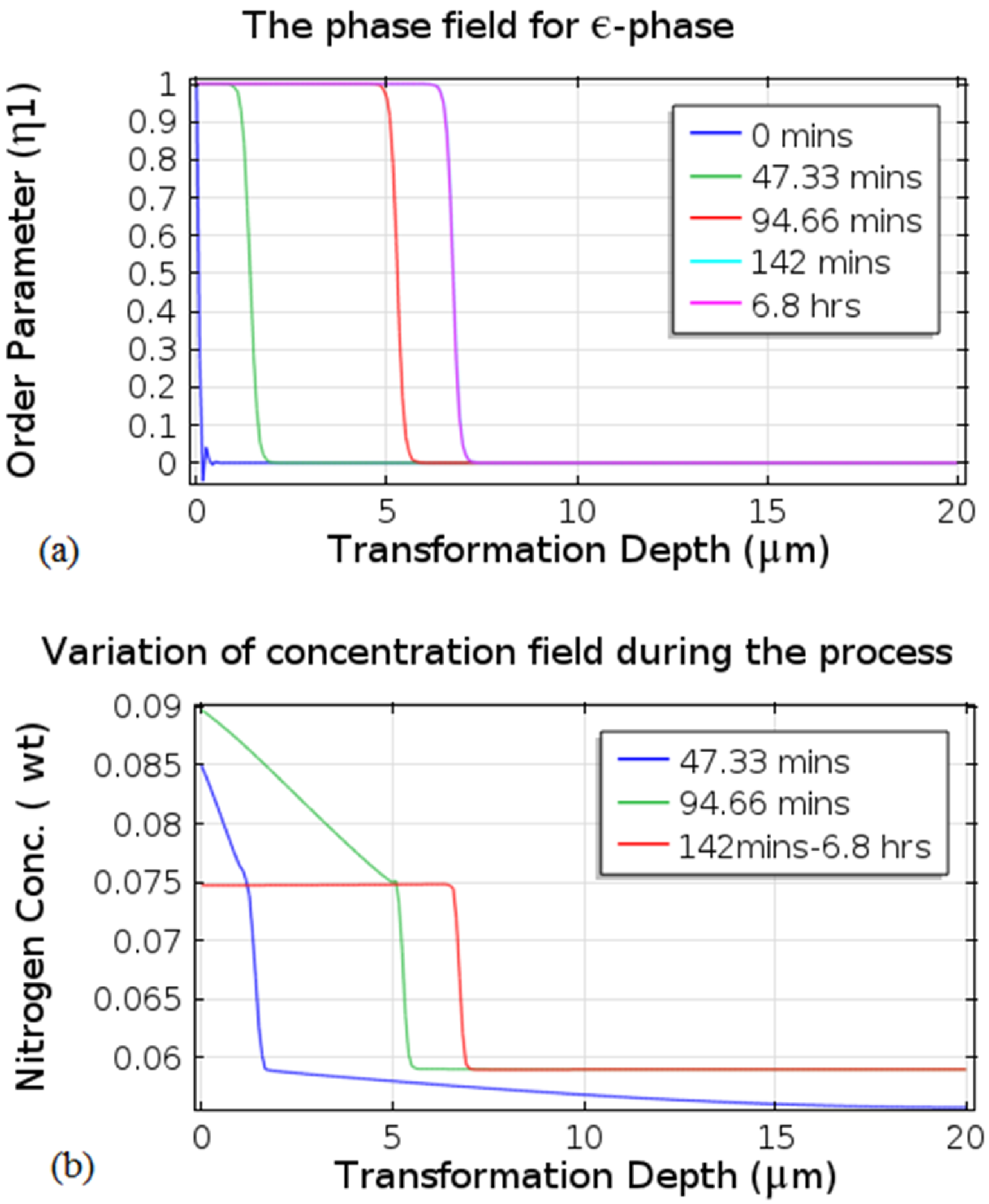

Figure 105: (a) order parameter, (b) concentration field during the process

Fig.107 shows the variation of transformation depth with time. It can be seen that, the transformation does not follow the regular parabolic growth. This is due to the continuous variation of the nitrogen concentration (or nitriding potential) in the nitrogenous atmosphere. The result shows that transformation depth of about 6.5 μm is achieved, where the transformation stops. This coincides to a previous experimental finding [**104**] that the transformation depth falls between the range of 6-8μm [**110**]. Therefore, it is interesting to see that the model has accurately predicted the experimentally observed thickness of the compound layer during the two-stage nitriding process in AISI H13 steel.

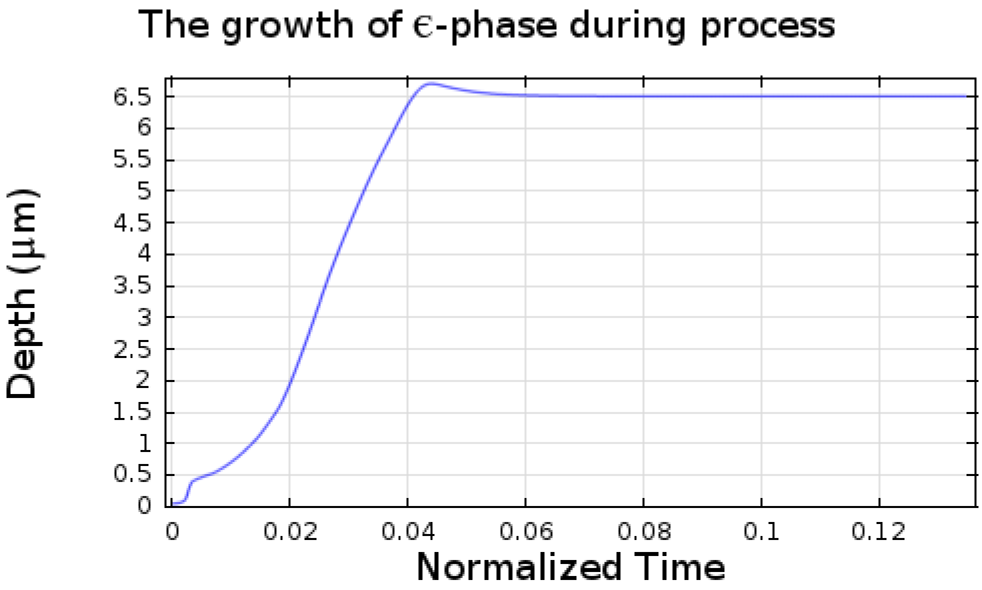

Figure 106: Growth of the ε-phase with time

Fig. 108 and 109 shows the temporal and spatial evolution of ε-phase during the process. The mixed nature of the ε-phase and α-phase across the interface can be seen clearly. Fig.110 and 111 shows the plots of the concentration field at various times of transformation. As prescribed, the transformation and diffusion of atomic nitrogen proceeds in a direction that is normal to the surface of the extrusion die. The results obtained for the order parameter and composition field are in conformity with conventional phase field model results. The slight fluctuation of nitrogen concentration before the start of the transformation comes from the definition of interpolation function for the controlled nitrogen gas concentration.

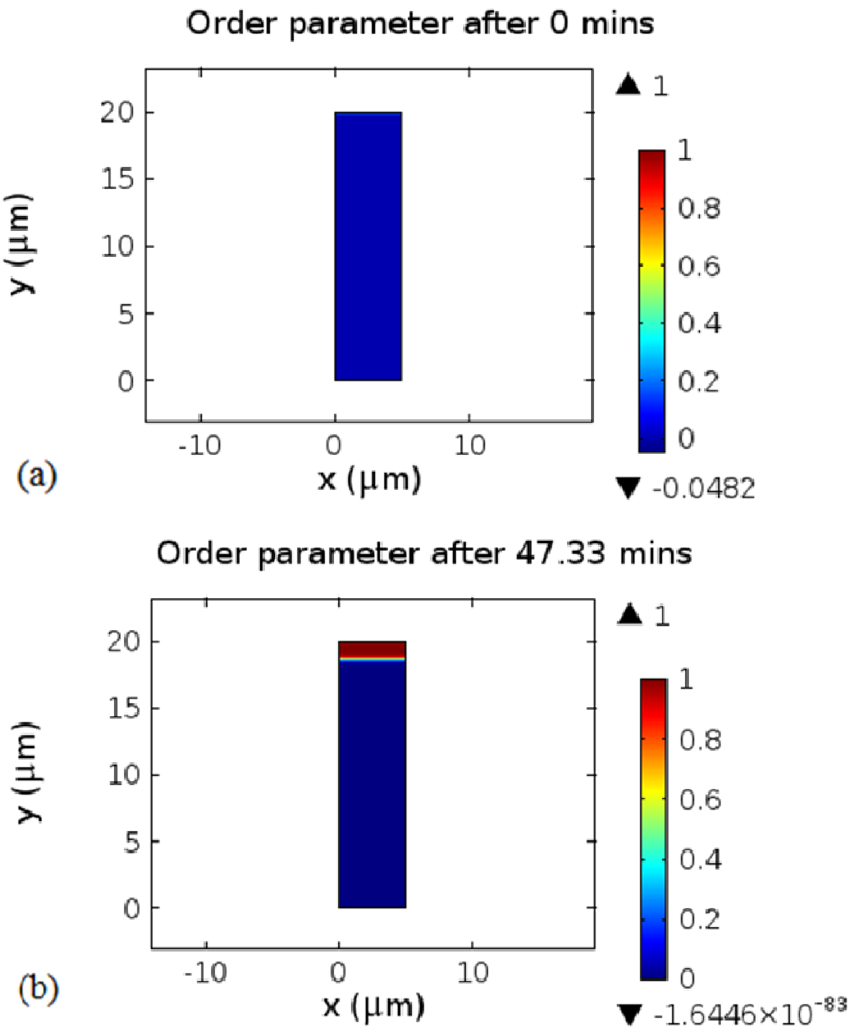

Figure 107: Evolution of the phase field after (a) 0 mins, (b) 47.33 mins

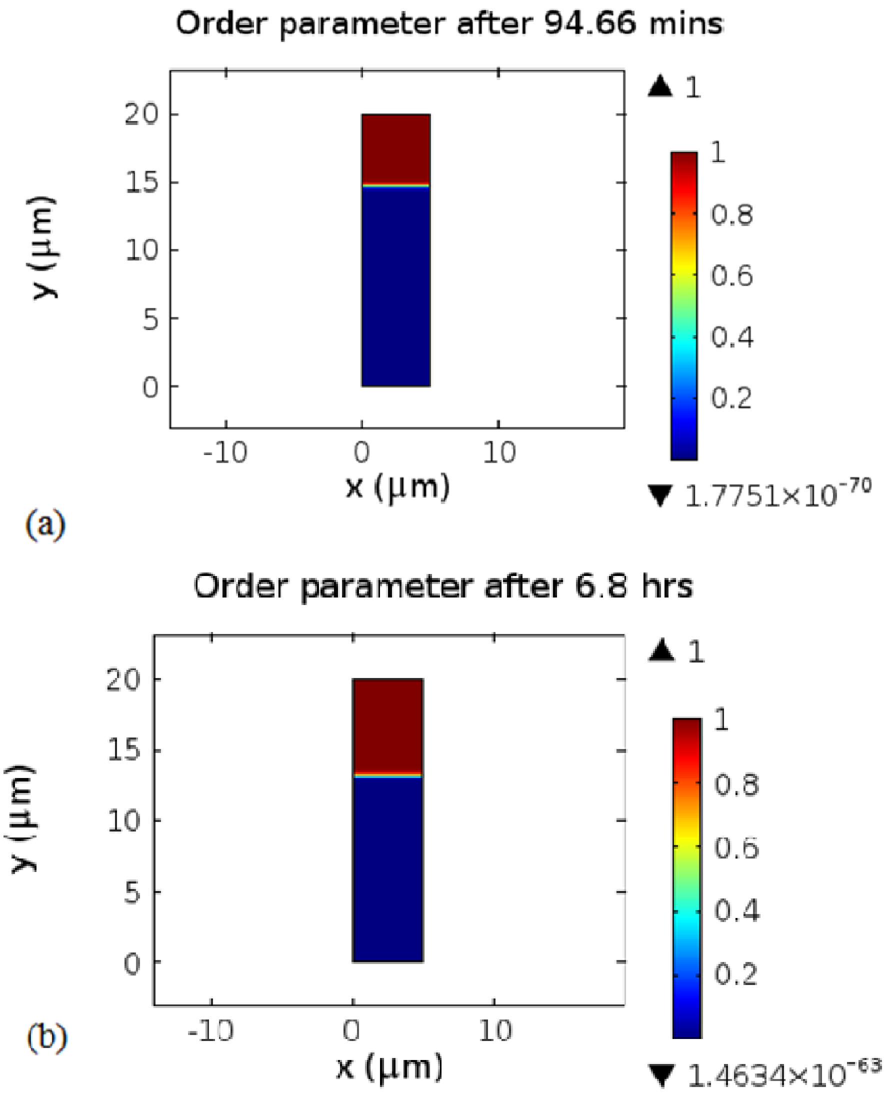

Figure 108: Evolution of the phase field after (a) 94.66 mins, (b) 6.8 hrs

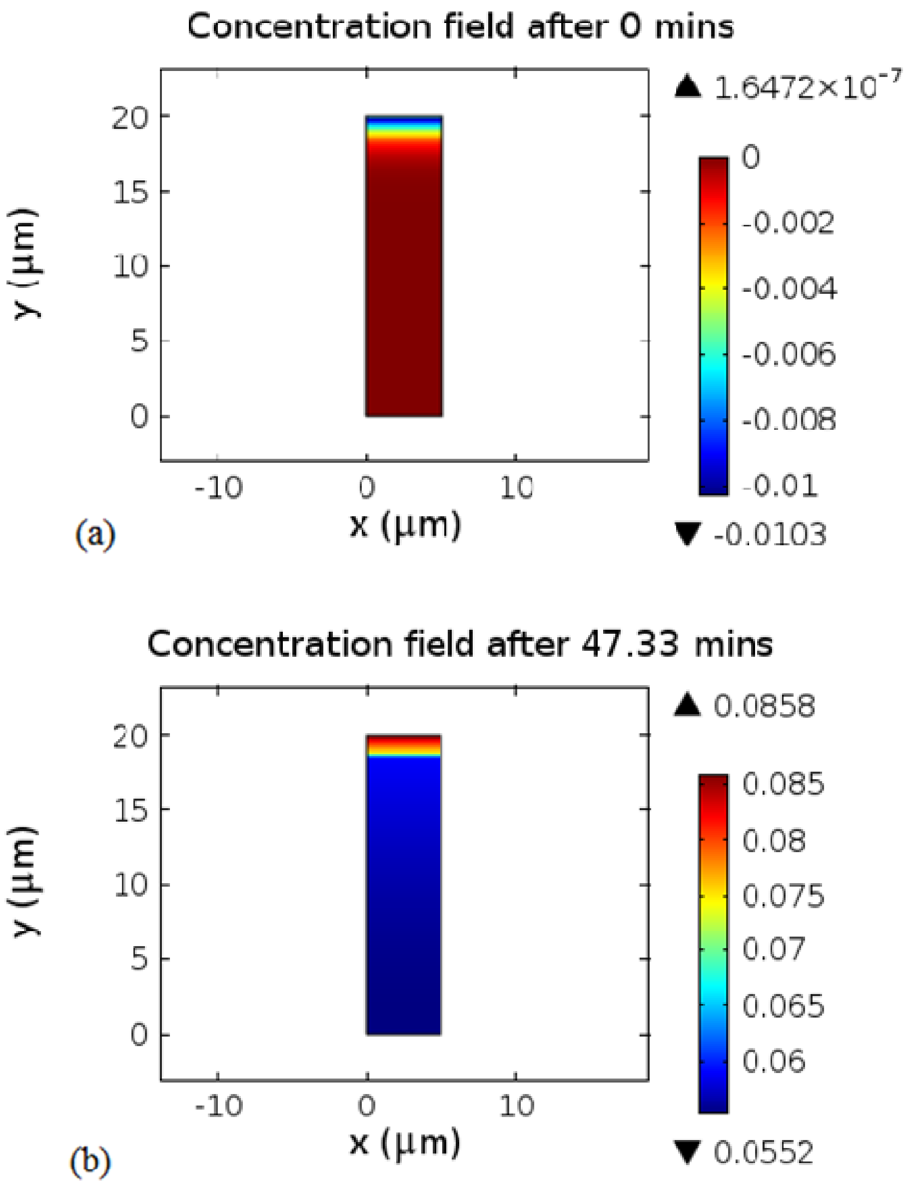

Figure 109: Evolution of the concentration field after (a) 0 mins, (b) 47.33 mins

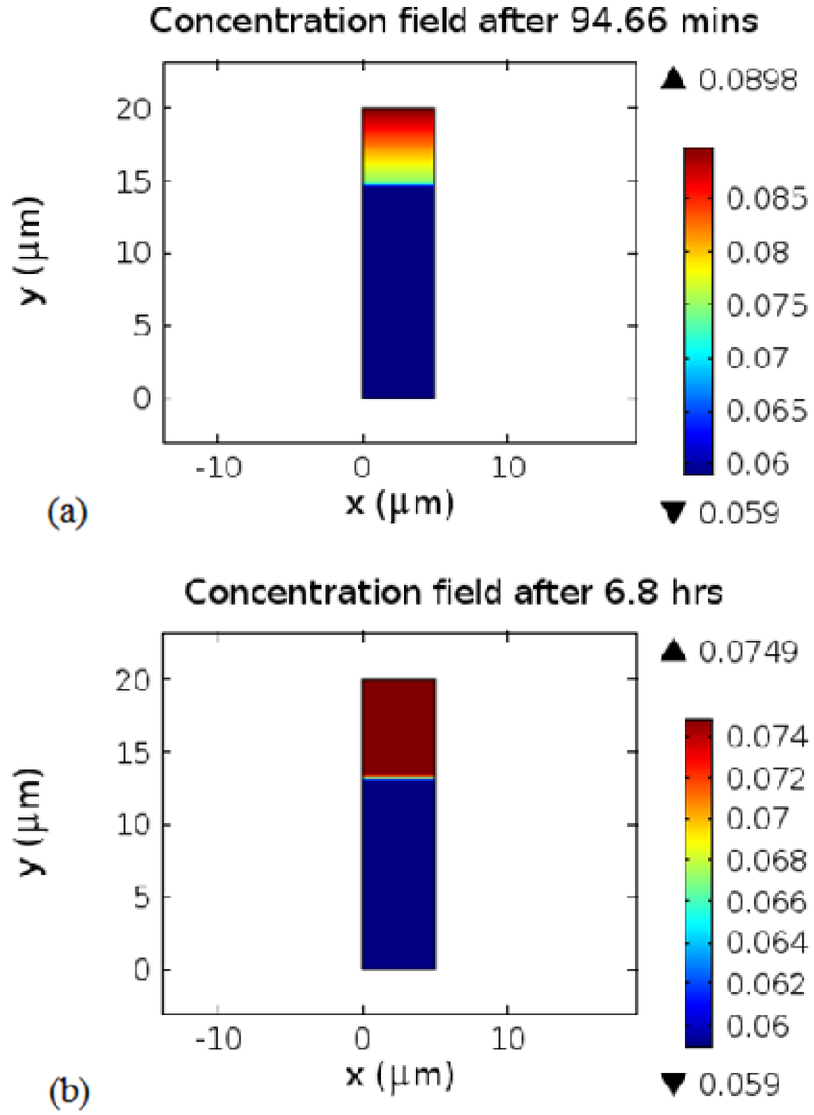

Figure 110: Evolution of the concentration field after (a) 94.66 mins, (b) 6.8 hrs

8.2.2 Residual Stresses

Fig. 112 shows the displacement fields in the X and Y-directions after the transformation stops. It is observed that, the displacement in Y-direction is positive at all points and higher than the displacement in X-direction. This is because the surface of the steel is load-free and the displacement in the X-direction is constrained by the periodic boundaries. Furthermore, Fig.113 shows the variation of the surface displacements with process time. It can be seen that vertical displacement in the Y-direction fluctuates slightly during the process due to the fluctuation of the controlled nitrogen concentration during the process.

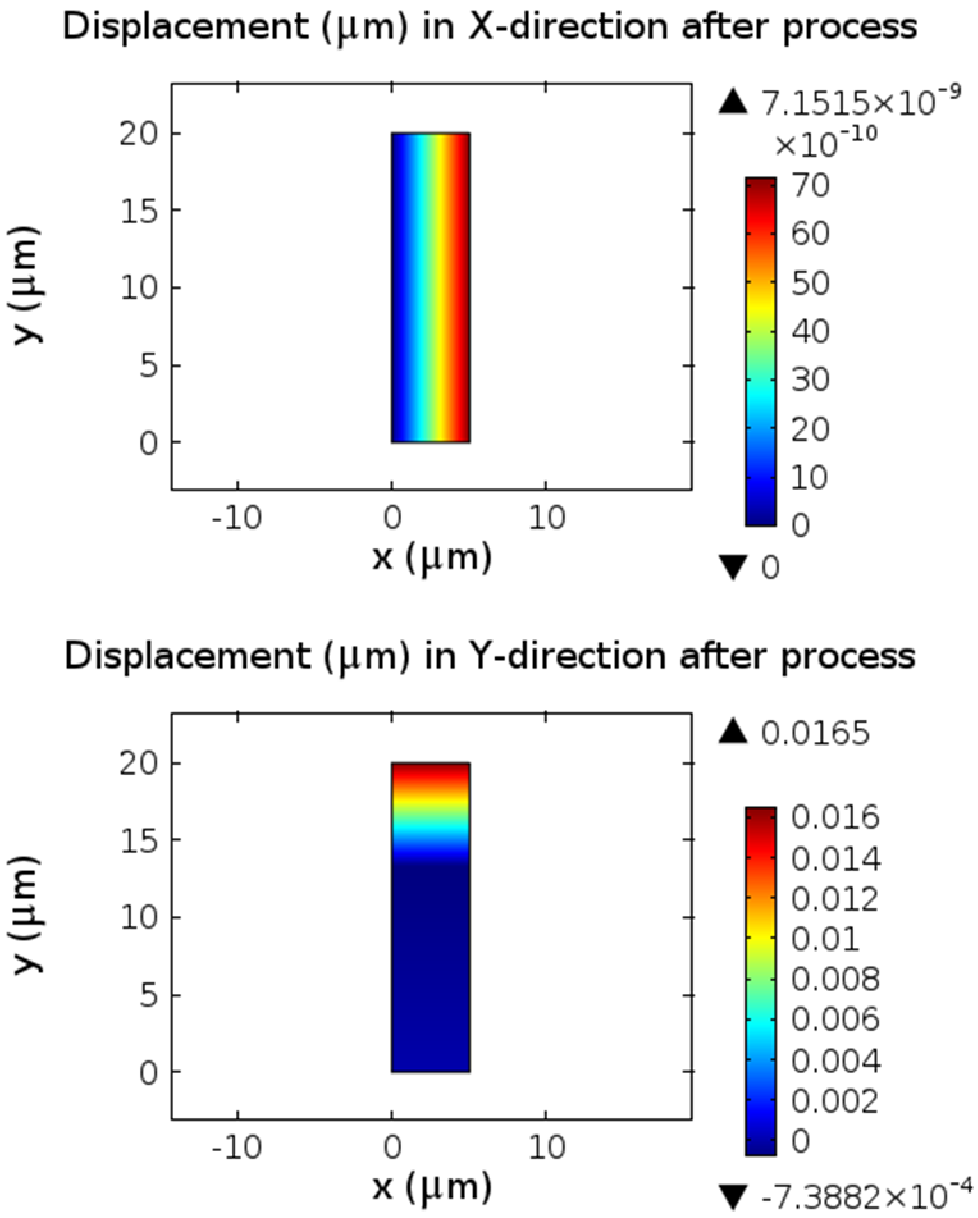

Figure 111: Displacement fields in (a) X-direction, (b) Y-direction

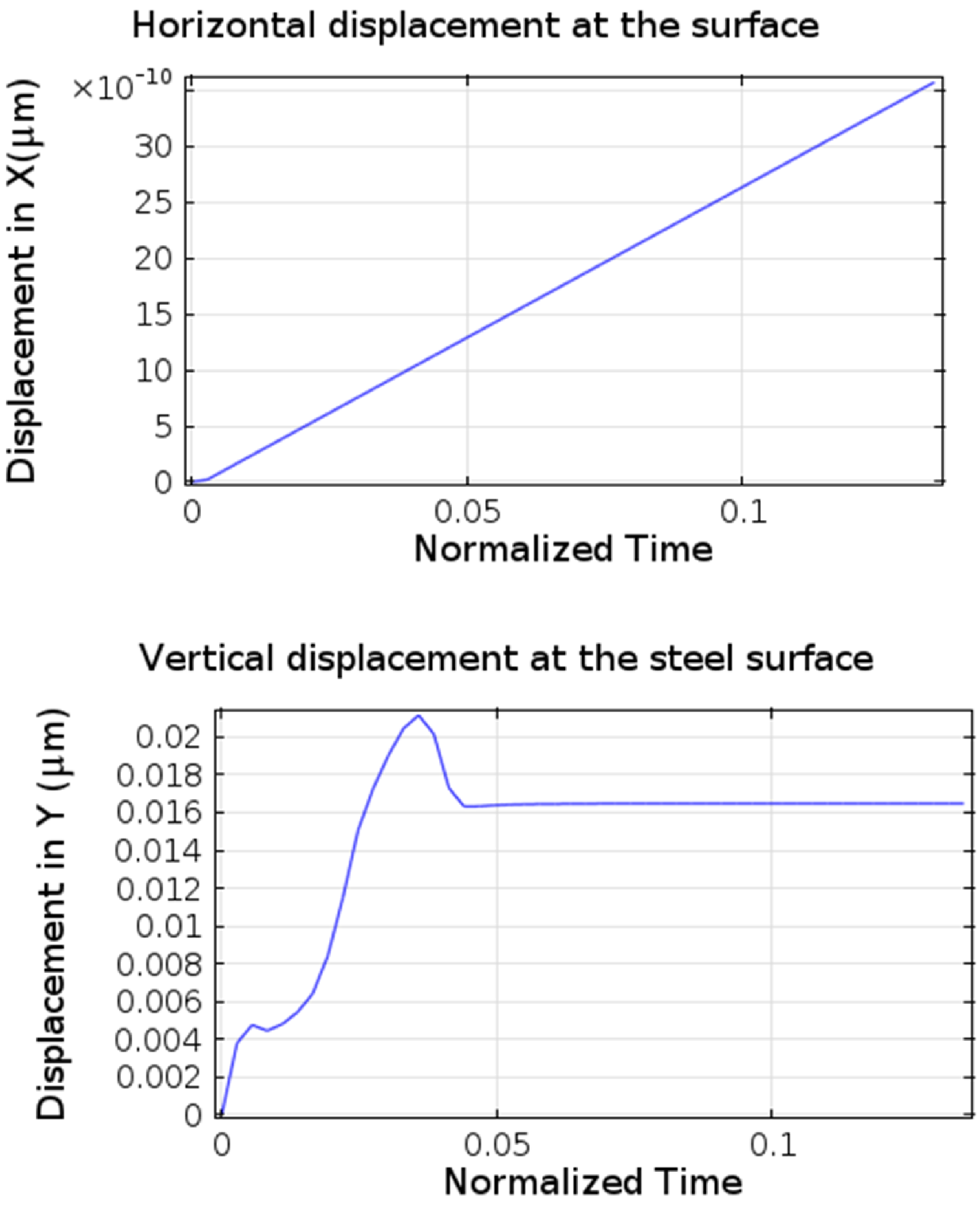

Figure 112: Variation of surface displacements with time

From the displacement fields, the compositional-mismatch strains in X and Y-directions were computed as shown in Fig.114. It can be seen that, the ε-phase experiences an expansion or tensile elastic strain in the Y-direction due to the stress-free nature of the die surface. On the other hand, the ε-phase experiences compression in the X-direction because of the periodic boundary conditions that were applied at both the left and right boundaries of the RVE. Similarly, the α-iron experiences contraction or compressive elastic strains in the Y-direction. This can be explain be the fact that, the Vegard's constants for the ε-phase is higher than those of the α-iron. Therefore, the ε-phase causes compression on the α-iron by expanding more. On the contrary, the α-iron experiences tensile elastic strain in the X-direction, because even though the expansion of the α-iron in the X-direction is less the periodic boundary condition has constrained all the nodes at the left and right boundaries of the RVE to move together.

The induced shear strain (shown in Fig. 115) in the XY-plane is found to be very close to zero, because the compositional strains are mainly dilational in nature. Furthermore, Fig. 116 shows the total strain, which is the sum of the elastic and compositional strain. It can be seen that, the total strain in the Y-direction is larger than the total strain in the X-direction due to the free nature of the surface as well as the periodicity of the RVE in the X-direction.

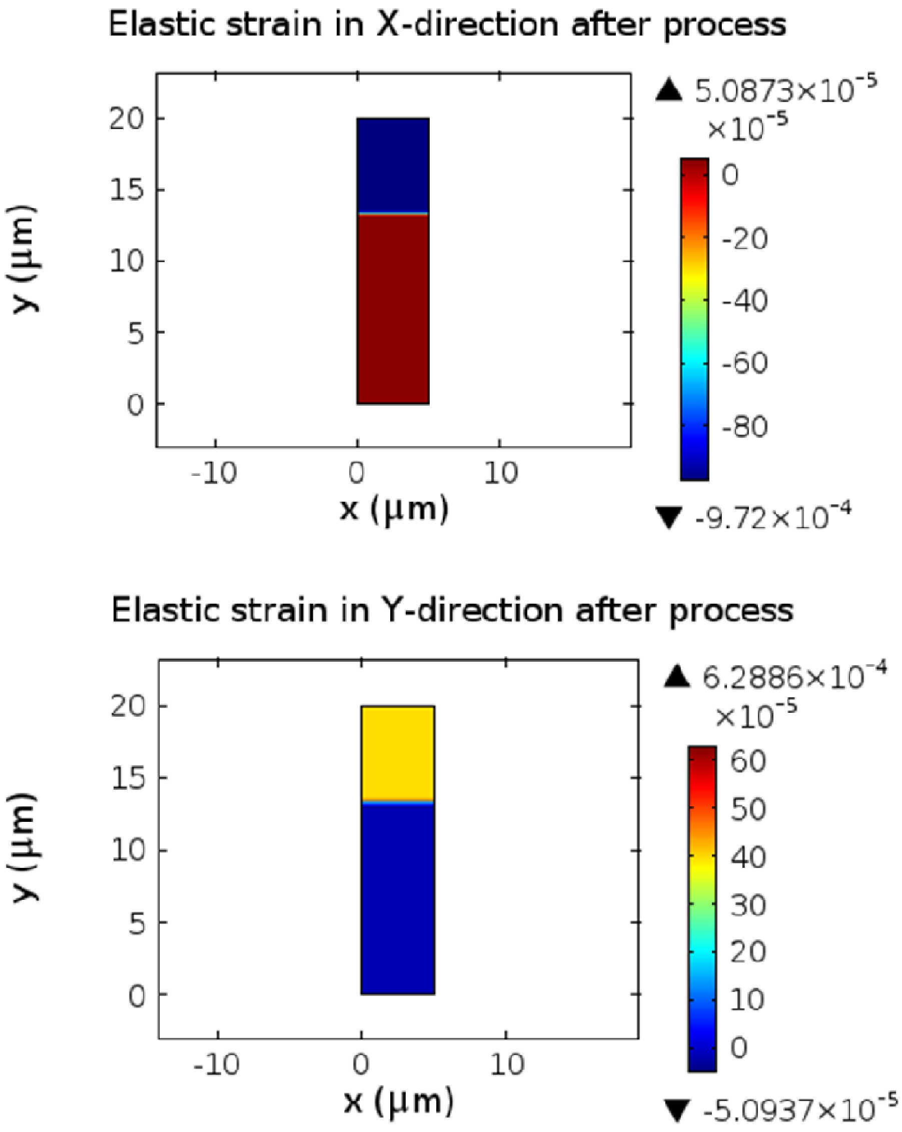

Figure 113: Induced elastic strains in (a) X-direction, (b) Y-direction

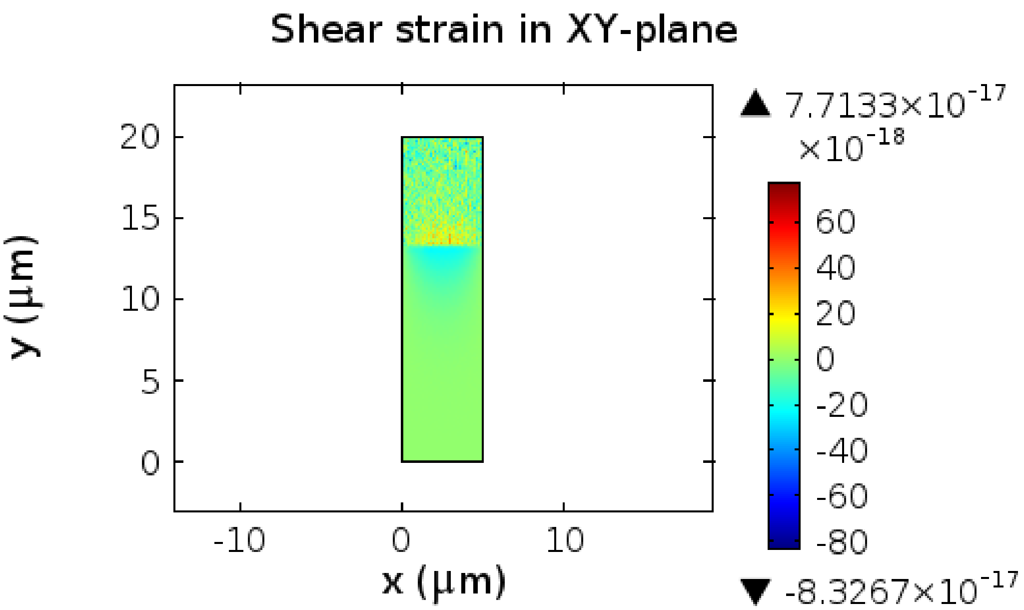

Figure 114: Induced shear strain

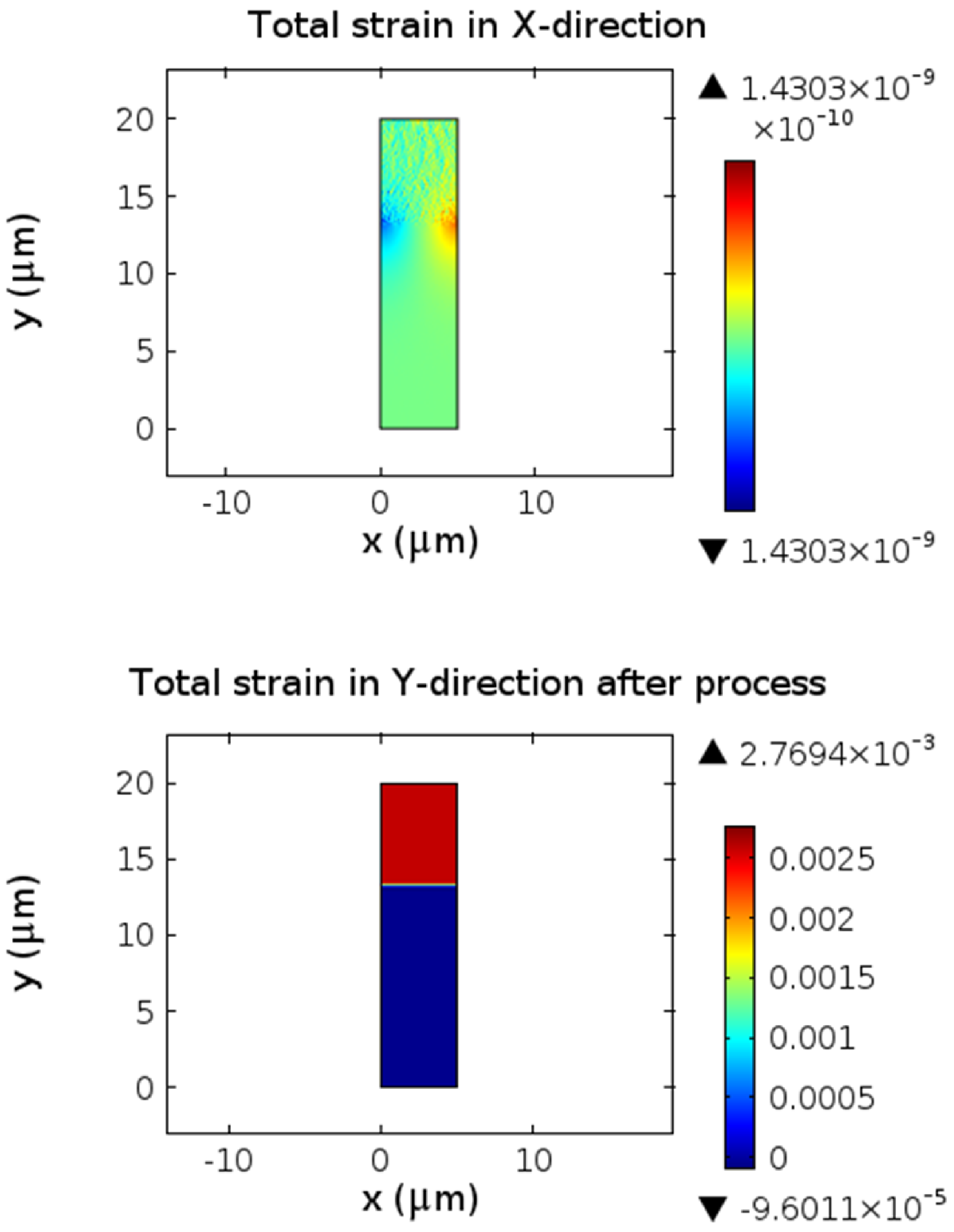

Figure 115: Total strains in (a) X-direction, (b) Y-direction

From the compositional-mismatch strains, the induced elastic (diffusive or residual) stresses are calculated. It can be seen that, higher stresses are developed in the ε-phase in both the X and Y-directions (shown in Fig.117). This is due to the fact that, the compositional lattice expansion in the ε-phase is not only anisotropic but also higher than that of the α-iron. A high stress of about 600 MPa and 300 MPa (tensile) is developed in the Y-directions and X-directions respectively. The higher stress in the X-direction is due to the periodicity of the domain along that direction. The induced residual stresses (of about 16 MPa in both X and Y-direction) in the α-iron are lower in magnitude due to the fact that the compositional lattice expansion of α-iron is far less than that of the ε-phase. Moreover, the stresses are expected to be higher at the sharp corners because the formation of compound layer will be more at such points. Fig. 118(a) shows the residual stresses that are induced in the Z-direction, where the stress has gone as high as about 750 MPa.

The plot of the induced shear stress (given in Fig. 118(b)) confirms the fact that, shear strain is not induced during the process. This is because the compositional strain tensor is purely dilational, and all shear components are conventionally taken as zero. But it is expected that shear stresses will be induced at the sharp corners of the extrusion die. Since there is no induced shear stress and the stress tensor components are tensile, the principal stresses are also expected to be purely tensile in the ε-phase. Thus, the principal stresses are not shown in the current work as there is no need. Also, the von Mises stress magnitude is expected to be uniform in the ε-phase and around 600 MPa. However, it is not shown in the current work as the stresses in the X, Y and Z-directions are more important. The variation of the induced residual stresses at the steel surface during the process is also shown in Fig.118. The fluctuation of the surface stresses is caused by the continuous variation of nitrogen concentration in the controlled nitrogenous atmosphere.

Previously, an experimental measurement[**117**] of the residual stresses showed that the overall residual stress (i.e. the sum of compositional stress, thermal stress and other possible stresses) in the compound layer is tensile at the surface, zero at some point in the middle and compressive at the interface. Also, the current results fall within the range of the previous experimentally measured residual stresses as discussed in chapter 6. The deviation of the simulation results with the experiments is due to the fact that only the compositionally-induced stresses are taken care of in the current work. Thus with the current result, the combined stress state (the summation of thermal and transformation stress) of compound layer may conform to the experimental findings since the thermal stresses have been previously determined to be compressive in nature[**117**].

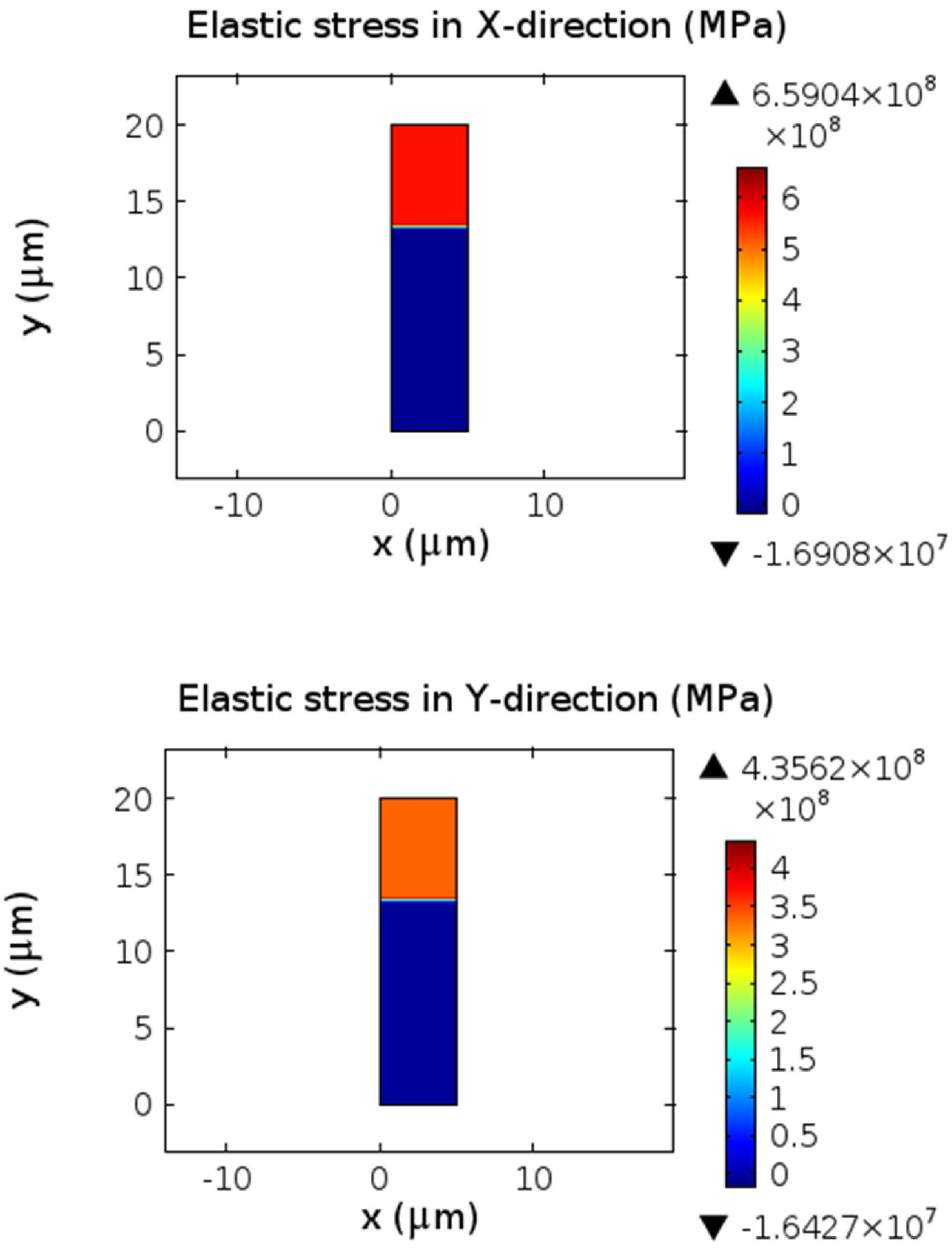

Figure 116: Induced elastic stresses in (a) X-direction, (b) Y-direction

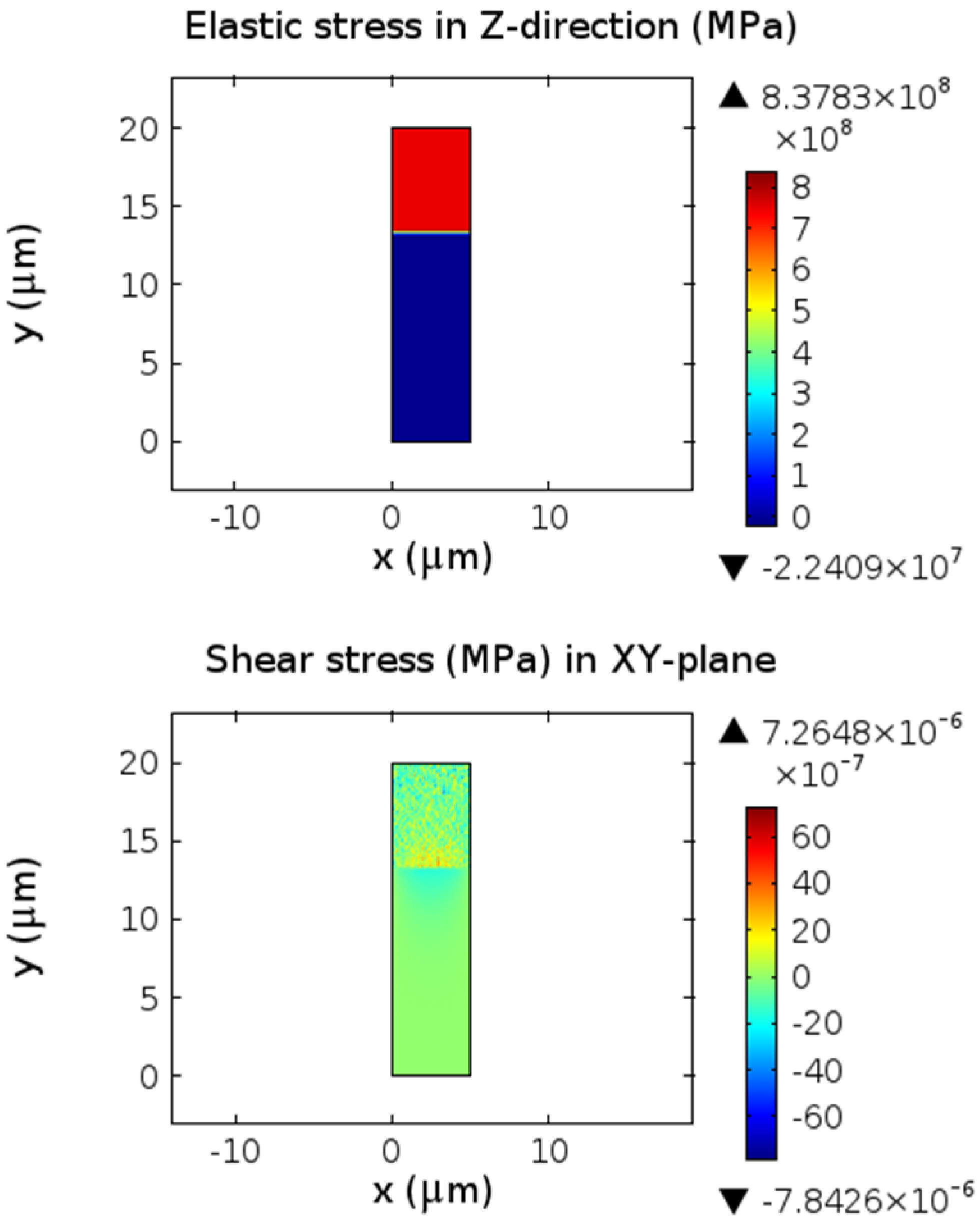

Figure 117: (a) Induced elastic stress in Z diection, (b) Induced shear stress

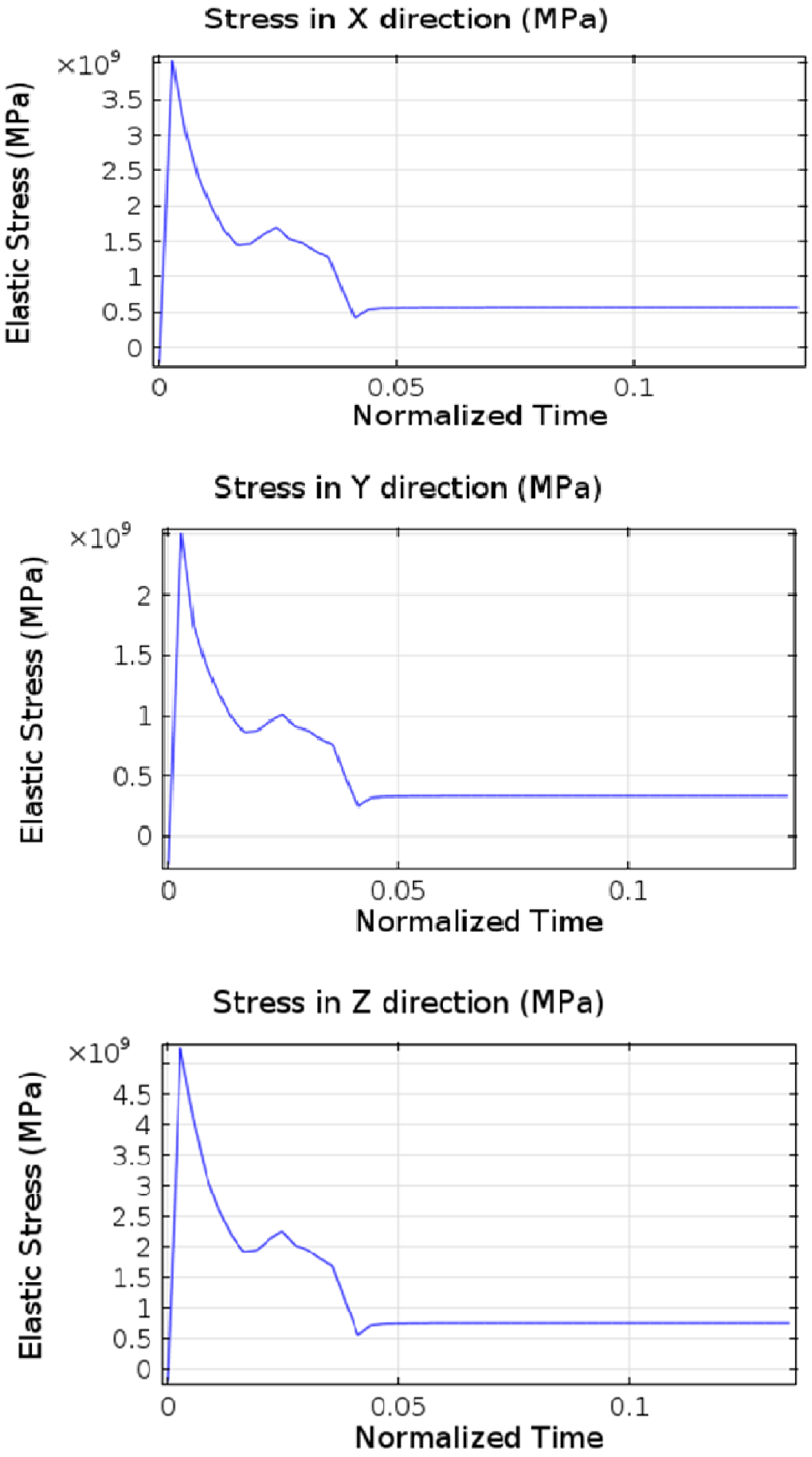

Figure 118: Variation of stress in (a) X-direction, (b) Y-direction, (c) Z-direction with time

8.2.3 Evolution of the compound layer at a corner in the die cavity

Even though the convergence of the governing PDEs is difficult to be achieved on complex geometries, an attempt was done to predict the evolution of the compound layer at the corner points. Fig.119 shows the evolution of the compound layer at the ROC point of the die sample. It can be seen that, the evolution of the compound layer at the corner point is more due to the simultaneous diffusion of nitrogen from the converging points. This also conforms to a previous experimental observation that is shown in Fig.40, chapter 6.

Moreover, the induced stresses in the X, Y and Z-directions are shown in Fig. 120, 121 and 122. As expected, the residual stresses are higher at the corner points, which lead to the frequent failure of extrusion dies at such points. Fig.120 shows that very high compressive and tensile stresses of about 8 GPa and -6.8GPa are induced at the ROC point in the X-direction. Similarly, Fig. 121 and 122 show that very high compressive and tensile stresses are induced at the corner points. By comparing the induced stresses magnitude at the ROC point with those at the flat regions, it can be seen there is a large difference in the magnitudes. Therefore, we have every reason to believe that the high magnitude of the residual stresses at the outer corner points are the main cause of the die failure as frequently observed in the industries.

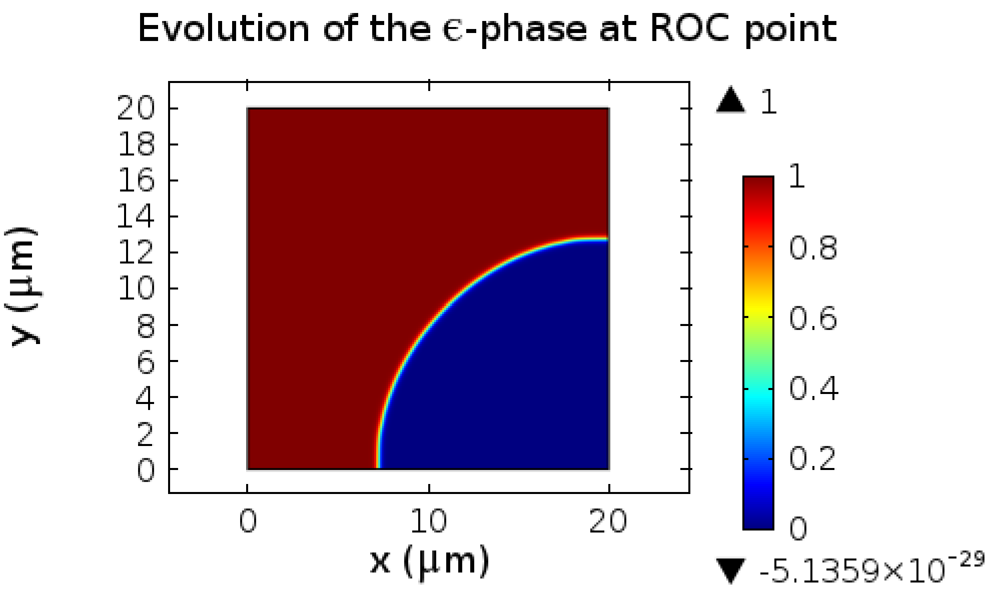

Figure 119: Compound layer at corner point

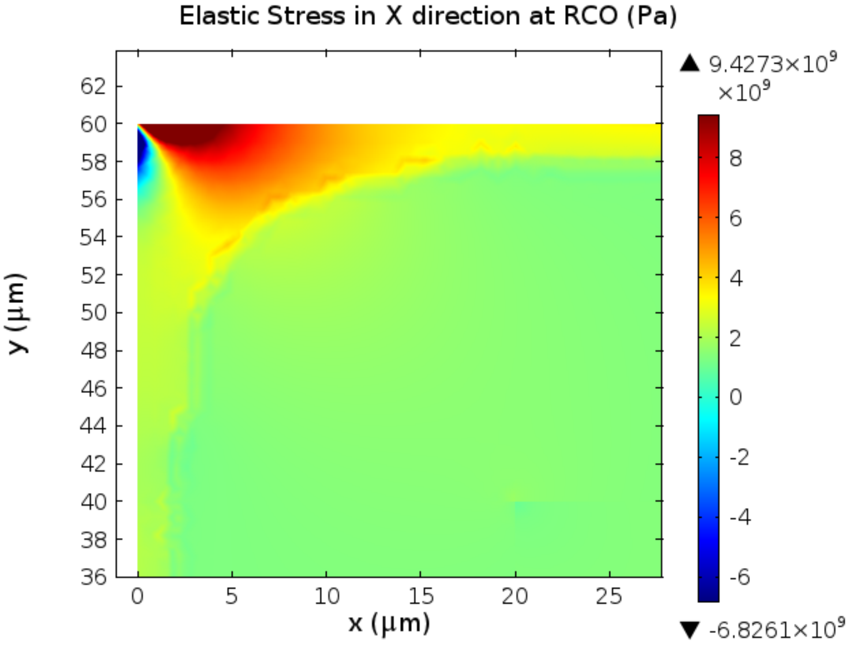

Figure 120: Elastic stress in the X-direction at corner point

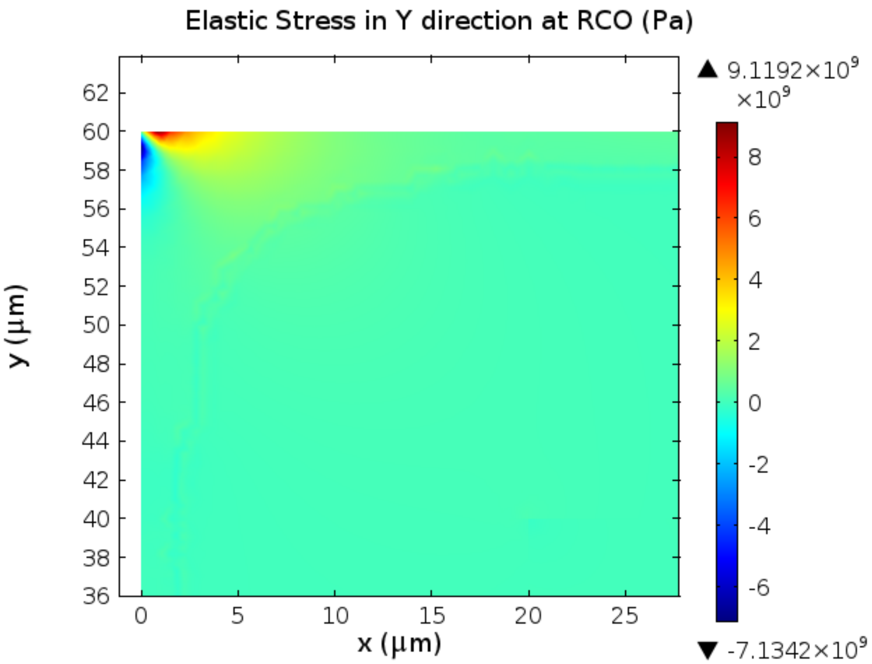

Figure 121: Elastic stress in the Y-direction at corner point

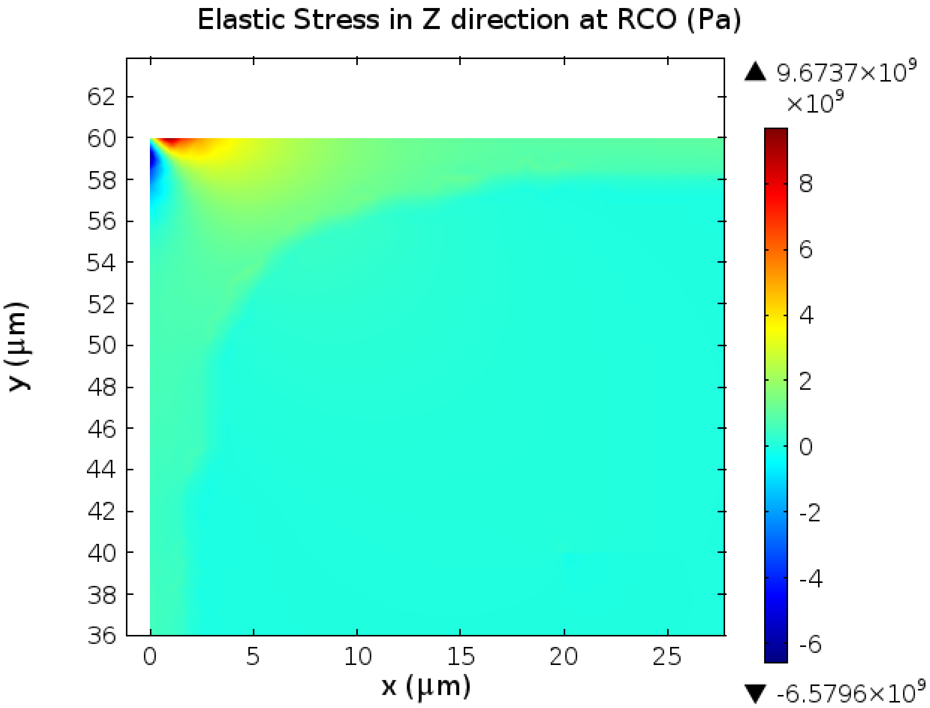

Figure 122: Elastic stress in the Z-direction at corner point

8.3 Conclusion

Gas nitriding is among surface treatment process that is used for AISI H13 tool steels. However, due to the presence of complex and sharp features in the die cavities, it has been observed that non-uniform nitride layers develops. Moreover, the formation of compound layer in the surface vicinity of nitrided surface is also observed. This leads to the development of transformation stresses at sharp and uneven features of the die cavities and the compound layer. It is important to note that eventhough the applied pressure on the die cavities is uniform, the non-uniform nitride layers as well as the compositional residual stresses causes the outer corner regions of the die to be more stressed than other other regions. Eventually, this lead to the premature failure of the die.

In the current work, the phase field method is used to model the kinetics of the two-stage gas nitriding process in AISI H13 tool steel, a material commonly used for Aluminum extrusion dies. The model is coupled with elasticity and the associated residual stresses are predicted. The model gives results that compare well with previous experiments. Both experimental and numerical results are found in close agreement in terms of nitrogen concentration and transformation depth for the diffusion and compound layers. The results show that residual stresses that develop due to the formation of the diffusion and compound layer are higher at the sharp corners where the failure of extrusion dies is frequently observed.

CHAPTER 9

CONCLUSION & RECOMMENDATIONS

9.1 Conclusion

A general numerical approach for transformation-induced failures in materials has been developed. The model was developed by formulating a set of governing PDEs for phase transformation that is coupled with elasticity. The transformation equations were formulated according to non-equilbrium and irreversible thermodynamic principle based on theories developed by Cahn-Hilliard[**5**] and Allen-Cahn[**6**]. The Kachaturyan microelasticity theory[**45**] enabled the coupling of the phase transformations directly with elasticity at the mesoscale. The coupling between the governing equations was done in such a way that phase transformations have effect on the elastic deformation of the material, and vice versa. The numerical implementation of the governing PDEs was done based on the finite element method.

The model was applied to two practical scenarios, the V_2O_5 hot corrosion of TBCs and gas nitriding of Aluminum hot extrusion dies. The model has been found to be reliable in predicting both the process kinetics as well as the transformation-induced stresses in the materials. The results show that, the phase transformations cause the development of high stresses that lead to the failure of the materials during operations. The current phase field model is unique in the sense that, it is able to predict phase transformations that are induced by the diffusion of chemical species from the external environment. Moreover, it couples the phase transformation with elastic interaction. The current work is the first application of the phase field method to a practical corrosion process. Despite with the complicated (or automated) nature of the two-stage gas nitriding process, the model was successfully used in predicting both the process kinetics and the associated residual stresses. Thus, the model can be used as a general tool for analyzing transformation-induced failures in materials.

9.2 Recommendations

The following are the recommendations for future work:

1. Further experimental investigation of V_2O_5 hot corrosion of TBC should be carried out. Most of the previous experiments were limited to microscopic observations. However, there is need for in depth experimental investigation of the complete corrosion kinetics in TBCs. This may lead to tremendous improvement in the design and performance of new materials for turbine blade in the world energy companies. It will also reduce the cost associated with the frequent failure of turbine blades in Saudi Arabian energy companies.
2. For simplicity, the materials used in the present study are assumed to be Isotropic, with averaged (poly-crystal) elastic stiffness constants. Even though that assumption is valid for the selected RVEs considered in the current work, the model can be improved further by assuming the materials to be anisotropic. In that case, single-crystal elastic stiffness constants will be used for the analysis, and the result will be more accurate. However, the computational intensity for the solution of the governing PDEs will be very high.

3. One basic assumption that was used in developing the current model is that the transformation occurs in a two phase system. But mostly the microstructure of materials contains more than two phases. Therefore, the model should be improved in order to take care of at least three coexisting phase transformations. This will help in incorporating the evolution of the yttrium vanadate during the hot corrosion of TBC. The growth of the yttrium vanadate is expected result in higher stresses in the system as demonstrated previously by Akhtar et al. [**3**]. The three-phase system will also be useful in predicting the kinetics as well as the transformation-induced stresses due to the formation of both ε-phase and γ^1-phase in the compound layer of gas nitrided tool steels.
4. As mentioned previously, most of the input parameters are determined using the CALPHAD approach. Even though the approach is widely used in determining properties of materials, it will be better if experimental methods for the determination of such input parameters are devised. This will not only develop the phase field method further, but also help in obtaining parameters that are not obtainable in the thermodynamic databases.
5. Thermal stresses should be incorporated into the model so it can tackle transformations that involve phases of different coefficient of thermal expansions. With such model, more realistic values for induced-residual stresses during the gas nitriding of tool steels would be obtained. However, the model will be far complex than the current one because of the temperature dependence of the input parameters.

6. Based on the present results, it is suggested that the metal forming industries modify the design of extrusion dies by incorporating fillet at sharp outer corners.

9.3 Further possibilities with the model

The basic numerical approach developed in the present study can be extended further to other practical applications. The capability of the model can also be enhanced further so the model can handle various complex scenarios. Some of the possibilities are discussed as follows.

9.3.1 Porous material study

The top coat of TBCs contains a certain percentage of porosity. The closed pores play a very significant role in the TBC system. They result in desirable properties such as lower thermal conductivity, lower elastic modulus, higher toughness, and high affinity for oxygen in TBCs. Similarly, the compound layer that forms during the gas nitriding of tool steels is found to contain certain amount of porosity [**117**]. It was reported that, the closed pores in the compound layer reduce the magnitude of the induced residual stresses by relaxation.

However, the closed pores are not included in the current analysis. This is due to the very high computational intensity that is required for the solution of the governing PDEs on a porous geometry. Therefore, it is recommended that future researchers use the current model in further investigating the effect of the transformations on the porous top coat or compound layer. Consequently, hidden information related to the failure of such materials may be obtained which may result in overall improvement in the design of the materials. In order to demonstrate that the current model can be applied to porous materials, trial simulations were carried out as shown in Fig.123 and 124.

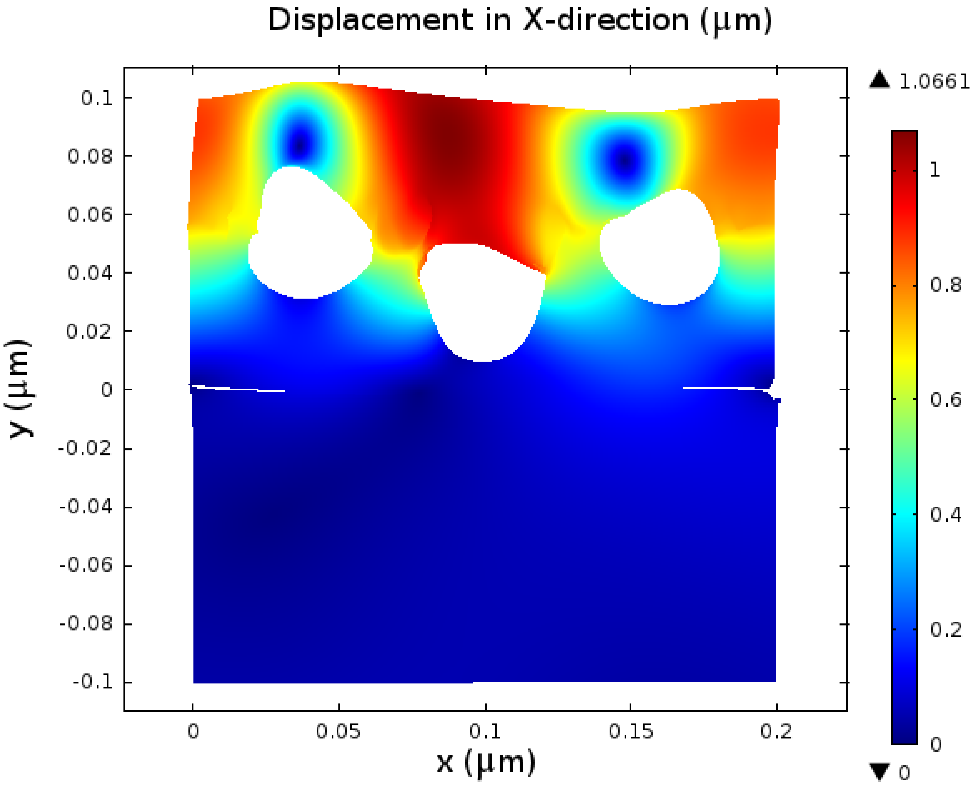

Figure 123: Transformation in porous top coat

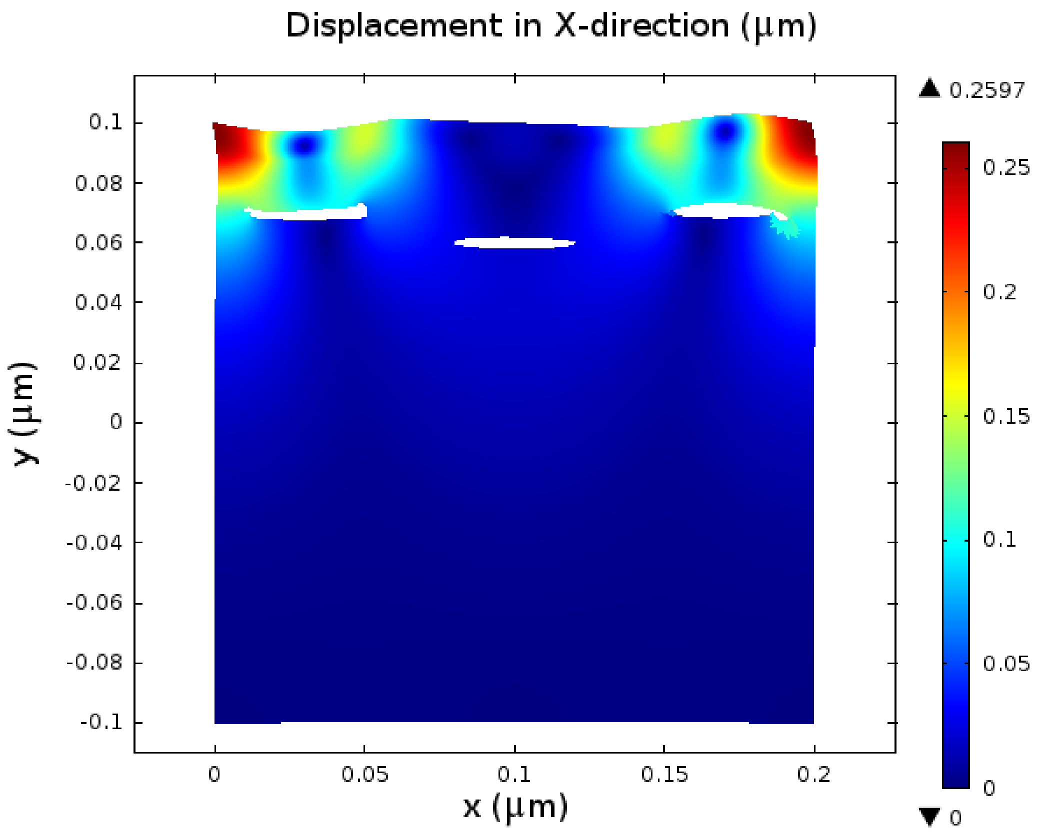

Figure 124: Transformation in porous top coat

9.3.2 Coupling with damage model

The model should be coupled with fracture mechanics in order to investigate further the effect of the induced-stresses on the failure of the materials. Such task can be achieved by sequential coupling of the current model with a damage model.

As shown in Appendix A, the phase field method has been successfully applied to evolution of damage parameters in materials. Therefore, defining another phase variable (or damage parameter) based on the Allen-Cahn theory [**6**] can be used in predicting the evolution of the damaged materials. However, this means that the number and complexity of the governing PDEs will increase.

Alternatively, the easiest way to predict the damage behavior of the materials using the current approach is to sequentially couple the current model with standard damage models, like Cohesive Zone or Johnson Cock's model. Therefore, future research should be directed towards the prediction of the damage in materials that fail due to phase transformations.

9.3.3 Computational Homogenization

Another possibility is also the use of the model in multi-scale simulation of the entire material behavior during the phase transformations. Due to high computational intensity and numerical instability, the current analysis was carried out based on RVEs. Even though most research works on materials rely on RVEs, improvement of the current model to full-scale simulation will be very great. It will bring out more information with regards to the macroscopic effect of the transformations on the materials.

REFERENCES

Bibliography

[1] Ramachandra C., Lee K.N., and Tewari S.N., "Durability of TBCs with a Surface Environmental Barrier Layer Under Thermal Cycling in Air and in Molten Salt," *Surf. Coat. Technol.*, vol. 172, pp. 150–7, 2003.

[2] Raghavan S. and Mayo M.J., "The Hot Corrosion Resistance of 20 mol% YTaO4 Stabilized Tetragonal Zirconia and 14 mol% Ta2O5 Stabilized Orthorhombic Zirconia for Thermal Barrier Coating Applications," *Surf. Coat. Technol.*, vol. 160, pp. 187–96, 2002.

[3] Akhtar S.S., Arif A.F.M., and Gasem Z., "Stress Field in the Top Coat of TBC due to the formation of YVO4-A Numerical Study," in *International conference on Surface Modification technologies*, France.

[4] Marple B.R., Voyer J., Moreau C., and Nagy D.R., "Corrosion of Thermal Barrier Coatings by Vanadium and Sulfur Compounds," *Mater. High Temp.*, vol. 17, no. 3, pp. 397–412, 2000.

[5] Cahn J.W. and Hilliard J.E, "Free energy of a non-uniform system. I. Interfacial free energy," *J. Chem. Phys*, vol. 28, no. 258, 1958.

[6] Allen S.M. and Cahn J.W., "A Microscopic Theory for Anti-phase Boundary Motion and Its Application to Anti-phase Domain Coarsening," *Acta. Mat.*, vol. 27, pp. 1085–1095.

[7] Wen Y., Chen L., and Hawk J.A., "Phase-field modeling of corrosion kinetics under dual-oxidants," *Modeling Simul. Mater. Sci. Eng.*, vol. 20, no. 035013, p. 12, 2012.

[8] Zhu WZ., *Ceram Int*, vol. 22, no. 389, 1996.

[9] Suresh A., Mayo M.J., and Porter W.D., *J Mater Res*, vol. 18, no. 2912, 2003.

[10] Navruz N., *Phys Metal Metallogr*, vol. 105, no. 580, 2008.

[11] Kelly P.M. and FrancisRose L., *Prog Mater Sci* , vol. 47, no. 463, 2002.

[12] Moelans N., Blanpain B., and Wollants P., "An introduction to phase-field modeling of microstructure evolution," *Computer Coupling of Phase Diagrams and Thermochemistry* , vol. 32, pp. 268–294, 2008.

[13] Kobayashi R., "Modeling and numerical simulations of dendritic crystal growth," *Physica D* , vol. 63, pp. 410–423, 1993.

[14] Moelans N., "Phase-field simulations of grain growth in materials," PhD Dissertation 90-5682-706-5, May 2006.

[15] Raabe D. and Aachen, *Computatioanal Material Science: The Simulation of Material Microstructures and Properties*, 1st ed. Pittsburg, PA, USA: Willey VCH, 1998.

[16] Miehe C., Hofacker M., and Welschinger F., "A phase field model for rate-independent crack propagation: Robust algorithmic implementation based on operator splits," *Computer Methods in Applied Mechanics and Engineering*, vol. 199, pp. 2765–2778, 2010a.

[17] Miehe C., Welschinger F., and Hofacker M., "Thermodynamically consistent phase-field models of fracture: variational principles and multi-field FE implementations," *International Journal for Numerical Methods in Engineering*, vol. 83, pp. 1273–1311, 2010b.

[18] Hohenberg P. and Halperin B., "Theory of dynamic critical phenomena," *Rev. Modern Phys.*, vol. 49 , pp. 435–479, 1977.

[19] Gunton J., Miguel M., and Sahni P., *The Dynamics of First-Order Phase Transitions*, Domb C. and Lebowitz J.L., Eds. New York: Academic press, 1983, vol. 8-3.

[20] Chen L.Q. and Khachaturyan A., "Computer simulation of structural transformations during precipitation of an ordered intermetallic phase," *Acta Mater.*, vol. 39, pp. 2533-2551, 1991.

[21] Wang Y., Chen L.Q., and Khachaturyan A., "Kinectics of strain-induced morphological transformation in cubic alloys with a miscibility gap," *Acta Metall. Mater.*, vol. 41, no. 1, pp. 279-296, 1993.

[22] Vaithyanathan V., "Phase-field simulations of coherent precipitate morphologies and coarsening kinetics," Department of Materials Science and Engineering, The

Pennsylvania State University, Ph.D. Thesis May 2002.

[23] Artemev A., Jin Y., and Khachaturyan A., "Three-dimensional phase field model of proper martensitic transformation," *Acta Mater.* , vol. 49, pp. 1165–1177, 2001.

[24] Miyazaki T., Takeuchi A., and Koyama T., "Computer simulations of the phase decomposition on Cu–Co binary alloys based on the non-linear diffusion equation," *J. Mater. Sci.* , vol. 27, pp. 2444–2448, 1992.

[25] Nishimori H. and Onuki A., "Pattern formation in phase-separating alloys with cubic symmetry," *Phys. Rev. B*, vol. 42 , pp. 980–983, 1990.

[26] Langer J., "Models of pattern formation in first-order phase transitions," *Directions in Condensed Matter Physics, World scientific, Singapore*, pp. 165–185, 1986.

[27] Caginalp G. and Fife P., ", Phase-field methods for interfacial boundaries," *Phys. Rev. B*, vol. 33, no. 11, pp. 7792–7794, 1986.

[28] Penrose O. and Fife P., "Thermodynamically consistent models of phase-field type for the kinetics of phase transitions," *Physica D* , vol. 43, pp. 44–62, 1990.

[29] Wang S.L. et al., "Thermodynamically-consistent phase-field models for solidification," *Physica D*, vol. 69, pp. 189–200, 1993.

[30] Wheeler A.A., Boettinger W.J., and McFadden G.B., "Phase-field model for isothermal phase transitions in binary alloys," *Phys. Rev. A* , vol. 45 , pp. 7424–7439, 1992.

[31] Kim S., Kim W., and Suzuki T., "Phase-field model for binary alloys," *Phys. Rev. E*, vol. 60, pp. 7186–7196, 1999.

[32] Karma A., "Phase-field formulation for quantitative modeling of alloy solidification," *Phys. Rev. Lett.*, vol. 87, p. 115701, 2001.

[33] Steinbach I. et al., "A phase field concept for multiphase systems," *Physica D* , vol. 94, pp. 135–147, 1996.

[34] Wang S., Asle Z.M., Horstemeyer M.F., and Wang P., "Thermal effects on the morphological evolution during crystallization of HCP metals: A three dimensional phase-field study," *Materials Technology* , vol. 27, no. 5, pp. 355-363, 2012.

[35] Kobayashi H., Ode M., Kim S., Kim W., and Suzuki T., "Phase-field model for

solidification of ternary alloys coupled with thermodynamic database," *Scr. Mater.* , vol. 48, pp. 689-694, 2003.

[36] Elder K. and Grant M., "Modeling elastic and plastic deformation innonequilibrium processing using phase field crystals," *Phys. Rev. E,* vol. 70, p. 051605, 2004.

[37] Elder K., Katakowski M., Haataja M., and Grant M., "Modeling elasticity incrystal growth," *Phys. Rev. Lett.*, vol. 88, p. 245701, 2002.

[38] Elder K., Provatas N., Berry J., Stefanovic P., and Grant M., "Phase-fieldcrystal modeling and classical density functional theory of freezing," *Phys. Rev. E* , vol. 75, p. 064107, 2007.

[39] Tiaden J., Nestler B., Diepers H.J., and Steinbach I., *Physica D* , vol. 115 , pp. 73-86, 1998.

[40] Eiken J., Bottger B., and Steinbach I., *Phys. Rev. E* , vol. 73066122, 2006.

[41] Kim S.G., Kim W.T., Suzuki T., and Ode M., *J. Crist. Growth* , vol. 261, no. 135 , 2004.

[42] Boussinot G. and Brener E.A., "Interface kinetics in phase-field models: Isothermal transformations in binary alloys and step dynamics in molecular-beam epitaxy," *Phys. Rev. E* , vol. 88, no. 022406, p. 14 pages, 2013.

[43] Xu Z. and Meakin P., "Phase-field modeling of solute precipitation and dissolution," *J. Chem. Phys.* , vol. 129, no. 014705, 2008.

[44] Ma X.Q., Shi S.Q., Woo C.H., and Chen L.Q., "The phase field model for hydrogen diffusion and γ-hydride precipitation in zirconium under non-uniformly applied stress," *Mechanics of Materials* , vol. 38, pp. 3-10, 2006.

[45] Khachaturyan A.G., *Theory of Structural Transformations in Solids*. Newyork, USA: Wiley-Interscience Publication, 1983.

[46] Fried E., Silva M.N., Duda F.P., and Souza A.C., "Phase-field Model for the Corrosion and Cracking of Metals in Aqueous Environments," in *Proceedings of the Twenty-first International Offshore and Polar Engineering Conference*, Hawaii, USA, 2011.

[47] Zaeem M.A., "Finite Element Method for Conserved Phase Field Models: Solid State Phase Transformations," School of Mechanical & Materials Engineering,

Washington State University, Washington, USA, PhD Dissertation 2010.

[48] Tijjani Y.A. and Ing., "Modeling and Simulation of Thermo-chemical Heat Treatment Processes: A Phase Field Calculation of Nitriding in Steel," Bremen University, Germany, PhD Dissertation 2008.

[49] Cho Y. et al., "Analysis of Transformation Plasticity in steel using Finite Element Method Coupled with Phase Field Model," *PLos ONE*, vol. 7, no. 4, 2011.

[50] Bertia A. and Bochicchio I., "A mathematical model for phase separation: a generalized Cahn–Hilliard equation," *Mathematical Methods in the Applied Sciences*, vol. 00, pp. 1–11, 2010.

[51] Tol´edano J.C. and Tol´edano P., "The Landau theory of phase transitions:Application to structural, incommensurate, magnetic, and liquid crystalsystems," *World Scientific Lecture Notes in Physics*, vol. 3, 1987.

[52] Mamivand M., Zaeem M.A., Kadiri H.E., and Chen L., "Phase Field Model of tetragonal-to-monoclinic phase transformation in Zirconia," *Acta. Mater.*, May 2013.

[53] wikipedia.phase field model. [Online].

[54] Caginalp G., "Stefan and Hele-Shaw type models as asymptotic of the phase field equations," *Phys. Rev. A*, vol. 39, pp. 5887-5896, 1989.

[55] Wang Y. and Khachaturyan A., "Three-dimensional field model and computermodeling of martensitic transformations," *Acta Mater.* , vol. 45, pp. 759–773, 1997.

[56] Dannan F. and Chen L.Q., ", 1995, ‘’Possibility of Spinodal Decomposition in ZrO2-Y2O3 Alloys: A Theoretical Investigation," *J. Am. Ceram. Soc.* , vol. 78, no. 6, pp. 680-86, 1995.

[57] [Online]. http://www.wikipedia.com\Vegard’s law

[58] Kryvasheyeu Y., "The Phase Field Simulation of Autocatalytic Nucleation," School of Physics, Monash University, Australia, thesis 2012.

[59] Johnson W.C., "Effect of elastic stress on two-phase binary diffussion couples," *Metall. Mater. Trans. A*, vol. 28A, pp. 27-38, 1997.

[60] Voyiadjis G.Z. and Mozaffari N., "Nonlocal damage model using the phase field method: Theory and application," *Int. J. Solids Struct.*, 2013.

[61] Furihata D., "A stable, convergent, conservative and linear finite differencescheme for the Cahn-Hilliard equation," *Japan J. Indust. Appl. Math.*, vol. 20, pp. 65–85, 2003.

[62] Eyre D.J., "An unconditionally stable one-step scheme for gradient systems.," *Preprint.*, 1998.

[63] Vollmayr-Lee B.P. and A.D. Rutenberg, "Fast and accurate coarsening simulation with an unconditionally stable time step," *Phys. Rev. E*, vol. 68, no. 066703, 2003.

[64] Chen K-Y. and Lai M-C., "Numerical Studies on the Allen-Cahn and Cahn-Hilliard Equations," Department of Applied Mathematics, Thesis 2007.

[65] Danilov D. and Nestler B., "Phase-field simulations of solidification in binary and ternary systems using a finite element method," *J. Cryst. Growth*, vol. 275, pp. e177–e182, 2005.

[66] Zhou J.X. and Li M.E., "Solving phase field equations using a meshless method," *Commun. Numer. Engng.*, vol. 22, pp. 1109-1115, 2006.

[67] Mackenzie J.A. and Robertson M.L., "A moving mesh method for the solution of the one-dimensional phase-field equations," *Journal of Computational Physics*, vol. 181, pp. 526-544, 2002.

[68] Leo P.H., Lowengrub J.S., and Hou H.J., "A diffuse interface model for microstructure evolution in elastically stressed solids," *Acta. Mater.*, vol. 61, pp. 2113-2130, 1998.

[69] Chen L.Q. and Shen J., "Applications of semi-implicit Fourier-spectral method to phase field equations," *Computer Physics Communications*, vol. 108, pp. 147-158, 1998.

[70] Zhu J., Chen L.-Q., Shen J., and Tikare V., "Microstructure dependence ofdiffusional transport," *Comput. Mater. Sci.* , vol. 20 , pp. 37–47, 2001.

[71] Padture N.P., "Thermal barrier coatings for gas turbine applications," *Science Magazine*, vol. 296 , no. 5566, pp. 280-284, 2002.

[72] [Online]. www.wikipedia.com\Thermal BarrierCoatings

[73] Sampath S., Schulz U., Jarligo M.O., and Kuroda S., "Processing science of advanced thermal-barrier systems," *MRS Bulletin*, vol. 37, October 2012.

[74] Schulz U., Fritscher K., Leyens C., Peters M., and Kaysser W.A., " ," *JOM*, vol. 49 , 1997.

[75] University of Cambridge, Online Class Material on Electrolytes. [Online]. http://www.doitpoms.ac.uk/tlplib/fuel-cells/sofc_electrolyte.php?printable=1

[76] Westerville OH, *Science and Technology of Zirconia, Advances in Ceramics*, 3rd ed., Heuer A.H. and Hobbs L. W., Eds.: The American Ceramics Society, 1981.

[77] Bouvier P., Djurado E., Lucazeau G., and Le Bihan T., *Phys. Rev. B*, vol. 62, no. 8731, 2000.

[78] Jones R.L., *in Metallurgical and Ceramic Coatings*, Stern K.H., Ed. London, UK: Chapman & Hall, 1996.

[79] Predith A., Ceder G., Wolverton C., Persson K., and Mueller T., *Phys. Rev. B*, vol. 77, no. 144104, 2008.

[80] Kuroda S. and Clyne T.W., "Thin Solid Films ," vol. 200, no. 1, p. 49 , 1991.

[81] Eaton H.E., Linsey J.R., and Dinwiddie R.B., *Thermal Conductivity*, Tong T.W., Ed. Technomic, Lancaster, PA, 1994, vol. 22.

[82] Niessen K.V. and Gindrat M., *J. Therm. Spray Technol.* , vol. 20, no. 4, p. 736, 2011.

[83] Pokluda J. and Kianicová M., "Damage and Performance Assessment of Protective Coatings on Turbine Blades, Gas Turbines," *Gurrappa Injeti (Ed.),ISBN: 978-953-307-146-6,InTech.*, 2010.

[84] Pokluda J. and Kianicová M., *Damage and Performance Assessment of Protective Coatings on Turbine Blades, Gas Turbines*, Injeti G., Ed.: InTech, 2010.

[85] Jones R.L., "Thermal Barrier Coatings," *Metallurgical and Ceramic Protective Coatings*, pp. 194–235, 1996.

[86] Jones R. L., Williams C. E., and Jones S. R., "Reaction of Vanadium Compounds with Ceramic Oxides," *J. Electrochem. Soc.*, vol. 133 , no. 1, pp. 227–30.

[87] Park S.Y., Kim J.H., Kim M.C., Song H.S., and Park C.G., ", 2005, “Microscopic Observation of Degradation Behavior in Yttria and Ceria Stabilized Zirconia Thermal Barrier Coatings under Hot Corrosion," *Surf. Coat. Technol.*, vol. 190, pp. 357– 65.

[88] Mohsen S., Abbas A., and Akira K., "Bond Coat Oxidation and Hot Corrosion Behaviour of APS YSZ Coating on Ni Super alloy," *T. Joining and Welding Research Institute*, vol. 36, no. 1.

[89] Chen Z., Mabon J., Wen J., and Trice R., "Degradation of plasma-sprayed Yttria-Stabilized Zirconia coatings via ingress of vanadium oxide," *Journal of the European Ceramic Society* , vol. 29, pp. 1647–1656, 2009.

[90] Sustitzky D.W., Hertl W., and Carter C.B., "Destabilization of Zirconia Thermal Barriers in the Presence of V2O5," *J. Appl. Phys.*, vol. 71, no. 11, pp. 992-1004, 1988.

[91] Hertl W., "Vanadia Reactions with Yttria Stabilized Zirconia," *J. Appl. Phys.*, vol. 63, no. 11, pp. 5514–20, 1988.

[92] Gonzalez E.S. et al., "Application of Hertzian Tests to measure Stress-Strain Characteristics of ceramics at elevated temperatures," *J. Am. Ceram. Soc.*, vol. 88, no. 10, pp. 2202-2208, 2005.

[93] Chen Z. et al., "Investigation of reactions between vanadium oxide and plasma-sprayed Yttria-Stabilized Zirconia coatings," *Journal of the European Ceramic Society*, vol. 29, pp. 1403-1411, 2009.

[94] Douglas R.V. et al, "Hot corrosion of lanthanum zirconate and partially stabilized zirconia thermal barrier coatings," *Journal of Engineering for Gas Turbines and Power*, vol. 128, no. 1, pp. 144-152, January 2006.

[95] Douglas R.V. et al, "Hot corrosion of lanthanum zirconate and partially stabilized zirconia thermal barrier coatings," *Journal of Engineering for Gas Turbines and Power*, vol. 128, no. 1, pp. 144-152, 2006.

[96] Batista C., Portinha A., Ribeiro R.M., Teixeira V., and Oliveira C.R., "Evaluation Of Laser-Glazed Plasma-Sprayed Thermal Barrier Coatings Under High Temperature Exposure To Molten Salts," Physics Department, University of Minho, Campus de Gualtar, Braga, Portugal, 4710-057,.

[97] Arisekola G.A., "Evaluation of the Effectiveness of Alkaline-Earth Metal Oxides in Inhibiting Vanadium-Induced Hot Corrosion of Yttria-Stabilized Zirconia Thermal Barrier Coatings," King Fahd University of Petroleum and Minerals, Dhahran, Thesis December, 2013.

[98] Scott X. M., "Impermeable thin Al2O3 overlay for TBC protection from sulfate and vanadate attack in gas turbines," Department of Mechanical Engineering, University of Pittsburgh, Quarterly Progress Report 2004.

[99] Saremi M., Keyvani A., and Sohi M.H., "Hot corrosion resistance and mechanical behavior of atmospheric plasma sprayed conventional and nanostructured zirconia coatings," *International Journal of Modern Physics: Conference Series*, vol. 5, pp. 720-7, 2012.

[100] Grafen W. and Edenhofer B., "New developments in thermo-chemical diffusion processes," *Surface and Coatings Technology*, vol. 200, no. 5-6, pp. 1830-1836, 2005.

[101] Franz C., Besserdich G., Schulze V., Mueller H., and Loehe D., "Influence of transformation plasticity on residual stresses and distortions due to the heat treatment of steels with different carbon contents," *J. Phys. IV*, vol. 120, pp. 481-488, 2004.

[102] Carbonitriding. Knowledge Article from Key To Steel. [Online]. http://www.keys-to-steel.com/Articles/Art126.htm

[103] Hernandez M., Staia M.H., and Puchi-Cabrera E.S., "Evaluation of microstructure and mechanical properties of nitrided steels," *Surf. Coat. Technol.*, vol. 202, pp. 1935-1943, 2008.

[104] Akhtar S.S., Arif A.F.M., and Yilbas B.S, "Evaluation of gas nitriding process with in-process variation of nitriding potential for AISI H13 tool steel," *Int. J. Adv. Manuf. Technol.*, 2009.

[105] Davis J.R. and Davis & Associates, *Surface Hardening of Steels-Understanding the Basics*.: ASM International, 2002.

[106] A.F.M. Arif, "Effect of Extrusion Die Profile on the Uniformity of Nitrided Layers, Materials and Manufacturing Processes," vol. 24, no. 6, pp. 619-625, 2009.

[107] Mittemeijer J., "The relation between macro- and microstresses and mechanical ," in *Proceedings of the TMS-AIME Session ”Microstructural and Residual Stress*

Effects on the Properties of Case-Hardened steels", Warrendale,U.S.A., 1984, pp. 161-187.

[108] Michalski J., Tacikowski J., Nakonieczny A., and Wach P., "Nitriding without the compound layer and with continuous in-process variation of the nitriding potential," *Int. J. Microstructure and Materials Properties*, vol. 2, no. 1, 2007.

[109] Akhtar S.S. and Arif A.F.M., "Experimental and Numerical Investigation of Extrusion Die Profiles for Uniform and Effective Case-Hardening Treatment (IMECE2012-87401), ," in *Proceedings of the ASME 2012 International Mechanical Engineering Congress & Exposition IMECE2012*, Houston, Texas, USA, November 9-15, 2012.

[110] Akhtar S.S., Arif A.F.M., and Yilbas B.S, "Influence of surface preparation on the kinetics of controlled gas-nitrided AISI H13 steel used in extrusion dies," *JMEPEG*, vol. 19, pp. 347-355, 2010.

[111] Mridha S. and Khan A.A., "The effect of process variables on the hardness of nitrided 3% chromium steel," *Journal of Materials Processing Technology*, vol. 201, pp. 325-330, 2008.

[112] Sueyoshi H., Hamaishi K., Nakamura Y., and Kiyofuji J., "Effect of mechanical pre-treatment on gas nitriding behavior in austenitic stainless steel," *Mater. Trans. JIM*, vol. 37, no. 2, pp. 150-156, 1996.

[113] Czelusniak A., Liliental W.K., and Tymowski G., "Influence of Die Handling Operations on Performance of Nitrided Aluminium Extrusion Dies," *Nitrex Metal Inc.*, 1997.

[114] Bei D.H., Lu J., Gu J.F., and Pan J.S., "Effects of Surface Nanocrystallization Pre-Treatment on Gas Nitriding Behavior of Mild Steel," *Trans. Mater. Heat Treat.*, vol. 23, no. 1, pp. 19-24, 2002.

[115] Wroblewski G. and Skalski K., "Properties of Surface Layer Generated by New Combined Process of Burnishing and Nitriding," *Surf. Eng.* , vol. 22, no. 2, pp. 138-146, 2006.

[116] Baranowska J., Szczecinski K., and Wysiecki M., "Increasing of Gas Nitriding Kinetics via Surface Pre-Treatment," *J. Surf. Coat. Techonol.*, vol. 151-152, pp. 534-539, 2002.

[117] Greßmann T., Leineweber A., and Mittemeijer E.J., "X-ray diffraction line-profile analysis of hexagonal ε-iron-nitride compound layers: composition- and stress-depth profiles," Universität Stuttgart, Dissertation September 2007.

[118] Hu M.J., Pan J.S., Li Y.J., and Ruan D., "Mathematical modeling and computer simulation of nitriding," *Material Science and Technology*, vol. 16-547, May 2000.

[119] Spies H.J., Le Thien H., and Biermann H.B., "Controlled Nitriding," *Metal Science and Heat Treatment*, vol. 46, no. 7-8, pp. 227-276, 2004.

[120] Kedam M., Djeghlal M.E., Barrallier L., and Salhi E., "Computer simulation of nitrided layers growth of pure iron," *Computational Materials Science*, vol. 29, pp. 43-48, 2004.

[121] Maldzinski L., Liliental W., Tymowski G., and Tacikowski J., "New possibilities for controlling gas nitriding process by simulation of growth kinetics of nitride layers," *Surf. Eng.*, vol. 15, no. 5, pp. 377-3848, 1999.

[122] Rozendaal H.C.F. et al., "The development of Nitrogen concentration profiles on nitriding iron," *Metallurgical Transactions*, vol. 14A, p. 395, March 1983.

[123] Ratajski J., Olik R., and Suszko T., "Precise formation of the phase composition and the thickness of nitrided layers," *Journal of Achivements in Materials and Manufacturing Engineering*, vol. 37, no. 2, December 2009.

[124] Teresa M. and Galdikas A., "Stress Induced Nitrogen Diffusion in Nitrided Austenitic Stainless Steel," *Material Science (Medziagotyra)*, vol. 17, no. 1, pp. ISSN 1392-1320, 2011.

[125] Grzegorz W. and Konstanty R.S., "Residual Stresses during Nitriding Process-Taking Diffusion and Phase Phenomena into Consideration," in *Fifth World Congress on Computational Mechanics*, Vienna Austria, 2002, July 7-12.

[126] Arif A.F.M., Akhtar S.S., and Yilbas B.S., "Effect of process variables on gas nitriding of H13 tool steel with controlled nitriding potential," *Int. J. Surface Science and Engineering*, 2008.

[127] Hu S.Y., Murray J., Weiland H., Liu Z.K., and Chen L.Q., "Thermodynamic description and growth kinetics of stoichiometric precipitates in the phase-field approach," *Computer Coupling of Phase Diagrams and Thermochemistry*, vol. 31, no. 2007, pp. 303-312.

[128] Levin F.M., "The system Y2O3-V2O5," *J Am Ceram Soc*, vol. 50, no. 7, p. 381, 1967.

[129] Knudsen J., Hottel H., Sarofim A., Wankat P., and Knaebel K., , 7, Ed.: McGraw-Hill, 1997, ch. Section 5-48: Heat and Mass Transfer, Table 5-13.

[130] NIMS Diffusion Database. [Online]. http://diffusion.nims.go.jp/index_en.html

[131] Katamura J. and Sakuma T., "Computer Simulation of the microstructural Evolution during the diffusionless cubic-to-tetragonal transition in the system ZrO2-Y2O3," *Acta mater.*, vol. 46, no. 5, pp. 1569-1575, 1997.

[132] Shian S., Sarin P., and Gurak M. et al., "The tetragonal–monoclinic, ferroelastic transformation in yttrium tantalate and effect of zirconia alloying," *Acta Materialia*, vol. 69, pp. 196-202, 2014.

[133] Chan S., Fang Y., and Grimsditch M. et al., "Temperature dependence of the elastic moduli of monoclinic Zirconia," *J Am Ceram Soc*, vol. 74, no. 7, pp. 1742-1744, 1991.

[134] Vaben R., Kerkhoff G., and Stover D., "Development of a micromechanical life prediction model for Plasma Sprayed Thermal Barrier Coatings," *Material Science and Engineering*, vol. A303, pp. 100-109, 2001.

[135] Washburn E.W., "Dynamics of capillary flow," *Phys. Rev.*, vol. 17, no. 3, pp. 273-283, 1921.

[136] Akhtar S.S., Arif A.F.M., and Abubakar A.A., "Gas Nitriding of AISI H13 Steel Extrusion Dies: Consideration of Sharp Features in the Die Profiles," in *Montreal'2014 AES-ATEMA 17th International Conference*, Canada, 2014.

[137] Watkins T.R., England R.D., Klepser C., and Jayaraman N., "Measurement and Analysis of Residual Stress in ε-Phase Iron Nitride Layers as a Function of Depth," *JCPDS-International Centre for Diffraction Data, Advances in X-ray Analysis*, vol. 43, p. 31, 2000.

[138] Hertzberg R.W., Vinci R.P., and Hertzberg J.L., *Deformation and Fracture Mechanics of Engineering Materials*, 5th ed., Welter J., Ed. Uited States: John Wiley & Sons, Inc., 2013.

[139] "Technology Characterization:Gas Turbines," Energy and Environmental Analysis,ICF International Company, Arlington, Virginia, 22209, 2008.

[140] Wen Y., Wang Y., and Chen L.Q., *Philos Mag A* , vol. 80, no. 1967, 2000.

[141] Zaeem M., El Kadiri H., Horstemeyer MF., Khafizov M., and Utegulov Z., *Asle Curr Appl Phys*, vol. 12, no. 570, 2011.

[142] Jin Y.M., Artemev A., and Khachaturyan A.G., "Three dimensional phase field model of low-symmetry martensitic transformation in polycrystal: Simulations of ζ 2 martensite in AuCd alloys," *Acta. Mater.* , vol. 49, pp. 2309–2320, 2001.

[143] Yamanaka A., Takaki T., and Tomita Y., *Mater Sci Eng A* , vol. 491, no. 378, 2008.

[144] Sankarasubramanian R., "Microstructural evolution in elastically-stressed solids: a phase-field simulation," *Defence Science Journal* , vol. 61, pp. 383–393, 2011.

[145] Levitas V.I. and Ozsoy I.B., "Micromechanical modeling of stress-induced phase transformations. Part 1: Thermodynamics and kinetics of coupled interface propagation and reorientation," *International Journal of Plasticity*, vol. 25, pp. 239–280, 2009a.

[146] Rodney D., Le Bouar Y., and Finel A., "Phase field methods and dislocations," *Acta Materialia* , vol. 51, pp. 17–30, 2003.

[147] Bhate D., Kumar A., and Bower A., ", Diffuse interface model for electromigration and stress voiding," *J. Appl. Phys.* , vol. 87, pp. 1712–1721, 2000.

[148] Wang Y., "Computer modeling and simulation of solid-state sintering: A phase field approach," *Acta Mater.*, vol. 54, pp. 953–961, 2006.

[149] Du Q., Liu C., and Wang X., "Simulating the deformation of vesicle membranes under elastic bending energy in three dimensions," *J. Comput. Phys.* , vol. 212 , pp. 757–777, 2006.

[150] Gaubert A., Le Bouar Y., and Finel A., "Coupling phase field and viscoplasticity to study rafting in Ni-based superalloys," *Philosophical Magazine*, vol. 90, pp. 375–404, 2010.

[151] Ode M., Suzuk T.i, Kim S.G., and Kim W.T., "Phase-field model for solidification of Fe-C alloys," *Science and Technology of Advanced Materials*, vol. 1, no. 2000, pp. 43-49, 2000.

[152] Voigt W., "Theoretische Studien uber die Elastizitätsverhhältnisse der Kristalle,"

Abh. Kgl. Ges. Wis. Göttingen,Math. Kl, vol. 34, no. 1, pp. 1–155, 1887.

[153] Reuss A., "Berechnung der Fliessgrenze von Mischkristallen auf Grund der Plastizitätsbedingungen für Einkristalle," *Z. ang. Math. und Mech.* , vol. 9, pp. 49–58, 1929.

[154] Dewit R., "Elastic Constants and Thermal Expansion Averages of a Nontextured Polycrystal," *Journal Of Mechanics Of Materials And Structures*, vol. 3, no. 2, 2008.

[155] Chen Z., "Hot Corrosion and High Temperature Deformation of Yttria-Stabilized Zirconia Thermal Barrier Coatings," Purdue University, West Lafayette, Indiana, Thesis December, 2006.

APPENDICES

Appendix A: Most recent applications of PFM

Table A.1: Most Recent Applications of Phase Field Model

APPLICATION	**DESCRIPTION**	**SOURCE**
Solidification	Solidification of HCP Metallic Alloys	[**34**]
Solid-state phase transformations	Corrosion Kinetics Under Dual Oxidants	[**140**]
	Phase Transformation of Low Carbon Steel	[**49**]
	Precipitation of Al-Cu and Ti-Ni alloys	[**58**]
	Precipitation Growth and Coarsening	[**141**]
	Martensitic Phase Transformations	[**142**]
	Grain Growth	[**141**]
	Tetragonal-to-Monoclinic (Diffusionless) Phase Transformation of Zirconia	[**52**]
	Cubic-to-Tetragonal Martensitic Phase Transformation under applied stresses	[**143**]
	Hexagonal-to-Orthorhombic transformation	[**140**]
	Spinodal Decomposition	[**56**]

	Nitriding Process in Steel	[**48**]
Other applications	Micro-void Evolution Under Elasto-Plastic Deformations	[**60**]
	Inhomogeneous Elasticity	[**144**]
	Stress-Induced Phase Transformations	[**145**]
	Dislocation Dynamics	[**146**]
	Crack Propagation & Fracture Models	[**16**], [**17**]
	Electro-migration	[**147**]
	Solid-State Sintering	[**148**]
	Vesicle Membranes in Biological Applications	[**149**]
	Elasticity Coupled with Diffusion	[**150**]
	Oswald Ripening	[**151**]
	Isothermal Dendrite Growth and Particle-Interface Interaction	[**151**]
	Two-Phase Flow	
	Damage Mechanics	[**60**]

Appendix B: Diffusion-induced transformations in YSZ

Hot corrosion is a type of high-temperature chemical reaction between a metal or metallic oxide and a molten salt in an oxidizing environment. Type-I Hot corrosion, where the contaminant is in molten form is one of the main causes of failure in thermal barrier coatings in Saudi Arabia. This is due to frequent use of low grade fuels in the kingdom, which allows a certain amount of impurities such as Vanadium, Sodium, Phosphorous, Sulfur, e.t.c. It is reported that [**97**], low grade fuels contain a large amount of Vanadium compounds (up to 100 ppm) which oxidizes to form V_2O_5 salt (with a melting point of 698^0C). The reaction between molten salt, V_2O_5, and air plasma-sprayed 8 mol% Y_2O_3-ZrO_2 (YSZ) has been reported [**88**] to be the main cause of the failure of TBC at high temperatures due to large volume changes associated with the tetragonal-to-monoclinic transformation. Previous experimental study shows that [**93**] for a temperature range of 698^0C to 800^0C, the transformation of the YSZ from the tetragonal to monoclinic phase of zirconia is very slow due to the formation of other compounds like zirconia-vanadate, ZrV_2O_7. For this reason, the highest degradation of the coating for Type I hot corrosion was found to be 900^0C, which is the most common operating temperature for land-based gas turbines in Saudi Arabia. Thus, the current work involves the investigation of the corrosion process at 900^0C.

For the hot corroded TBC, the tetragonal-to-monoclinic transformation is mainly caused by the diffusion of V_2O_5, and its reaction with the stabilizer (Y_2O_3) to form YVO_4. The Y_2O_3-ZrO_2 phase diagram [**75**] showed that, non-transformable tetragonal phase forms for about 8 mol% of Y_2O_3 in the zirconia at virtually all temperatures. The V_2O_5-ZrO_2 phase diagram (Fig. 6 of Ref.[**93**]) showed that, the partial melting of pure Zirconia is very negligible for the amount of V_2O_5 obtainable in low grade fuels even at high temperatures. From Fig.B.1, the V_2O_5-Y_2O_3 phase diagram showed that the formation of YVO_4 is possible for V_2O_5-Y_2O_3 mol% ratio of 0.2-0.5., which corresponds to 1.6 and 8 mol% V_2O_5 on the Y_2O_3-ZrO_2 scale. Thus, the equilibrium concentrations for formation of YVO_4 and the evolution of the m-phase are taken as 1.6 and 8 respectively.

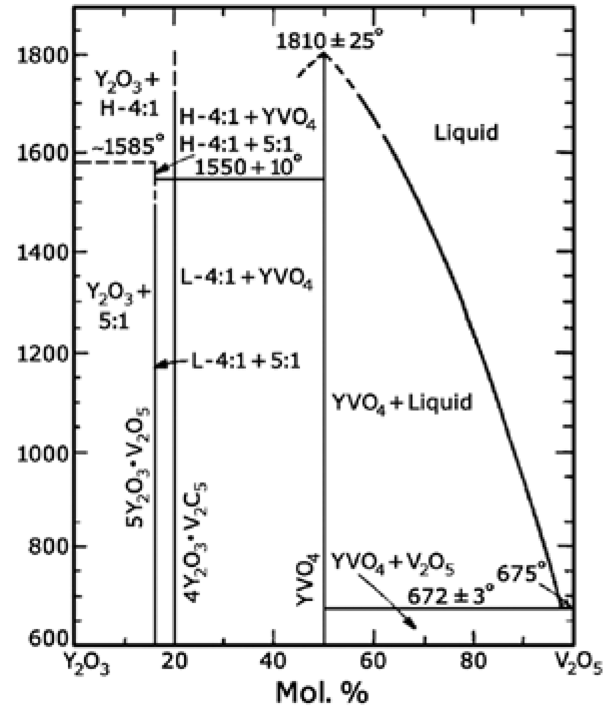

Figure B.1: V_2O_5-YVO_4 phase diagram[128]

Appendix C: More on the estimate for material parameters for TBC problem

a. Chemical free energy

Analytical solution for the KKS free energy density exists as [**58**]:

$$f(\eta_1, X_{VO}) = \frac{A(T) \cdot B(T)[X_{VO} - X_{t-z}{}^{eq} - (X_{m-z}{}^{eq} - X_{t-z}{}^{eq}) \cdot h(\eta_1)]^2 + w_1 g(\eta_1)}{B(T) + [A(T) - B(T)]h(\eta_1)} \qquad (C.1)$$

For parabolic chemical free energies approximation with similar curvatures, the expression reduces to [**58**]:

$$f(\eta_1, X_{VO}) = A(T)[X_{VO} - X_{t-z}{}^{eq} - (X_{m-z}{}^{eq} - X_{t-z}{}^{eq}) \cdot h(\eta_1)]^2 + w_1 g(\eta_1) \qquad (C.2)$$

Where,

$A(T)$ = proportionality constant

$X_{t-z}{}^{eq}$ and $X_{m-z}{}^{eq}$ are equilibrium mole composition for the formation of $\mathrm{m}-\mathrm{phase}$.

And from Appendix A, $X_{t-z}{}^{eq} = 0.016$ and $X_{m-z}{}^{eq} = 0.08$.

The proportionality constant is obtained by fitting the chemical free energies (from thermodynamic databases) of the t-phase and m-phase with the parabolic approximations as shown in chapter 5.

The chemical free energy of the YSZ (t-phase) is obtained by the following the approximation which is obtained from the thermodynamic database [**131**].

$$G(x, \eta, T) = G_0(x, T) + a \cdot \left(T - T_c(x)\right) \cdot \eta^2 + B \cdot \eta^4 \qquad (C.3)$$

Where,

$$T_c(x) = 2650 \cdot \left(1 - \frac{x}{0.208}\right)^{\frac{1}{2}}$$

$$G_0(x, T) = RT\left[(1-x) \cdot ln(1-x) + xlnx + 2 \cdot \left(1 - \frac{x}{4}\right) ln\left(1 - \frac{x}{4}\right) + 2 \cdot \frac{x}{4} \ln\left(\frac{x}{4}\right)\right]$$
$$+ (-1.397 \times 10^6 + 2.888 \times 10^8 \cdot \delta^2) \cdot x$$
$$+ (-2.343 \times 10^5 + 2.464 \times 10^7 \cdot \delta^2) \cdot x^2$$
$$+ (1.633 \times 10^6 - 3.131 \times 10^8 \cdot \delta^2) \cdot x^3$$

T = temperature(K)

x = dopant composition (mol%)

δ = misfit parameter, function of ionic radius of dopant cations = 2.868×10^{-2}

a = 30.2 J/molK and B = 4.00×10^4 J/mol

η=1 for t-phase

Similarly, an approximation for the chemical free energy of the m-phase (ZrO_2) is given by (Equation (1): [**52**]):

$$G_m(T) = -1126163.5 + 424.8908T - 69.38751T\ln(T) - 0.0037588T^2 + 683000T^{-1} \quad (C.4)$$

At 900^0C, the chemical free energies of the t-phase and m-phase were obtained as:

$$G_t(X_t, T) = -85.4085 \times 10^3 \text{ J/mol} = -3.928791 \times 10^9 \text{ J/m}^3$$

$$G_m(X_t, T) = -1.207576277 \times 10^6 \text{ J/mol} = -5.554850874 \times 10^{10} \text{ J/m}^3$$

Therefore, the chemical driving force for the transformation is,

$$\Delta G = G_t(X_t, T) - G_m(X_t, T) = 5.161971774 \times 10^{10} \text{J/m}^3$$

Using the aforementioned equations and constants, the following plots for the free energy density are obtained.

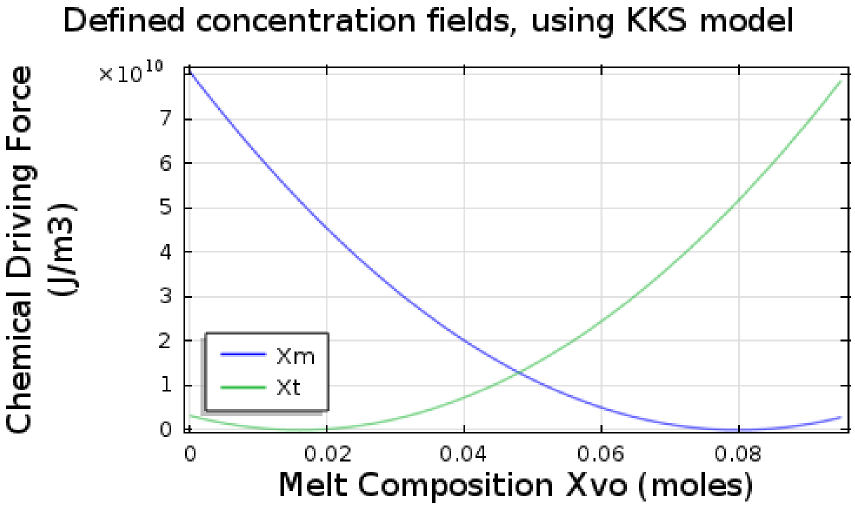

Figure C.1: Variation of composition with chemical driving force according to the KKS model

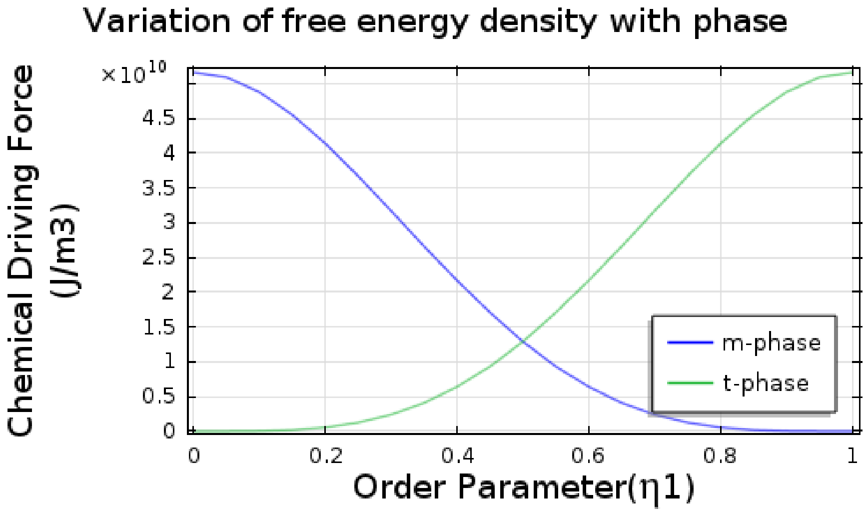

Figure C.2: Variation of free energy density with phase

b. Diffusion Coefficient

For simplicity, constant diffusion coefficient is assumed for both phases. Approximate diffusion coefficient for V_2O_5/YSZ system was obtained from the NIMS Diffusion database [**130**]. The following constants were obtained:

$D_0 = 3.77 \times 10^{-8}\ \mathrm{m^2/s}$, diffusion constant

$Q = 87\ \mathrm{KJ/mol}$, activation energy

$R = 8.314\ \mathrm{J/molK}$, molar gas constant

Then, the diffusion coefficient becomes,

$$D(T) = D_0 \exp\left(\frac{-Q}{RT}\right) = 5 \times \frac{10^{-12}\mathrm{m}^2}{\mathrm{s}} \qquad (\mathrm{C}.5)$$

The plot for the diffusivity as obtained from the database is given in Fig. C.3. The diffusion coefficient also falls within acceptable range for such material as shown in [**129**].

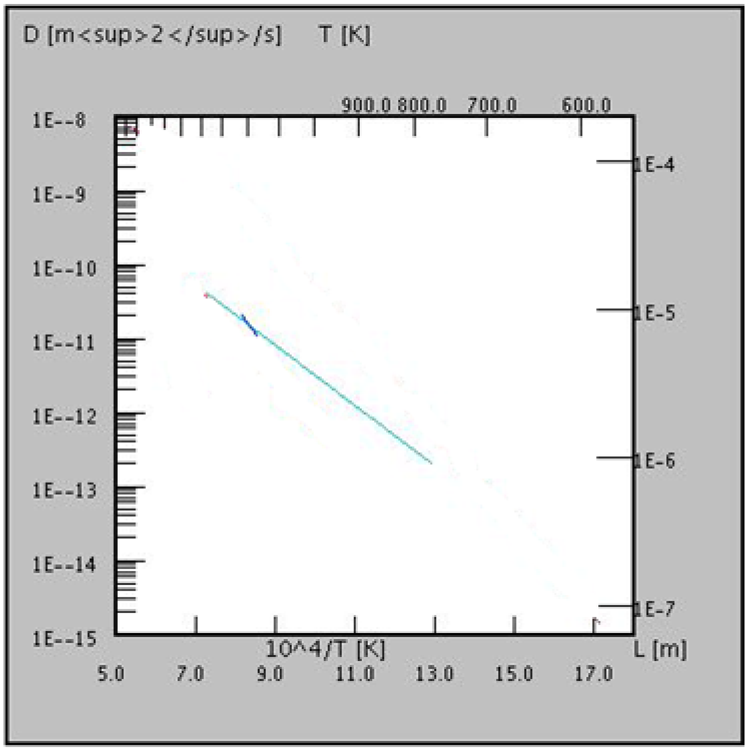

Figure C.3: Diffusivity for V2O5/YSZ system [**130**]

c. Atomic Mobility

The relationship between the diffusion coefficient and the diffusion mobility is usually obtained by comparing the Cahn-Hilliard equation and Fick’s second law. Thus by such comparison, the atomic or diffusion mobility is related to the diffusivity of the chemical specie by [**58**]:

$$M_S = \frac{D(T)}{2A(T)} \tag{C.6}$$

Where, the diffusion coefficient and proportionality constant, $D(T)$ and $A(T)$, have been defined previously.

d. Height of the double-well potential, energy barrier and interface thickness

Based on the KKS model, an energy barrier that separates the free energy of the coexisting phases are represented by $w_1 g(\eta_1)$, where $g(\eta_1)$ represents a function for the double-well potential. It was reported that [**58**], such energy barrier does not affect the bulk properties of the phases and the height of the double-well potential (w_1) is given by:

$$w_1 \approx 16\Delta f_{max} \qquad (C.7)$$

Where,

Δf_{max} = energy barrier between bulk properties of the coexisting phases

The energy barrier is obtained from the interfacial properties as follows.

$$\sigma \approx \sqrt{\alpha_1 \Delta f_{max}} \qquad (C.8)$$

$$\Delta f_{max} \approx \frac{\sigma^2}{\alpha_1} \qquad (C.9)$$

Where,

σ = interfacial energy (given in Ref. [**52**])

α_1 = gradient energy coefficient (given in Ref. [**52**])

It is important to select an appropriate interface thickness for the correct behavior of the phase field simulation. So, by defining the interface width to correspond to the distance between η_1=0.05 and η_1=0.95, the interface thickness can be obtained from equation (C.10).

$$l = \alpha^* \sqrt{2} \sqrt{\frac{\alpha_1}{w_1}} \approx \sqrt{\frac{\alpha_1}{\Delta f_{max}}} \ \ for \ \ \alpha^* = 2.94 \qquad (C.10)$$

e. Transformation strains, and Elastic stiffness matrix

As reported previously [**52**], there are two orientations for each variant and there are two variants for each of the three possible correspondences of the tetragonal-to-monoclinic transformation (i.e. ABC, CAB, and BCA correspondences). The ABC correspondence (shown in Fig.C.4) is selected for the current work because it has the smallest volumetric expansion and lead to a transformation with the smallest strain energy.

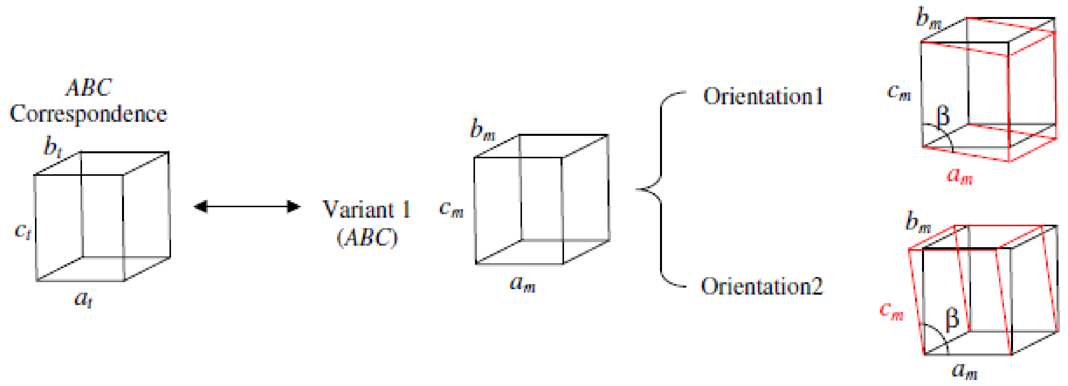

Figure C.4: ABC correspondence for tetragonal-to-monoclinic transformation of zirconia [52]

The transformation or bain strains for the tetragonal-to-monoclinic phase transformation of the ABC correspondence can be expressed in terms of the lattice parameters as follows [**133**].

$$\varepsilon_{12}{}^{\eta_1} = \frac{a_m}{a_t} - 1$$

$$\varepsilon_{22}{}^{\eta_1} = \frac{b_m}{b_t} - 1$$

$$\varepsilon_{33}{}^{\eta_1} = \frac{c_m sin\beta}{c_t} - 1$$

$$\varepsilon_{12}{}^{\eta_1} = \varepsilon_{21}{}^{\eta_1} = \varepsilon_{23}{}^{\eta_1} = \varepsilon_{32}{}^{\eta_1} = 0$$

$$\varepsilon_{13}{}^{\eta_1} = \varepsilon_{31}{}^{\eta_1} = -\frac{c_m cos\beta}{c_t}$$

Where [**52**],

$$a_m = 5.184 \times 10^{-10}\text{m}, \qquad b_m = 5.207 \times 10^{-10}\text{m}, \qquad c_m = 5.370 \times 10^{-10}\text{m}$$

$$a_t = 5.14 \times 10^{-10}\text{m}, \qquad b_t = 5.14 \times 10^{-10}\text{m}, \qquad c_t = 5.26 \times 10^{-10}\text{m}$$

For a 2D phase field model, the x and y axes can be made to correspond to either $a - b$ plane or the $a - c$ plane. In the current work, the $a - c$ plane is assumed to lie on top surface of the TBC and transformation on such plane produces the monoclinic twins as reported in Ref. [**52**]. The current work involves the simulation of the transformation along the depth of the coating during the hot corrosion process. Thus, it corresponds to the transformation on the $a - b$ plane which has the following transformation or Eigen strains.

$\varepsilon_{12}{}^{\eta_1} = 0.0049$

$\varepsilon_{22}{}^{\eta_1} = 0.013$

$\varepsilon_{12}{}^{\eta_1} = \varepsilon_{21}{}^{\eta_1} = 0$

For the size of the Representative Volume Element (RVE) that is selected for the current work, the materials of the top coat can be assumed to be polycrystalline, isotropic and inhomogeneous with elastic stiffness constants that vary smoothly from one phase to the other. The elastic stiffness constants are defined as:

$$C_{ijkl} = C_{ijkl}{}^{m} \cdot h(\eta_1) + C_{ijkl}{}^{t} \cdot \left(1 - h(\eta_1)\right) \qquad (C.11)$$

Where,

$h(\eta_1)$ = Type II interpolation function (previously defined in chapter 5)

${C_{ijkl}}^m$ = elastic stiffness constant for the m − phase

${C_{ijkl}}^t$ = elastic stiffness constant for the t − phase

The polycrystalline average of the anisotropic elastic stiffness constants was carried out using the Voigt [**152**] and Reuss [**153**] models. The effective elastic stiffness constants was then taken as the average of the two isotropic elastic stiffness constants that were obtained using the Voigt and Reuss models. Details regarding the procedure and equations for such calculation can be found in Ref. [**154**].

Appendix D: Normalization

The length (x), free energy (f), and diffusion mobility (M_S) are normalized by the following characteristic constants:

$$x_c = l_0, \qquad f_c = \Delta f_{max}, \qquad M_{Sc} = M_S$$

Where,

$\Delta f_{max} = height\ of\ the\ energy\ barrier$

$l_0 = characteristic\ lenght$

Therefore the normalized length, free energy, and the diffusion mobility are normalized by:

$$\bar{x} = \frac{x}{l_0}, \qquad \bar{f} = \frac{f}{\Delta f_{max}}, \qquad \bar{M}_S = \frac{M_S}{M_{Sc}} = 1$$

By denoting the normalization constants for the kinetic mobility, time, gradient energy coefficient, and the elastic stiffness constant as:

$$L_{1c}, \qquad T, \qquad \alpha_{1c}, \qquad C_c$$

Then the normalized kinetic mobility, time and gradient energy coefficients becomes:

$$\bar{L}_1 = \frac{L_1}{L_{1c}}, \qquad \bar{t} = \frac{t}{T}, \qquad \bar{\alpha}_1 = \frac{\alpha_1}{\alpha_{1c}}, \qquad C_c = \frac{C}{C_c}$$

Then substituting the normalized variables in the Cahn-Hilliard equations, the normalization constants for time is obtained as follows:

$$\frac{\partial X_S}{\partial t} = \nabla \cdot \left[M_S \nabla \left(\frac{\partial f}{\partial X_S} \right) \right]$$

$$\frac{\partial X_S}{T \partial \bar{t}} = \frac{\bar{M}_S M_{Sc} \Delta f_{max}}{{l_0}^2} \bar{\nabla} \cdot \left[\bar{\nabla} \left(\frac{\partial \bar{f}}{\partial X_S} \right) \right]$$

$$\therefore T = \frac{{l_0}^2}{M_{Sc} \Delta f_{max}} = \frac{{l_0}^2}{M_S \Delta f_{max}}$$

$$\therefore \frac{\partial X_S}{\partial \bar{t}} = \bar{M}_S \, \bar{\nabla} \cdot \left[\bar{\nabla} \left(\frac{\partial \bar{f}}{\partial X_S} \right) \right]$$

Similarly, substituting the normalized variables in the Allen-Cahn equations, the normalization constants for the gradient energy and kinetic mobility is obtained as follows.

$$\frac{\partial \eta_1}{\partial t} = -L_1 \left(\frac{\partial f}{\partial \eta_1} - \alpha_1 \nabla^2 \eta_1 + \frac{\partial f_{el}}{\partial \eta_1} \right)$$

$$\frac{\partial \eta_1}{T \partial \bar{t}} = -L_{1c} \bar{L}_1 \left(\Delta f_{max} \frac{\partial \bar{f}}{\partial \eta_1} - \frac{\alpha_{1c} \bar{\alpha}_1}{l_0} \nabla^2 \eta_1 + C_c \frac{\partial \overline{f_{el}}}{\partial \eta_1} \right)$$

$$\therefore\ L_{1c} = \frac{M_S}{{l_0}^2}\ \ \&\ \ \alpha_{1c} = \Delta f_{max} {l_0}^2\ \ \&\ \ C_c = \Delta f_{max}$$

$$\frac{\partial \eta_1}{\partial \bar{t}} = -\bar{L}_1 \left(\frac{\partial \bar{f}}{\partial \eta_1} - \bar{\alpha}_1 \nabla^2 \eta_1 + \frac{\partial \overline{f_{el}}}{\partial \eta_1} \right)$$

Likewise, the variation of the elastic strain energy with the concentration field is also normalized by $C_c = \Delta f_{max}$. And all the variables in the equation have been defined in Chapter 5.

Appendix E: Governing Equations

a. Governing equations for hot corrosion of TBC

In complete form, the PDEs for the V2O5 hot corrosion of TBC can be expressed as:

$$\frac{\partial X_{VO}}{\partial \bar{t}} = \nabla \cdot \left[\frac{2A(T)}{1000 \times \Delta f_{max}} \left[\bar{\nabla} X_{VO} - \left({X_m}^{eq} - {X_t}^{eq} \right) \cdot \bar{\nabla} h(\eta_1) \right] \right] \qquad (E.1)$$

$$
\begin{aligned}
\frac{\partial \eta_1}{\partial \bar{t}} = -\bar{L}_1 \Bigg[\Bigg\{ \Bigg(& \frac{2A(T)}{1000 \times \Delta f_{max}} \left[X_{VO} - {X_t}^{eq} - ({X_m}^{eq} - {X_t}^{eq}) \cdot h(\eta_1) \right] \times \frac{\partial h(\eta_1)}{\partial \eta_1} \\
& \times -({X_m}^{eq} - {X_t}^{eq}) \Bigg) + \frac{w_1}{1000 \times \Delta f_{max}} \frac{\partial g(\eta_1)}{\partial \eta_1} - \bar{\alpha}_1 \nabla^2 \eta_1 \Bigg\} \\
& - \frac{1}{1000} \Big\{ \big[2(\bar{C}_{11}\, {\varepsilon_{11}}^{\eta_1}\, \eta_1 + \bar{C}_{12}\, {\varepsilon_{12}}^{\eta_1}\, \eta_1) u_{1,1} + 4\bar{C}_{66}\, {\varepsilon_{21}}^{\eta_1} (u_{1,2} + u_{2,1}) \\
& + 2(\bar{C}_{12}\, {\varepsilon_{11}}^{\eta_1}\, \eta_1 + \bar{C}_{22}\, {\varepsilon_{22}}^{\eta_1}\, \eta_1) u_{2,2} \big] + 2(\bar{C}_{11} ({\varepsilon_{11}}^{\eta_1})^2\, {\eta_1}^2 \\
& + 2\bar{C}_{12}\, {\varepsilon_{11}}^{\eta_1}\, {\varepsilon_{22}}^{\eta_1}\, {\eta_1}^2 + 4\bar{C}_{66} ({\varepsilon_{12}}^{\eta_1})^2\, {\eta_1}^2 \\
& + \bar{C}_{22} ({\varepsilon_{22}}^{\eta_1})^2\, {\eta_1}^2) \Big\} \Bigg] \qquad (E.2)
\end{aligned}
$$

$$
\begin{aligned}
& \bar{C}_{11}\bar{u}_{1,11} + \bar{C}_{12}\bar{u}_{2,21} + \bar{C}_{44}(\bar{u}_{2,12} + \bar{u}_{1,22}) - (\bar{C}_{11}\, {\varepsilon_{11}}^{\eta_1} + \bar{C}_{12}\, {\varepsilon_{22}}^{\eta_1}) \frac{\partial ({\eta_1}^2)}{\partial x} \\
& - 2\bar{C}_{44}\, {\varepsilon_{12}}^{\eta_1} \frac{\partial ({\eta_1}^2)}{\partial y} = 0 \qquad (E.3)
\end{aligned}
$$

$$
\begin{aligned}
& \bar{C}_{22}\bar{u}_{2,22} + \bar{C}_{12}\bar{u}_{1,12} + \bar{C}_{44}(\bar{u}_{1,21} + \bar{u}_{2,11}) - (\bar{C}_{12}\, {\varepsilon_{11}}^{\eta_1} + \bar{C}_{22}\, {\varepsilon_{22}}^{\eta_1}) \frac{\partial ({\eta_1}^2)}{\partial y} \\
& - 2\bar{C}_{44}\, {\varepsilon_{21}}^{\eta_1} \frac{\partial ({\eta_1}^2)}{\partial y} = 0 \qquad (E.4)
\end{aligned}
$$

Where,

$h(\eta_1) = TYPE\ II\ interpolation\, function = -2{\eta_1}^3 + 3{\eta_1}^2$

$g(\eta_1) = Double - well\, potential = {\eta_1}^2 (1 - \eta_1)^2$

a. Governing equations for gas nitriding of hot extrusion dies

For analysis in the diffusion layer

In complete form, the PDEs for the analysis within the diffusion layer during the gas nitriding of hot extrusion dies can be expressed as:

$$\frac{\partial X_N}{\partial \bar{t}} = \nabla \cdot [D(T)\bar{\nabla} X_N] \qquad (E.5)$$

$$\bar{C}_{11}\bar{u}_{1,11} + \bar{C}_{12}\bar{u}_{2,21} + \bar{C}_{44}\left(\bar{u}_{2,12} + \bar{u}_{1,22}\right) - (\bar{C}_{11}\,\varepsilon_{11}{}^{c} + \bar{C}_{12}\,\varepsilon_{22}{}^{c})\frac{\partial X_N}{\partial x} = 0 \qquad (E.6)$$

$$\bar{C}_{22}\bar{u}_{2,22} + \bar{C}_{12}\bar{u}_{1,12} + \bar{C}_{44}\left(\bar{u}_{1,21} + \bar{u}_{2,11}\right) - (\bar{C}_{21}\,\varepsilon_{11}{}^{c} + \bar{C}_{22}\,\varepsilon_{22}{}^{c})\frac{\partial X_N}{\partial y} = 0 \qquad (E.7)$$

For analysis in both compound and diffusion layer

In complete form, the PDEs for the analysis within the diffusion and compound layer during the gas nitriding of hot extrusion dies can be expressed as:

$$\begin{aligned}\frac{\partial X_N}{\partial \bar{t}} = \nabla \cdot \Bigg[\frac{2A(T)}{\Delta f_{max}}&[\bar{\nabla} X_N - (X_e{}^{eq} - X_a{}^{eq}) \cdot \bar{\nabla} h(\eta_1)] \\ &+ \nabla\left\{-\frac{1}{2}(\bar{C}_{11} + \bar{C}_{21})\,\varepsilon_{11}{}^{c}\left[\bar{u}_{1,1} - \varepsilon_{11}{}^{c}\left(X_N - \bar{X}_{avg}\right)\right] - (\bar{C}_{12}\right. \\ &\left.+ \bar{C}_{22})\,\varepsilon_{22}{}^{c}\left[\bar{u}_{2,2} - \varepsilon_{22}{}^{c}(X_N - \bar{X}_{avg})\right]\right\}\Bigg] \qquad (E.8)\end{aligned}$$

$$\begin{aligned}\frac{\partial \eta_1}{\partial \bar{t}} = -\bar{L}_1 \Bigg[\Bigg\{\Bigg(&\frac{2A(T)}{\Delta f_{max}}[X_N - X_a{}^{eq} - (X_e{}^{eq} - X_a{}^{eq}) \cdot h(\eta_1)] \times \frac{\partial h(\eta_1)}{\partial \eta_1} \\ &\times -(X_e{}^{eq} - X_a{}^{eq})\Bigg) + \frac{w_1}{\Delta f_{max}}\frac{\partial g(\eta_1)}{\partial \eta_1} - \bar{\alpha}_1 \nabla^2 \eta_1\Bigg\}\Bigg] \qquad (E.9)\end{aligned}$$

$$\bar{C}_{11}\bar{u}_{1,11} + \bar{C}_{12}\bar{u}_{2,21} + \bar{C}_{44}\left(\bar{u}_{2,12} + \bar{u}_{1,22}\right) - (\bar{C}_{11}\,\varepsilon_{11}{}^{c} + \bar{C}_{12})\,\varepsilon_{22}{}^{c}\frac{\partial X_S}{\partial x} = 0 \qquad (E.10)$$

$$\bar{C}_{22}\bar{u}_{2,22} + \bar{C}_{12}\bar{u}_{1,12} + \bar{C}_{44}\left(\bar{u}_{1,21} + \bar{u}_{2,11}\right) - (\bar{C}_{21}\ \varepsilon_{11}{}^{c} + \bar{C}_{22}\ \varepsilon_{22}{}^{c})\frac{\partial X_S}{\partial y} = 0 \qquad (E.11)$$

Appendix F: Implementation Details

a. TBC Hot Corrosion

For Analysis in the PRZ

Table F.1 gives a brief description of the COMSOL implementation parameters used in the simulation.

Table F.1: Implementation details for analysis in PRZ

Parameter	Description
Physics node	PDE Interface
Element type	Lagrange-quadratic discretization Four-noded quadrilateral elements Aspect ratio=1 Number of elements=8,000 Number of degree of freedoms=129,924
Mesh type	Mapped mesh (shown in Fig. F.1)

Time stepping	Backward Difference Approximation (BDA) Variable time steps used based on 1st-5th BDA approximation
Relative tolerance	1 x 10^{-10}
Absolute tolerance	1 x 10^{-3}
Solution time	40 minutes 6 s
Mesh Convergence test Time independence test	Passed Passed

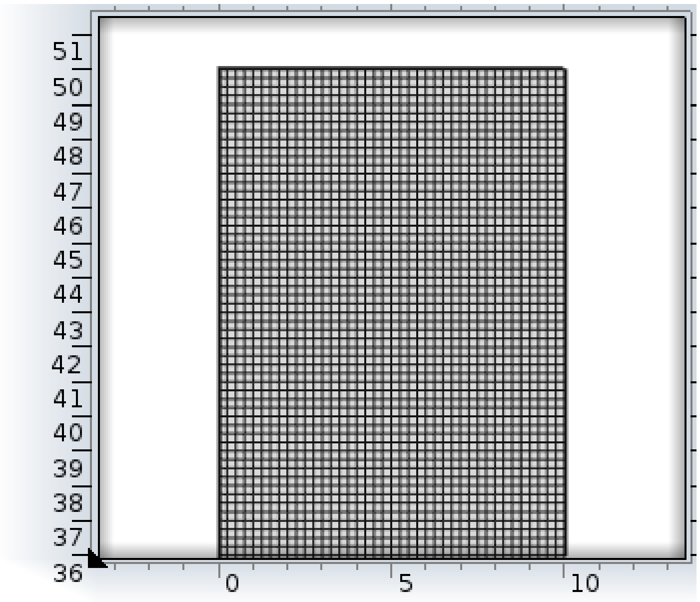

Figure F.1: Mesh for PRZ

For analysis in MIRZ

Table F.2 gives a brief description of the COMSOL implementation parameters used in the simulation.

Table F.2: Implementation details for analysis in PRZ

Parameter	Description
Physics node	PDE Interface
Element type	Lagrange-quadratic discretization Four-noded quadrilateral elements Aspect ratio=0.5301 Number of elements=9,000 Number of degree of freedoms=145,324
Mesh type	Mapped mesh shown in Fig. F.2
Time stepping	Backward Difference Approximation (BDA) Variable time steps used based on 1st-5th BDA approximation
Relative tolerance	1×10^{-10}
Absolute tolerance	1×10^{-3}
Solution time	23 mins 50 s

Mesh Convergence test	Passed
Time independence test	Passed

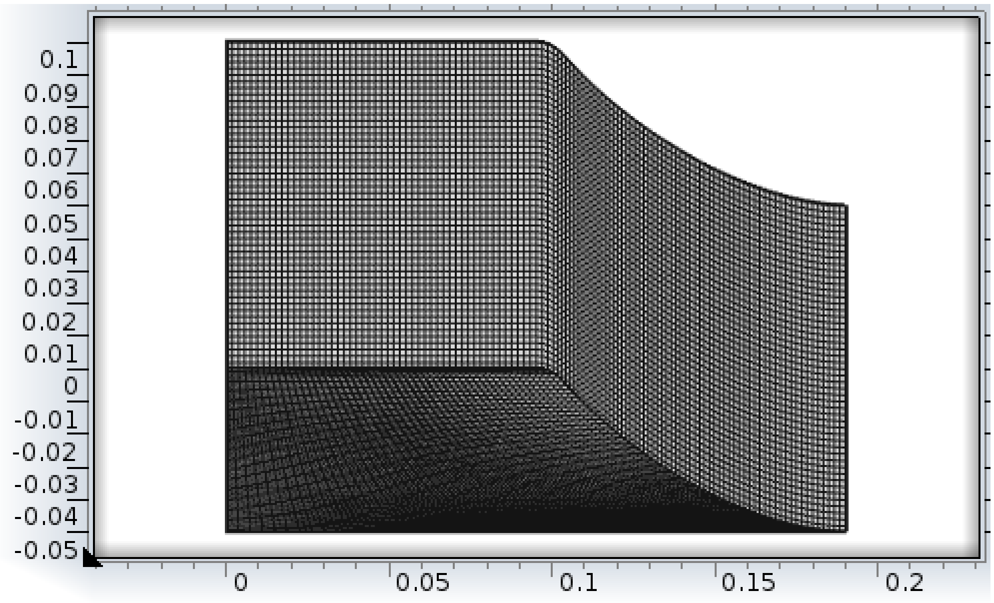

Fig. F.2: Mesh for MIRZ

a. Gas nitriding of hot extrusion dies

For Analysis in the diffusion layer

Table F.3 gives a brief description of the COMSOL implementation parameters used in the simulation.

Table F.3: Implementation details for analysis in PRZ

Parameter	Description

Physics node	PDE Interface
Element type	Lagrange-quadratic discretization three-noded triangular elements Aspect ratio=0.9259 Number of elements=201,495 Number of degree of freedoms=1319063
Mesh type	Physics controlled mesh shown in Fig. F.3
Time stepping	Backward Difference Approximation (BDA) Variable time steps used based on 1st-5th BDA approximation
Relative tolerance	1×10^{-10}
Absolute tolerance	1×10^{-3}
Solution time	20 mins 5 s
Mesh Convergence test Time independence test	Passed Passed

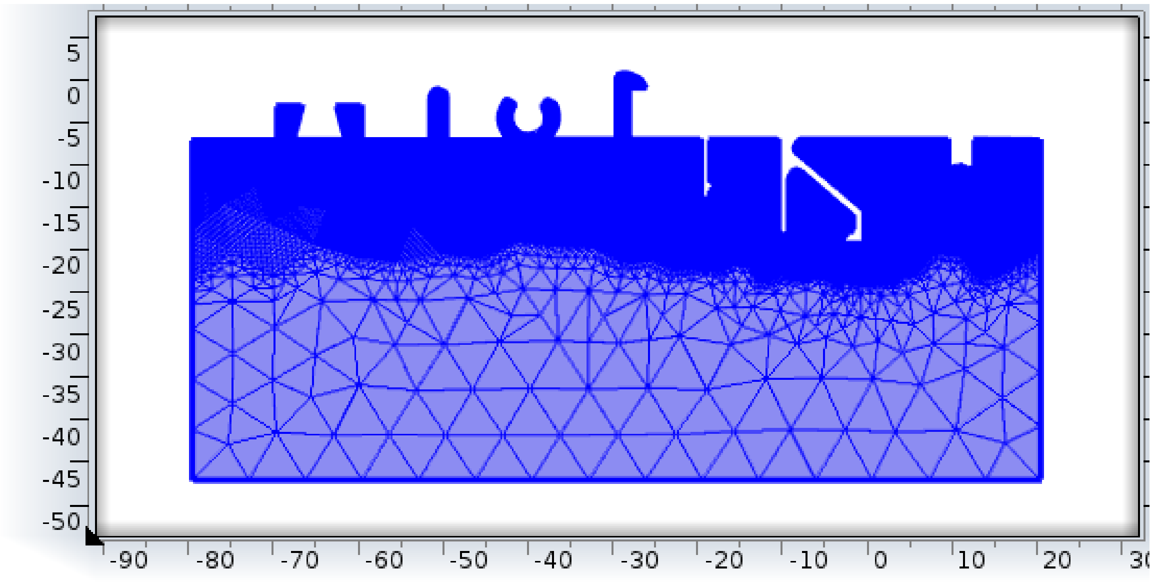

Fig.F3: Mesh for analysis in Diffusion layer

For analysis in the compound layer

Table F.4 gives a brief description of the COMSOL implementation parameters used in the simulation.

Table F.4: Implementation details for analysis in PRZ

Parameter	**Description**
Physics node	PDE Interface
Element type	Lagrange-quadratic discretization Four-noded quadrilateral elements Aspect ratio=1 Number of elements=1600

	Number of degree of freedoms=26,565
Mesh type	Mapped mesh shown in Fig. F.4
Time stepping	Backward Difference Approximation (BDA) Variable time steps used based on 1st-5th BDA approximation
Relative tolerance	1×10^{-10}
Absolute tolerance	1×10^{-3}
Solution time	7 mins 47 s
Mesh Convergence test Time independence test	Passed Passed

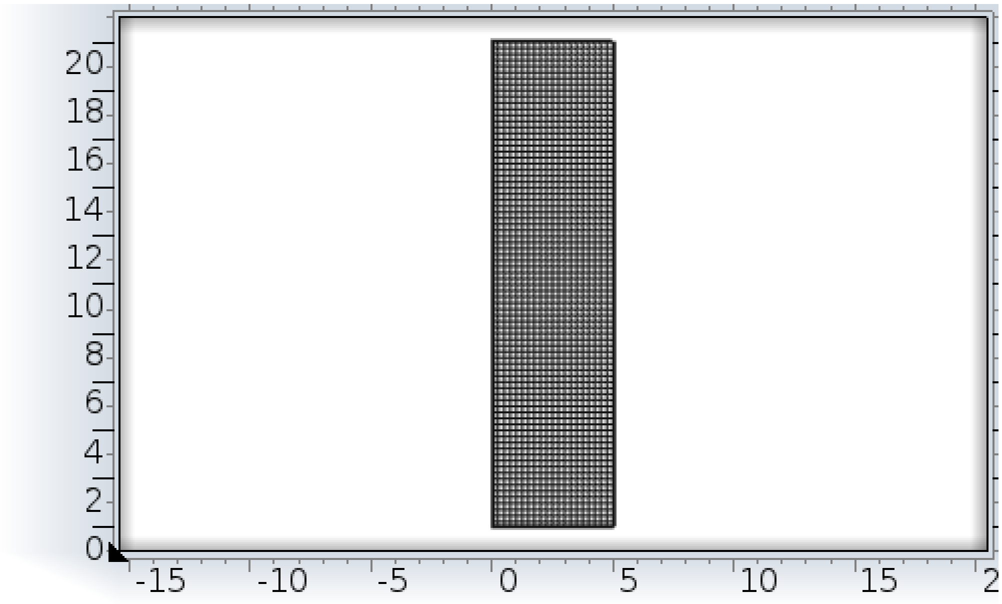

Fig. F.4: Mesh for analysis in compound layer

VITAE

Name : Abba Abdulhamid Abubakar

Nationality : Nigerian

Date of Birth : 2/1/1988

Email : abbamec@yahoo.com

Telephone Numbers : +2348067196429

Permanent Address : No. 125 Kurawa Quarters, Kano City

Academic Background : B.Eng Mechanical Engineering (2011)

First Class Honours

Bayero University Kano, Nigeria

Research Papers

1. **Abubakar A.A.**, Akhtar S.S., and Arif A.F.M., "Phase transformation stress field due to hot corrosion in the top coat of TBC," in Proceedings of the ASME 2013 International Mechanical Engineering Congress and Exposition, IMECE2013, San Diego, California, USA, November 15-21, 2013. **(Presented)**
2. **Abubakar A.A.**, Akhtar S.S., and Arif A.F.M., "The Effect of V_2O_5 Melt Infiltration on the Failure of Thermal Barrier Coatings," in AES-ATEMA'2014 Eighteen International Conference on Advances and Trends in Engineering

Materials and their Applications, Toronto, CANADA, August 11 – 15, 2014. **(Accepted)**

3. Akhtar S.S., Arif A.F.M., and Abubakar A.A., "Gas Nitriding of AISI H13 Steel Extrusion Dies: Consideration of Sharp Features in the Die Profiles," in Montreal'2014 AES-ATEMA 17th International Conference, Toronto, CANADA, August 11-15, 2014, pp. MONTREAL'2014-50. **(Accepted)**
4. Akhtar S.S., Abubakar A.A., and Arif A.F.M., "Prediction of transformation-induced residual stresses during gas nitriding of H13 steels using Phase Field Approach," in Proceedings of the ASME 2014 International Mechanical Engineering Congress & Exposition IMECE2014, Montreal, Quebec, Canada, November 14-20, 2014. **(Accepted)**
5. Abubakar A.A., Aktar S.S., Arif A.F.M., "Phase Field Modeling of V_2O_5 Corrosion Kinetics in Thermal Barrier Coatings", Computational Material Science Journal. **(Under Review)**